Controlling structural, chemical and electronic properties of single molecules on surfaces

Inauguraldissertation

zur

Erlangung der Würde eines Doktors der Philosophie

vorgelegt der

Philosophisch-Naturwissenschaftlichen Fakultät

der Universität Basel

von

Tobias Meier

aus Lörrach, Deutschland

Basel, 2018

Genehmigt von der Philosophisch-Naturwissenschaftlichen Fakultät
auf Antrag von:

Prof. Dr. Ernst Meyer
Prof. Dr. Martino Poggio

Basel, den 27. Februar 2018

Prof. Dr. Martin Spiess, Dekan

Abstract

With the prospects of realizing electronic circuitry and machinery consisting of a single-molecule, the control of the molecular characteristics down to the atomic level is essential. In this thesis, fundamental investigations of structures, electronic properties and diffusion of molecules on surfaces are presented. The experiments are performed by means of scanning tunneling microscopy (STM) and atomic force microscopy (AFM) at low temperature in ultra-high vacuum. The control of elaborated structures is achieved by studying on-surface chemical reactions and spray-deposited molecules by high-resolution AFM imaging with CO terminated tips. To mimic a p-n junction, a donor-acceptor (DA) molecule on a thin insulating film is probed to disentangle its structure, electronic states and charge redistribution. Interestingly, the DA character of the molecule is altered at specific atomic positions, and thus controlled by inducing a change of the adsorption site by tip manipulation. This consists of an example of a molecular switch. In this line, tip manipulation experiments are pushed forward during the NanoCar Race by steering a single molecule over the surface using tunneling electrons. The results of this thesis demonstrate the impact of the molecular design on electronic and adhesion properties influencing the performance of such molecular systems.

Keywords: molecular electronics, molecular machines, scanning tunneling microscopy, atomic force microscopy, force spectroscopy, molecules, donor-acceptor molecules, tip manipulation

Zusammenfassung

Um elektronische Schaltungen und Maschinen aus nur einem Molekül zu realisieren, ist die Kontrolle molekularer Eigenschaften bis zu einem atomaren Niveau essenziell. In dieser Dissertation werden grundlegende Untersuchungen der Strukturen und elektronischen Eigenschaften von Molekülen auf Oberflächen sowie deren Diffusion vorgestellt. Die Experimente werden mithilfe der Rastertunnel- (STM) und Rasterkraftmikroskopie (AFM) im Ultrahochvakuum bei tiefen Temperaturen durchgeführt. Aufwendige Strukturen können durch chemische Oberflächenreaktionen oder aufgesprühte Moleküle gezielt erzeugt und mit hochauflösenden AFM-Messungen mit CO-Spitzen untersucht werden. Um einen p-n-Übergang zu imitieren, wird ein Donor-Akzeptor (DA)-Molekül auf einem dünnen Isolatorfilm positioniert, sodass seine Struktur, elektronischen Eigenschafen und Ladungsumverteilung entflochten werden. Interessanterweise wird der DA-Charakter des Moleküls auf bestimmten atomaren Positionen verändert und durch einen herbeigeführten Wechsel der Adsorptionsposition mit Spitzen-Manipulation kontrolliert. Somit handelt es sich um ein Beispiel für einen molekularen Schalter. Beim NanoCar Race werden Spitzen-Manipulationen weiterentwickelt, indem ein einzelnes Molekül mit Tunnelelektronen über eine Oberfläche gesteuert wird. Die Ergebnisse dieser Dissertation heben den Einfluss des molekularen Designs auf elektronische und adhäsive Eigenschaften hervor, welche die Leistungsfähigkeit der erwähnten molekularen Systeme prägen.

Contents

Introduction

In 1974, Aviram and Ratner theoretically proposed a molecule with properties that mimic a p-n junction. [1] Such a molecular p-n junction consists of a molecule with an electron donor moiety and an electron acceptor moiety connected by a σ-bridge as depcited in Fig. 1.0. Due to the donor-acceptor character of the molecular moieties, such a single molecule could rectify currents or create currents by absorbing light. Thus, the molecule acts as a diode which pushes the limits of miniaturization to the nanometer scale. By following this approach and testing single molecules as nanometer sized components for electric circuits, the field of molecular electronics was formed.

To build electric circuits, molecules have to be adsorbed on surfaces to control the molecular alignment. However, on surfaces, the electronic properties can be altered by interaction with the substrate. Since exactly these properties are essential for the functionality of molecular electronics, physical and chemical understanding is required to adapt the electronic properties of the molecule relative to the substrate, or, to protect the properties from the influence of the substrate. An experimental level might be reached, where electronic properties of molecules are intentionally controlled by manipulating their adsorption sites or their coupling to single atoms. Hence, measurements with high spatial resolution on the atomic level in combination with the quantification of local charge distributions and electronic states are needed to realise prospects in

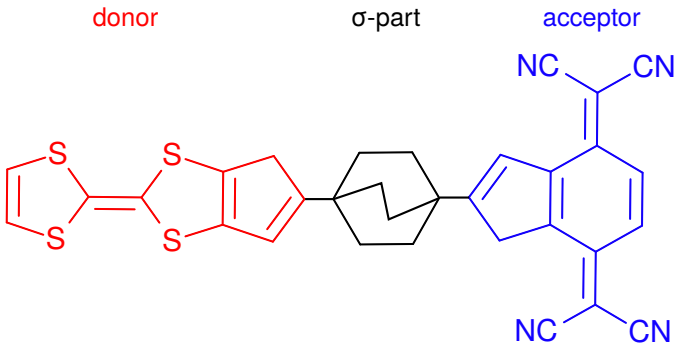

Fig. 1.0: Molecular p-n junction as proposed by Aviram and Ratner *[1]*

molecular electronics.

In 1981, a breaktrough in measurement technique was achieved by the invention of scanning tunneling microscopy (STM) [2,3] which was awarded with the Nobel Prize in Physics in 1986. STM allows to measure the tunneling current between tip and surface with atomic precision. In 1986, atomic force microscopy (AFM) [4] was further developped which permits to quantify forces at the atomic scale. Consequently, structures and properties of molecules, atoms and surfaces could be imaged at the nanoscale. Interestingly, the tip can also be used to controllably displace single molecules or atoms on a surface as shown 1993 in a famous experiment. A so-called quantum corral was built by individually arranging single atoms to a circle on a metal surface by using a STM tip. [5] The obtained corral is a barrier for surface electrons which leads to their scattering and the appearance of standing waves demonstrating quantum confinement.

In 2004, the control of charge states in single atoms was demonstrated using STM. [6] In 2005, the spatial distribution of molecular orbitals was imaged by STM. [7] In 2009, the chemical structure of a single molecule was revealed atom-by-atom using AFM. [8] Furthermore, the charge state of a single atom was determined by measuring the electrostatic forces between tip and atom in AFM. [9] In 2012, using the same technique, the charge distribution within a single molecule was uncovered. [10] Consequently, molecules similar to the proposed molecular p-n junction from Aviram and Ratner can be investigated at the nanoscale.

Molecules mimicking organic machines which perform tasks such as molecular switches [11, 12] or skeletal muscle [13] have already been synthesized and operated in solutions. In 2016, the design and synthesis of molecular machinery was awarded with the Nobel Prize in Chemistry. Molecular machines are rarely operated on surfaces [14, 15] since adsorption of molecules on surfaces leads to spatial confinement due to molecule-surface interactions. [16] Adhesion occurs between molecule and surface which complicates movements and increases friction. Thus, the mechanics of the molecular machines working in solutions might be hindered on surfaces. The influence of the surface on single molecules and tip-induced controlling mechanisms of molecular displacements could be studied by STM and AFM.

In the first chapter of this thesis, the basic concepts of STM and AFM techniques to image single atoms and molecules with atomic resolution are explained (Ch. 1). The technical prerequisites allowing single atom and molecule investigations, such as sample preparation in UHV conditions are discussed in the second chapter (Ch. 2). In Chapter 3, the capabilities of STM and AFM to atomically resolve structures and to characterize electronic and chemical properties are demonstrated. Examples are presented which show the controlled bond formation by on-surface chemical reactions and the formation of quantum states in one dimensional chains of single atoms. In Chapter 4, mechanisms for electrically propelling a molecular vehicle on a surface by a STM tip are presented which allow actuation and steering with high reliability. Electron donor-acceptor properties of a single molecule, similar to the molecular p-n junction as proposed by Aviram and Ratner, are studied on a surface (Ch. 5). The charge distribution and electronic states are characterized by combined STM and AFM measurements showing the influence of a single surface atom on the molecular properties.

Single atoms adsorbed on the surface can be attached to molecular binding sites by tip manipulation which demonstrates the controlled complex formation between a single donor-acceptor molecule and an atom. In a tentative experiment using sample illumination, the property of donor-acceptor molecules to transfer charges upon photon absorption is investigated. Additionally, the complex chemical structure of another donor-acceptor molecule which is used as dye in organic solar cells is imaged with atomic resolution.

1 Physical bases of STM and AFM

Quantum mechanics revolutionized the physical understanding of processes at the scale of atoms. New phenomena were described such as the quantized emitted energy of black bodies (Planck 1901) [17], quantization of light in the photoelectric effect (Einstein 1905) [18], quantized energy states of atoms (Bohr 1913) [19, 20], wave-particle duality (De Broglie 1924) [21], spins (Stern, Gerlach 1922) [22–24], the uncertainty principle (Heisenberg 1927) [25] and the tunneling effect (Hund, Gamow 1927, 1928) [26–28]. In 1981, Binnig, Rohrer and Gerber measured the current caused by the tunneling effect between two electrodes: a tiny metallic tip and a sample surface. [2] This experiment lead to the invention of scanning tunneling microscopy (STM: abbreviation for scanning tunneling microscopy or scanning tunneling microscope) because of the high vertical and lateral resolution explained by the exponential distance dependence of the tunneling current. [3] To investigate insulator surfaces at the atomic scale, a STM tip was mounted on a cantilever beam in order to measure small deflections coming from forces between atoms of the cantilever's tip and the sample. Thus, in 1986, Binnig, Quate and Gerber had built the first atomic force microscope (AFM: abbreviation for atomic force microscopy or atomic force microscope) [4] which was awarded with the Kavli Prize in 2016.

The microscope, used in this thesis, has the capability to apply both methods simultanously by using a tuning fork sensor [29–31], which consists of two prongs and a tip mounted to one of the prongs (Fig. 1.1). The tuning fork is oscillated at its eigenfrequency. Due to tip-sample interactions, a frequency shift occurs which can be read out for AFM operation. Furthermore, the metallic tip of the tuning fork allows to measure the tunneling current by applying a bias voltage between tip and sample enabling STM. The tip is scanned over the sample and records line by line a STM or AFM image. Additionally, scanning tunneling spectroscopy (STS) or force spectroscopy can be performed to probe local properties. The underlying physical bases of STM and AFM imaging, tunneling and force spectroscopy as well as the special features of tuning fork based AFM are explained in the following.

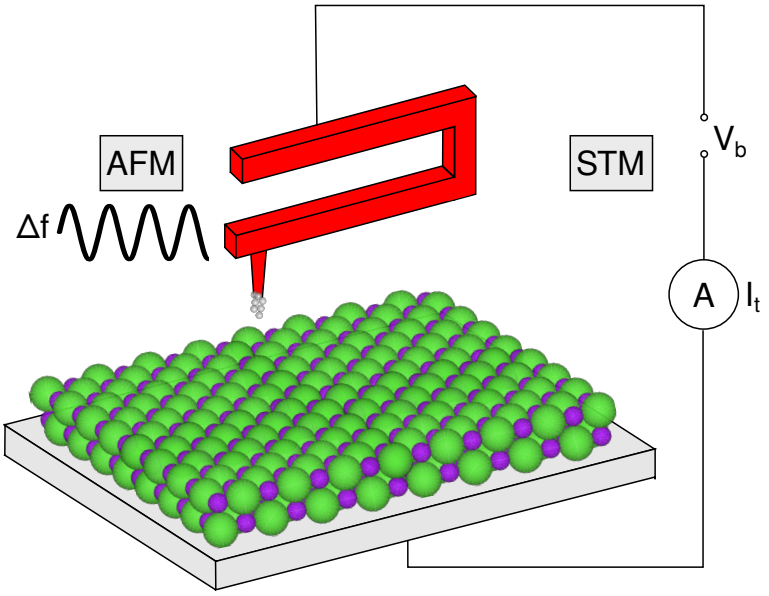

Fig. 1.1: Schematic setup of a scanning probe microscope with a tuning fork sensor. *A voltage is applied between tip and sample. The STM measures the current occurring because of the quantum tunneling effect. For the AFM, the tip oscillates at its eigenfrequency and the frequency shift Δf due to tip sample interactions is measured.*

1.1 Scanning Tunneling Microscopy

1.1.1 Historical background

After the invention of the STM by Binnig, Rohrer and Gerber in 1981 [2], atomic resolution was achieved on the structure of the Si(111)-(7x7) surface [32], of cleaved GaAs(110) [33], and of Ge(111) layers [34]. Charge-density waves could be studied [35] and atomic scale manipulations in real space were performed [36]. Later, single adatoms were laterally manipulated by a STM tip [37]. Crommie *et al.* created a quantum corral and studied the confinement of the electron gas as well as the standing waves in nearly free electron gas of noble metals. [5, 38] Furthermore, decoupling adatoms and molecules from metallic substrates by using thin NaCl layers was an important step which allowed to charge single adatoms [6] and image molecular orbitals [7]. On this basis, STM became an indispensable tool in surface science.

1.1.2 Physical basis of STM

STM is based on the quantum mechanical tunneling effect which states that an electron has a low probability to tunnel through a potential barrier that separates two electrodes (Fig. 1.2). One electrode is the STM tip with a work function Φ_{tip}, the other is the sample surface with a work function Φ_{s} which is separated by a vacuum gap of the width z. By approaching the tip and by applying a bias voltage V_b between tip and sample, a tunneling current I_t flows. Binnig, Rohrer and Gerber measured the tunneling current by approaching a piezo-controlled tip to the proximity of a surface which established

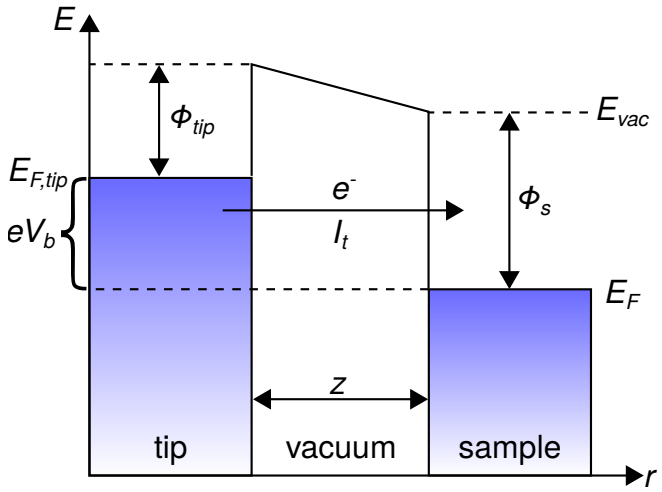

Fig. 1.2: Tunneling barrier in a STM. *Because of the quantum tunneling effect an electron has a low probability to tunnel through a barrier (vacuum) if the tip-sample distance z is small enough and a bias voltage V_b is applied.*

a controllable tunneling gap. [3] The tip-sample distance is controlled via a feedback loop which is set to keep the tunneling current constant. The distance adjustment of the tip is recorded and generates the topographic image of the surface reflecting the constant current isosurface. Another operation mode is to scan at constant tip height to map the tunneling current varying with the sample corrugation. Since STM relies on the flow of a current, the sample surface has to be electrically conductive.

The tunneling current between two electrodes in first order following Bardeen's formalism [39] is expressed by

$$I_t = \frac{2\pi e}{\hbar} \sum_{\mu,\nu} f(E_\nu) \left[1 - f(E_\mu + eV_b)\right] |M_{\mu\nu}|^2 \delta(E_\mu - E_\nu) \tag{1.1}$$

where E is the energy, e is the elementary charge, $f(E)$ is the Fermi function, $\hbar$ is the reduced Planck constant, and $M_{\mu\nu}$ describes the tunneling matrix element between the state Ψ_μ of the tip and Ψ_ν of the sample. E_μ and E_ν are the corresponding energies of the states of tip and sample, respectively. [40, 41]

Assuming small voltages and and absolute zero temperature, the tunneling current becomes

$$I_t = \frac{2\pi}{\hbar} e^2 V_b \sum_{\mu,\nu} |M_{\mu\nu}|^2 \delta(E_\mu - E_F)\delta(E_\nu - E_F). \tag{1.2}$$

where E_F is the Fermi energy.

The tunneling matrix element can be expressed as an integral over any surface which is entirely in the vacuum gap between tip and sample [39, 40]

$$M_{\mu\nu} = \frac{\hbar^2}{2m} \int d\boldsymbol{S} \cdot (\Psi_\mu^* \nabla \Psi_\nu - \Psi_\nu \nabla \Psi_\mu^*) \tag{1.3}$$

where $d\boldsymbol{S}$ is the surface element and $(\Psi_\mu^* \nabla \Psi_\nu - \Psi_\nu \nabla \Psi_\mu^*)$ is the current operator describing the probability of current flow in quantum mechanics.

At this step, the tip geometry has to be considered. In an ideal case, the tip can be described as a single point probe with localized wave functions and placed at the position $\boldsymbol{r}_{\text{tip}}$. The tunneling matrix element is then only proportional to the probability amplitude of the sample's wave function Ψ_ν which results in the expression for the tunneling current of

$$I_t \propto \sum_\nu |\Psi_\nu(\boldsymbol{r}_{\text{tip}})|^2 \delta(E_\nu - E_F) = \rho(\boldsymbol{r}_{\text{tip}}, E_F). \tag{1.4}$$

$\rho(\boldsymbol{r}_{\text{tip}}, E_F)$ is the local density of states (LDOS) of the surface at the Fermi energy E_F. Hence, the tunneling current measured in STM is proportional to the LDOS of the surface at the position of the tip. A STM image at constant current corresponds to a contour map of constant LDOS of the investigated sample surface which highlights that the STM can probe the electronic states of a sample. [40] By tuning the bias voltage, different occupied and unoccupied states of the sample contribute to the tunneling current. This is especially used in scanning tunneling spectroscopy described in Sec. 1.3.2.

To model the experimental results, more realistic tip shapes have to be considered. [42, 43] Tersoff and Hamann demonstrated that Eq. 1.4 holds for more realistic tip shapes if the elements of the tunneling matrix can be described by wave functions of a s-wave tip. [40, 42, 44, 45] By assuming a spherical tip shape with a radius of curvature R at the position $\boldsymbol{r}_{\text{tip}}$ and for simplicity, an equal work function Φ of tip and sample, the tunneling current is

$$I_t = \frac{32\pi^3 e^2 V_b \Phi^2 \rho_{\text{tip}}(E_F) R^2}{\hbar \kappa^4} \mathrm{e}^{2\kappa R} \underbrace{\sum_\nu |\Psi_\nu(\boldsymbol{r}_{\text{tip}})|^2 \delta(E_\nu - E_F)}_{\rho(\boldsymbol{r}_{\text{tip}}, E_F)} \tag{1.5}$$

where ρ_{tip} is the density of states per unit volume of the tip, κ is the minimum inverse decay length for the tunneling electrons, defined as

$$\kappa = \frac{\sqrt{2m\Phi}}{\hbar} \tag{1.6}$$

Comparison of Eq. 1.5 to Eq. 1.4 shows that the tunneling current is proportional to the LDOS of the sample also for more realistic tip models. The amplitude of the wave function is $|\Psi_\nu(\boldsymbol{r}_{\text{tip}})|^2 \propto e^{-2\kappa(R+z)}$ where d is the smallest tip-sample distance, which leads to

$$I_t \propto \mathrm{e}^{-2\kappa z} \tag{1.7}$$

Thus, the tunneling current is exponentially dependent from the tip-sample distance z which points out the high sensitivity of the STM in z-direction since the tunneling current changes in the order of magnitudes as function of atomic distances.

1.2 Atomic Force Microscopy

1.2.1 Historical background

After the invention of the first AFM in 1986 by Binnig, Quate and Gerber [4], AFM measurements were further improved by oscillating the tip and using AFM in a dynamic mode. [30, 46–48] True atomic resolution [49] was achieved by resolving atomic scale defects and the atomic surface lattice in the same image which demonstrated the capability of AFM to resolve structures at the atomic scale comparable to the STM. [50–53] Especially, insulator surfaces can be investigated by AFM since an electrical conductivity is not required as for STM. [54, 55] Fluoride and oxide surfaces as well as semiconductor surfaces were explored by means of AFM. [50, 52, 56–58] Also on metals, the atomic surface structure was resolved as well as on thin NaCl films on metal substrates. [59–61] Molecules can be studied on metallic and on insulating surfaces by AFM. [62, 63] Additionally, AFM operation was also achieved in liquid-solid interfaces. [64, 65] Moreover, AFM could prove its versatility by imaging a wide range of samples such as DNA, proteins, viruses, and polymers. [66–69]

Equipped with the tuning fork setup [29, 30], AFM allows stable measurements with small amplitudes at low temperature (LT). Most notably, purely metallic tips can be used which enables the controlled preparation of the tip apex and simultaneous STM and AFM measurements. By means of tuning fork AFM at LT in ultra-high vacuum (UHV), tips terminated with single CO molecules could be prepared and used to resolve the chemical structure of single molecules. [8, 70]

In the following, the forces acting between tip and sample and the physical principles of AFM, considering the special features of tuning fork setups, are discussed.

1.2.2 Force contributions

AFM is sensitive to forces which arise between the atoms of the tip and the sample. In contrast to the tunneling current which is monotonically and exponentially increasing by reducing the tip sample distance, the various forces acting on the tip have different interaction regimes leading to a non-monotonic behavior (Fig. 1.3).

In vacuum there are electrostatic $F_{\mathrm{elec,lr}}$ and van der Waals forces $F_{\mathbf{vdW}}$ having a long-range order and contribute in a distance range of 100 nm, contrary to chemical forces F_{chem} having a short-range order and acting only in the sub-nm distance regime. [30] The electrostatic force has also short-range components $F_{\mathrm{elec,sr}}$. All together they create the total force between tip and sample, F_{ts}, which is attractive in the far distance and repulsive in the close distance regime:

$$F_{\mathrm{ts}} = \underbrace{F_{\mathrm{vdW}} + F_{\mathrm{elec,lr}}}_{\text{long range}} + \underbrace{F_{\mathrm{chem}} + F_{\mathrm{elec,sr}}}_{\text{short range}} \tag{1.8}$$

Thus, stable operation of an AFM using a feedback loop is more elaborated than for STM. The total force is measured with a spring which is, most commonly, a silicon cantilever or, as in this thesis, a quartz tuning fork (Fig. 1.1). Because of the general

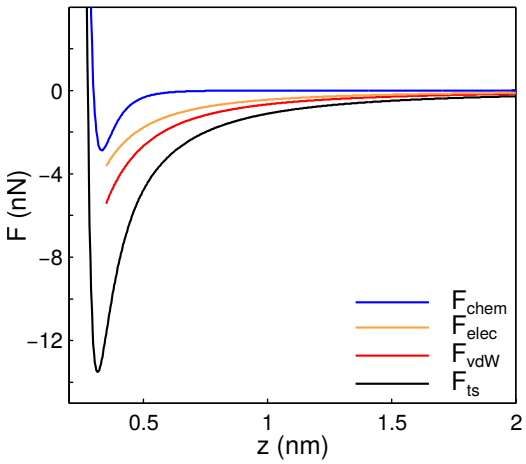

Fig. 1.3: Different forces acting between tip and sample in AFM. *Van der Waals F_{vdW} and electrostatic forces F_{elec} have long-range order whereas chemical forces F_{chem} are short-range which is expressed by the Lennard-Jones-potential U_{LJ}. The tip-sample forces F_{ts} are plotted as the sum of all force contributions. Plots based on Eqs. 1.8, 1.12, 1.15 and 1.16. Plotting parameters: $\sigma = 300\,pm$, $A_H = 1.25\,eV$, $R = 20\,nm$, $E_{bond} = 2\,eV$, $V_b - V_{CPD} = 0.2\,V$.*

force sensitivity AFM is not limited to conductive sample surfaces and can scan every flat surface in principle.

Van der Waals forces Van der Waals (vdW) forces are present between all atoms. They are caused by fluctuations of the electron density by approaching two atoms to each other. Several contributions are attributed to vdW forces. It has to be distinguished between the interactions of

- permanent charges (Keesom interaction)
- a permant charge and an induced multipole in another molecule (Debye force)
- instantaneously developing multipoles (London dispersion force)

In AFM, vdW forces between tip and sample refer to London dispersion forces.

By approaching two neutral atoms A and B to a distance z, their spherical-symmetrical electron cloud is mutually influenced which leads to the formation of an induced dipole moment $\boldsymbol{p}_{\mathrm{ind}}$ in both atoms, parallel to the connecting axis. Because the electric field $\mathcal{E} \propto \frac{1}{z^3}$ and the potential energy of a dipole $U_{\mathrm{dip}}(z) = -\boldsymbol{p}_{\mathrm{ind}}\mathcal{E}$, it follows that their interaction potential is

$$U_{\mathrm{attr}}(z) \propto -\boldsymbol{p}_{\mathrm{ind,A}} \cdot \boldsymbol{p}_{\mathrm{ind,B}} \propto -\alpha_{\mathrm{A}} \cdot \alpha_{\mathrm{B}} |\mathcal{E}|^2 \tag{1.9}$$

$$\propto -\frac{\alpha_{\mathrm{A}} \cdot \alpha_{\mathrm{B}}}{z^6} \tag{1.10}$$

where α_{A} and α_{B} are the polarizabilities of atom A and B. Eq. 1.10 shows that the vdW forces lead to an attractive potential U_{attr} between tip and sample atoms. By modelling

the tip with a sphere which is interacting with a planar sample surface, Hamaker showed that adding up the vdW forces of the contributing atoms yields [30, 71, 72]

$$U_{\mathrm{vdW}} = -\frac{A_{\mathrm{H}} R}{6z} \tag{1.11}$$

$$F_{\mathrm{vdW}} = -\frac{A_{\mathrm{H}} R}{6z^2} \tag{1.12}$$

for the vdW potential and vdW force, respectively. A_{H} is the so-called Hamaker constant which depends on the material of tip and sample. By increasing the tip radius R, the vdW forces are increasing. Therefore, a sharper tip leads to less long range contributions from vdW forces and is benefitial for high resolution measurements.

Chemical forces The short-range contribution on the total tip-sample force emerges from the chemical forces which arise when two atoms are approached in the range of few Angstroms. [73] The front atoms of the tip temporarely form covalent bonds with atoms of the surface leading to the so-called chemical force. The chemical interaction can be expressed by the Morse potential

$$U_{\mathrm{Morse}} = -E_{\mathbf{bond}} \left(2\mathrm{e}^{-\xi(z-\sigma)} - \mathrm{e}^{-2\xi(z-\sigma)}\right) \tag{1.13}$$

where $E_{\mathbf{bond}}$ is the bonding energy, σ is the equilibrium distance and ξ is the decay length. The Morse potential qualitatively describes the distance dependence of chemical forces arising in the direction of the bonds. However, the directionality of chemical bonds, especially covalent ones, leading to an angular dependence of the bonding strength is not included in the Morse potential. [30]

Further decreasing the distance between tip and sample leads to a repulsive force caused by Pauli repulsion and ion-ion interaction of the unshielded atomic cores. The repulsive interaction force in the short-distance regime is empirically described by a z^{-12}-dependence. Combined with the z^{-6}-term of the long-range vdW forces (Eq. 1.10), the Lennard-Jones potential [74]

$$U_{\mathrm{LJ}} = -E_{\mathrm{bond}} \left(2\left(\frac{\sigma}{z}\right)^6 - \left(\frac{\sigma}{z}\right)^{12}\right) \tag{1.14}$$

$$F_{\mathrm{LJ}} = -\frac{12E_{\mathrm{bond}}}{\sigma} \left(\left(\frac{\sigma}{z}\right)^7 - \left(\frac{\sigma}{z}\right)^{13}\right) \tag{1.15}$$

describes the interaction between two approaching atoms (Fig. 1.3).

For high resolution in AFM, it is required to sense the chemical forces which vary with atomic dimensions. Therefore, the tip has to be approached to the close-distance regime, where the short-range chemical forces contribute considerably to the total tip-sample force. [30] The long-range forces are reduced by sharpening the tip which decreases the number of interacting atoms on the tip apex. Thus, AFM provides a local probe to test chemical interaction forces at the atomic scale. [75]

Electrostatic forces In general, tip and sample have different electrostatic potentials which leads to the contact potential difference (CPD) creating long-range electrostatic forces. The CPD between tip and sample can be compensated by applying a voltage V_{CPD} which is used in Kelvin probe force microscopy (KPFM), explained in Sec. 1.3.1.

The system of tip and sample can be described by a charged plate capacitor whose capacitance $C(z)$ is distance dependent. Assuming a conductive spherical tip with radius R and a conductive planar surface, the electrostatic force is expressed by [76]

$$F_{\mathrm{elec,lr}}(z) = \frac{1}{2}\frac{\partial C}{\partial z}\left(V_b - V_{\mathrm{CPD}}\right)^2 = -\pi\epsilon_0 \frac{R^2}{z(z+R)}\left(V_b - V_{\mathrm{CPD}}\right)^2 \tag{1.16}$$

where ϵ_0 is the vacuum permittivity.

Short-range electrostatic forces arise from local charges, *e.g.* of ions in ionic thin films or charge distributions in molecules. The force sensitivity of AFM, which is the topic of the next section, allows to detect local variations of the short-range electrostatic forces. This is used in force spectroscopy measurements (Sec. 1.3.1).

1.2.3 Physical basis of AFM

Tuning fork based AFM in UHV conditions is usually operated in the non-contact mode. In non-contact AFM, the tuning fork is driven to oscillate with an amplitude A perpendicular to the surface at its resonance frequency f_0. The tuning fork has a stiffness k_{c} and is oscillating with a quality factor Q. By using an oscillating tip, the average tip-sample distance is increased which leads to a total tip-sample force staying in the attractive, non-contact regime. [30] Non-contact AFM can be performed with the amplitude-modulation (AM) technique. [46] In AM-AFM the cantilever is driven by a fixed driving amplitude and driving frequency which is slightly off the resonance. Tip-sample interactions cause a change of amplitude and phase between driving and detected oscillation. The amplitude is used as input for the feedback system. However, in UHV conditions, AM-AFM is rarely operated because the high Q factors slow up the amplitude change and consequently the whole feedback system. [30] In the tuning fork based AFM measurements in this thesis, the frequency-modulation (FM) technique is applied to drive the oscillation always at its eigenfrequency. [47] This is realized by a phase-locked loop which records the frequency shift due to tip-sample interaction and adjusts the excitation frequency by keeping a constant phase lag between the excitation and oscillation.

By approaching the tip to the sample, the eigenfrequency of the oscillator shifts to lower values due to attractive interaction forces leading to a more negative frequency shift Δf (Fig. 1.4). Approaching the tip further, repulsive forces induce a shift of the eigenfrequency to higher frequencies resulting in a more positive Δf. When performed with cantilever sensors, AFM is usually conducted by recording the topography at constant frequency shift which is controlled by the feedback loop. In tuning fork AFM the constant-height mode is most commonly used to achieve high resolution on atomically flat samples at low temperature with reduced thermal drift. In this mode, the frequency shift which varies depending on the local tip-sample distance and tip-sample interactions is recorded at a fixed absolute height.

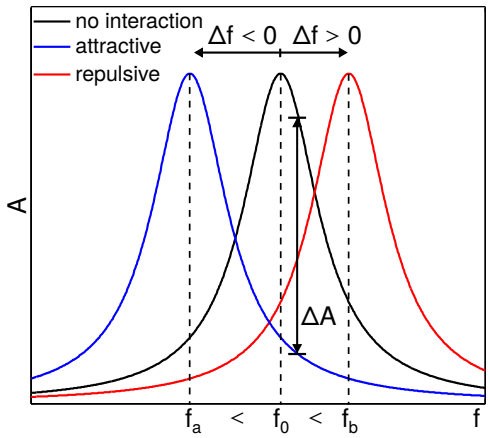

Fig. 1.4: Amplitude vs. frequency in AFM. *Frequency shift Δf and amplitude change ΔA due to attractive or repulsive interaction used for the feedback of FM-AFM or AM-AFM, respectively.*

The frequency of the tuning fork's oscillation changes due to the tip-sample forces

$$f = f_0 + \Delta f \tag{1.17}$$

where f_0 is the eigenfrequency of the tuning fork far away from the surface. The vertical unperturbed motion of the tuning fork can be described as an harmonic oscillator by

$$s(t) = A\cos(2\pi f_0 t) \tag{1.18}$$

Thus, the eigenfrequency of the harmonic oscillator is described by

$$f_0 = \frac{1}{2\pi}\sqrt{\frac{k^*}{m^*}} \tag{1.19}$$

where k^* and m^* are the effective spring constant and mass, respectively. Under the condition that the potential is two times differentiable for the whole oscillation cycle $\partial U_{\mathrm{ts}}^2/\partial z^2 = k_{\mathrm{ts}} = const.$, k^* is given by

$$k^* = k_c + k_{\mathrm{ts}}. \tag{1.20}$$

where k_c is the stiffness of the tuning fork and k_{ts} is the tip-sample stiffness. [30, 47, 77] Eq. 1.19 can be written as a Taylor series if $k_{\mathrm{ts}} \ll k_t$ which yields for Δf

$$\Delta f = \frac{f_0}{2k_c}k_{\mathrm{ts}} \tag{1.21}$$

This expression points out, that, by detecting Δf in AFM, the force gradient between tip and sample is measured, if the assumption

$$k_{\mathrm{ts}} = -\frac{\partial F_{\mathrm{ts}}}{\partial z} = \text{const.} \tag{1.22}$$

is fulfilled. This is only the case for small oscillation amplitudes. In tuning fork based AFM the oscillation amplitudes are typically $\leq 100\,\mathrm{pm}$ which allows this assumption for k_{ts}.

Furthermore, Eq. 1.21 highlights that softer cantilevers (smaller k_c, *e.g.* Si-cantilever $k_c \approx 40\,\mathrm{N/m}$) increase the measured frequency shift and therefore, the sensitivity to tip-sample forces. However, a major drawback of softer cantilevers is that snap-into-contact can occur if the attractive forces are higher than the cantilever stiffness. Especially, at small amplitudes where the average tip-sample distance is reduced, snap-in prevents stable measurement conditions with softer cantilevers. Tuning forks have a high stiffness of $\approx 1800\,\mathrm{N/m}$ which allows measurements at small amplitudes in the close-distance regime without snap-into-contact.

For larger amplitudes, k_{ts} is not constant during one oscillation cycle and changes by orders of magnitude due to various tip-sample forces. Consequently, a more general expression of Δf is needed. By means of the Hamilton-Jacobi approach, the frequency shift Δf is expressed as following [77–81]

$$\Delta f(z) = -\frac{f_0}{\pi k_c A} \int_{-1}^{1} F_{\mathrm{ts}}(z + A(1+u)) \left(\frac{u}{\sqrt{1-u^2}} \right) du \tag{1.23}$$

where the substitution $\cos(2\pi f_0 t) = u$ is used. The term $\left(\frac{u}{\sqrt{1-u^2}}\right)$ determines the contributions of various forces to Δf in dependence of the amplitude. For large amplitudes, the main contribution of tip-sample interactions to the measured Δf occurs when the tip is at the closest point during an oscillation cycle. Due to the large amplitude, the distance at the point where the tip is furthest away from the sample in one oscillation cycle is elevated which results in negligible force contributions there. For small amplitudes, the last term in the integral guarantees that the long-range forces are partially eliminated if their variation is small enough during one oscillation cycle. [81]

It was shown that by decreasing the amplitude, the weight of the long-range force contributions is reduced and the weight of the short-range forces increases. [30] Consequently, various force contributions can be accessed in AFM by tuning the amplitude in the FM-mode. To achieve atomic contrast short-range forces have to be sensed by the tip which requires the use of small amplitudes. [30] Tuning forks permit oscillation with small amplitudes in the range of 50 to 100 pm. The possible application of small amplitudes in combination with the high stiffness that prevents snap-into-contact allows measurements in the close-distance regime where chemical forces arise. Therefore, tuning fork based AFM can sense atomic scale features such as chemical structure and bonds of molecules. [8] However, the high stiffness has also its drawback since the sensitivity and therefore the signal-to-noise ratio is low (Eq. 1.21) compared to Si-cantilever based AFM.

From the general formula for Δf (Eq. 1.23) the tip-sample forces can be extracted by mathematical inversion of the frequency shift. Several approximation methods have been proposed for this inversion. [79, 82, 83] Sader and Jarvis developed an analytical solution to determine F_{ts} at the closest tip-sample distance d from the measured

$\Delta f(z)$ [84]:

$$F_{ts}(d) = \frac{2k_c}{f_0}\int_d^\infty \left(1 + \frac{A^{1/2}}{8\sqrt{\pi(z-d)}} - \frac{A^{3/2}}{\sqrt{2(z-d)}}\frac{\partial}{\partial z}\right)\Delta f(z)dz \tag{1.24}$$

The tip-sample surface potential U_{ts} is yielded by integration:

$$U_{ts}(d) = \frac{2k_c}{f_0}\int_d^\infty \left(z - d + \frac{A^{1/2}}{4}\sqrt{\frac{z-d}{\pi}} + \frac{A^{2/3}}{\sqrt{2(z-d)}}\right)\Delta f(z)dz \tag{1.25}$$

By employing the Sader-Jarvis-method, measured $\Delta f(z)$ data can be used to calculate the tip-sample interaction force. It is important to record $\Delta f(z)$ in a range from the closest tip-sample distance d to a distance ∞ which is far away ($\approx 5 - 10\,\mathrm{nm}$) from the surface. At the far distance regime, the tuning fork is undisturbed from short range forces. Consequently, the long-range interaction forces which are independent of the position on the sample can be determined and extracted from the data. In this way, the background of vdW forces can be subtracted from the data set to obtain the short-range interaction forces between tip and sample. [73, 75]

1.3 Spectroscopy

Spectroscopy is used to characterize the local sample properties which goes beyond normal topographic imaging modes in STM or AFM (Fig. 1.5).

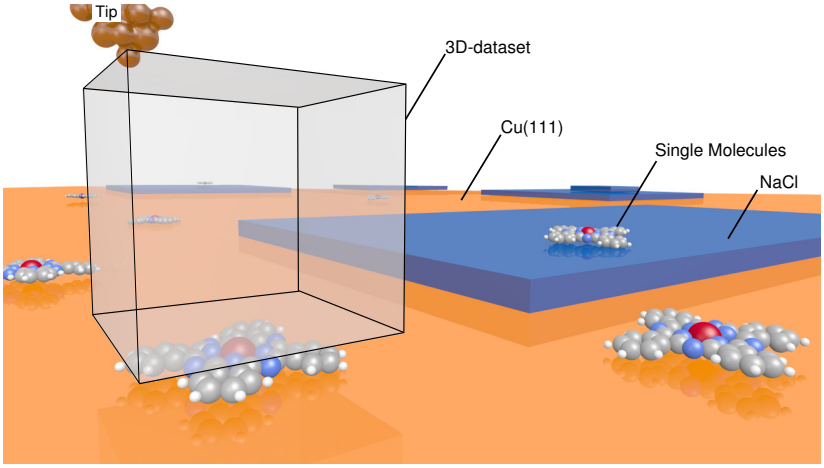

Fig. 1.5: Schematic representation of a 3D-spectroscopy measurement. *Force fields or differential conductance maps in three dimensions can be recorded above single molecules. To decouple the molecules from the metal electrons, they are deposited on thin insulating NaCl films. (Figure by courtesy of R. Pawlak. Reprinted by permission from Springer Nature. [85])*

The aim in spectroscopy is to analyse electronic states and charge distributions of single molecules at the atomic level. Thus, intramolecular processes, the interplay

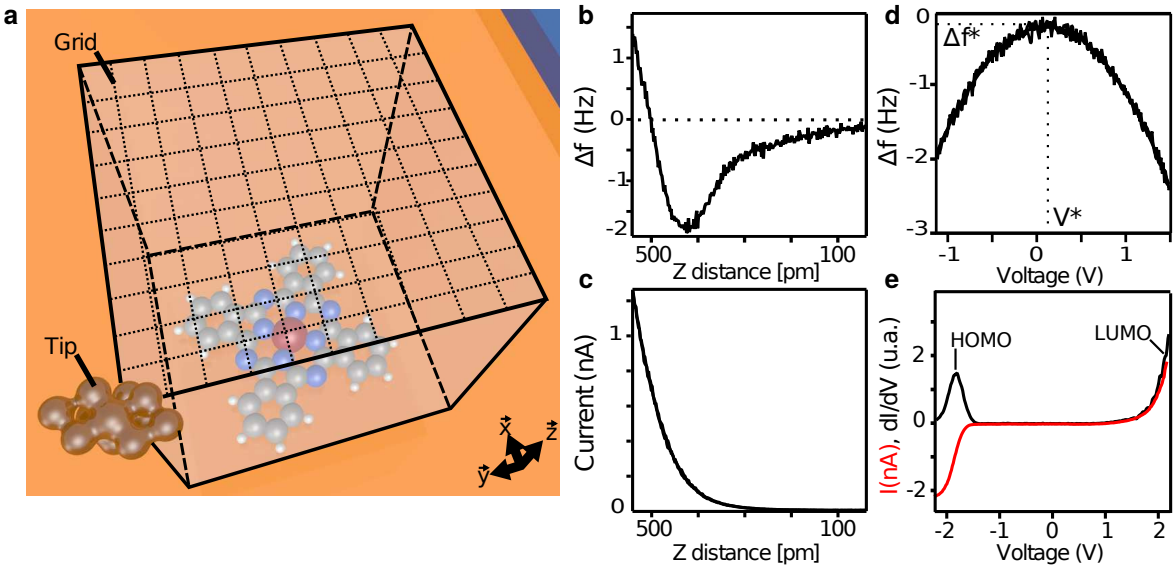

Fig. 1.6: Different spectroscopy methods. *Frequency shift and tunneling current curves as function of the distance ($\Delta f(z)$ (**a**), $I_t(z)$ (**c**)) or as function of the bias voltage ($\Delta f(V_b)$ (**d**), $\frac{dI_t}{dV_b}(V_b)$ (**e**)) can be recorded. Figure by courtesy of R. Pawlak. Reprinted by permission from Springer Nature. [85]*

between molecule and surface, and intermolecular interactions in assemblies are elucidated. Since the total tip-sample force contains different components, it is important to define theoretically the measured physical quantities. By acquiring spectroscopy curves in a cubic grid over the sample, complete three-dimensional (3D) force fields of the investigated molecules (Fig. 1.6) can be obtained which explicitly highlight the distance and site dependence of the tip-sample forces.

Furthermore, the surface potential landscape can be extracted from the data by mathematical conversion from the measured Δf values (Eq. 1.25 in Sec. 1.2.3). Molecules on metallic surfaces are interacting with the metal electrons leading to quenching and hybridization which affects the molecular properties. To avoid the molecular interaction with metals, the molecules are decoupled from metallic substrates by thin insulating films, *e.g.* NaCl (Fig. 1.5), to probe the intrinsic molecular properties by spectroscopy. By measuring the tunneling current as a function of tip-sample distance or applied voltage, the sample conductivity can be accessed to determine the electronic band gap of materials or electronic states of single molecules. The tuning fork setup allows to investigate molecules with scanning tunneling spectroscopy and with force spectroscopy which is explained in the following.

1.3.1 Force spectroscopy

In force spectroscopy, using FM-AFM, the frequency shift Δf is measured and afterwards converted into forces following the mathematical procedure described in Sec. 1.2.3 (Eq. 1.24). Either the distance dependence $\Delta f(z, V_b = \text{const.})$ or the voltage dependence $\Delta f(V_b, z = \text{const})$ is recorded to analyse the sample.

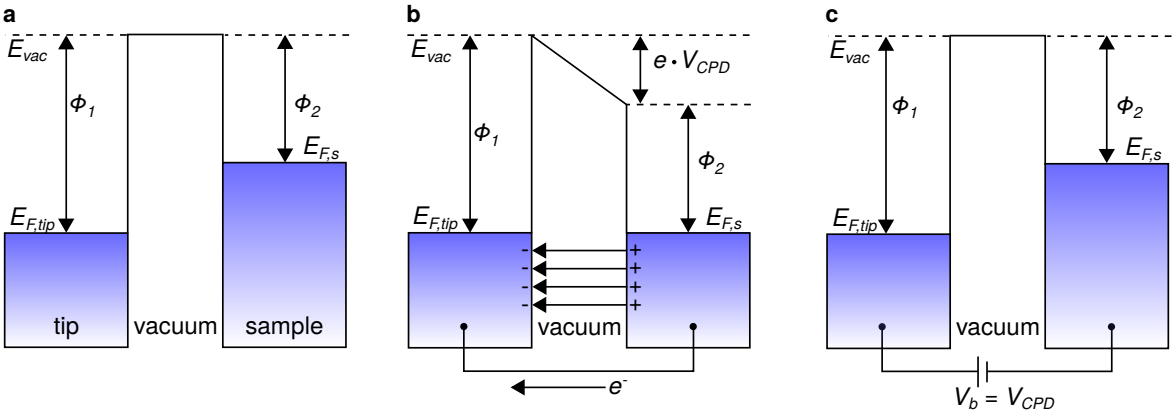

Fig. 1.7: Contact potential difference. *Two metals with different work function are brought together. By contacting them with a back electrode, electrons flow until the Fermi levels are aligned. Consequently an electric field evolves between the two metals. By applying an bias voltage $V_b = V_{CPD}$ this electric field is compensated and thus the work function can be determined with V_{CPD}.*

$\Delta f(z)$-spectroscopy For $\Delta f(z)$-spectroscopy, the tip-sample distance is varied. In Fig. 1.6b, a typically obtained curve is shown. The $\Delta f(z)$-curve qualitatively displays the different tip-sample force contributions which are first attractive and then repulsive, corresponding to the theoretical total force curve as depicted in Fig. 1.3. The background of long-range vdW forces is determined by measuring the forces at a far tip-sample distance, typically few nm away from the surface. [86]. To explore short-range chemical or electrostatic forces, the vdW background is subtracted from the $\Delta f(z)$-curves because the long-range vdW forces do not depend on the local tip position. $\Delta f(z)$-spectroscopy is used *e.g.* in single molecule manipulation or friction experiments to get information of atomic scale processes. [87, 88] Furthermore, the structural alignment of molecules [89] or the chemical composition of surfaces on the atomic level are investigated. [90] A more detailed overview of recent results of $\Delta f(z)$-spectroscopy is given in Sec. 3.1.

$\Delta f(V_b)$-spectroscopy/LCPD mapping The aim in $\Delta f(V_b)$-spectroscopy is to measure electrostatic forces. The contact potential difference between tip and sample and local charges lead to long-range and short-range electrostatic forces, respectively (Sec. 1.2.2).

Two metals with work functions Φ_1 and Φ_2, refering to tip and sample, are brought into close vicinity (Fig. 1.7a). If they are electrically connected via a back electrode, electrons flow from the metal with higher Fermi energy to the one with lower Fermi energy until the Fermi levels are aligned (Fig. 1.7b). In 1898, Lord Kelvin measured this current created by the CPD between two metallic plates which are electrically connected. [91] By applying a voltage V_{CPD} which is [92]

$$V_{\mathrm{CPD}} = \frac{\Phi_1 - \Phi_2}{e} \tag{1.26}$$

the current flow stops which indicates the compensation of the CPD (Fig. 1.7c).

The electrical field evolving from the CPD between tip and sample can be modelled by the field of a charged plate capacitor (Sec. 1.2.2). For the electrostatic potential it follows that

$$U_{\mathrm{el}} = \frac{1}{2} C (V_b - V_{\mathrm{CPD}})^2 \tag{1.27}$$

Consequently, the measured $\Delta f(V_b)$ curve has a parabolic shape due to (Fig. 1.6d)

$$\Delta f(V_b) \propto \frac{\partial^2 U_{\mathrm{el}}}{\partial^2 z} \tag{1.28}$$

$$\propto \frac{1}{2} \frac{\partial^2 C}{\partial^2 z} (V_b - V_{\mathrm{CPD}})^2 \tag{1.29}$$

To measure variations of short-range electrostatic forces and determining local charges, spectroscopy is performed at small distances in the order of molecular dimensions. At this distance regime, the local contact potential difference (LCPD) is measured. The LCPD is defined as [92]

$$\mathrm{LCPD} = -eV^* = \Phi_{\mathrm{t,local}} - \Phi_{\mathrm{s,local}} \tag{1.30}$$

where $\Phi_{\mathrm{t,local}}$ and $\Phi_{\mathrm{s,local}}$ are the local work functions of tip and sample, respectively.

The LCPD can be determined from the measurement by fitting a parabola to the $\Delta f(V_b)$ curves and extracting the corresponding voltage and frequency shift values of the maximum $(V^*, \Delta f^*)$. At the maximum of the parabola the electrostatic force is compensated and $V_b = V^*$.

Measuring the LCPD can be experimentally realized in two ways:

1. by using an additional feedback loop that adjusts V_b to V^* during an AFM scan (KPFM) or

2. by recording the whole $\Delta f(V_b)$ curve at constant height for a range of few volts (LCPD mapping).

By means of tuning fork AFM, LCPD mapping is conducted with submolecular resolution. Thus, the charge states of atoms [9], molecules [10, 93, 94] and vacancies in ionic thin films [95] were determined.

LCPD mapping offers the advantage to investigate and analyze the whole $\Delta f(V_b)$ spectrum after the measurement. Additionally, the voltage dependence of the tunneling current $I_t(V_b)$ is simultaneously recorded by using tuning fork sensors. High spatial stability is required to perform spectroscopy on a single molecule or atom. Therefore, drift compensation methods, position tracking and cryogenic temperatures are used.

LCPD mapping is more time-consuming than KPFM since several hundreds of spectroscopy curves, each with an acquisition time of few tens of seconds, are recorded for a two-dimensional LCPD map of few nm^2. This leads to a measurement time of several hours. In KPFM, the same area could be scanned in several minutes. V^* is detected

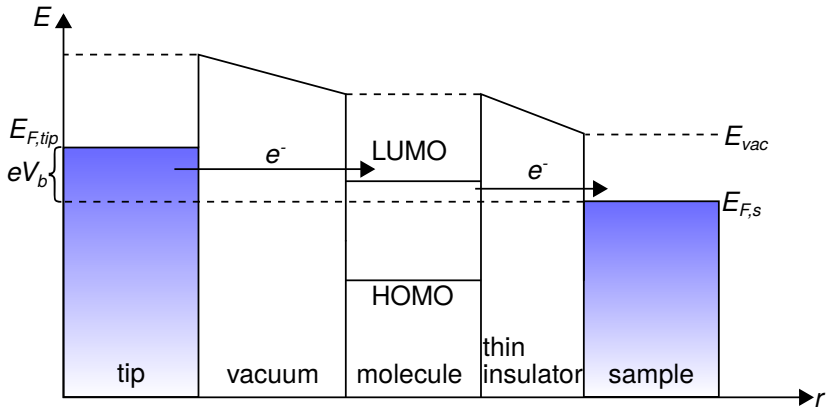

Fig. 1.8: Double barrier tunneling junction. *Electrons can tunnel resonantly through molecular orbitals if the molecule is well decoupled from the metallic substrate by an insulating film. This principle is used in scanning tunneling spectroscopy.*

simultaneously to the Δf-signal for the topography and used to create a KPFM image. [92]

KPFM is usually performed with Si-cantilever based AFM because of their higher sensitivity due to the lower cantilever stiffness. By applying a small ac-voltage between tip and sample, the influence of the electrostatic forces on Δf of the cantilever oscillation can be read out by using the lock-in technique. In tuning fork based AFM, the change of Δf due to a small ac-voltage is under the detection limit because of the high sensor stiffness. Therefore, KPFM is rarely used with tuning fork sensors. [96]

1.3.2 Tunneling spectroscopy

Scanning tunneling spectroscopy In scanning tunneling spectroscopy (STS) the differential conductance dI_t/dV_b is recorded which is proportional to the local density of states ρ of the sample at constant height following the Tersoff-Hamann model [40]

$$\frac{dI_t}{dV_b} \propto \rho(\boldsymbol{r}, E_F + eV_b). \tag{1.31}$$

To obtain dI_t/dV_b, a small ac-voltage is applied between tip and sample which modulates the tunneling current. By using a lock-in amplifier, the dI_t/dV_b signal is directly recorded during a bias sweep (Fig. 1.6e).

By positioning the tip over a molecule which is decoupled from the metallic substrate by a thin insulator film, the tunneling barrier described in Fig. 1.2 becomes a double-barrier tunneling junction (Fig. 1.8). One barrier is the vacuum between tip and molecule, the other one is the insulating film, usually with a thickness of two atomic monolayers. The molecule has specific states. The closest to the Fermi energy E_F are the highest occupied molecular orbital (HOMO) and the lowest unoccupied molecular orbital (LUMO). By sweeping the bias voltage to these energies, the molecular states are in resonance with the applied voltage which leads to a peak in the dI_t/dV_b signal (Fig. 1.6e).

Thus, electronic states of surfaces [97–99], single molecules [7, 100] and atoms [101] can be investigated.

The described double barrier tunneling process is elastic, in contrast to inelastic tunneling which occurs when vibration modes of molecules are excited. A part of the electrons' energy is transferred for the activation of phonons in molecules. This process can be used to move adsorbates on the surface [102–104] or create images. [105]

$I_t(z)$-spectroscopy By varying the tip-sample distance, the exponential distance dependence of the tunneling current is probed (Eq. 1.7). Thus, the local potential barrier height can be extracted from the slope of the logarithmic $I_t(z)$-plot since the decay length κ depends on the work function at the tip position (Eq. 1.6). The local potential height reveals information about the electronic alignment of a sample, *e.g.* of the charge transfer between molecules and a metallic substrate. [106]

In conclusion, tuning fork based STM and AFM is capable to simultaneously measure currents and forces at the atomic scale which is mainly due to following characteristics of the tuning fork sensor:

1. large stiffness and small amplitudes allowing stable measurements at close distance
2. metallic tips enabling STM operation and tip preparation
3. technically simple read-out at low temperature

Atomic structures as well as electronic properties of samples can be characterized by STM, AFM as well as current and force spectroscopy. In this thesis, all STM images are recorded in the constant current mode. AFM measurements are exclusively performed in the FM-mode at constant height at $V_b = 0\,\mathrm{V}$ with CO-terminated tips. The amplitudes used are in a range of 50 to 100 pm. Point 3 of the tuning fork characteristics and other technical requirements for STM and AFM at low temperature with atomic resolution are discussed in the next chapter.

2 Experimental setup

In this chapter, the experimental realisation of the STM and AFM is described. To achieve stable scanning conditions, the microscope is mounted in an ultra-high vacuum (UHV) chamber and cooled down by liquid nitrogen and helium. For highest resolution measurements, the outermost tip consists of a CO molecule. The preparation technique to obtain a CO tip is explained as well as the experimental prerequisites to prepare single molecules or complex molecular structures on the surface. Moreover, the chemical structures and properties of the investigated molecules are given.

2.1 Low temperature tuning fork STM/AFM in ultra-high vacuum

The used measurement system is an Omicron [1] LT UHV STM/AFM with tuning fork setup (Fig. 2.1). The UHV chamber is separated in the analysis chamber and the preparation chamber.

Analysis chamber The microscope head is placed in the analysis chamber (A chamber) with a base pressure of around 10^{-11} mbar which allows the investigation of atomically clean surfaces. The microscope head consists of a piezo scanner, a tuning fork and a sample stage (Fig. 2.2). The sample stage is thermally connected to the cryostat which is located above the microscope head. The cryostat consists of an outer and an inner bath. The outer is filled with liquid nitrogen ($T_{\mathrm{B,N2}} = 77\,\mathrm{K}$), the inner with liquid helium ($T_{\mathrm{B,He}} = 4.2\,\mathrm{K}$). Thus, the sample is cooled down to the operating temperature of 4.7 K, which is slightly higher than $T_{\mathrm{B,He}}$ due to heat transfer. The microscope head is suspended by springs to damp vibrations. Furthermore, an eddy current damping system is installed. Samples are introduced in the sample stage in the microscope by using the wobble stick (Fig. 2.1). The sample surface is facing downwards and the tuning fork sensor approaches from the bottom. The sensor is movable in all three dimensions whereas the sample is fixed.

[1] former Omicron NanoTechnology GmbH, now Scienta Omicron (www.scientaomicron.com)

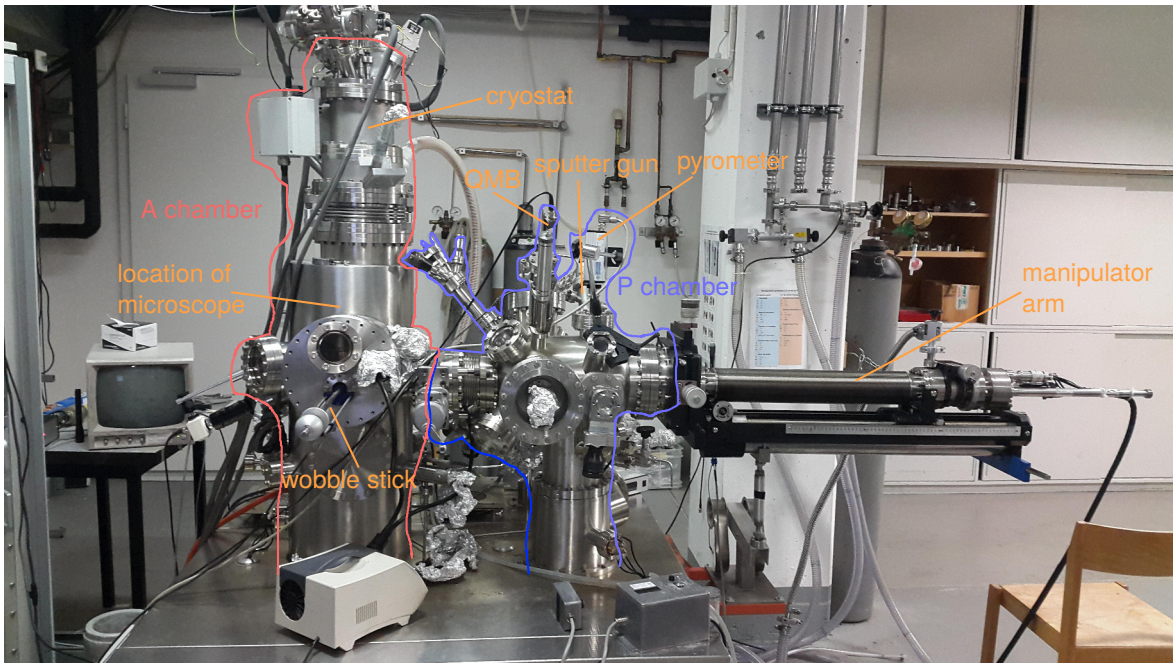

Fig. 2.1: Photograph of the microscope. *The microscope is located in the analysis chamber (A chamber). The cleaning of the sample and molecule deposition is done in the preparation chamber (P chamber). The sample is transferred between A and P chamber by the manipulator arm.*

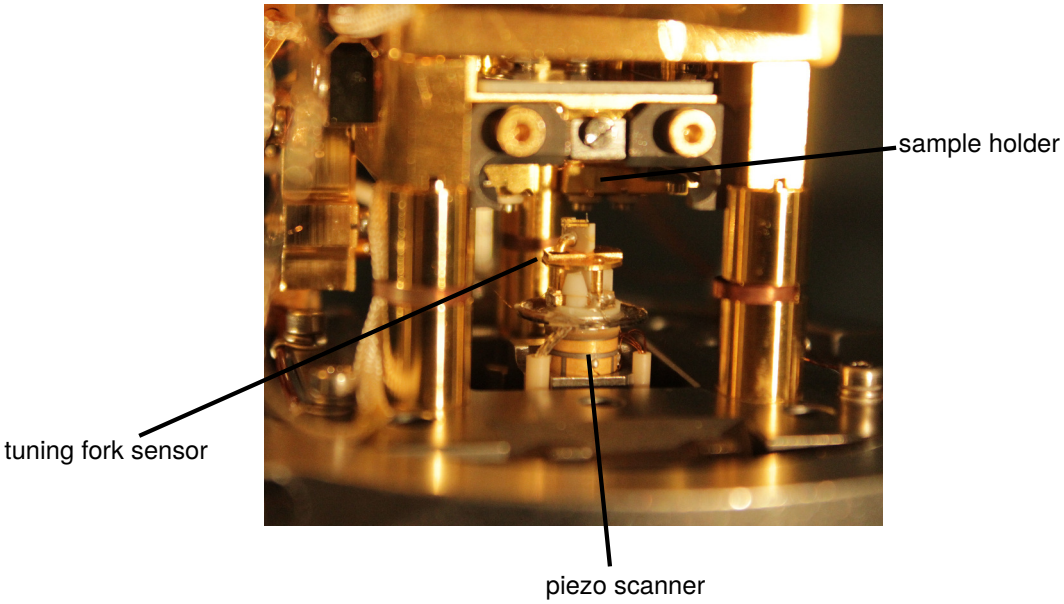

Fig. 2.2: Photograph of the microscope head. *The sample can be inserted in the sample holder. The piezo scanner with the tuning fork sensor is approached from the bottom to the sample surface for scanning (Photograph by courtesy of R. Pawlak).*

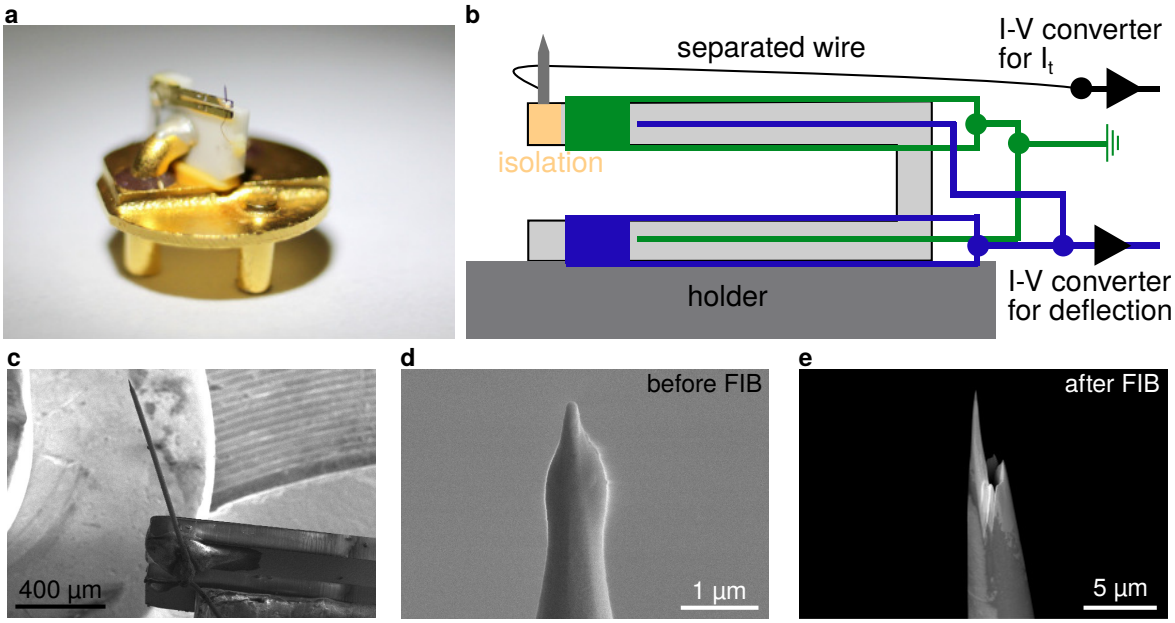

Fig. 2.3: qPlus sensor and tip. ***a,*** *Photograph of a qPlus tuning fork sensor from Omicron.* ***b,*** *wiring diagram of the tuning fork sensor. Electron microscope image of* ***c,*** *the tip glued to the end of the upper prong,* ***d,*** *the tip before preparation and* ***e,*** *after preparation with FIB.*

Preparation chamber The preparation chamber (P chamber) reaches a base pressure of 10^{-10} mbar which allows the preparation of atomically clean surfaces. For preparation, the samples are put into the manipulator arm (Fig. 2.1) which can be displaced in the P chamber. Samples are cleaned by bombarding the surface with Ar^+ ions from the sputter gun attached to the P chamber. To achieve flat surfaces, the samples can be annealed by the e-beam heater in the manipulator arm. Specific molecular compounds are controllably deposited by the Knudsen cell molecule evaporator connected to the P chamber and containing three crucibles (more details about molecule deposition in Sec. 2.3). The deposition rate can be checked by a quartz micro balance or a quadrupole mass spectrometer which detects masses up to 100 u. Furthermore, a metal evaporator is attached to the P chamber.

The transfer from the P to the A chamber and *vice versa* is performed by the manipulator arm. New samples from outside can be introduced by a load lock which is connected to the P chamber.

Tuning fork sensor The tuning fork sensor has the qPlus design [29] meaning that one prong is fixed to the holder (Fig. 2.3a). The sensors are purchased from Omicron. Tuning forks are a mass product in watch industries where they are used as timekeeper. The prongs consist of quartz crystal (SiO_2) whereas the tip is made out of an etched tungsten wire which is glued to the electrically isolated end of one prong (Fig. 2.3c). [107] A separated wire is mounted directly to the tip which conducts the tunneling current to the I-V converter (Fig. 2.3b).

Due to the piezoelectric property of the quartz material, the tuning fork is self-sensing, *i.e.* the deflection signal of the oscillation can be read out without using an optical setup as for cantilever based AFM. This principle facilitates operation at low temperature and in limited space in UHV conditions. Due to the separated wire, the tunneling current does not flow through the prongs of the tunning fork which reduces capacitive cross-coupling at high tunneling currents. [108]

The tuning fork has a stiffness of around 1800 N/m and its resonance frequency is ≈ 25 kHz. For AFM measurements, amplitudes in the range of 50 to 100 pm are used. The bias voltage is applied to the tip. In this thesis, the bias voltage is transformed and given as sample bias voltage for comparability with literature. The STM and AFM scans are performed with Nanonis OC3 (later OC4) controller from SPECS Zurich[2] with an internal phase locked loop and lock-in amplifier.

2.2 Tip preparation

First, the tuning fork sensor with the mounted tip are imaged with an electron microscope to check for contaminations or other irregularities at the tip apex (Fig. 2.3c,d). Second, the tip is shaped with a focused ion beam (FIB) by milling off a donut shape with various depth from top of the tip. Thus, a conical shape with a smaller tip diameter (typically less than 20 nm and an increased tip aspect ratio is achieved (Fig. 2.3e). After the FIB preparation, the sensor is introduced in the microscope head and atomically sharp metallic tips with a CO termination are prepared as described in the following.

Atomically sharp metallic tips To get an atomically sharp tip, clean metal surfaces are scanned and the tip is mechanically indented by few nm in the surface until the contrast gets sharper (Fig. 2.4a-c). Furthermore, voltage pulses up to ± 10 V are applied to the tip which lead to a reshapening of the tip by the high electric field. Sharp tips show high contrast in the STM topography images, especially the step edges or adsorbates whose STM appearance is known from previous measurements are properly resolved, which indicates the state of the tip. Since in STM it is assumed that only the outermost tip atoms contribute to the tunneling current because of the exponential decay of the tunneling current, the tip can be qualified as atomically sharp. However, for AFM, also long-range forces contribute which are sensed by atoms of the tip apex further away.

CO terminated tips For AFM imaging with atomic resolution on molecules or substrates, a single CO molecule is attached to the tip (Fig. 2.4d-g). The C atom is connected to the tip whereas the O atom is facing the sample and used as probe. [8, 109–111] The CO molecule at the tip enhances the contrast through bending. [8] The CO gas is controllably leaked into the analysis chamber up to a pressure of around $p_A = 3 \cdot 10^{-8}$ mbar for around one minute. The sample in the microscope is kept cold,

[2] www.specs-zurich.com

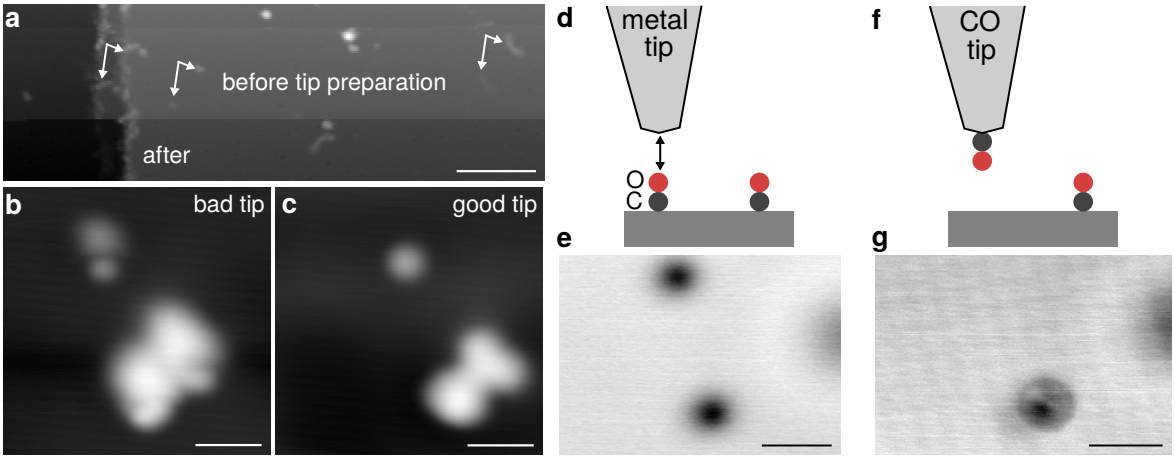

Fig. 2.4: Tip preparation procedure. ***a,*** *STM topography image with tip preparation on Cu(111) substrate with adsorbates. Before tip preparation, the tip is a double tip which can be seen by the repeated structures (white double arrows). After the tip preparation, one step edge and the repeated structures disappear indicating an improvement of the tip shape. The scale bar is* 15 *nm.* ***b,*** *Two adsorbates resolved by a bad tip and* ***c*** *by a good tip after tip preparation.* ***d, f,*** *Schematic drawing of tip functionalization with a single CO molecule.* ***e,*** *The tip is already a sharp metallic tip. The CO molecules appear as depressions on NaCl thin films. The upper CO molecule is picked up with the tip.* ***g,*** *Subsequently, the contrast changes and the Cl ions of the NaCl layer can be seen. The adsorbed CO looks different with a CO tip. It shows a halo around the dark depression. The scale bars in the STM images in* ***b, c, e, g*** *correspond to* 1 *nm.*

so that the CO molecules adsorb all over the surface. They are recognized as dark depressions on a NaCl thin film (Fig. 2.4e). A CO tip is obtained by performing a $I_t(z)$-curve on top of a CO molecule. By approaching the tip to a adequate distance, the CO molecule jumps to the tip which can be seen as current jump in the $I_t(z)$-curve. Afterwards the STM contrast changes and the atomic lattice of the NaCl becomes visible (Fig. 2.4g). A first quality check of CO tips can be done by scanning CO or other molecules with a CO tip. The CO can be placed asymmetrically on the tip leading to a double tip effect. Also instabilities can occur when the CO is moving on the tip. Approved CO tips however, produce symmetric and stable images in STM and AFM.

The ability to atomically shape the tip and control the tip termination is a tremendous advantage of tuning fork based AFM. The sophisticated tip preparation is possible due to the metallic tips of tuning fork sensors. Additionally, the operation at low temperature in UHV conditions is required for the controlled tip termination.

2.3 Sample preparation

First, the basic sample preparation of metal crystals used as substrate for all measurements, the deposition by thermal evaporation of NaCl thin films and molecules as well

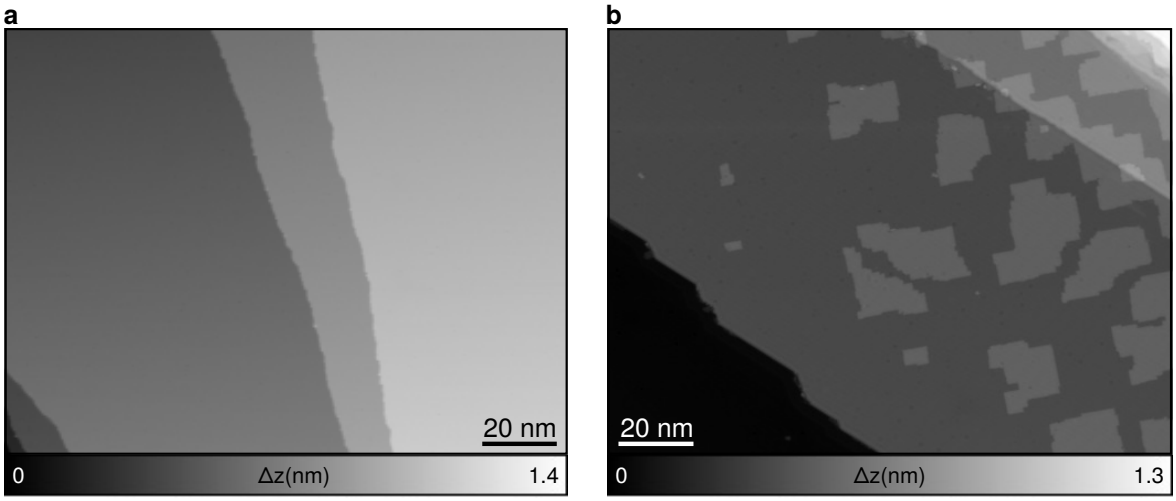

Fig. 2.5: Sample preparation. ***a,*** *STM topography image of Cu(111) surface with atomic step edges after sputtering and annealing cycles. ($I_t = 10\,pA$, $V_b = 0.3\,V$).* ***b,*** *STM topography of Cu(111) with deposited NaCl thin film with a thickness of two monolayers. The islands on NaCl correspond to the third and forth monolayer. The dark area at the bottom left shows the uncovered Cu(111) surface ($I_t = 3\,pA$, $V_b = 0.3\,V$).*

as the deposition of Fe are explained. Second, the application of home built mobile evaporators is described which are used for deposition on cold samples in order to obtain single adatoms or molecules on NaCl thin films. Molecules that are not thermally sublimable are deposited by the electrospray technique.

2.3.1 Basic preparation

Metal crystals The crystals are purchased from MaTeck GmbH [3]. All metal crystal surfaces are cleaned by sputtering with Ar^+ ions at a pressure of around $5 \cdot 10^{-6}$ mbar for 10 min in the preparation chamber (Fig. 2.5a). Subsequently, they are annealed (temperatures for Cu(111) $T_{\mathrm{Cu}} = 620°\mathrm{C}$, for Ag(111) $T_{\mathrm{Ag}} = 480°\mathrm{C}$, for Au(111) $T_{\mathrm{Au}} = 400°\mathrm{C}$ and for Pb(110) $T_{\mathrm{Pb}} \approx 150°\mathrm{C}$). The surface temperature is controlled by a pyrometer (Pyrospot DG 10N from DIAS Infrared GmbH [4], emissivity $\varepsilon = 0.05$) except for the Pb(110) crystal because the annealing temperature is lower than the minimum detectable temperature of the pyrometer ($T_{\mathrm{min}} = 250°\mathrm{C}$). The sputtering and annealing cycles are performed twice for samples which are kept in UHV before. Samples introduced from outside the chamber are prepared more times.

NaCl thin films NaCl of high purity ($\geq 99.999\%$) is purchased from Sigma-Aldrich Chemie GmbH [5]. NaCl is thermally evaporated from a Knudsen cell evaporator (TCE-

[3] www.mateck.com
[4] www.dias-infrared.de
[5] www.sigmaaldrich.com

BSC from Kentax GmbH [6]) at a temperature of $T_{\mathrm{NaCl}} = 485°\mathrm{C}$ on a previously cleaned Cu(111) sample at room temperature. Subsequently, the sample surface is partially covered with NaCl films of a thickness of two monolayers (Fig. 2.5b). The islands on the NaCl films correspond to additional monolayers. The bare Cu(111) surface is necessary to prepare clean metallic tips during the measurements.

Molecules Sublimable molecules are thermally evaporated from a Knudsen cell evaporator (evaporator specified above for NaCl thin films in Sec. 2.3.1) at their specific sublimation temperature which is checked before with the QMB. The deposition rate is also controlled with the QMB to adjust the evaporation time. The specific sublimation temperatures are given in Tab. 2.1. If the molecules need to be deposited on the cold sample, the preparation is done in two steps using a mobile evaporator which is described in Sec. 2.3.2. Non-sublimable molecules are deposited with the electrospray deposition technique which is explained in Sec. 2.3.3.

Molecule	T_{evap} (°C)
I-DNT-VW	167
DBBN	93
tDBA	100
$\mathrm{HBC6C_{12}}$	ESD
Tolyl-terpyridine	107
TTF-dppz	215
TTF-dye	ESD

Table 2.1: Evaporation temperatures of investigated molecules. *Complex molecular compounds are deposited by the electrospray deposition technique (ESD).*

Atoms Fe atoms are evaporated from an e-beam metal evaporator from FOCUS GmbH [7] on sample surfaces at room temperature or increased temperatures. For the preparation of single Fe adatoms, it is required to deposit on cold samples. In this case, the procedure described in Sec. 2.3.2 is used.

2.3.2 Mobile evaporators

Mobile molecule evaporator To study single molecules and adatoms on thin insulating films on metallic substrates, the deposition on cold samples is mandatory. At room temperature the molecules diffuse to the metallic substrate because this adsorption position is energetically preferred. To prevent such diffusion, molecules have to be deposited on samples kept at a few tens of Kelvin and the sample has to stay at this temperature without interruption. An increase of temperature occurs when a sample transfer has to be done or when the microscope stage with the sample warms up because the liquid nitrogen and helium bath became empty. The only possibility to deposit molecules on cold samples in the system used for this thesis was to cool

[6] www.kentax.de
[7] www.focus-gmbh.com

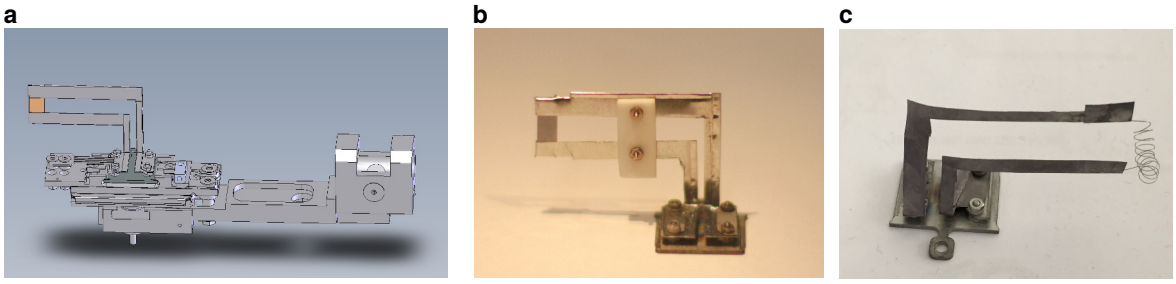

Fig. 2.6: Mobile evaporators constructed for single molecule/atom deposition. ***a,*** *3D drawing of the mobile evaporator inside the manipulator arm (by courtesy of Y. Pellmont).* ***b,*** *Photograph of the mobile molecule evaporator and* ***c,*** *of the mobile Fe evaporator. A Fe piece was added later in the middle of the filament for deposition.*

down the manipulator with liquid nitrogen. However, a subsequent sample transfer from the manipulator to the microscope stage has to be done which breaks the cold temperature chain. Consequently, it was not possible to analyse single molecules or adatoms on thin insulating films. To solve this problem technically, a mobile molecule evaporator was designed and constructed. It consists of an Omicron sample plate with the mounting stages and a tantalum carrier which is holding a piece of a silicon wafer (Fig. 2.6b). The mobile evaporator can be introduced in the manipulator which automatically connects one side of the mounting stage with a clamp (Fig. 2.6a). This side of the mounting stage is electrically isolated from the sample holder with ceramics between the screws and the holder. The mounting stage on the opposite site is electrically grounded. Consequently, an electrical current can be passed through the tantalum carrier and the silicon wafer piece. The current flow leads to a temperature increase of the silicon because of resistive heating. Therefore, the molecule evaporation on cold sample is done in the following way:

1. The molecules are deposited on the silicon plate in the P chamber with the same procedure as for the molecule deposition on normal samples (Sec. 2.3.1), but increased deposition times to increase the number of deposited molecules in the following second step.

2. The mobile evaporator is transferred to the A chamber and placed in front of the entrance of the microscope stage. The sample with the insulating thin film is already inside the microscope stage and hence cooled down with the liquid He bath. The silicon plate is heated with a current of $I_{\mathrm{Si}} = 1.4\,\mathrm{A}$ and a voltage of $V_{\mathrm{Si}} = 3.5\,\mathrm{V}$ for $\Delta t = 1\text{-}2\,\mathrm{min}$ which flash evaporates the deposited molecules on the silicon plate.

During the evaporation procedure the sample temperature does not rise above 10 K which ensures that the molecules do not diffuse from the NaCl film to the metal substrate. After the deposition with the mobile evaporator, the sample can be scanned directly to investigate the surface with single adsorbed molecules on insulating films.

Mobile Fe evaporator The preparation of single Fe adatoms also requires the deposition on cold samples which causes the same problem as for molecules. The metal e-beam evaporator is placed in the preparation chamber, so that a sample transfer at room temperature is necessary which prevents the preparation of single adatoms due to diffusion. Hence, a mobile Fe evaporator is built up with a similar construction as the mobile molecule evaporator (Fig. 2.6c). The basic construction stays the same, but the silicon plate is replaced by a spiral tungsten filament. By resistive heating, the filament heats up to a temperature of 1300°C which is tested by a pyrometer. In the middle of the filament spiral a small Fe plate is folded around the tungsten wire. The Fe plate consists of a Fe foil with thickness 0.05 mm and a purity grade of m4N8, t4N+ from Alfa Aesar [8]. By heating the filament, the Fe plate also heats up and Fe atoms are evaporated. For deposition on cold samples, the mobile Fe evaporator is placed directly in front of the entrance to the microscope head like the mobile molecule evaporator.

2.3.3 Electrospray deposition

The thermal deposition of molecules described in Sec. 2.3.1 is limited to the group of UHV sublimable molecules. Molecules, *e.g.* with functional anchor groups to bind to a surface, with long alkyl chains or carboxylic acid end groups, are too fragile to evaporate them in UHV for sample preparation.

With the implementation of electrospray deposition (ESD), which is a preparation technique commonly applied in biology, samples with complex molecular compounds can be prepared under UHV conditions with the required cleanliness for AFM measurements. [112] ESD is based on the principle of electrospray ionization. [113, 114]

The setup of the electrospray is displayed in Fig. 2.7a. The electrospray is plugged to the P chamber of the system. A solution of the molecules is prepared (Fig. 2.7d) and put into an automatically driven syringe which guarantees a constant solvent flow through the capillary. A rate of maximum 60 μl/h is used. At the end of the capillary small droplets of the solvent are ionized by the applied electric field ($V_{\mathrm{ESD}} = 1.5\,\mathrm{kV}$) and directed towards the sample through several pumping stages (Fig. 2.7a-c). On the path to the sample, a fraction of the solvent evaporates and is pumped. Subsequently, the molecular beam hits the surface of the previously cleaned sample which is kept in vacuum in the P chamber. During ESD, the pressure in the P chamber rises from 10^{-10} mbar to 10^{-7} mbar. Molecules are dissolved in a mixture of toluene and methanol (ratio 4:1) of high purity (HPLC quality) purchased from Sigma-Aldrich Chemie GmbH.

[8] www.alfa.com

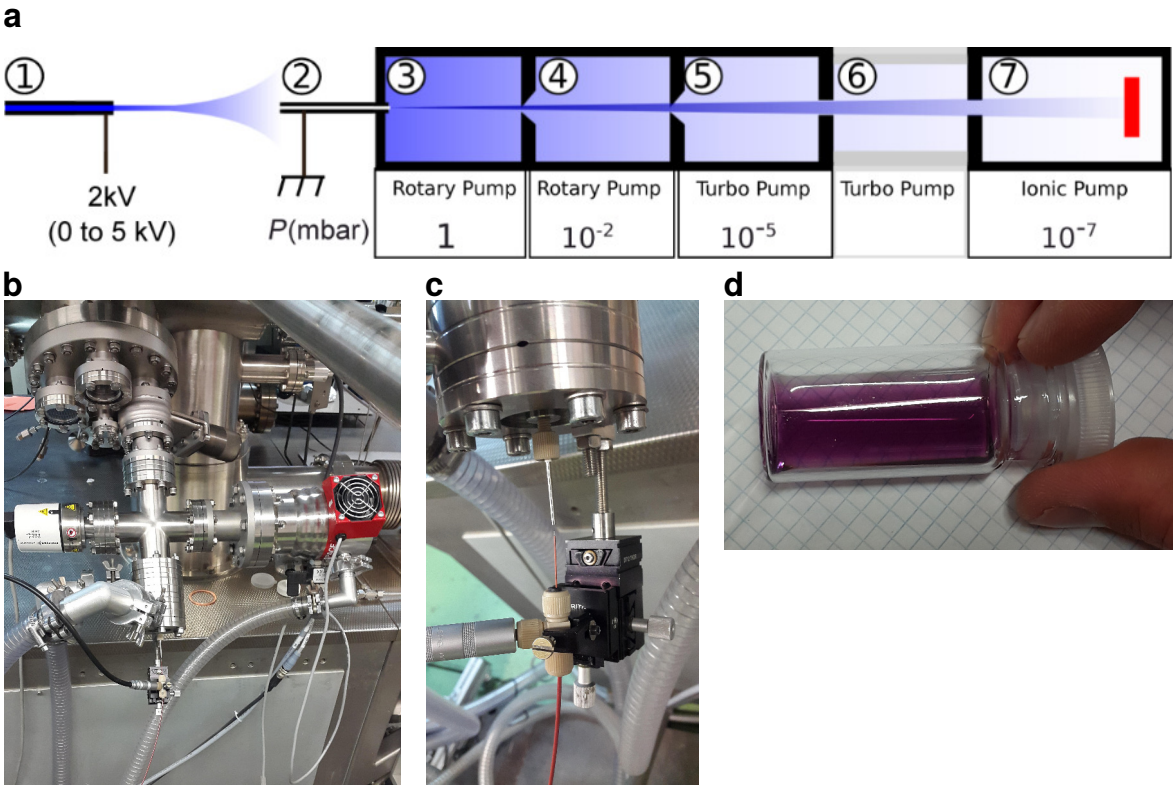

Fig. 2.7: Electrospray setup. ***a,*** *Schematic drawing of the electrospray setup with different pumping stages (by courtesy of A. Hinaut, [112])* ***b,*** *Photograph of the electrospray (mounted on a different microscope),* ***c,*** *Photograph of the capillary and the entrance to the pumping stages,* ***d,*** *Solution of toluene and methanol (4:1) with TTF-dye molecules.*

2.4 Investigated molecules

Synthetic chemistry allows to implement a variety of properties into molecular structures. Electron donor-acceptor systems can be built which transfer charges inside the molecule upon light absorption [115], ligands can be added to form coordination complexes with ions [116] or halogen atoms can be connected to trigger on-surface chemical reactions. [117] The chemical structures of the investigated molecules leading to specific properties are explained in the following.

2.4.1 I-DNT-VW

I-DNT-VW molecules consist of a V-shaped dinaphthothiophene core with two iodine atoms attached on both sides (Fig. 2.8a). The molecules are synthesized by the group of Toshihiro Okamoto and Jun Takeya. [118] In solution, C–I and C–Br bonds react with Cu atoms which induces dehalogenation and forms C–C bonds between the molecules which is called Ullmann coupling. [119]

Recently, a similar process has been demonstrated on metallic surfaces, such as Ag, Au and Cu, [120–126] and can be expected to occur with the I-DNT-VW molecules. As C–I bonds are cleaved on the Ag(111) surface (Fig. 2.8a), the molecular units are connected with organometallic bonds (Fig. 2.8b). By annealing the sample, the Ag atoms of the organometallic bonds are released and covalent bonds between adjacent molecules are formed. Thus, by on-surface chemical reactions, molecules can be covalently linked to create polymeric chains or networks which opens new synthetic routes by using surfaces as catalysts.

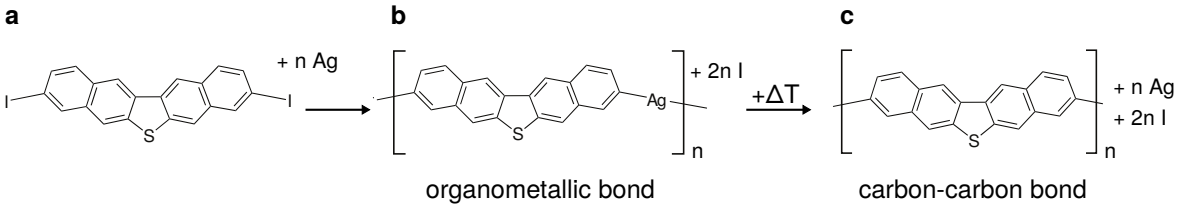

Fig. 2.8: On-surface chemical reaction by Ullmann type coupling. ***a,*** *I-DNT-VW molecules react with Ag surface atoms by dehalogenation and form an organometallic bond, shown in* ***b****.* ***c,*** *After annealing, Ag atoms of the organometallic bonds are released and a carbon-carbon link is formed between the molecules.*

2.4.2 tDBA

The triangular dehydrobenzo[12]annulene molecule (tDBA) is synthesized by the group of Kazukuni Tahara and Yoshita Tobe. [127] It has a planar structure with three benzene rings linked by three acetylene units (Fig. 2.9b). The molecule is employed as a precursor for chemical transformation processes since acetylene moieties are known to react to aromatic molecules and π-conjugated oligomers by inducing transannular cyclization on metallic substrates. [128] Consequently, the internal chemical structure of molecules can be transformed by on-surface reactions.

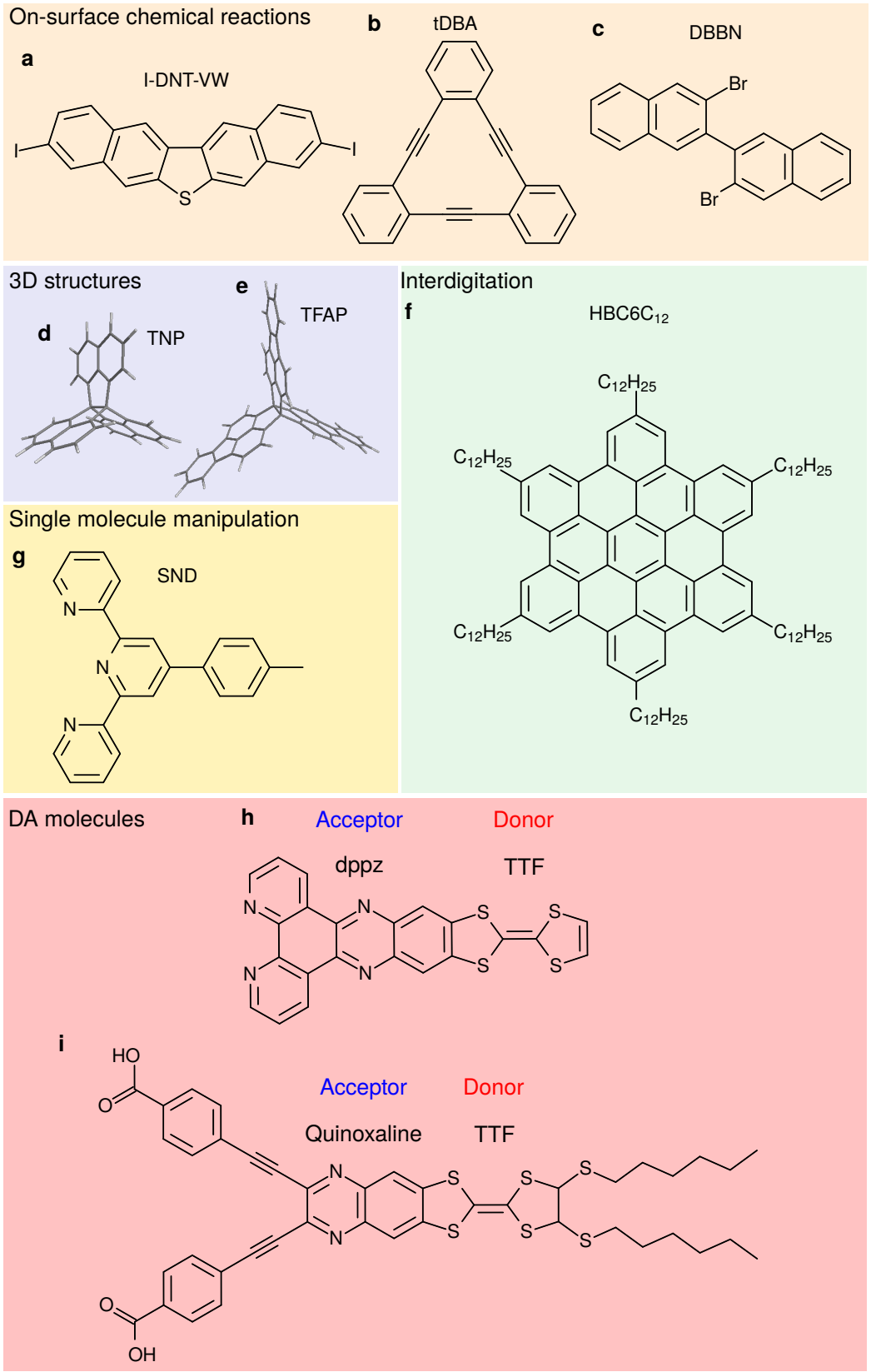

Fig. 2.9: Chemical structures of investigated molecules.

2.4.3 DBBN

3,3'-dibromo-2,2'-binaphthalene (DBBN) is synthesized by the group of Shingo Ito and Kyoko Nozaki (Fig. 2.9c). [129] By an Ullmann-type on-surface reaction, the Br atoms of DBBN can be cleaved and covalent intramolecular bonds are formed. This is employed to study the competition of aromaticity and anti-aromaticity of the molecular structure.

2.4.4 TNP and TFAP

Trinaphtho[3.3.3]propellane (TNP) and trifluorantheno[3.3.3]propellane (TFAP) are synthesized by the group of Tomohiko Nishiuchi and Takashi Kubo (Fig. 2.9d,e). [130] The molecules have three-dimensional structures which allow the vertical access to hydrogen atoms of the upstanding rings with the tip. Thus, intermolecular interaction between the CO at the tip and the hydrogen atoms of the molecule can be studied.

2.4.5 HBC6C$_{12}$

Hexadodecyl-hexa-perihexabenzocoronene (HBC6C$_{12}$) molecule is synthesized by the group of Klaus Müllen. [131] Six long alkyl chains are connected to a large aromatic core as peripheral side groups (Fig. 2.9f). Alkyl chains interact by vdW forces with adjacent alkyl chains which leads to interdigitation. [132] Interdigitation governs the assembly formation which is observed at liquid-solid interfaces by STM. [132–134]

However, large molecular structures with peripheral side groups are thermally fragile which prevents the deposition in UHV and the study of their molecular assembly formation on solid surfaces. HBC6C$_{12}$ is used to demonstrate the application of electrospray deposition technique to obtain such chemical structures on surfaces in UHV.

2.4.6 SND

The tolyl-terpyridine molecule, so-called Swiss Nano Dragster (SND), is synthesized by the group of Prof. Catherine Housecroft. [135] It is composed of three pyridine units and one front methylphenyl (tolyl) unit linked by C-C bonds (Fig. 2.9g). The structure is planar and the terpyridine moieties act as coordination center favouring the formation of coordination bonds with transition metals *via* the lone-pairs of the pyridine nitrogens. [135] This functionality is used in dye sensitized solar cells (DSSC) where SND molecules are employed as bridge between the electrode and the sensitizer. [136] In DSSC, the tolyl unit couples to the electrode. On the other side of the molecular structure, a coordination complex between the pyridine units and a metal ion is formed. Sensitizer molecules can dock on this metal ion. Thus, an efficient charge transfer through the SND molecule from the sensitizer to the electrode is achieved.

On metalic surfaces in UHV, the localized coordination center of the terpyridine unit is expected to dominate the interaction with the metallic substrate whereas the tolyl unit only weakly physisorbs due to van der Waals interactions. [137] This might be favorable for single molecule manipulation.

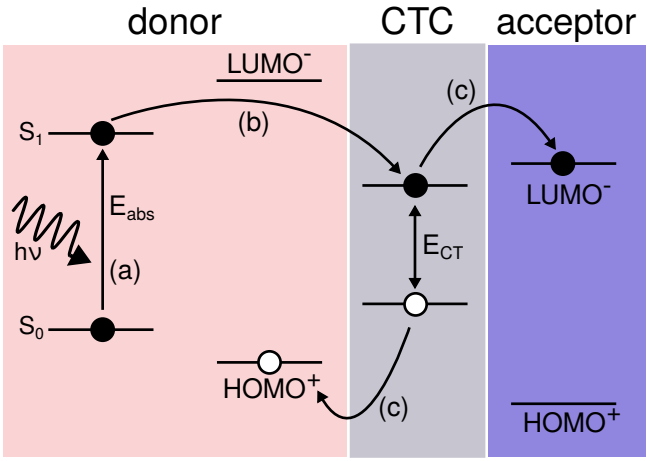

Fig. 2.10: Intramolecular charge transfer at DA interfaces in heterojunction solar cells. *Schematic drawing of the energy levels involved in the charge transfer.* ***a*** *Upon photon absorption, a transition between the singlet ground state S_0 and the first excited state S_1 occurs which leads to the creation of an exciton in the donor molecule.* ***b****, The exciton diffuses to the interface between the donor and acceptor molecules where a charge transfer complex with a CT state is formed. The CT state is populated if $E_{abs} > E_{CT}$.* ***c,*** *The charges of the exciton can be separated by transfering the electron to the LUMO of the acceptor and the hole to the HOMO of the donor if the Coulomb binding energy is overcome.*

2.4.7 Donor-acceptor molecules

In organic solar cells using donor-acceptor (DA) heterojunctions, electron donor molecules are mixed with electron acceptor molecules to build interfaces. [138–141] The DA interface leads to the formation of a charge transfer complex (CTC) where electron-hole pairs (excitons) can be separated which creates charge transfer (CT). [139, 142, 143] Excitons are generated in the donor by absorption of photons with a higher energy than E_{abs} (Fig. 2.10a). For the creation of free charge carriers which can be extracted at the electrodes, excitons have to diffuse to the DA interface which results in a population of the CT state if $E_{\mathrm{abs}} > E_{\mathrm{CT}}$ (Fig. 2.10b). [139] If the Coulomb binding energy of the exciton is overcome, the electron can be transferred from the CT state to the LUMO of the acceptor whereas the hole can be transferred to the HOMO of the donor (Fig. 2.10c). Thus, the exciton is separated and free charges are created which is used for the photocurrent generation in organic solar cells. The reason for overcoming the binding energy of the exciton has been under debate. [139, 142, 143]

Recombination can occur which prevents the creation of free charges. Recombination of CT states can be induced by transition to the ground state, by electron back transfer to the donor exciton state or by diffusion of the CTC to the surface where one of the constitutes of the exciton recombines. Consequently, the separation of the CT state strongly depends on the contribution of the different recombination mechanisms. [139] To control the exciton separation and recombination processes, the interplay between molecular properties, electronic states and surface interactions has to be understood.

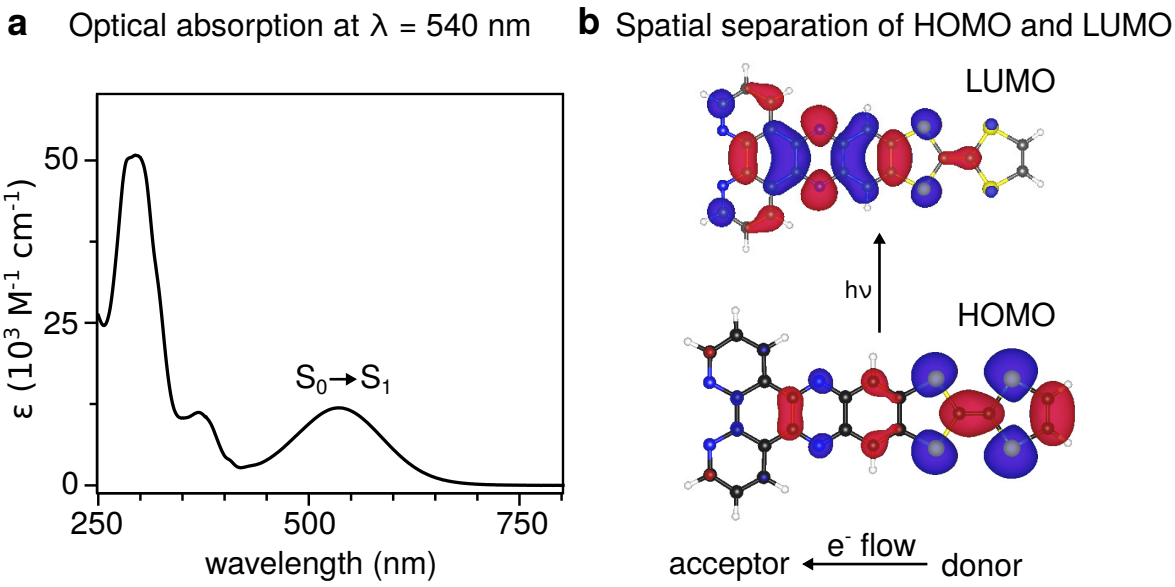

Fig. 2.11: Intramolecular charge transfer in TTF-dppz. ***a,*** *Absorption spectrum of TTF-dppz in CH_2Cl_2 solution with an absorption peak at $\lambda = 540$ nm, corresponding to a S_0-S_1 transition. Adapted from ref. [144].* ***b,*** *DFT calculation of the free molecule in the gas phase showing the spatial distribution of the HOMO and LUMO which is responsible for the ICT from the donor to the acceptor. [145]*

By fusing an electron donor moiety to an electron acceptor moiety, a single DA molecule is obtained which builds a well-defined CTC on the nanometer scale. Absorptions bands different from the absorption of the isolated molecular moieties occur which indicates the creation of a charge transfer state. [144] Thereby, DA properties leading to the CT state can be studied independently from diffusion processes at the DA interface in macroscopic devices. The HOMO of the donor and the LUMO of the acceptor, which are involved in the CT separation process, are implemented in one single molecule, but spatially separated on the different molecular moieties. Thus, after creating excitons and separating the CT state, charge is transferred from the donor to the acceptor which leads to a directional charge flow in a single molecule.

2.4.8 TTF-dppz

The tetrathiafulvalene-fused dipyridophenazine (TTF-dppz) is a fused electron DA molecule (Fig. 2.9h) which is synthesized by the group of Silvio Decurtins and Shi-Xia Liu. [144] DA molecules are candidates for the application in single-molecule based electronic devices because of their unique DA properties. In TTF-dppz, the DA properties are obtained by fusing TTF, a well-studied donor extensively used in charge transfer salts [146], to dppz, which acts as an acceptor. [144] Dppz has a metal chelating diimine side which can be used to tune the light absorption properties by coordination complex formation. [116, 147]

The HOMO and the LUMO are spatially separated (Fig. 2.11b) which leads to the outstanding property of TTF-dppz to split electron-hole pairs upon photon absorption

creating intramolecular charge transfer (ICT) from the donor to the acceptor. The absorption peak for the HOMO-LUMO transition is at a wavelength of $\lambda_{\mathrm{abs}} = 540\,\mathrm{nm}$ (Fig. 2.11a) which is tested by optical spectroscopy in solution. [144] The absorption induces the intramolecular charge transfer due to excitation of an electron from the HOMO to the LUMO. Thus, a change of the dipole moment of the TTF-dppz molecule from 0.9 D in the ground state to 5.9 D in the excited state occurs, as calculated by time dependent DFT. [144]. The ability to convert light into electrical current is applied in organic solar cells based on DA molecules. [148]

The DA property of the fused, π-conjugated TTF-dppz molecule leads to spatially separated electron-rich and electron-deficient moieties which corresponds to the acceptor and donor, respectively. By connecting the donor and acceptor to electrodes and applying a voltage, electrons could resonantly tunnel in and out of the molecule. Because one direction of the charge flow is preferred, DA molecules rectify the current and act as molecular diodes [149] which can be investigated by using the mechanically controllable break-junction technique. [150]

2.4.9 TTF-quinoxaline

The tetrathiafulvalene-quinoxaline molecule (TTF-dye) is a fused electron donor-acceptor system with benzoic acid and alkyl end groups (Fig. 2.9i) which is synthesized by the group of Shi-Xia Liu and Silvio Decurtins. [148] Similar to the TTF-dppz molecule, the TTF-dye shows for the HOMO-LUMO transition an intramolecular charge transfer upon photoexcitation with a wide spectral absorption range centered at 526 nm (Fig. 2.12a). [148] The peripheral end groups, benzoic acid and alkyl chains, are attached to molecular core to enhance the anchoring of the dye with titaniumdioxide commonly used as wide bandgap semiconductor material in DSSC. [151, 152] DSSC sensitized with the TTF-dyes exhibit one of the highest power conversion efficiencies for TTF-based sensitzers. [148]

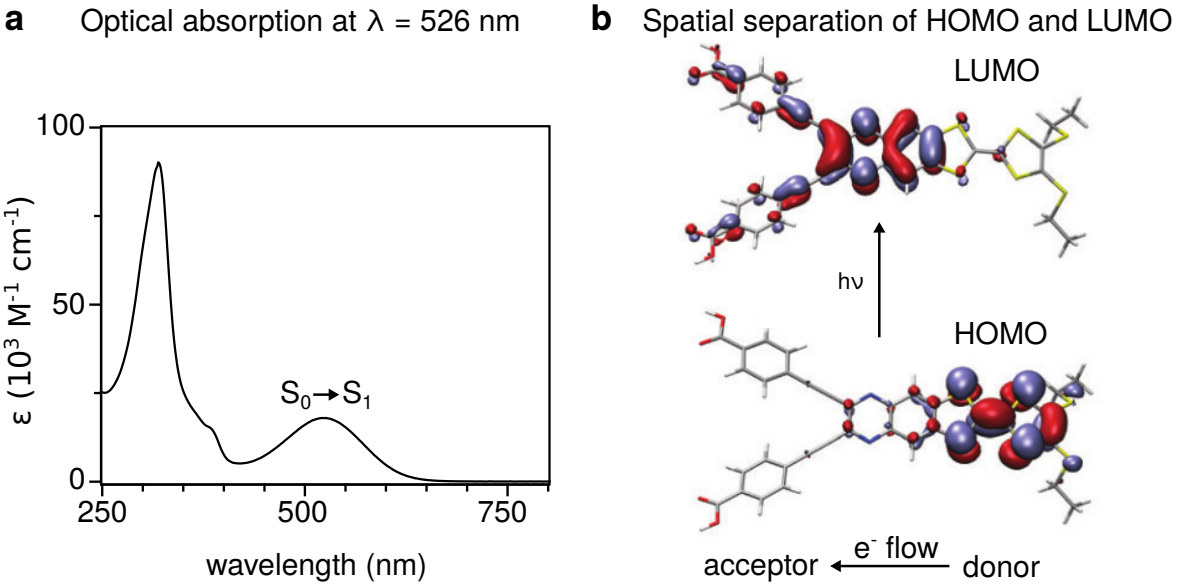

Fig. 2.12: Intramolecular charge transfer in TTF-dye. ***a,*** *Absorption spectrum of the TTF-dye in THF solution. The S_0-S_1 transition occurs at a wavelength of 526 nm.* ***b,*** *DFT calculated spatial distribution of the HOMO and LUMO. The spatial separation leads to the ICT upon photoexcitation. Adapted from ref. [148].*

3

Exploring characteristics of molecules and atoms on surfaces

To access structural and electronic properties at the atomic level, STM and AFM are indispensable tools for surface science. Targeting the goal to control displacements and electronic states of molecules on a surface, the interplay between molecules, *i.e.* bond formation, has to be understood. Intermolecular bonds, such as hydrogen bonds or van der Waals interactions between molecules influence the formation of molecular assemblies. Moreover, intramolecular bonds determine properties like the aromaticity of single molecules. Understanding and controlling bond formation between molecules or within a molecule might be employed to create chemical compounds by on-surface chemical reactions. An additional route to explore molecules with more complex chemical structures on a surface in UHV is to apply adapted deposition techniques ensuring the structural integrity of the molecules. In this chapter, examples for the analysis of inter- and intramolecular bond formation of molecules on metal substrates are shown.

Beyond structural investigations, STM and AFM also allow to examine electronic states at the dimensions of atoms. Especially, the simultaneous acquisition of both physical quantities, the tunneling current and the frequency shift, provides structural and electronic information that can be correlated directly.

3.1 State of the art

Molecules on metal surfaces have been intensively studied by STM and AFM to reveal bonding motifs and structures of molecular assemblies. Assembly formation can be controlled by adapting the molecular structure, the bonding motif and the coverage of the substrate. Non-covalent bonding between the molecular precursors, such as hydrogen bonding, leads to small molecular islands, such as trimers or tetramers, molecular wires or two-dimensional assemblies. [153–155] Analysis of individual molecules revealed the influence of the surface on the conformation of molecules. [156] By controlling the coverage of molecules on the surface, the structure of assemblies can be varied. [157] Additionally, molecular assemblies are formed by metal-organic coordination [158] and can be tuned by deposition of metal atoms on the surface. [159] These

metal-organic coordination networks can build nano-pores that can be filled with guest atoms or molecules and used as nanometer sized cavities. [160–163] Covalent bonding between molecules in an assembly can also be established by adding peripheral groups to the molecular structures that break and form covalent bonds upon annealing on the surface. [117, 164] In the following chapter the achievements of controlling molecular assemblies on metal surfaces are combined with the resolution imaging of CO terminated tips allowing to image the chemical structures of molecular assemblies, determine bond formation and also analyse the bond order. [8, 70]

Force spectroscopy performed by measuring the frequency shift as a function of the tip sample distance, offers the possibility to locally probe and quantify the interaction force between tip and sample at the atomic level (Sec. 1.3.1). Force spectroscopy was used to quantify short-range chemical bonding forces between atoms of the tip and of the Si(111) 7×7 surface. [75] Sublattice sites of alkali halides surfaces were classified by determining the tip polarity. [165] To perform force spectroscopy at the atomic level, the thermal drift has to be compensated which can be done using atom tracking. [166, 167] By measuring and normalizing the short-range forces arising from tip-sample interactions on different sites, single atoms of a surface alloy can be chemically identified. [90] Furthermore, atoms in heterogeneous atomic chains on Si(100) were distinguished by force spectroscopy. [168] Weak interactions on single-walled carbon nanotubes [169] as well as structural deformations accompanied by electronic changes of the surface due to large chemical forces during bond formation [170] can be studied. Employing three-dimensional force spectroscopy, complete force maps with detailed information about site-specific interaction on graphite [171], on C_{60} [87] and on other organic molecules [89] are obtained. Van der Waals interactions between two noble gas atoms were measured by terminating the tip with Xe and probing Xe, Ar and Kr which are stabilized by the nodes of a metal-organic framework. [172] The last example demonstrate that weak interactions between a previously functionalized tip and adatoms on the surface can be analysed.

3.2 Analysis of intermolecular bonds

Intermolecular interactions mainly determine the structure of a molecular assembly. Adsorbed on a surface, the molecules of an assembly also interact with the underlying metal substrate. By controlling these two interactions, chemical reactions can be intentionally induced to form covalent bonds leading to one-dimensional polymeric chains or two-dimensional molecular sheets on a surface. The intermediate steps of such an on-surface chemical reaction can be followed and analyzed by STM and AFM. For the control of intermolecular bonds, side groups are added to the molecular cores as for example alkyl chains, carboxylic acid or cyano groups. As a consequence, the molecular weight increases which requires special deposition techniques for UHV. Van der Waals interactions between long alkyl chains can be studied on a surface as well as single hydrogen bonds between the hydrogen atoms of an adsorbed molecule and the CO of the tip.

Organometallic bond in Ullmann-type chemical reaction *The results presented in the next paragraph have been published in the journal Small.*[a] *[173] Figures are reproduced with permission from John Wiley and Sons.*

STM and AFM enable the investigation of intermediate steps of chemical reactions on surfaces on the molecular level. Here, the formation of an intermediate organometallic C–Ag–C bond of an Ullmann-type chemical reaction is studied on a Ag(111) surface by STM and AFM. Ullmann coupling [119] is well known from solution chemistry and imply metal ions that act as catalysts for dehalagogenation to form C–C bonds (Sec. 2.4.1). On surfaces, molecules can also be coupled in this way leading to the synthesis of new chemical structures. [117, 120–122, 174, 175]

The I-DNT-VW molecules are deposited on a clean Ag(111) surface which is kept at 150 K to prevent further chemical reactions activated by temperature. In the STM image, different features can be recognized (Fig. 3.1b). It shows that the molecules are V-shaped and lie in rows as indicated by the yellow marks. For further analysis AFM with CO terminated tips is performed which reveals the structure and bonding motives (Fig. 3.1c). The protruding part of the molecule is the S atom (inset Fig. 3.1b) of the molecular structure. The dots located between the rows of molecules (indicated by blue arrows) are cleaved I atoms which stay on the surface. The brightest protrusions in the STM image, highlighted by white arrows, are seen in the rows of molecules (Fig. 3.1b). The AFM image shows that these are I atoms which are still bound to the molecular backbone (Fig. 3.1c). In contrast, the dots which connect two molecular structures are less bright in the STM image and show a white blurry "cloud" in the AFM image (dashed area). Since the AFM image is recorded at constant height, this indicates that the ends of the molecules are located closer to the substrate than the centers so that the tip-sample distance is too large to show a contrast in the frequency shift.

Consequently, the tip is approached and only the blurry region between the molecules is scanned (dashed rectangle in Fig. 3.1c). The resulting AFM image is shown in the inset of Fig. 3.1c. A bond-like connection between the molecules is observed. Since bond-like features can occur in AFM images even if there is not a real bond, but elevated electron density, the interpretation has to be made carefully. [176] However, it is known from solution chemistry that I-DNT-VW forms organometallic bonds by dehalogenation and also STM studies identified the same features as seen in the STM image in Fig. 3.1a as organometallic bond. [177] Furthermore, the molecular structure is unambiguously identified in the AFM image, so that the conclusion is made that the feature in the AFM inset is caused by the organometallic C–Ag–C bond.

To confirm this assumption, the bond length is measured which yields a length of 270 pm. The measured value is much higher than the calculated bond length of 423 pm. The difference is due to the tilt effect of the CO which increases the apparent size of the carbon rings. [178]

[a] Kawai, S., Sadeghi, A., Okamoto, T., Mitsui, C., Pawlak, R., Meier, T., Takeya, J., Goedecker, S., Meyer, E. Organometallic Bonding in an Ullmann-Type On-Surface Chemical Reaction Studied by High-Resolution Atomic Force Microscopy *Small* **12,** 5303 (2016).

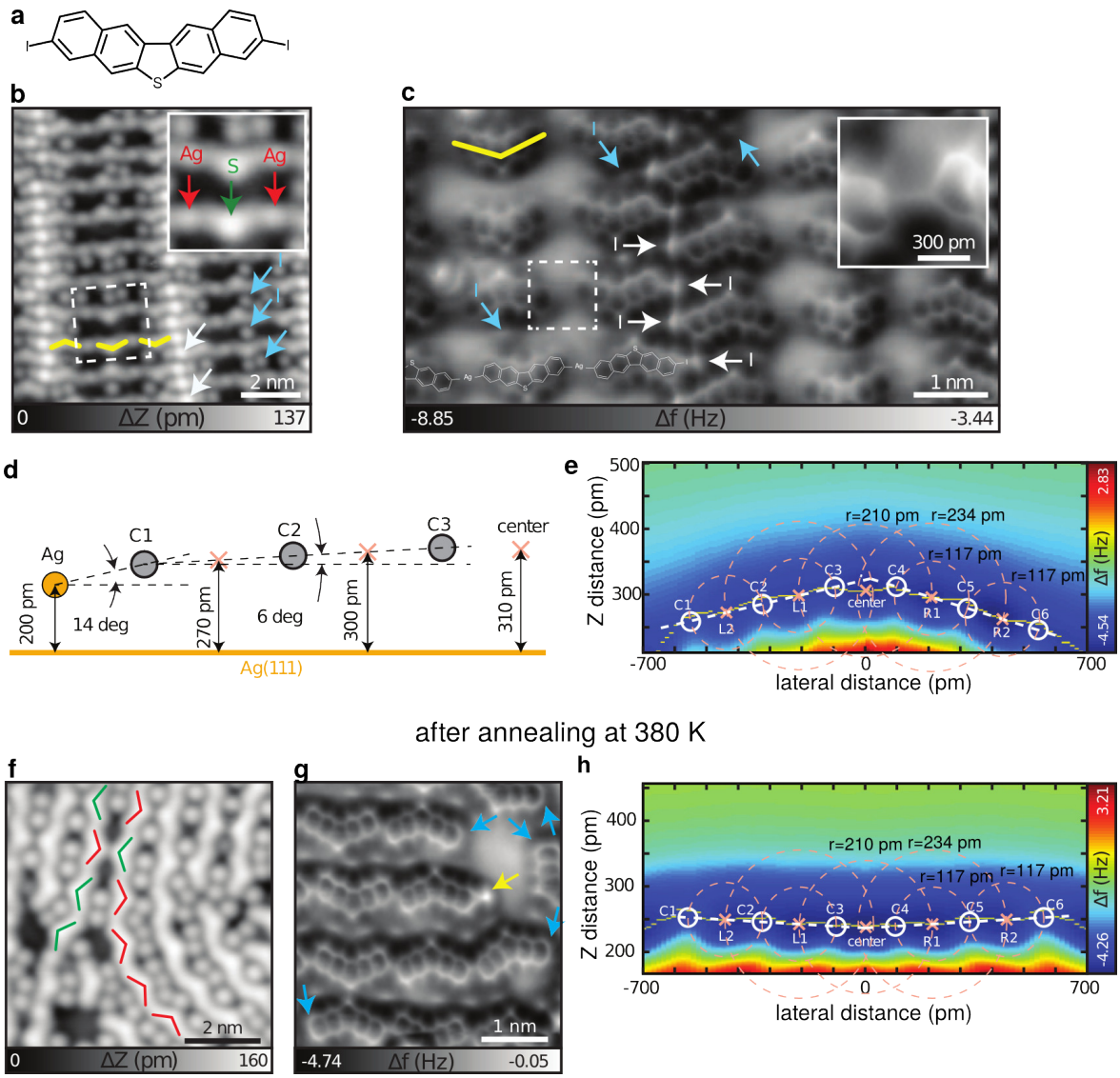

Fig. 3.1: STM, AFM and force spectroscopy maps on I-DNT-VW. ***a,*** *Chemical structure of I-DNT-VW molecule.* ***b,*** *STM image of I-DNT-VW deposited on Ag(111) below* $150\,K$*. Dashed area marks the scan frame of the inset* ($V_b = -200\,mV, I_t = 2\,pA$)*.* ***c,*** *AFM image of I-DNT-VW molecules. The inset shows an AFM image of the area around the organometallic bond which is marked by a dashed square. The image is recorded* $70\,pm$ *closer to the sample than the overview AFM image.* ***d,*** *Calculated positions of the atoms extracted from the measured geometry in the frequency shift map of* ***e****,* ***e,*** *Two-dimensional frequency shift map recorded along the V-shaped longitudinal axis of the molecule. The dashed circles illustrate the gaps between the centers of the carbon rings and between two bonds.* ***f,*** *STM topography after annealing the sample at* $380\,K$ ($V_b = -200\,mV, I_t = 2\,pA$)*.* ***g,*** *AFM image showing the covalently linked molecules and* ***h,*** *two-dimensional frequency shift map showing the flat geometry of the molecules. [173]*

To investigate the bent structure of the molecule, two-dimensional Δf maps are recorded along the V-shaped longitudinal axis of the molecule (Fig. 3.1e). The most negative frequency shift value is used to determine the corrugation of the molecule. [89] At the center the molecule has an adsorption height of 310 pm. Single C atoms on the left (260 pm) and on the right (250 pm) are closer to the substrate. This leads to a bending angle of the left and right napthalene unit to the substrate of 6° and 8°, respectively. The bent angle of the whole molecule is 14° (Fig. 3.1d) which is in agreement with crystal structure observations. [118] The asymmetry of the molecular bending can be related to the different adsorption sites of the Ag atoms (one on hollow and one on bridge site) on the left and right side of the molecule which was determined by resolving the surface lattice of Ag(111) by AFM and comparing them with DFT calculations. [173] If both Ag atoms are located on equivalent sites, the bending of the molecule is symmetric. The adsorption height of the Ag is 200 pm (Fig. 3.1d) which is a clear evidence that the Ag atom is an adatom.

Following from these results, the deposition of I-DNT-VW molecules on cold Ag(111) at 150 K leads to the cleaving of the C–I σ-bond and to the formation of a C–Ag bond. This product is short-lived because organometallic C–Ag–C bonds to other molecules are immediately formed. The cleaved I atoms stay on the surface.

In a further step, the sample is annealed at 380 K to dissociate the Ag atoms and form C–C bonds (Fig. 3.1f-h). The molecules are polymerized and depending on the orientation, the chain is straight or curved (Fig. 3.1f). This highlights the flexibility of the C–C bond compared to the organometallic C–Ag–C bond where the molecules align in straight rows (Fig. 3.1b). The structure after annealing at 380 K can be observed in an AFM image (Fig. 3.1g) which shows that the molecules are linked to each other in a planar configuration. The extracted bond length between the C atoms of adjacent molecular units is 120 pm which is shorter than organometallic bond length (270 pm). The calculated length for the C-C bond is 136 pm which is slightly higher than the measured one due to the effect of the CO bending in the AFM scan. The two-dimensional Δf map in Fig. 3.1h reveals the lowering of the adsorption height by 70 pm and the flat geometry of the polymerized chain in comparison to the molecule in the map in Fig. 3.1e.

In conclusion, the intermediate steps of the formation of covalently bound molecular chains are observed by STM and AFM in combination with DFT calculations. The presence of I atoms in the molecular structure leads to the formation of organometallic bonds between the molecules and Ag adatoms on the surface upon deposition on the Ag(111) sample kept at 150 K. Due to the C–Ag–C bond, both ends of the molecular structure are bent towards the surface. By further annealing at 380 K, the Ag adatoms are removed and covalent bond formation is induced which links the molecules to one-dimensional polymeric chains. The polymeric chain is lying flat on the surface with a lower adsorption height. The results show that STM and AFM can be used to study chemical on-surface reactions in detail by resolving the molecular geometry and structure. In the case of I-DNT-VW, I atoms are used to trigger a chemical reaction which finally forms a covalently bound molecular chain. More complex side groups can be added to molecular structures in order to dominate intermolecular interactions which is presented in the following.

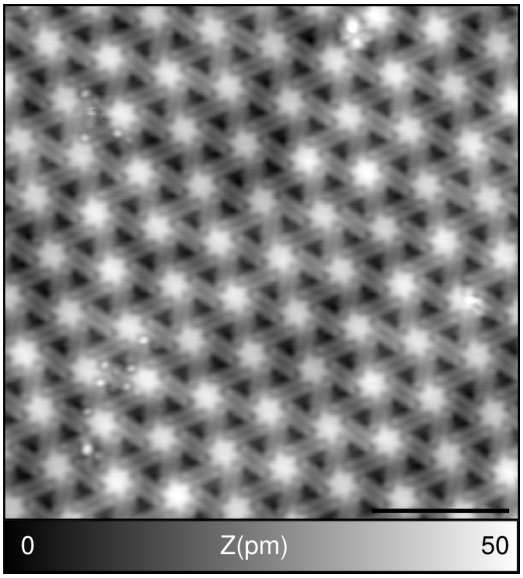

Fig. 3.2: STM image of HBC6C$_{12}$ molecules on Au(111) *($I_t = 2\,pA, V_b = -200\,mV$, scale bar = 5 nm) [179]*

HBC6C$_{12}$ molecules deposited by electrospray *The results presented in the next paragraph have been published in an article of the journal Nanoscale.*[b] *[179] Figures are reproduced with permission from the Royal Society of Chemistry.*

Molecular assemblies can also be obtained by weaker interactions than covalent bonding. Incorporating long alkyl chains is known to lead to interdigitation which can result in the formation of large islands. [133, 180–183]

However, attaching side groups leads to an increase of the molecular complexity and weight which might cause fragmentation of the molecules during deposition by thermal evaporation. This standard deposition technique limits the structural complexity of observable molecules in UHV. Consequently, studies of molecules with long peripheral alkyl chains are usually performed at liquid-solid interfaces since in UHV, only small peripheral alkyl chains could be investigated. [133,181,184] The electrospray deposition (ESD) technique (Sec. 2.3.3) solves this problem by transfering molecules from solution onto a surface in UHV enabling the deposition of large molecules with side groups. [112, 185–189] Electrospray ion beam deposition methods with soft landing devices or mass spectrometry offer additional features in sample preparation. [190–192]

Here, a polycyclic aromatic hydrocarbon molecule, HBC6C$_{12}$ (Sec. 2.4.5), with six dodecyl chains attached to the HBC core, is used to demonstrate the deposition by ESD of intact large molecules with long and numerous alkyl chains. Only the HBC core is thermally stable and studied at surfaces under UHV conditions. [70, 193]

In Fig. 3.2 an overview STM image of HBC6C$_{12}$ molecules on the surface as it is received after electrospray deposition is shown. The sample is kept at room temperature

[b] Hinaut, A., Meier, T., Pawlak, R., Freund, S., Jöhr, R., Glatzel, T., Decurtins, S., Müllen, K., Narita, A., Liu, S.-X., Meyer, E. Electrospray Deposition of Structurally Complex Molecules Revealed by Atomic Force Microscopy. *Nanoscale* **10,** 1337 (2018).

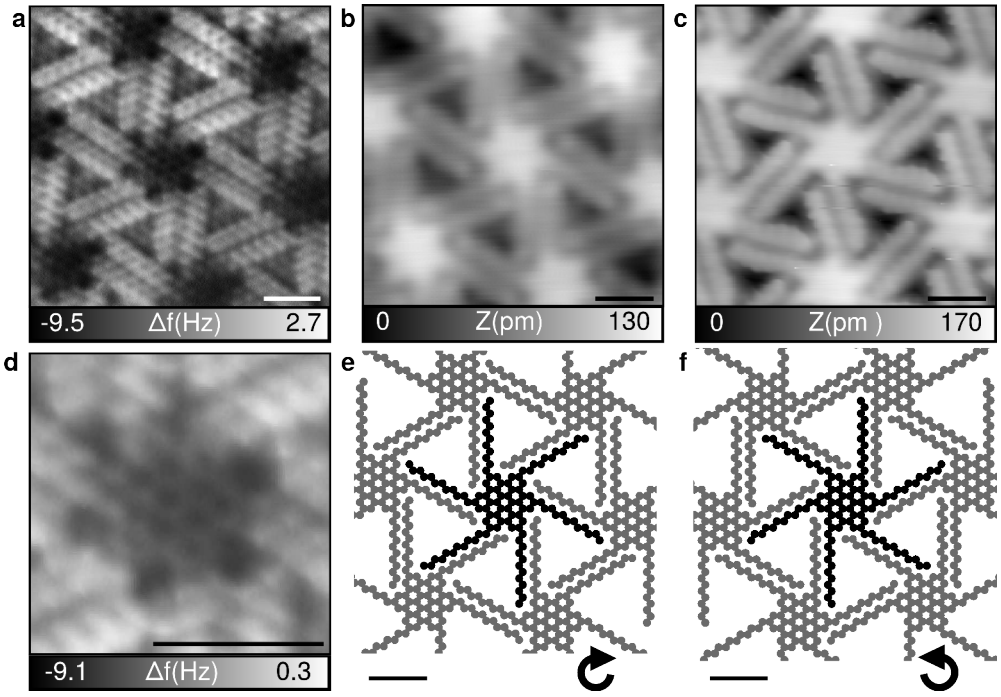

Fig. 3.3: High resolution imaging of the HBC6C$_{12}$ assembly on Au(111). ***a,*** *AFM image of interdigitated alkyl chains and* ***d,*** *of the HBC core.* ***b,c,*** *STM images of two different islands with two different enantiomer orientations (in* ***e****,* $I_t = 2\,pA, V_b = -200\,mV$*, in* ***c****,* $I_t = 1\,pA, V_b = -1.5\,V$*, scale bars =* $1\,nm$*).* ***e, f,*** *Model of the molecular alignment corresponding to* ***b*** *and* ***c****. [179]*

during deposition and no post-annealing is performed. Large molecular assemblies in the range of hundred nanometer are formed on the Au(111) substrate. The star-like HBC core and the individual alkyl chains are clearly observed in the STM image. The lattice constant of the molecular assembly is $\sim 2.2\,nm$.

From AFM images recorded at room temperature (RT), it is known that each molecule aligns with the alkyl chains pointing straight toward the center of the HBC core leading to interdigitation. [179] At LT however, the alkyl chains are oriented with a certain angle with respect to the HBC core (Fig. 3.2). To get detailed information about the interdigitation, the molecules are scanned with higher resolution. The surrounding alkyl chains are revealed as zig-zag structures which are brighter than the core indicating a smaller tip-sample distance on the chains (Fig. 3.3a). A zoom on the area of the core reveals its expected chemical structure (Fig. 3.3d) as already observed in literature. [70] The higher resolved STM images (Fig. 3.3b,c) highlight that the alkyl chains leave the core with an angle and are not pointing straight forward to the center of the opposite molecule. As consequence of this exit angle of the alky chains, the HBC6C$_{12}$ shows a chiral conformation (compare Fig. 3.3b to c) resulting in enantiomeric assemblies at LT. The molecular assemblies are compressed with respect to the assemblies at RT to maximize the interdigitation between the alkyl chains and increase van der Waals interactions. Subsequently, the lattice parameter at LT (2.2 nm) decreases in comparison to assemblies at RT (2.6 nm) due to the observed

chirality at LT. [179, 194]

The results show that the formation of extended islands of $HBC6C_{12}$ is promoted by the long alkyl chains which are attached to the molecular core. Such large molecular structures can be investigated by STM and AFM in UHV due to the electrospray deposition technique. The bonding motive of the molecular assembly is revealed by observing the interdigitation and the chiral phase transition induced by van der Waals interactions. Other important intermolecular interactions in nature are hydrogen bonds which are studied in the following.

Quantitative force measurement by detection of a hydrogen bond *The results presented in the next paragraph have been published in the journal Science Advances.*[c] *[195] Figures are reproduced with permission from AAAS.*

The attraction between covalently bound hydrogen atoms to close-by electronegative atoms, also called hydrogen bond, is present in many systems in nature such as DNA, water or organic molecules. For example in DNA, hydrogen bonds are created between the complementary base pairs which leads to the formation of the three-dimensional double helical structure, responsible for its possible replication. Due to its importance in nature, atomically precise studies of intermolecular interactions induced by hydrogen bonding are of fundamental interest to understand biological and chemical processes. The use of AFM is mandatory since commonly employed spectroscopy techniques like nuclear magnetic resonance spectroscopy or X-ray crystallography cannot resolve hydrogen bonds. In AFM, tips can be terminated by CO molecules which creates a probe for local chemical reactivity since it senses Pauli repulsion as well as chemical forces (Sec. 1.3). [196] Consequently, the C=O· · ·H–C hydrogen bonding between the CO tip and hydrogen atoms of an adsorbed molecule could be directly detected. However, most of the investigated molecules on surfaces are planar, which prevents the direct measurement of the hydrogen bonding. By choosing a three-dimensional molecular setup which allows that CH groups stick out of the surface plane, the CO tip could be vertically approached to perform force measurements. For this reason, three-dimensional propellane derivatives are used (Fig. 3.4a,b and Sec. 2.4.4).

The propellane molecules have two CH groups pointing out from the surface plane when adsorbed in the upright position. In Figure 3.4c upright (red arrows) and side-lying (yellow arrows) configurations of the TNP molecules (Fig. 3.4a) on the Ag(111) surface can be observed. The double dot structure indicates the upright position as it is also seen for the TFAP molecules (Fig. 3.4b). This position allows a direct access the C=O···H–C interaction when the tip is approached. To measure the force between tip and hydrogen atoms, a two-dimensional Δf map is recorded on the axis of the two dot structure (Fig. 3.4e, f). The measured frequency shift is converted into forces using the method described in Eq. 1.24 in Sec. 1.2 which leads to a two-dimensional force map (Fig. 3.4g). The potential is also obtained by integrating the force field (Fig. 3.4h)

[c] Kawai, S., Nishiuchi, T.; Kodama, T., Spijker, P., Pawlak, R.; Meier, T., Tracey, J., Kubo, T., Meyer, E., Foster, A. S. Direct quantitative measurement of the C=O...H-C bond by atomic force microscopy. *Sci. Adv.* **3,** 1603258 (2017).

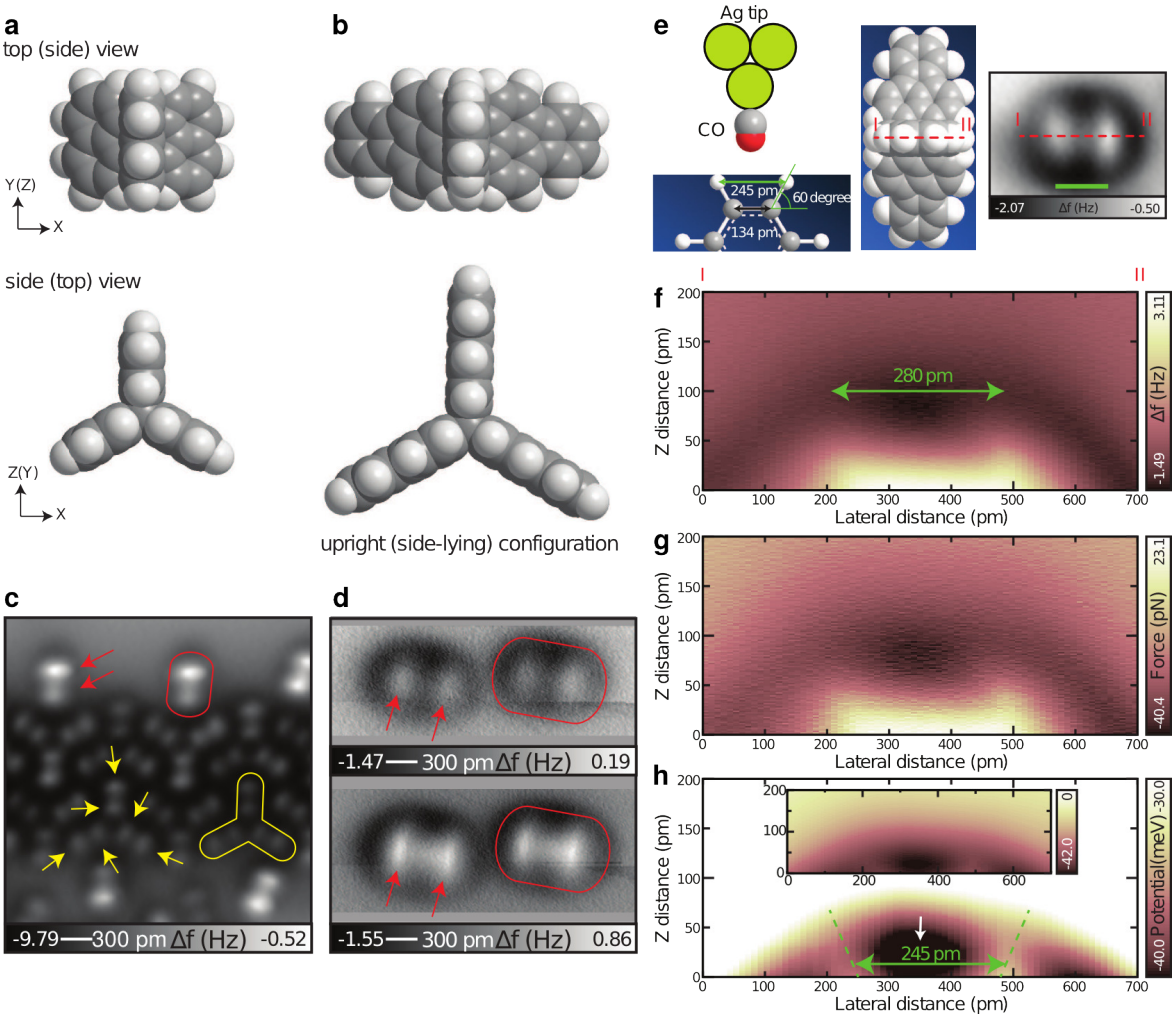

Fig. 3.4: Direct quantitative measurement of the C=O···H–C bond. *Chemical structures of* ***a,*** *TNP and* ***b,*** *TFAP. The upper structures represents the top (side) view if the molecules are in the upright (side-lying) position. The lower structures show the side (top) view for the upright (side-lying) adsorption geometry.* ***c,*** *AFM image of the upright (red arrows and area) and side-lying (yellow arrows and area) molecules of TNP on Ag(111).* ***d,*** *Higher resolution AFM image of upright TNP molecules with a CO terminated tip.* ***e,*** *Schematic representation of the experiment with AFM image of upright TFAP molecule on Ag(111).* ***f,*** *Two-dimensional frequency shift map of TFAP molecules in the upright position* ***g,*** *Corresponding converted force map and* ***h,*** *Potential map. [195]*

following Eq. 1.25.

Figure 3.4g shows a dark halo around the molecule representing attractive forces. Its minimum corresponding to the most attractive site is located between two hydrogen atoms and has a strength of −40 pN. This strength is of comparable order to van der Waals interaction forces between atoms. [172] In the potential map a dip is located at the same position (Fig. 3.4h). The minimum of the experimentally determined potential is about 40 meV which is comparable to the DFT calculated value of 35 meV. [195] The ridge lines of the potential tails can be used to measure the angle between the two C–H and the C–C axis (Fig. 3.4h). The measured angle of 55° is close to the angle from the model (60°, Fig. 3.4e). The theoretical distance between the two hydrogen atoms is 245 pm which would lead to an experimentally determined position of the hydrogen cores at $z = 25$ pm (arrow in Fig. 3.4h). The comparison of DFT calculated potentials with the experimental data shows that the energy minimum is located at a distance of 300 pm between the oxygen of the tip and the hydrogens in the molecule. This distance would be typical for a weak hydrogen bond. [197]

Furthermore, DFT studies of the electrostatic potentials of tip and sample demonstrate that the interaction between the tip and molecule is caused by the negative charge of the O atom at the tip with the weakly charged hydrogen atoms. The O···H interaction leads to a nonlinear bond angle which is not characterstic for van der Waals interactions [198] and supporting the influence of the hydrogen bonding.

In conclusion, the direct interaction between C=O···H–C is demonstrated by resolving the outmost hydrogen atoms in a upright standing hydrocarbon molecule. This method using a vertical molecular geometry and performing two-dimensional force spectroscopy maps, shows the capability of AFM to quantify forces between single atoms which can be generally applied to investigate intermolecular interactions. The high lateral resolution of CO terminated tips also allows to reveal the intramolecular bonds which is presented in the next section.

3.3 Analysis of intramolecular bonds

Intramolecular bonds determine the chemical structure of a molecule and therefore also its properties. The capabilities of STM and AFM allow to characterize bonds within a molecule. Here, two examples are demonstrated. First, the aromaticity of molecules is analysed. It describes organic molecules that are cyclic and planar which leads to a low chemical reactivity and higher stability compared to non-aromatic ones. Second, a thermally induced chemical reaction which induces the structural transformation of a single molecule is characterized. Several products are formed during chemical reactions which depend on several possible reaction pathways. AFM offers the advantage to analyse these products by resolving their chemical structure.

Competing annulene and radialene structures *The results presented in the next paragraph have been published in the journal ACS Nano.*[d] *[129] Figures are reproduced with permission from the American Chemical Society.*

Hückel's rule says that cyclic molecules with $(4n + 2)$ π-electrons are stable and aromatic because of the efficient delocalization of π electrons (n is an positive integer). Whereas cyclic molecules which only possess $(4n)$ π-electrons are destabilized by the delocalization. These molecules are defined as anti-aromatic. The 4-membered ring, cyclobutadiene (Fig. 3.5a), is an example for an unstable anti-aromatic molecule (4 π-electrons). The cyclobutadiene core can be fused to two phenyl rings leading to biphenylene (Fig. 3.5c) which is stabilized by radialene structures. They form cross-conjugated double bonds in the phenyl rings as shown by X-ray and electron diffraction. [199–203]

Following the pioneering work from Gross *et al.* that has shown the possibility to distinguish bond order by measuring their length [70], AFM is used to analyze the aromatic behaviour of a single dibenzo[*b,h*]biphenylene molecule.

As a precursor 3,3'-dibromo-2,2'-binaphthalene (DBBN) is used which can form inter- or intramolecular single bonds by means of Ullmann type reactions on metal surfaces (Fig. 3.5d and Sec. 2.4.3). Annealing DBBN on a Ag(111) surface at a temperature of 406 K leads to the synthesis of new chemical structures including inter- and intramolecular bonds. [129] To investigate the competing annulene and radialene structures, the formation of the intramolecular bonds in dibenzo[*b,h*]biphenylene (Fig. 3.5g, h) is exclusively discussed in the following.

A STM overview image is shown in Fig. 3.5e. The molecules have a pill-like shape and form assemblies. In between the molecules the deconnected Br atoms can be seen (yellow arrows in Fig. 3.5e). High-resolution AFM imaging at constant height with a CO terminated tip reveals the chemical structure of the synthesized dibenzobiphenylene molecule (Fig. 3.5f, i). The two naphthalene moieties and the cyclobutadiene core are clearly resolved.

Even though the structure of the molecule is visible, the aromatic behaviour study imply the measurement of bond lengths. The direct determination of the bond length of the cyclobutadiene core is not possible because of the CO tilting at the tip. The rectangular shape of the molecule leads to asymmetric force gradients of the short and longitudinal axis which causes the molecular structure to appear larger in the AFM image in the direction of the short molecular axis compared to long molecular axis. [8, 204] This prevents a direct analysis of the bond order of the cyclobutadiene core.

However, the aromaticity or anti-aromaticity affects the bond order of the bonds in the naphthalene moieties which can be analysed since the lateral force field along the long molecular axis is almost constant (except an edge effect which causes the bonds at edges to be longer). Based on the molecular schemes (Fig. 3.5g, h), two criteria are

[d] Kawai, S., Takahashi, K., Ito, S., Pawlak, R., Meier, T., Spijker, P., Canova, F. F., Tracey, J., Nozaki, K., Foster, A. S., Meyer, E. Competing Annulene and Radialene Structures in a Single Anti-Aromatic Molecule Studied by High-Resolution Atomic Force Microscopy *ACS Nano* **11,** 8122 (2017).

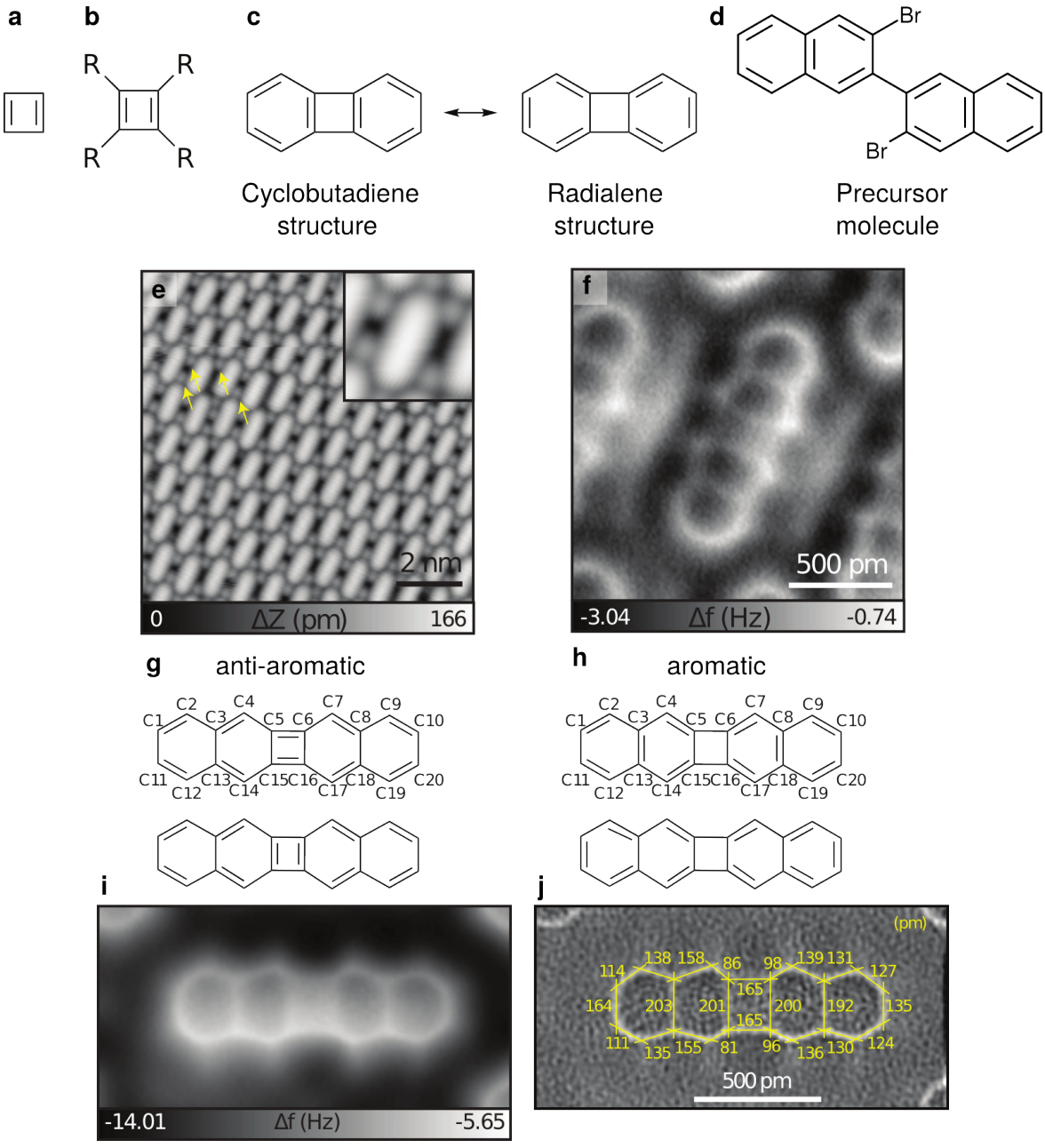

Fig. 3.5: Bond order analysis of the dibenzo[*b,h*]biphenylene molecule. ***a,*** *cyclobutadiene,* ***b,*** *tetrasubstituted cyclobutadiene,* ***c,*** *biphenylene.* ***d,*** *Chemical structure of precursor molecule 3,3'-dibromo-2,2'-binaphthalene (DBBN)* ***e,*** *Overview STM image of dibenzob,hbiphenylene molecules on Ag(111) with yellow arrows indicating Br atoms, the inset shows a single molecule in the assembly ($V_b = -200\,mV$, $I_t = 0.8\,pA$).* ***f,*** *AFM image at constant height with CO terminated tip* ***g,*** *Schemes of anti-aromatic and* ***h,*** *aromatic structures of dibenzo[b,h]biphenylene molecules.* ***i,*** *high-resolution AFM image and* ***j,*** *corresponding Laplace filtered image for better recognition of the bonds. The numbers are the measured bond lengths in pm. [129]*

chosen to determine the aromaticity and anti-aromaticity:

1. for anti-aromaticity: C3–C4 (double) < C4–C5 (single)
2. for aromaticity: C1–C2 ≈ C2–C3 and C1–C2/C2–C3 < C3–C4 (single)

The bond order analysis is done with the AFM image shown in Fig. 3.5i. The image is Laplace filtered for better contrast and the mean values of equivalent bonds are taken to get rid of anisotropic tip effects (Fig. 3.5j).

For criteria 1, it follows that C3–C4 (146 pm) $\not<$ C4–C5 (89 pm) which means that the anti-aromaticity is drastically reduced in the cyclobutadiene core by the fused naphthalene moieties.

For criteria 2, it follows that C3–C4 (146 pm) > C2–C3 (132 pm) > C1–C2 (118 pm). Since C1–C2 is shorter than C2–C3 even if the C1–C2 is an edge bond which already appears elongated, a purely radialene structure is not possible. The annulene structure has a certain influence in the observed molecular structure which leads to the shortening of the C1–C2 bond, but the radialene structure is still dominant.

The competition between radialene and annulene structures in the dibenzo-biphenylene molecule which is synthesized on the surface is reported. AFM imaging with CO terminated tips allows to resolve intramolecular bonds whose lengths can be compared and correlated to the bond orders. This shows the capability of AFM to study unknown aromatic structures of single molecules on surfaces.

Sequential transformation of a single molecule *The results presented in the next paragraph have been published in the journal Nature Communications.*[e] *[205] Figures are reproduced with permission from Springer Nature.*

The transformation of the structure of a single molecule is investigated on a surface by choosing a precursor molecule without side groups in contrast to Ullmann-type coupling reactions where intermolecular bond formation is induced. Here, the used precursor is a tDBA molecule with included acetylene units which are expected to promote intramolecular transformation processes (Fig. 3.6b and Sec. 2.4.2).

The molecules are first deposited on a Ag(111) substrate to show the intact molecular structure resolved by AFM with a CO tip (Fig. 3.6a). To perform the transformation by on-surface chemical reactions, tDBA is deposited on a Cu(111) substrate kept at below 150 K (Fig. 3.6c). The appearing molecular structures on the surface do not have the flat shape as the intact tDBA molecules on Ag(111). The molecules exhibit an elevated dot at the middle corner of the triangular structure. This prevents high-resolution over the whole molecule in constant height AFM (Fig. 3.6d). DFT leads to the conclusion that this structure is identified as a biradical molecule (Fig. 3.6g) which is stabilized by the interaction with the Cu(111) and 1.4 eV more stable than the intact

[e] Kawai, S., Haapasilta, V., Lindner, B. D., Tahara, K., Spijker, P., Buitendijk, J. A., Pawlak, R., Meier, T., Tobe, Y., Foster, A. S., Meyer, E. Thermal Control of Sequential On-Surface Transformation of a Hydrocarbon Molecule on a Copper Surface. *Nat. Commun.* **7,** 12711 (2016).

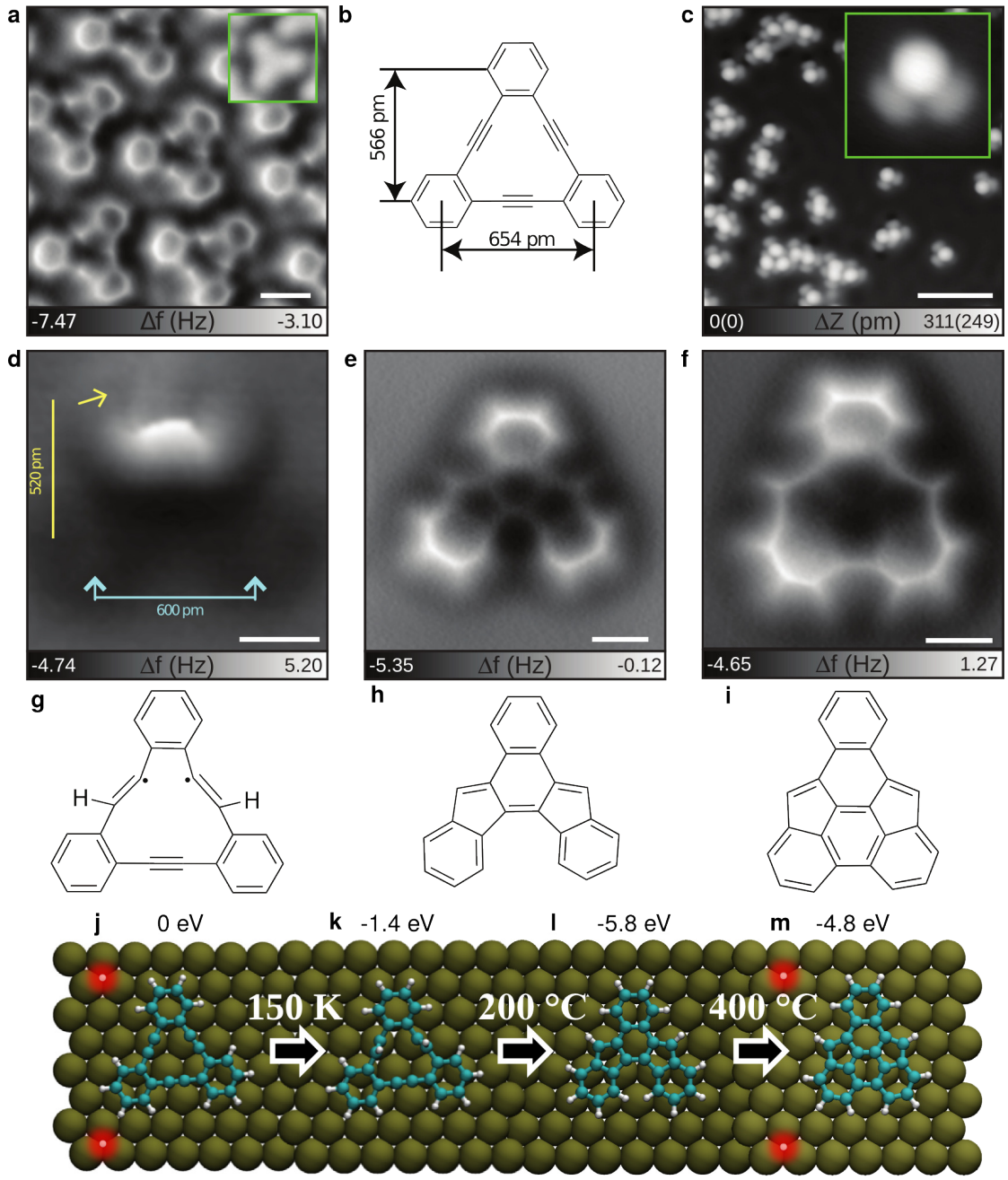

Fig. 3.6: Sequential transformation of the tDBA molecule. ***a,*** *Intact tDBA on Ag(111) (scale bar 500 pm, inset: STM image).* ***b,*** *Chemical structure of tDBA,* ***c,*** *STM image of tDBA on Cu(111) after deposition on sample kept at 150 K with $I_t = 2\,pA$, $V_b = 200\,mV$ (Inset: STM image of a single molecule, $I_t = 1\,pA$, $V_b = 200\,mV$)* ***d,*** *Biradical first reaction product corresponding to the molecules shown in* ***c,*** ***e,*** *Benzo[a]indeno[2,1–c]fluorene (second reaction product) and* ***f,*** *third reaction product on Cu(111) (scale bars 300 pm) and* ***g-i,*** *their corresponding chemical structures.* ***j-m,*** *DFT calculated structures of reaction products on Cu(111) with their adsorption energy. In* ***k*** *and* ***l*** *the structures contain two H atoms more which are placed on the Cu(111) in* ***j*** *and* ***m*** *(red dots). [205]*

tDBA on Cu(111) substrate (Fig. 3.6k). In Ullmann-type reactions, it was found that the reaction temperature on Cu(111) is lower than on Ag(111) which indicates the higher chemical reactivity of the Cu(111) surface. [206] The additional H atoms are placed on the Cu(111) substrate before the reaction in the calculations (red dots in Fig. 3.6j, m). In the experiment H atoms are present even in UHV environments.

By annealing the sample at 200°C a tandem cyclization is induced and a second reaction product, the benzo[a]indeno[2,1-c]fluorene, is observed (Fig. 3.6e, h). Interestingly, the synthesis of this product, which is a member of the indenofluorenes family, has never been observed before. [207] Benzo[a]indeno[2,1-c]fluorene is very stable on the Cu(111) surface which can be seen in the drop of the adsorption energy in DFT by more than 4 eV compared to the first biradical structure (Fig. 3.6l). During the annealing step, chain like structures are also formed by C–Cu–C organometallic bonds. [205] However, these chains also exhibit the same internal molecular structure which means that no side-products are observed. The number of chains is reduced if the sample is not kept at room temperature during deposition, but heated up to 200°C. In this case, transformed isolated molecules are predominantly obtained which demonstrates that the formation process is temperature dependent.

In a third reaction process induced by annealing at 400°C cyclodehydrogenation occures and a third reaction product is formed (Fig. 3.6f, i). Two hydrogen atoms are removed and the two bottom benzene rings are connected by a new C–C bond. Through the new bond formation which is shorter than the distance between the benzene rings of the second reaction product, the molecular structure gets compressed to a bowl-like shape in the center. This is observed in the frequency shift image by a darker contrast on the two pentagon and two hexagon rings in the center of the molecule (Fig. 3.6f). In all isolated molecules on the surface the transformation processes of the first and second annealing is observed which demonstrates the controlled transformation process and the highly selective chemical reaction.

Intramolecular bonds, determining the chemical structures of molecules, are resolved by AFM with CO terminated tips. The studies of the aromaticity and structural transformation of molecules emphasize the capability of AFM to gain structural information at the atomic level which can be used to control and observe chemical reactions on surfaces. The high lateral resolution and force sensitivity of AFM can be combined with STM measurements that probe electronic states of the sample. Thus, the position of atoms in molecules or in atomic chains on the surface can be determined by AFM and the electronic states locally probed by STM.

3.4 Analysis of electronic states

Majorana bound states *The results presented in the next paragraph have been published in the journal npj Quantum Information.*[f] *[208] Figures are reproduced with permission from Springer Nature.*

STM and AFM allow to study single adatoms on surfaces. [6,209] The results of both methods can be combined to correlate structure and electronic properties of adsorbates on surfaces. Here, AFM is used to characterize the structure of monoatomic Fe chains which is linked to the formation of quantum states investigated by STM. The Fe chains form a topological superconducting phase and at their edges signatures for Majorana fermions are observed. [210]

The Majorana fermion is a fermionic particle and its own antiparticle at the same time. [211] Theory predicted that they can occur as quasi-particle bound states in solid-state systems. [212, 213] Majorana bound states (MBS) can potentially be used for the promising field of topological quantum computing and therefore have attracted a lot of attention in research [210, 214–222]. The recipe to create MBS in a solid state system is to deposit Fe atoms on a superconducting Pb(110) surface. [212, 213] The Fe atoms build chains with a spin texture (Fig. 3.7a) and due to the presence of the superconducting Pb(110) surface, they become topological superconductors which is a new state of mater. These chains exhibit MBS at their extremities which can be observed as zero bias peaks (ZBP) in STS spectra. [210, 212]

To achieve such structures, Fe is deposited by means of the iron evaporator described in Sec. 2.3.1 on the clean Pb(110) kept at $\approx 400\,\mathrm{K}$. The STM image in Fig. 3.7b shows the formation of Fe chains which are partially covered with Fe clusters in their centers which is known from literature. [210, 223] By zooming on the ends of the chains, two different kinds of chain terminations are recognized: one with a small protruding feature at the end, one without (Fig. 3.7c,d). The small protrusion is about 10 pm in height. This small height difference suggests that the feature is not originating from a cluster or deformation. STS spectra at the chain ends reveal a ZBP for the chain with protrusion (Fig. 3.7e) and no ZBP for the chain without protrusion. The measured superconducting gap, acquired with a tip in the metallic state, is $\Delta = 1.1\,\mathrm{meV}$ which is expected by the Bardeen-Cooper-Schrieffer (BCS) theory.

To test the origin of the ZBP a two-dimensional STS map is recorded on the same chain end at 5 K in the superconducting state and at 10 K which is above the critical temperature T_c for superconductivity for lead ($T_c = 7.2\,\mathrm{K}$). The map of the LDOS shows drastic differences (Fig. 3.8d). At 5 K a ZBP is clearly observed whereas the signal of the ZBP completely disappears at 10 K. The LDOS along the Fe chain is compared with the theoretical Majorana wavefunction which exhibits an oscillation pattern. At 5 K a clearly distinguishable peak and some smaller oscillations can be observed, however at 10 K the LDOS is flat without any peak or sign of an oscillation pattern (Fig. 3.8e). This finding demonstrates that the observed protrusion in STM

[f] Pawlak, R., Kisiel, M., Klinovaja, J., Meier, T., Kawai, S., Glatzel, T., Loss, D., Meyer, E. Probing Atomic Structure and Majorana Wavefunctions in Mono-Atomic Fe Chains on Superconducting Pb Surface. *npj Quantum Information* **2,** 16035 (2016).

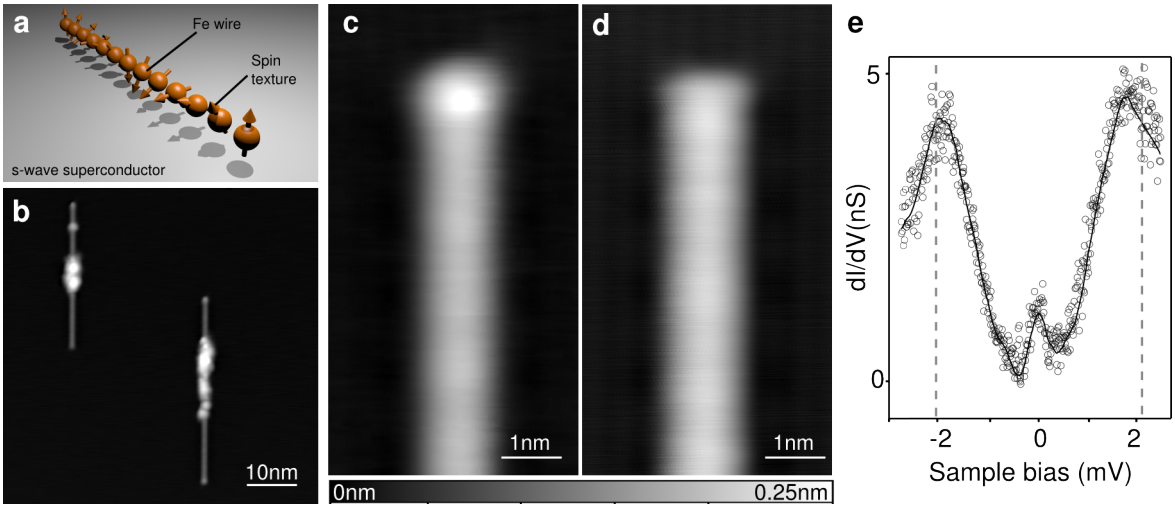

Fig. 3.7: Fe chains on Pb(110). ***a,*** *Schematical drawing of the experiment,* ***b,*** *STM image of self-assembled Fe chains on Pb(110),* ***c,d,*** *STM images of different chain terminations ($I_t = 100\,pA$, $V_b = 10\,mV$),* ***e,*** *dI_t/dV_b spectrum with a ZBP performed at the chain end in* ***c****. [208]*

and the ZBP in STS is induced by the topological superconductivity of the Fe chain on the Pb(110) surface which is cancelled at a higher temperature of 10 K.

To further investigate the structure of the Fe chain and especially the protrusion at the extremity, AFM constant height images are recorded (Fig. 3.8c). The AFM image shows that the chain consists of single Fe atoms which are aligned between the rows of the Pb(110) substrate. At the chain end, on the last two Fe atoms, a brighter, round-shaped area with more positive frequency shift is seen (arrow 1 in Fig. 3.8c). Since the atoms are perfectly aligned with the chain, in contrast to the arrow at position 2, a chain deformation or corrugation effect can be excluded. The location of the brighter peculiarity in AFM corresponds to the position of the protrusion in STM where also the ZBP is observed. The more positive frequency shift at this position implies that additional repulsive force contributions are acting on the tip. Around this spot a dark halo of more negative frequency shift is observed. Since the AFM tip is sensitive to Pauli repulsion if the wavefunctions of the tip and sample atoms start to overlap, the observed AFM features at the chain end may be related to force contributions coming from the presence of the MBS. If MBSs are located on both sides of the chains, one chain end can only host one fermion which could lead to repulsion between tip and sample following the exclusion principle similar to Pauli repulsion.

These experiments demonstrate that the combination of STM and AFM opens the way to investigate new states of matter at the atomic level which may be used in the future to build quantum computers based on topological superconductivity.

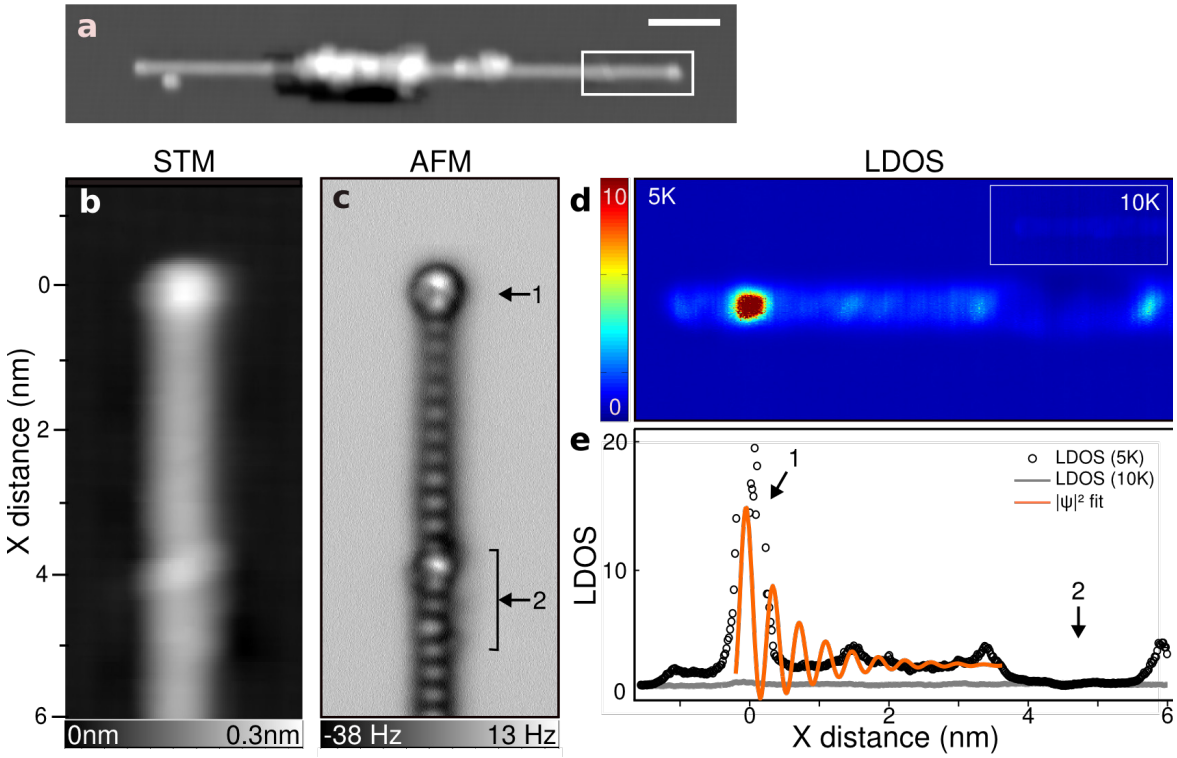

Fig. 3.8: Electronic and structural characterisation of the Fe chain. ***a,*** *STM image of the complete chain with a marked white rectangle to indicate the area that is investigated in the rest of the figure ($I_t = 80\,pA$, $V_b = 11\,mV$, scale bar = 5 nm).* ***b,*** *STM image ($I_t = 10\,pA$ $V_b = -10\,mV$) and* ***c,*** *corresponding AFM image at constant height. Each atom is displayed as brighter protrusion.* ***d,*** *Zero-bias normalised conductance maps proportional to LDOS. At 5,K a ZBP is clearly observed which disappears at 10 K (inset) due to the suppression of superconductivity.* ***e,*** *LDOS profiles extracted from the LDOS map at 5 K and 10 K compared to a fit of the theoretical MBS wavefunction. [208]*

3.5 Conclusion

In this chapter, it is shown that molecule-surface interactions as well as inter- and intramolecular bonds between molecules can be studied on the atomic level using STM and AFM. On-surface chemical reactions enable the transformation of chemical structures by cleaving triple bonds or halogen atoms of the molecular compounds. The aromaticity after structural transformation is investigated by bond-order analysis. Reaction products that have not been observed in solution chemistry are identified by AFM. These findings demonstrate that on-surface chemical reactions offer new possibilities for synthesis since reaction products can be created using surface atoms as catalysts.

The intermolecular interactions of long alkyl chains which lead to interdigitation are studied as well as hydrogen bonding between the CO molecule on the tip and hydrogen atoms of adsorbed molecules. For both experiments, technical challenges

have to be overcome. To quantify the force induced by hydrogen bonds, a three-dimensional molecular structure is used. To deposit molecules with long alkyl chains, the electrospray deposition technique is applied. Thus, intermolecular interactions known from various systems in nature can be studied in detail on the surface by STM and AFM.

Furthermore, it is demonstrated that induced cleaving of halogen bonds allows the controlled formation of covalent links between molecules by intermediate organometallic bond formation. AFM and force spectroscopy are employed to observe the coupling of molecules to surface atoms and subsequent intermolecular bond formation. This Ullmann-type on-surface reactions enable the formation of stable molecular networks from single molecule building blocks in a controlled way. Thus, by understanding intra- and intermolecular bond formation, structural control is achieved which is a prerequisite for bottom-up fabrication of molecular electronics.

For the realisation of molecular electronics and machinery, specific properties are implemented in single molecules. These properties have to be understood within a molecule on the atomic level. In this chapter, the investigations of atomic wires showing Majorana bound states and topological superconductivity demonstrate that STM and AFM allow to combine the characterization of electronic properties with structural information on the atomic scale. Hence, the combination of STM and AFM is used in the following to analyze structures and properties of single, isolated molecules.

4 Efficient steering of a single molecule

The results presented in this chapter have been published in the journal ACS Nano.[a] *[224] Figures are reproduced with permission from the American Chemical Society.*

As presented in the former chapter, STM and AFM are suitable tools to reveal structural and electronic information. Beyond imaging and spectroscopy, the tip of the microscope can be used to manipulate single adsorbates on the surface with atomic precision. [225–228]

To succeed repeated manipulation of a single molecule, the propulsion and steering technique has to be reliable, the design of the molecule robust and the surface-molecule interactions well understood. In this chapter, the tip-induced displacement of a single molecule on a surface over a distance in the range of hundred times the molecular lengths is studied. For the molecule manipulation, exclusively the tunneling current and the bias voltage is used. Mechanical pushing is not applied to move the molecules since the presented results are in the context of the first international NanoCar Race which took place in Toulouse, France, in spring 2017. [229, 230] The challenge was to move molecular vehicles by a STM tip over a well-defined race track on Au(111) by electrical activation. Mechanical pushing of the molecules was forbidden.

Molecule translation [102–104], rotation [231,232] as well as chemical reactions [233–236] can be induced by excitation of vibronic modes by inelastic electron tunneling. However, the directionality of molecular displacements induced by inelastic electron tunneling has mainly a stochastic character which hinders the controlled movement in a repeatable manner. To impose directionality, an external electric field in the tunneling junction [103, 237, 238] or a suitable molecular design [239] are required. Moreover, the subtle interplay between molecules and surfaces determines the diffusion properties. Molecules can diffuse to step edges after adsorption if the diffusion barrier is low or, in contrast, if there is a strong coupling, molecules stick to their adsorption sites. In both cases, further controlled movements by tip manipulation become difficult. Thus, a fundamental understanding of the molecule-surface interactions is crucial to design

[a] Pawlak, R., Meier, T., Renaud, N., Kisiel, M., Hinaut, A., Glatzel, T., Sordes, D., Durand, C., Soe, W-H., Baratoff, A., Joachim, C., Housecroft, C. E., Constable, E. C., Meyer, E. Design and Characterization of an Electrically Powered Single Molecule on Gold. *ACS Nano* **11,** 9930 (2017).

a molecular vehicle that can be reliably displaced on a surface. [240–242]

4.1 State of the art

The concept of molecular vehicles describes single molecules that can be controllably displaced on a surface by a STM tip. For such single molecule manipulations, molecules were used that are equipped with a chassis, four weels and a motor. [14, 243] These nanocars were driven by wheel-like rotation induced by thermal energy or manipulation with the tip which differs from sliding or stick-slip motion. Molecules with different wheel structures were also displaced by a STM tip. [244] Importantly, the conversion of electric energy from the tunneling current into mechanical motion by the motor of a nanocar was realized. [15]

Molecular vehicles consisting of molecular structures without wheels were loaded by a single adatom and their structure could be repaired after accidents by tip manipulation. [241, 242] Translation of individual NH_3 molecules was obtained by inelastic electron tunneling. [102] The influence of non-metallic substrates such as NaCl thin films on the diffusion of single molecules was also studied. [103, 104] Using the interaction of a single molecule with the applied electric field in a STM tunneling junction enabled the precise positioning of single molecules on metallic substrates. [237]

These achievements highlight the versatility of manipulation and molecular design to propel molecular vehicles on a surface. Typically, the molecules were moved over some lattice sites which corresponds to a distance of a few nanometers. However, manipulations of single molecules over distances of about hundred times the molecular length ($\approx 130\,\mathrm{nm}$ for the SND molecule) require a high degree of reliability in order to be able to perform hundreds of manipulation cycles. The actuation and steering mechanism has to be studied in detail to reduce the stochastic character of molecular displacements. Possible obstacles coming from pinning sites on the surface and possible destructive events such as decomposition due to high currents or jumps to the tip have to be considered.

4.2 The Swiss Nano Dragster

The 4'-(4-methylphenyl)-2,2':6',2"-terpyridine molecule [135], so-called Swiss Nano Dragster (SND) consists of three pyridine units and a methylphenyl unit linked by interannular C-C bonds (Fig. 4.1a and Sec. 2.4.6). The molecule has a planar structure. The terpyridine units build a coordination center because of the lone pairs of the N atoms which can form coordination bonds with transition metals. [135] This property is also expected to influence the molecular adsorption on a surface since the N atoms interact with the metallic substrate.

The molecules are deposited on a clean Au(111) substrate which is defined as the surface for the NanoCar Race. The front methylphenyl unit weakly physisorbs on gold by van der Waals interactions [137] which is expected to reduce friction forces during translation on the gold surface. The Au(111) surface shows a herringbone

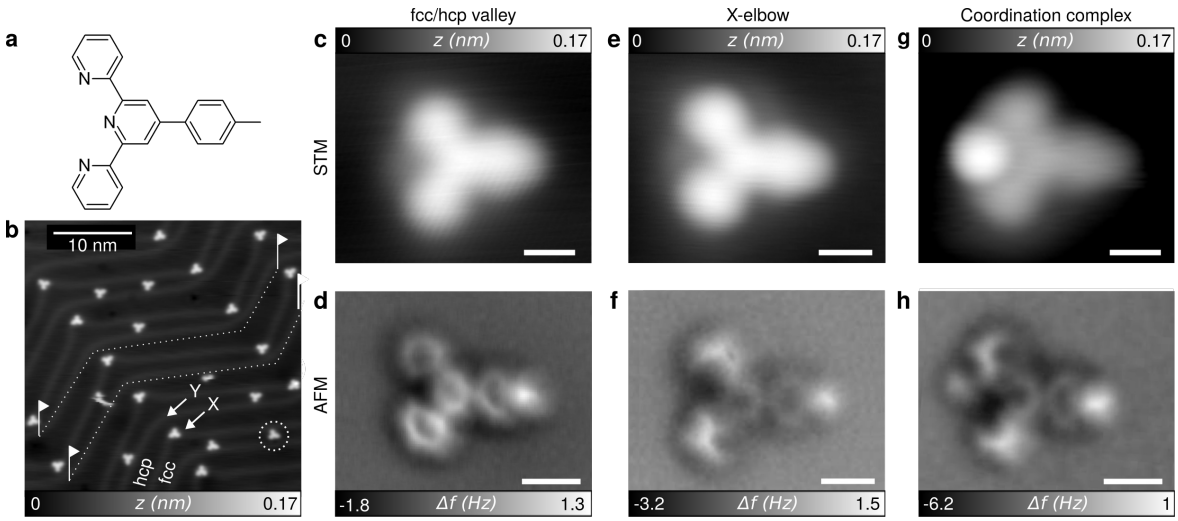

Fig. 4.1: Comparison of the adsorption geometries of single SND molecules on Au(111). ***a,*** *Chemical structure of the Swiss Nano Dragster (SND) molecule, 4'-(4-methylphenyl)-2,2':6',2"-terpyridine.* ***b,*** *STM overview of the adsorbed molecules on Au(111). The molecules first adsorb at specific elbows of the herringbone structure denoted "X" and then along the valleys of the fcc/hcp reconstruction, ($I_t = 2\,pA$, $V_b = 150\,mV$). The dashed lines represent the racetrack defined for the NanoCar Race.* ***c,*** *STM image of the molecule at the valley and* ***d,*** *the corresponding AFM image.* **e,** *STM image of the molecule at the X elbow and* ***f,*** *the corresponding AFM image.* ***g,*** *STM topographic image of an Au coordination complex and* ***h,*** *the corresponding AFM image. Scale bars are* $0.5\,nm$. *[224]*

reconstruction because of alternating face-centered-cubic (fcc) and hexagonal-close-packed (hcp) regions. This leads to valleys, ridges and elbows on the surface. There are two different kinds of elbows which are denoted X and Y elbow (Fig. 4.1b). At the elbow sites adsorption pecularities of atoms and molecules occur which has to be considered for molecule manipulation. [245,246] Depending on the adsorption site in the fcc/hcp valley or at elbow sites, the molecules adapt different geometries. Furthermore for some of the molecules an Au adatom is attached to the terpyridine. The different structural observations obtained by STM and AFM are explained in the following sections.

SND adsorbed in the valley The SND molecules adsorb preferentially at the X elbow sites. By increasing the deposition the X elbows get saturated and molecules in the fcc/hcp valleys are also observed (dashed circle in Fig. 4.1b). The Y elbow sites always remain unoccupied. The SND molecule adsorbed in the valley shows a planar structure in STM and AFM (Fig. 4.1c,d). The terpyridine moiety is clearly identified in the AFM image. On the other side of the molecule the methylphenyl unit exhibits a more positive frequency shift, indicating a sticking out of the surface plane leading to a smaller distance to the tip. This observation is in agreement with the expected weak physisorption of methylphenyl on gold.

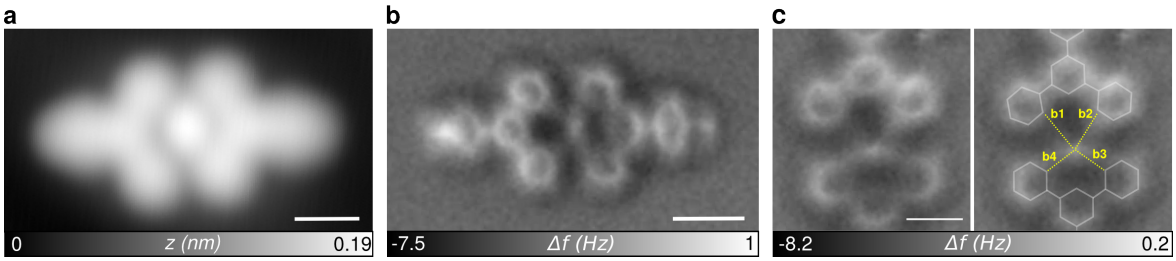

Fig. 4.2: Adsorption geometry of The SND-Au-SND complex on Au(111). ***a,*** *STM topographic image of the SND-Au-SND coordination complex (I_t = 2 pA, V_b = 150 mV) and* ***b,*** *The corresponding AFM image with a CO-terminated tip.* ***c,*** *Close-up AFM image of the coordination center revealing the Au-molecules bonding. The yellow dashed lines symbolizes the coordination bonds expected for such planar coordination geometry. The bond lengths are b1= 315 pm, b2= 330 pm, b3= 223 pm and b4= 224 pm. Scale bars are 500 pm. [224]*

SND adsorbed at elbows STM images of SND molecules adsorbed on X elbows do not reveal drastic differences with respect to the valley site (Fig. 4.1e). However, AFM elucidates that the adsorption at elbows leads to a conformational change of the molecule (Fig. 4.1f). The peripheral pyridine units show a slight rotation along the C-C bonds which is different to their flat adsorption in the valley. The conformational change suggests a variation of the molecule-surface interaction. Since terpyridine can form coordination complexes with metal atoms, it is assumed that on the elbow sites, coordination bonds between N atoms and the X elbow sites are formed. The following description of the SND coordination complex supports this interpretation.

SND as coordination complex SND coordination complexes are spontaneously formed by interaction with Au adatoms on the surface. In STM a round protrusion attached to the terpyridine is visible which corresponds to a small dot like feature in AFM (Fig. 4.1g, h). Since other adsorbates can be excluded in UHV conditions, the feature is identified as Au adatom available on the Au(111) surface. Interestingly, the rotation of the peripheral pyridine units is similar to the observation at X elbow sites (Fig. 4.1f). There, the rotation occurs without showing the presence of an atom as coordination center. Atoms involved in the complex formation are not always detectable in AFM since the observation depends on their vertical position with respect to the molecular plane. [247, 248] At the elbow site, the atoms of the reconstruction are slightly out of the surface plane. Consequently, the atom is not observed in the AFM scan. In the case of the complex shown in Fig. 4.1g,h, the atom is adsorbed on the surface, hence it becomes visible in the AFM image due to the elevated adsorption height.

Furthermore, SND-Au-SND complexes are also observed on the surface (Fig. 4.2). The terpyridine units are rather flat as seen in the AFM image in Fig. 4.2b which could be attributed to the increase of coordination bonds from three for the SND-Au case to four for the SND-Au-SND complex. One terpyridine unit is adsorbed slightly further away from the surface compared to the other which is indicated by the more positive frequency shift. This height difference is also reflected in the measurement

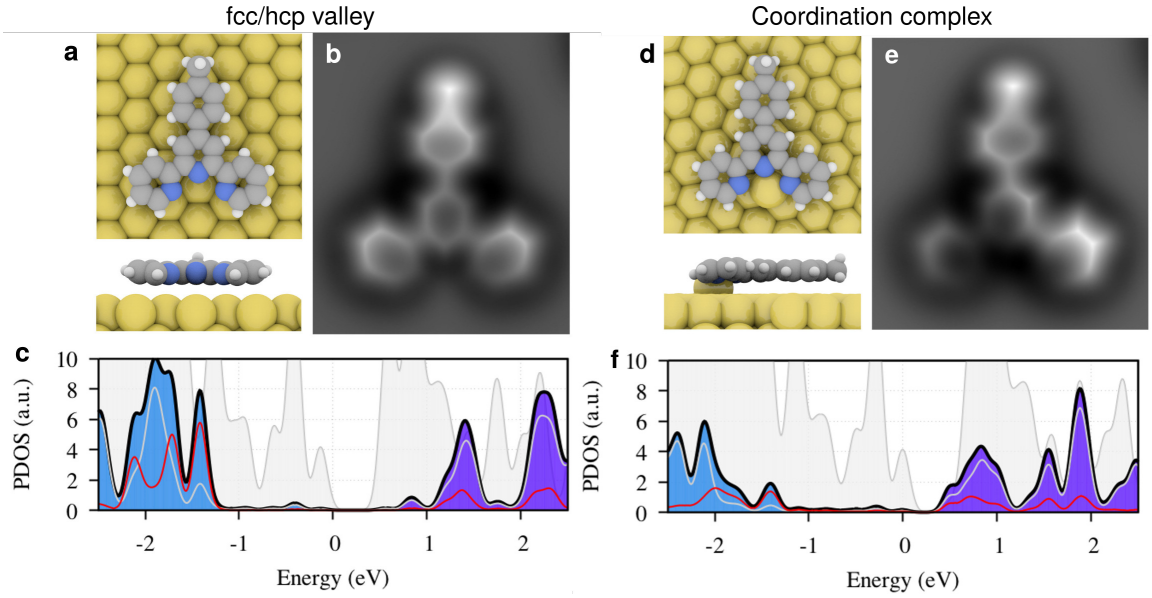

Fig. 4.3: Flat-lying molecule *vs.* **Au-SND coordination complex.** ***a,*** *Top and side views of the adsorption geometry of the molecule at the valley location obtained by DFT calculations.* ***b,*** *Simulated AFM image from the relaxed structure of* **a**. **c,** *Projected density of states (blue).* ***d,*** *Top and side views of the absorption geometry at the Au-molecule coordinate obtained by DFT optimization using VASP.* ***e,*** *Simulated AFM image revealing the tilting of the pyridine end-groups due to coordination.* ***f,*** *Projected density of states of the system. In* ***c*** *and* ***f****, the contribution of the gold is shown by the grey shaded areas, carbon by grey lines and nitrogen by blue lines, respectively. The total PDOS of the molecule is shown as blue and purple shaded area for the occupied and unoccupied states. [224]*

of the bond lengths (b1 to b4) from the AFM image (Fig. 4.2c). The bond lengths of the slightly lifted terpyridine (b1 and b2) are 315 pm and 330 pm whereas b3 and b4 show values of 223 pm and 224 pm. A measurement error of ±25 pm is estimated. The difference of the bond lenghts points out that the Au adatom is placed closer to the molecule that shows a darker contrast in AFM. The smaller bond lengths of b3 and b4 are in agreement with values for porphyrin or phthalocyanine macrocycles (≈ 205 pm and 190 pm), but much larger than for coordination bonds in other studied complexes. [247, 248] The SND-Au-SND complex forms a square planar geometry in analogy to porphyrin macrocycles and in contrast to the trigonal pyramidal alignment in the Au-SND case (Fig. 4.1h).

Electronic character of the SND conformations To better understand the adsorption geometries and electronic properties of single SND molecules and coordination complexes, DFT calculations on an unreconstructed gold surface are performed. Fig. 4.3 shows the relaxed structure of the flat-lying SND molecule (Fig. 4.3a) and the Au-SND complex (Fig. 4.3d). With the relaxed structure from DFT, simulated AFM images with the probe particle model [249] are obtained (Fig. 4.3b) which correspond

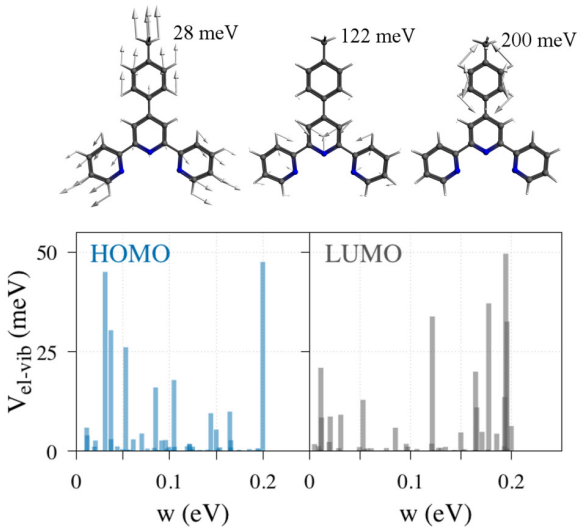

Fig. 4.4: Vibration modes and electrons-phonon coupling of the "flat" molecule. *The top images show the vibration modes of the SND molecule structure. The graphs show the coupling between electrons or holes of energy w with phonons of the flat SND molecule through LUMO (gray) and HOMO (blue) excitations. The vibration modes and electron-phonon coupling are obtained by numerical calculations. [224]*

to the experimental images (Fig. 4.1d). Note that in the calculations several local minima are also possible for such flat conformation in terms of position with respect to the surface lattice.

The projected density of states (PDOS) of the flat conformation with the occupied and unoccupied molecular states coloured in blue and purple, respectively, are depicted in Fig. 4.3c. The PDOS of the gold surface is shown in gray. The HOMO is located at $\approx -1.25\,\mathrm{eV}$ and the LUMO at $\approx 0.8\,\mathrm{eV}$ which leads to a HOMO-LUMO gap of $2.05\,\mathrm{eV}$.

To test the electronic properties of the SND molecules on the surface, differential conductance dI_t/dV_b spectra are recorded (Fig. 4.5a). On the positive range of the sample bias, a resonance appears at $\approx 1.6\,\mathrm{V}$ which is attributed to the LUMO of the molecule. On the negative bias range, a broad resonance with a shoulder at $-0.5\,\mathrm{eV}$ is observed which is caused by gold states (Fig. 4.3c). The HOMO of the molecule is theoretically predicted at energies around $-1.25\,\mathrm{eV}$ which prevents a direct assignment in the experimental data because at these energies the gold states mainly contribute to the dI/dV signal.

The calculated AFM image of the Au-SND complex in Fig. 4.3e shows the rotation of the pyridine units as observed in the experiment for the Au-SND complex and the molecules adsorbed at elbow sites (Fig. 4.1f,h). In the experimental AFM image of the Au-SND complex, the Au adatom is visible indicating that it is adsorbed on the surface and not part of the surface. In contrast, the Au atom in the simulated image is a surface atom and slightly below the molecule plane. Thus, the Au atom is not displayed in the simulated AFM data. However, the conformational change of the molecule from a flat to a tilted geometry is observed in DFT calculations. Additionally the electronic

properties are also influenced by the complex formation. In the PDOS in Fig. 4.3f of the Au-SND complex the LUMO is shifted to the Fermi level and located at $\approx 0.5\,\mathrm{eV}$. The HOMO remains at its energetic position ($\approx -1.25\,\mathrm{eV}$). As a consequence of the complex formation the HOMO-LUMO gap decreases to $\approx 1.75\,\mathrm{eV}$.

4.3 Manipulation of SND molecules

The structure determination of different molecular geometries and the SND complex on the Au(111) substrate is a prerequisite to control the displacement of individual SND molecules over long distances. In this section the actuation by inelastic electron tunneling and the steering by field-assisted excitation is discussed.

4.3.1 Actuation by inelastic tunneling electrons

Among all reported geometries, the flat conformation is used for single manipulation experiments because it is expected to have the smallest adhesion. [103,104,231,232,250] To get insight into the vibrational excitation, the coupling between charge carriers and vibration modes is investigated by numerical calculations (Fig. 4.4). Vibration modes can be excited by electrons or holes with energies w in the range of 0 to 0.2 eV which highlights the possibility to induce molecular motion by the tunneling current with both polarities.

To investigate the electron-phonon coupling in the experiment, $I_t(V_b)$ curves above the molecules are measured and analysed. A typical $I_t(V_b)$ curve is depicted in Fig. 4.5b. At the positive and negative bias range jumps of the current are observed. At $\approx -0.5\,\mathrm{V}$ the current increases abruptly in the forward curve (black line) and stays at higher values during the backward sweep (red line). This indicates a movement of the molecule towards the tip position. At $\approx 0.5\,\mathrm{V}$ the current jumps to 0 pA and remains zero meaning that the molecule moves away from the tip position. Consequently, there are two modes of excitation: an attractive mode for negative sample voltages $\leq -500\,\mathrm{mV}$ and a repulsive mode for positive sample voltages $\geq 500\,\mathrm{mV}$. The experimentally observed threshold voltage for molecular displacements of $\pm 500\,\mathrm{mV}$ is higher than the calculated excitation energy for vibronic modes (Fig. 4.4). However, these vibronic modes might still be inelastically excited by indirect tunneling processes at higher voltages. Interestingly, the direction of displacement depends on the polarity of the applied bias voltage which points out that the electric field may couple to the excited vibration modes of the molecule in analogy to reference [237].

4.3.2 Steering by field-assisted excitation

Experimentally, it is observed that the $I_t(V_b)$ curves at positive bias voltages always lead to repulsion of the SND molecules (Fig. 4.5c) and at negative bias voltages result in attraction (Fig. 4.5d). Even if the mean displacement distance per cycle of the repulsive mode is higher (≈ 2 to 3 nm) than for the attractive mode (≈ 0.6 to 0.8 nm), the attractive mode has the advantage that the molecule is displaced towards the tip

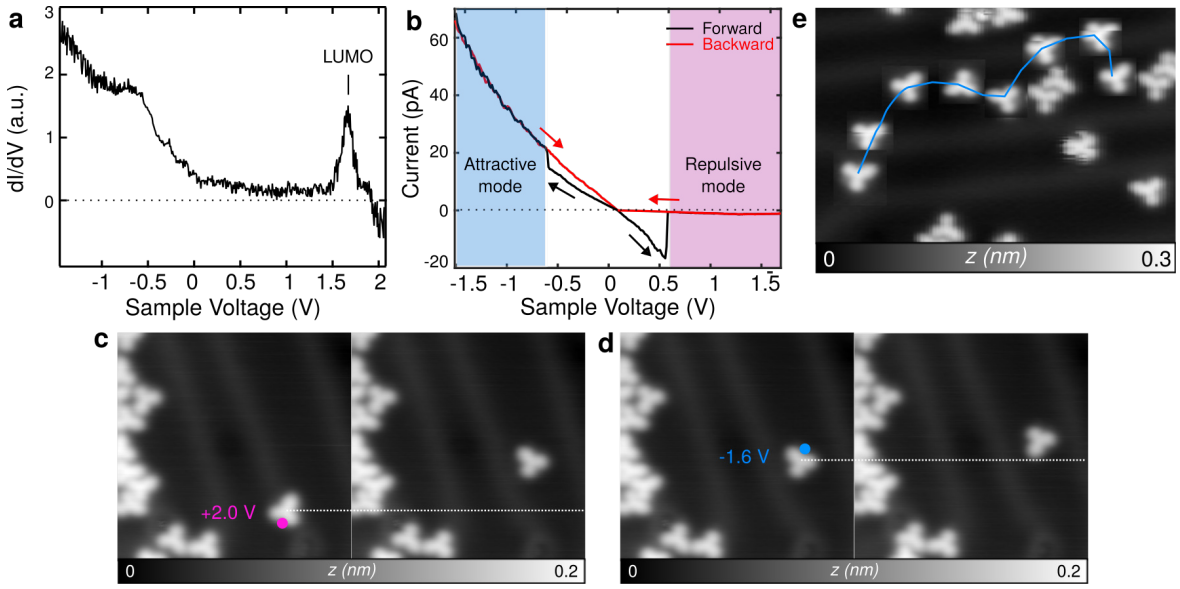

Fig. 4.5: Single-molecule displacements induced by inelastic electrons. ***a,*** *Experimental differential conductance, dI_t/dV_b, of the SND molecule at valley position.* ***b,*** *Current-voltage spectra, $I_t(V_b)$, obtained at 4.7 K with a gold-coated tip showing the minimum threshold voltages ($\pm 500\,mV$) inducing the molecule motion. Depending on the polarity, the molecule is either repelled (negative tip voltage) or attracted (positive tip voltage) from the tip position where the pulse is applied.* ***c,*** *STM images showing controlled translations using the repulsive mode ($V_b = 2.0\,V$) and the attractive mode ($V_b = -1.6\,V$), ($I_t = 2\,pA$, $V_b = -150\,mV$). The red and yellow dots refer to the tip position prior to the excitation at the corresponding voltages.* ***e,*** *Snapshots of an elaborated manipulation path across ridges and valleys (in blue) using the attractive mode. [224]*

position (Fig. 4.5c,d). Thus, control of the directionality can be achieved since the tip position determines the final position of the molecule. In contrast, the repulsive mode causes an arbitrary displacement direction in an angle of 180°.

To demonstrate the high control of the molecular displacements, a complex manipulation path is realised crossing the herringbone reconstruction and avoiding obstacles like other molecules (Fig. 4.5e). The total distance of the molecule displacement is $\approx 27\,nm$ performing approximately 45 $I_t(V_b)$ curves in 90 min. The free mean path of the molecule displacement is $\approx 0.6\,nm$ and the maximum speed is in a range of 16 to 20 nm/h. The speed is mainly limited by the acquisition time of the STM images (≈ 3 min per image) in-between the bias sweeps since one sweep only takes 1-2 seconds. Consequently the speed of the SND could be increased by reducing the STM imaging time, *e.g.* by reducing the number of pixels, which would, however, also reduce the quality of the data.

The minimum tunneling current to displace a molecule is $I_t = \pm 20\,pA$ at voltages of $V_b = \pm 500\,V$ which results in a minimum electrical power of $P_{elec} = V_b \times I_t = 10\,pW$. [240, 241] Increasing the voltages to values around $V_b = 1.8\,V$ corresponding

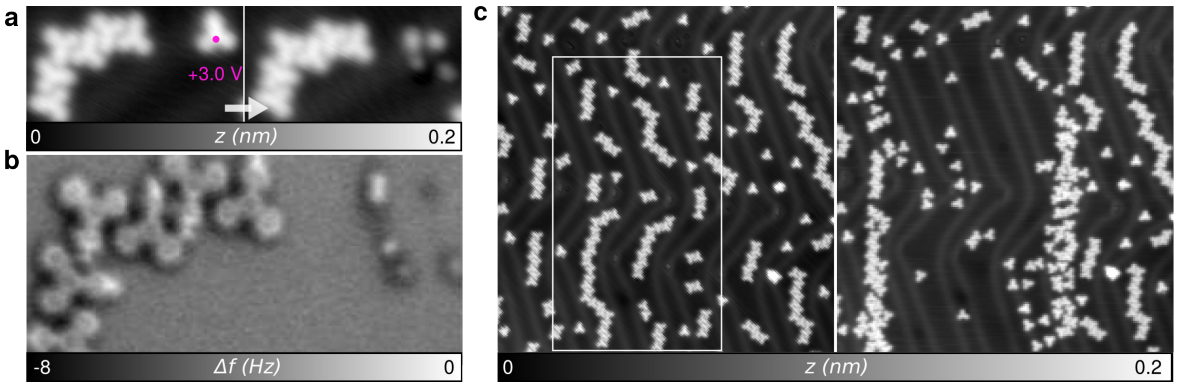

Fig. 4.6: Destruction of SND molecule vehicle and preparation of the racetrack. ***a-b,*** *"Accident" that can occur when using too high excitation power to displace the SND molecule. Upon trapping at elbows or close to molecule assemblies, the electronic excitation requires higher voltages. For voltages of* ± 2.8 *V, the molecule structure can be destroyed as revealed in the STM and corresponding AFM image with a CO-terminated tip (**b**).* ***c,*** *Successive STM images with a Au-coated tip showing the removal of surrounding SND molecules from the gold racetrack, (*$I_t = 2\,pA$*,* $V_b = -100\,mV$*). A STM image is acquired at the white rectangle with a smaller tunneling resistance to wipe away the molecules (*$I_t = 250\,pA$*,* $V_b = -100\,mV$*). Some of the molecules do not move away which suggests a stronger coupling to the surface due tot pinning sites at elbows or defects. [224]*

to the LUMO energy, leads to a higher possibility for a successful manipulation process. [237] With these typical parameters the power is in the range of $P_{\text{elec}} = 36\,\text{pW}$. If the excitation power is too large, the molecule is destroyed as shown in Fig. 4.6a, b.

The parameters for the destructive manipulation are $V_b = \pm 3\,\text{V}$, $I_t = 100\,\text{pA}$. From this observation, the maximum electrical power the molecule can withstand is deduced which is less than $P_{\text{elec,max}} = 300\,\text{pW}$. Note that this power is not the effective power needed to excite molecule displacements because the main part of the electrons tunnel into the substrate without exciting any vibration mode in the molecule. To remove molecules from the manipulation track, the current for the tunneling setpoint is increased, so that the molecules are wiped away by the tip (Fig. 4.6c). The remaining molecules are assumed to be stronger coupled to the surface due to pinning sites induced by elbows or defects.

Inelastic excitation of vibronic modes of the molecules do not lead to a directional motion in principle. As observed in the described manipulation experiments the SND molecules show a response to the electric field applied in the tunneling junction. To clarify the response to tip polarity and position, an excitation map with a grid of 25×25 pixels^2 is acquired above the molecule (Fig. 4.7a). The intensity of each pixel represents the number of successful manipulations at this location. In total 200 manipulations are performed. The blue pixels refer to the attractive mode ($V_b = -1.8\,\text{V}$) whereas the red pixels refer to the repulsive mode ($V_b = +1.8\,\text{V}$). The red pixels are localized at the coordination center of the terpyridine units which indicates that excitation in the repulsive mode can only be conducted at a relatively small region. Contrary, the blue

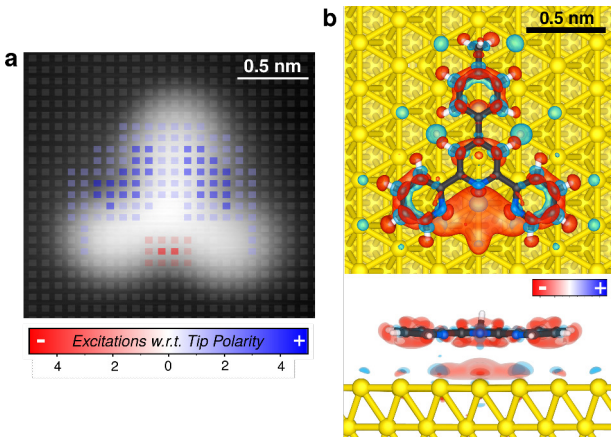

Fig. 4.7: Comparison between the experimental excitation map And the charge density difference obtained from DFT calculations. ***a,*** *Excitation map of the molecule as a function of the tip position and polarity. The blue and red pixels refers to positive tip voltages (attractive mode) and negative tip voltages (repulsive mode) of* $\pm$ *1.8 V, respectively.* **b,** *Modification of the electronic density of the molecule-surface complex upon adsorption. The red and blue area corresponds to an excess and lack of electrons, respectively. [224]*

pixels are spread over both sides of the molecules which leads to a larger excitation area for the attractive mode. The red pixels also have less counts than the blue pixels which highlights that the probability to induce a motion of the molecule is higher in the attractive mode.

The experimentally obtained excitation map is compared to the DFT calculated charge density difference map of the SND molecule on Au(111) (Fig. 4.7b). In the charge density difference map, the regions with electron excess are in red whereas a lack of electrons is indicated by blue. On the gold surface the molecule has a negative charge of $-0.36\,\mathrm{e}$ which results in a charge depletion area in the underlying substrate. At the terpyridine units' coordination center electrons accumulate and build a region of negative charge. Considering this region as a localized point charge, the molecular motion can be explained by the response of the point charge to the applied electric field by the tip. If the tip has positive polarity (negative sample bias voltage) the point charge is attracted and the molecule jumps to the tip position. Negative biased tips lead to the repulsion of the negative point charge observed by a movement away from the tip position. It is important to emphasize that the inelastic excitation of vibronic modes by the tunneling current is mandatory. Positioning the tip relatively far away from the molecule and applying a high electrical field does not induce a displacement as observed in the excitation map. At distances further away from the molecule (further than the mean free path of $\approx$ 0.6-0.8 nm), no successful manipulation experiment is reported. Only the combination of electrons inelastically tunneling through the molecule and exciting vibration modes in addition to the applied electrical field allow the controlled and reliable molecule displacement. As introduced by Ohara [237], this way of molecule displacements is called "field-assisted vibrationally-excited molecular

motion".

On the surface spontaneously formed Au-SND complexes are also found as discussed in Sec. 4.2. The complex has an altered charge distribution which leads to a different propulsion mechanism. [238] For the two other described adsorption conformations, in the valley and at the elbow sites, the lateral force needed to mechanically move the molecule is further investigated in the following section.

4.3.3 Site-dependent lateral force required to move the molecule: effect of the elbow

To quantify the variation of the diffusion barrier for molecules adsorbed on X elbow sites and in valleys, force spectroscopy is performed. [251–254] By applying this method, the required forces to move the molecules over different adsorption sites can be extracted from the measured frequency shift as well as the local potential variation which determines the diffusion properties of the molecules. In Fig. 4.8, $\Delta f(x)$ curves above a molecule on a X elbow and in a valley are depicted. The tip is scanned laterally over the molecule and the distance is successively reduced down to a difference of 300 pm with respect to the initial height.

The last $\Delta f(x)$ curve which induces a displacement of the molecule is depicted in red. The molecule is pushed over the surface which leads to a modulation pattern (Fig. 4.8a) related to the atomic lattice of the surface and typically observed in molecular friction experiments. [254–256]

The force required to displace the molecule from the elbow and induce the stick-slip pattern is $F_{\mathrm{L}}^{\mathrm{X\ elbow}} \approx -400\,\mathrm{pN}$ (Fig. 4.8c). In the valley the molecular motion starts when pushing with a force of $F_{\mathrm{L}}^{\mathrm{valley}} \approx -120\,\mathrm{pN}$ (Fig. 4.8f). The force determination for the valley position is less clear than for the elbow site because of the less pronounced stick-slip pattern suggesting weaker molecule-substrate interactions. However, by comparing the traces before the displacement occurs, it can be observed that repulsive features are already present at higher vertical distances (at $x = 2.5\,\mathrm{nm}$). At the position of the red arrow the gray traces show a Δf decrease originating from attractive forces. At this position the tip-sample interaction changes drastically when displacing the molecule. Hence, it is assumed that this is the onset of the molecular motion and the force is extracted there. Even if the onset of the movement is located at a different lateral position, the force remains in a range between -100 and $-200\,\mathrm{pN}$, thus less negative than at the elbow position. The force spectroscopy curves reveal a difference in the order of 200 to 300 pN between the elbow and the valley site. This force variation can be directly related to the structure and electronic state of the molecules at different adsorption sites analysed in Sec. 4.2.

At the elbow the SND molecule shows the structure of a coordination complex. The coordination bonds result in higher lateral force values required to move the molecule. In the valleys the molecular structure is not affected by strong interactions with the substrate going along with reduced absolute force values for induced molecular displacements. The diffusion barrier to move the molecule from one atomic site to the

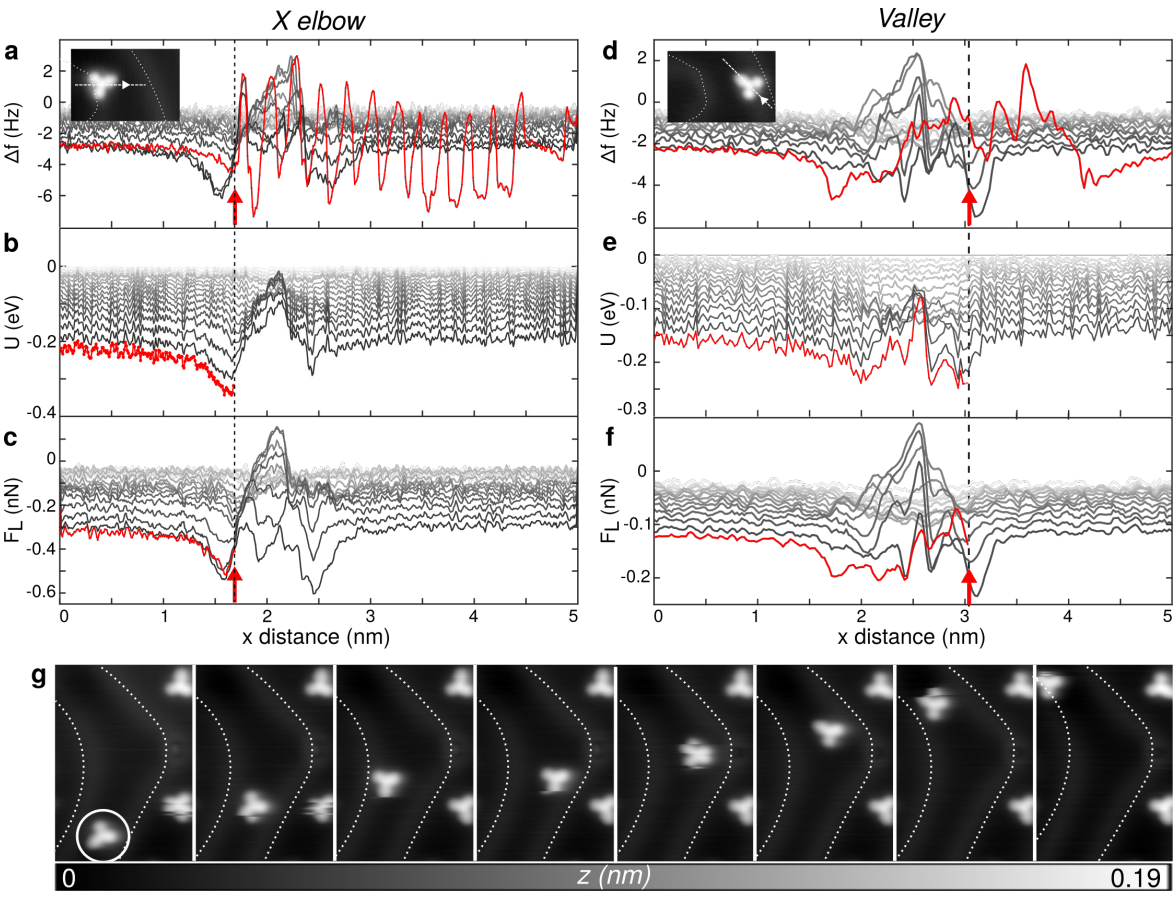

Fig. 4.8: Lateral force to move the molecule: elbow vs. valley. **a,** *Successive* $\Delta f(x)$ *traces acquired above a SND to mechanically induce its motion from an elbow position.* **b-c,** *Extracted potential* $U(x)$ *and lateral forces* $F_L(x)$ *from* **a**. *The displacement occurs at the red arrow in* **c** *and* **f** *and corresponds to an attractive lateral force of* $-400\,pN$ *and* $-120\,pN$*, respectively.* **d,** $\Delta f(x)$ *traces acquired above a SND to mechanically induce its motion along the Au(111) valley.* **e-f,** *Extracted potential and lateral forces from* **d**. *The motion is obtained at the red arrows and corresponds to an attractive lateral force of* $\approx 170\,pN$. **g,** *Successive STM images showing how a curve is realized with the SND molecule (circle) by avoiding the X elbow of the gold reconstruction,* $(I_t = 5\,pA,\ V_b = 150\,mV)$. *[224]*

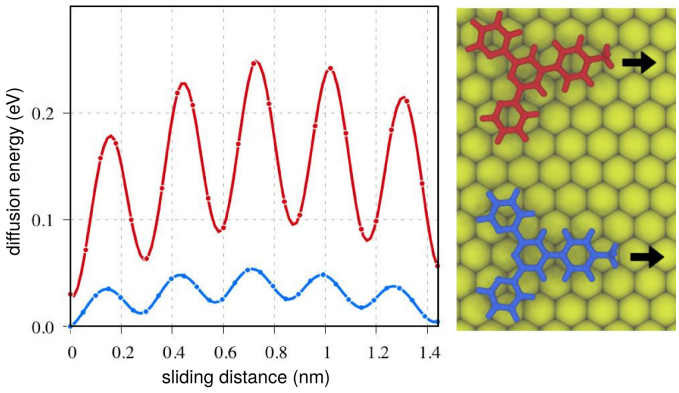

Fig. 4.9: Diffusion energy barrier of the flat SND molecule. *Energy landscape for the diffusion along a straight path for two distinct orientation of the molecule on an unreconstructed gold surface. [224]*

next is increased at the X elbow (330 meV) compared to the valley (230 meV). The values correspond well to DFT calculated values presented in other studies of organic molecules on gold. [241, 257]

The same magnitude of the potential energy is found in DFT calculations performed on an unreconstructed Au(111) surface where the SND molecule is displaced for two different orientations with respect to the surface lattice (Fig. 4.9). Likewise, the periodicity in the calculated curves (288 pm) is in agreement with the values in the experimental data corresponding to the Au-Au interatomic distance. The experiments and combination with the calculations highlight the interaction between the molecules and the Au(111) surface. The empirical observation that only the molecules in the valleys can be propelled is explained by the formation of coordination bonds at the X elbows and, beyond, is quantified by force spectroscopy. The detailed investigations of the molecular properties interacting with the substrate are mandatory to perform long distance manipulation experiments. Especially the understanding to avoid X elbow sites on the manipulation path helped to control the molecule displacements even in curves of the track created by the herringbone reconstruction (Fig. 4.8g). In combination with the highly controllable field-assisted vibrationally-excited molecular motion, the SND molecule can be propelled as a molecular vehicle over distances corresponding to multiple molecular lengths on the gold substrate. The performance of the SND manipulation was tested in the first NanoCar Race.

4.4 The NanoCar Race

The NanoCar Race was the first international race with molecular vehicles propelled by a STM tip. It took place in spring 2017 in Toulouse, France. [229, 230, 258, 259] The aim was to electrically drive specially-designed molecules along a well defined race track following the herringbone reconstruction of Au(111).

The racetrack is depicted in Fig. 4.1b. Three straight lines, two curves and a total

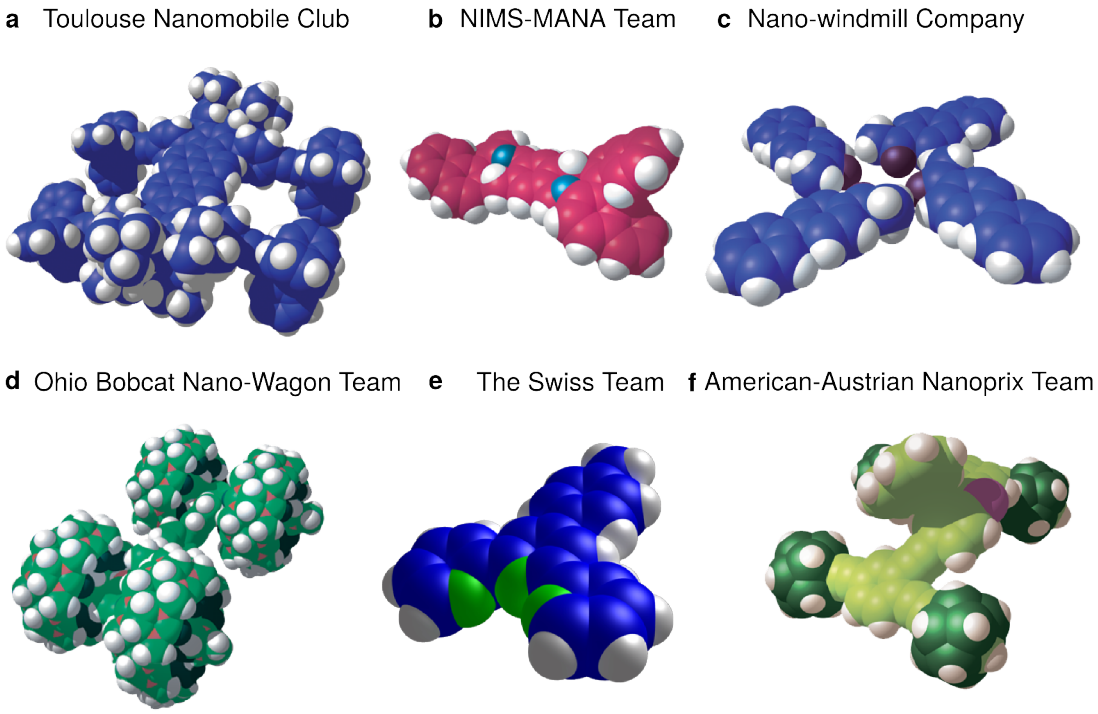

Fig. 4.10: The 6 teams (team leaders) participating at the NanoCar Race. ***a,*** *team from CEMES Toulouse (Gwénaël Rapenne),* ***b,*** *team from NIMS Tsukuba (Waka Nakanishi),* ***c,*** *team from TU Dresden (Francesca Moresco),* ***d,*** *team from Ohio University (Saw-Wai Hla),* ***e,*** *team from University of Basel (Ernst Meyer),* ***f,*** *team from University of Graz (Leonhard Grill)/Rice University (James M. Tour). [260]*

distance of 100 nm had to be achieved in the shortest time possible. The design of the molecular vehicle as well as the mechanism of electric propulsion (up to a maximum bias voltage of ± 3 V) were open in order to trigger scientific ideas for realising fast molecular vehicles. The NanoCar Race was held at the CEMES institute in Toulouse and organized by Christian Joachim, director of research at CEMES. In Toulouse, a 4-probe low temperature STM is mounted, so that each driver of a NanoCar could use one of the four tips to control the molecule displacement of his/her NanoCar. This setup allows to drive the NanoCars in parallel on the same Au(111) sample. A maximum time of 36 hours was given to finish the race track. Consequently, there were at least two pilotes in order to alternate on the driving seat.

As discussed in the previous sections, reliable molecule manipulation over many lattice sites is a scientific challenge and requires understanding of the molecular actuation, steering and the molecule-surface interactions. Therefore, the NanoCar Race teams were interdisciplinary consisting of physicists and chemists working together on the design, synthesis and driving of the NanoCar. Our team members were Dr. Rémy Pawlak (1^{st} pilot), Tobias Meier (2^{nd} pilot), Prof. Catherine Housecroft (chemistry) and Prof. Ernst Meyer (team leader). The other teams coming from all over the world are presented in Fig. 4.10.

The teams had to qualify for the race and test their NanoCars in the 4-probe STM

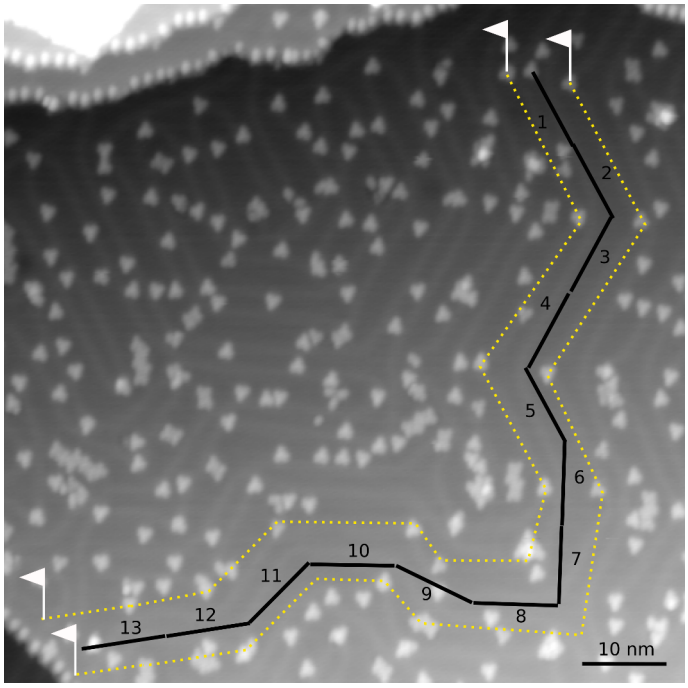

Fig. 4.11: The Racetrack during the NanoCar Race. *The track consists of nine straight lines and nine curves for a length of* 133 *nm. Each segment (black lines) is* 10 *nm long. A total of 6 hours and 30 min was required to complete it using four molecules and* ≈ *250 excitations. Before the race, several molecules were removed from the track by tip-induced manipulations and parked along the racetrack. (I_t = 5 pA, V_b = 250 mV). This STM image was recorded at the 4-probe microscope at the CEMES in Toulouse. [224]*

in Toulouse. The trainings in Toulouse to prepare the race were a crucial step to realise the NanoCar Race. The deposition of 4 different molecules on different areas of the same sample by taking into account different deposition and annealing temperatures was technically challenging. Furthermore, for the pilots, the handling of the microscope in Toulouse had to be learnt to propel the molecular vehicles with the same propulsion technique as in their own STMs. Since there were only 4 tips in the STM in Toulouse, only 4 teams could drive there (French, Japanese, German and Swiss team). Two teams participated at the NanoCar Race by remote controlling their own microscopes located in Ohio, United States, and Graz, Austria, from the "race office" in Toulouse. The team from Graz (Austrian-American team) was using an Ag(111) substrate instead of Au(111) and achieved remarkable results showing a displacement of 150 nm of their molecular vehicle in 1 hour and 33 minutes. [261] Because of the complex molecule-surface interaction, especially at the elbow sites on Au(111), a direct comparison between the manipulation paths on Ag and Au cannot be done.

During the NanoCar Race, we propelled the SND molecule over a distance of 133 nm on Au(111) in 6 hours and 30 min with more than 250 manipulations steps (Fig. 4.11). With this performance, we ranked first. The achieved average speed was 20 nm/h. The main limitation of the driving speed was the number of STM images between the

manipulations required to follow the complex path and to avoid obstacles like elbow sites and other molecules. In order to reduce possible interactions with other molecules on the race track, we removed single molecules from the track prior to the race and parked them aside in case of accidents. In the case of self-assemblies blocking the track we reduced the tunneling resistance compared to stable scan conditions to wipe away the obstacles as shown in Fig. 4.6c recorded in one of the training sessions. In total, we used 4 molecules during the race because of accidents. The molecule can jump to the tip, crash into obstacles or be destroyed. In this case it was allowed to take another molecule, propel it to the last position and continue the race. In the race, we propelled molecules in the flat geometry (Sec. 4.2) by applying the attractive mode discussed in (Sec. 4.3).

The SND molecule was the smallest NanoCar consisting of 43 atoms and an atomic weight of 323.9 u. Typical powers to electrically drive the molecule with the STM tip were in the order of 100 pW. It follows that the power-to-atomic-weight ratio is approximately 0.3 pW/u. Scaled up, this leads to a power-to-weight ratio of $\approx 10^{14}$ W/kg. For comparison a Boeing 747 has a power-to-weight ratio of 1376 W/kg, which is many orders of magnitude less. These values show that the molecular propulsion technique is highly inefficient since most electrons directly tunnel into the substrate without activating a motion. In the future, studies could focus on the increase of this ratio to improve the long distance manipulations of single molecules by a STM tip.

4.5 Conclusion

In this chapter, the controlled manipulation of a single molecule with a high level of repeatability is shown. The Swiss Nano Dragster molecule is propelled by a STM tip over 133 nm during the NanoCar Race performing more than 250 manipulation cycles. To induce molecular motion, the SND molecules adsorbed in valleys are used which differ in geometry and electronic properties from the other two coexisting types on the surface. Vibration modes are inelastically excited by the tunneling electrons which lead to an actuation of the molecules. The applied electric field allows the efficient steering of the molecular motion since the negative charge at the terpyridine centers is attracted or repelled as a function of tip polarity. With the field-assisted vibrationally-excited motion the SND molecule can be driven along the valleys and also over the ridges of the herringbone reconstruction on Au(111) with high precision and repeatability. Force spectroscopy reveals that the diffusion barrier varies by 100 meV depending on the surface location. The force to laterally move the molecule rises by 280 pN for the conformation at the elbow site where the molecules are pinned compared to the flat conformation in the valleys which can be propelled.

In summary, these results show the realisation of a molecular vehicle controlled by a STM tip and the complex interactions between molecules and the reconstructed Au(111) surface at the atomic scale. Such results particularly underline the impact of friction and adhesion onto the molecule machine performance. It might also help to optimize the design of molecular machines, to control adhesion properties or to build molecular transporters of single-atoms on surfaces.

5 Single donor-acceptor molecules

Fused electron donor-acceptor (DA) molecules have the unique property to transfer charges between the molecular moieties. The intramolecular charge transfer can be induced by optical excitation. Furthermore, contacting the molecule on both sides and applying a suitable voltage leads to current rectification due to the electronic alignment of donor and acceptor. Rectification is experimentally observed by the break-junction technique [262] and intramolecular charge transfer is measured by optical spectroscopy [144], both carried out in solution. However, on surfaces single DA molecules can be strongly influenced by the substrate altering the DA character of the molecules. In this chapter, the question is addressed if the intrinsic DA properties of tetrathiafulvalene-fused dipyridophenazine (TTF-dppz, Sec. 2.4.8) remain unchanged on thin insulating NaCl films on Cu(111).

Beyond the study of the electronic properties of DA molecules, their chemical structure is also analysed. The TTF-dppz molecules have a compact structure which allows thermal deposition in UHV. However, in applications like organic solar cells, peripheral side groups are attached to the core of the DA molecules to promote more efficient coupling between the molecules and the substrate. In the case of the TTF-dye molecule, alkyl chains and carboxyl groups are bound to the TTF-quinoxaline core of the molecule (Sec. 2.4.9). Peripheral side groups are thermally fragile and can be decomposed upon evaporation. In parallel the molecular weight increases by attaching side groups which leads to higher evaporation temperatures and consequently, possible fragmentation of the whole molecule during the heating process. Thus, the complexity of DA molecules, explorable by STM and AFM in UHV, is limited. The electrospray deposition (ESD) technique allows to deposit more complex molecular structures on surfaces in the vacuum chamber as shown for the $HBC6C_{12}$ molecule (Sec. 3.2) which can be employed to study DA molecules with peripheral side groups.

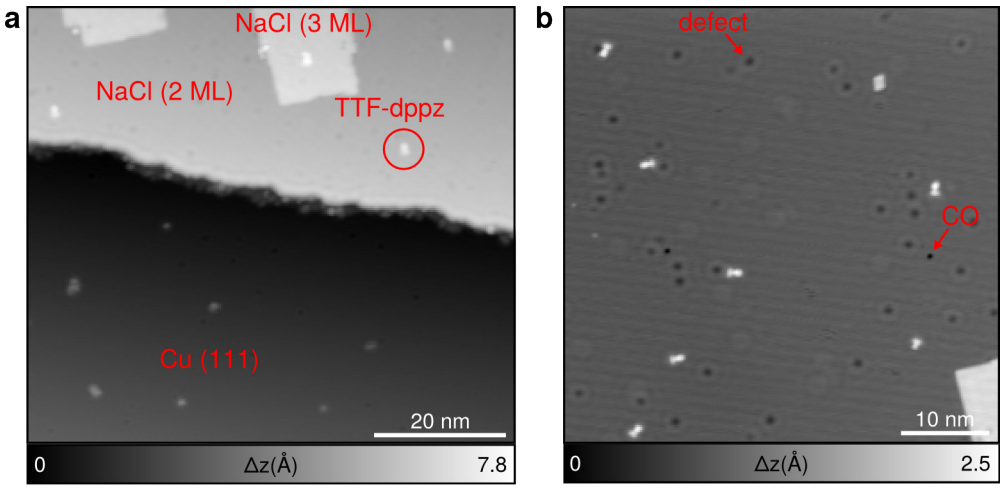

Fig. 5.1: STM overview images of NaCl thin films on Cu(111) with TTF-dppz molecules. ***a,*** *the Cu(111) substrate is partially covered with NaCl films consisting of 2 or 3 monolayers ($V_b = 0.3$ V, $I_t = 3$ pA). TTF-dppz molecules are found on NaCl and on Cu.* ***b,*** *higher resolution image of a NaCl film with adsorbed TTF-dppz and CO molecules ($V_b = 0.3$ V, $I_t = 1$ pA). Additionally, defects can be recognized.*

5.1 Donor-acceptor molecules on thin insulating films

The results presented in this section have been published in the journal ACS Nano.[a] *[145] Figures are reproduced with permission from the American Chemical Society.*

Thin ionic films with a thickness of few monolayers are generally used to decouple molecules from metallic substrates. Thus, the molecular orbitals as well as the charge distributions of single molecules become accessible. It was shown, particularly for DA [94] as well as other molecules [7, 10, 263], that they are similar to the gas-phase demonstrating decoupling from the metal surface. On metal substrates, the intrinsic electronic properties of the molecules are altered due to hybridisation of the molecular orbitals and quenching of their fluorescence due to non-radiative decay mechanisms linked to the surface. On thin insulating films tunneling currents can be detected through the thin film from the conducting substrate which is not possible for bulk insulator surfaces. This allows the application of the STM on thin insulating films on the one hand. On the other, the small distance between the molecules on the thin film and the metal substrate can lead to charge transfer from the molecules to the metal which may prevent the observation of charge states and excitations in some cases. Relaxations of the ions in the thin film, however, may stabilize the charge state of adsorbates as shown for charged single atoms. [6, 8, 101] Depending on the charge of the atom, certain adsorption sites on the thin ionic film are preferred. The alternating charges of the ionic film may also interact with DA molecules exhibiting regions with

[a] Meier, T., Pawlak, R., Kawai, S., Geng, Y., Liu, X., Decurtins, S., Hapala, P., Baratoff, A., Liu, S.-X., Jelínek, P., Meyer, E., Glatzel, T. Donor-Acceptor Properties of a Single-Molecule Altered by On-Surface Complex Formation. *ACS Nano* **11,** 8413 (2017).

electron excess and depletion.

TTF-dppz molecules are deposited on the Cu(111) sample, partially covered with NaCl thin films (Sec. 2.3.1), kept in the microscope at 5 K following the procedure described in Sec. 2.3.2. The deposition on the cold substrate is mandatory to prevent diffusion from the NaCl films to the bare Cu(111) surface which is energetically preferred. Fig. 5.1a shows that the Cu(111) sample is partially covered with NaCl islands of the height of two monolayers (ML) which is verified by measuring the height of the islands with respect to the bare Cu(111) substrate by STM. The islands on the two ML correspond to the third ML of NaCl. TTF-dppz molecules can be found on two and three ML of NaCl as well as on the Cu(111) substrate. On NaCl films, the TTF-dppz molecules are aligned along different directions (Fig. 5.1b) which will be further analysed in this chapter. Furthermore, single CO molecules become visible as dark depressions and defects can be recognized as depressions with a brighter halo.

5.1.1 Structure determination by STM and AFM

In order to analyze the conformation of TTF-dppz molecules on the NaCl film, higher resolved STM topography images are recorded (Fig. 5.2). The molecular structure of TTF-dppz in STM has a fish-like shape. The comparison with the chemical structure (Fig. 5.3a) suggests that the larger part of the molecule in STM corresponds to the dppz part of the molecule. The two molecules, adsorbed next to each other, exhibit different types of geometries at a closer look. The molecules, that are called *bound* in the following, have a distinct height maximum in the center of the molecular structure (Fig. 5.2b) whereas the other molecules, labelled *free*, have two local maxima and a larger width at the assumed position of the dppz (Fig. 5.2c). From the height profiles along the longitudinal axes of the molecules in STM mode, a height difference between the molecule's center and dppz of $\Delta z = 27\,\mathrm{pm}$ is found for the *bound* type whereas for the *free* molecule it is only $\Delta z = 12\,\mathrm{pm}$ (Fig. 5.2d,e). Interestingly, the two molecules are adsorbed in an angle of approximately 45° with respect to each other which may indicate a correlation to the underlying NaCl film.

In order to reveal the molecular structure at the atomic level, the molecules are scanned by AFM with CO terminated tips (Fig. 5.3). [89] The dppz moiety consisting of the pyridyl rings and the phenazine subunit as well as the TTF moiety with four S atoms are clearly recognized in the AFM images in Figs. 5.3b, c. The dot in the top left in the image in Fig. 5.3b corresponds to a single CO molecule that is adsorbed next to the TTF-dppz molecule and has no further influence on the structure determination of the molecule. The comparison with the molecular structure (Fig. 5.3a) demonstrates unambiguously that *bound* and *free* molecules are chemically intact on the surface. However, the observed height differences are also reflected in the AFM measurements. For the *bound* molecule in Fig. 5.3b the dppz part of the molecule appears with more negative frequency shift indicating that the molecule is further away from the tip. The TTF is closer to the tip which increases the frequency shift signal at this location leading to a bright contrast. The bright stripe in the middle of the molecule has been described for S containing molecules in literature. [16] This position coincides with the topographic maximum in the STM images. Overall, the *bound* molecule is in a

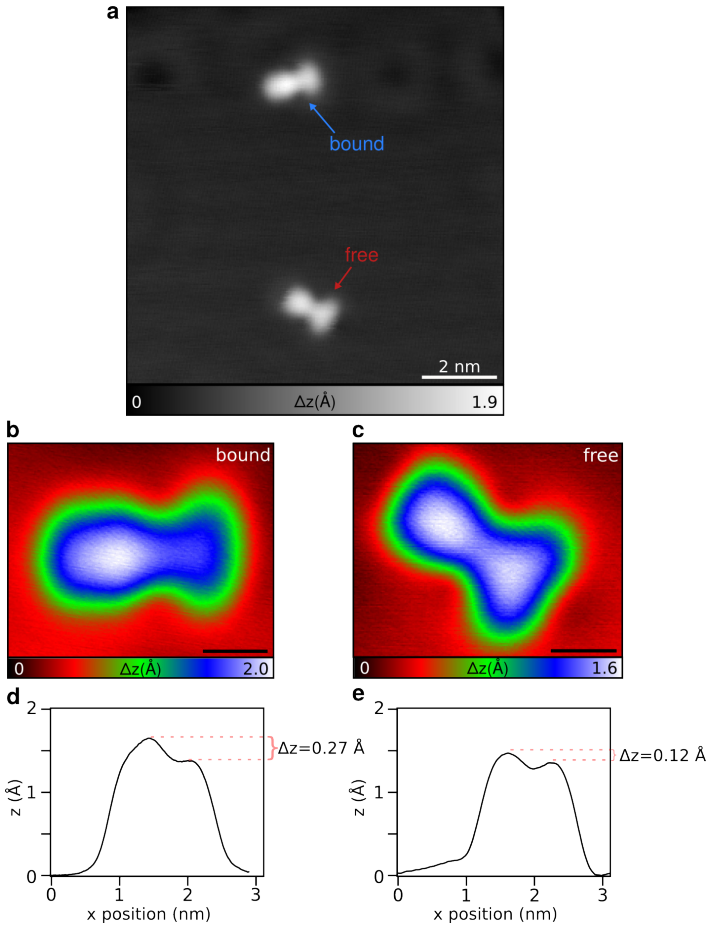

Fig. 5.2: Molecular geometries of TTF-dppz on NaCl thin films. ***a,b,c*** *STM topography images of TTF-dppz on NaCl(3 ML)/Cu(111) showing the different geometries of the bound and free molecules. ($V_b = 0.3$ V, $I_t = 3$ pA)* ***d,e,*** *Height profiles along the longitudinal axes of the molecules. The scale bars in* ***b,c*** *are* 500 pm. *[145]*

bridge-shape geometry with an elevated center and decreasing sides. In contrast, the *free* molecule is flat along the molecular axis (Fig. 5.3c). Furthermore, the molecule has a slight inclination and one axis of S atoms is rotated.

The probe-particle model of P. Hapala *et al.* [264] is employed to simulate the experimental AFM data (Figs. 5.3d, e). In this model a probe particle, *i.e.* a CO molecule, is attached to a tip by a spring. The probe particle scans over a molecular structure which is in its relaxed position, previously calculated by DFT simulations. The tip-sample interactions in the model are extracted to create a simulated AFM image. The bridge-shape of the *bound* type as well as the flat, partially inclined geometry of the *free* molecule is well reproduced. The rotation of the axis of S atoms is not observed in the simulated image. This may be related to the fixed molecular structure in the model which differs to the experiment where the molecule could relax. The experimentally observed ratio of *bound* to *free* molecules is approximately 2:1 indicating that the *bound* geometry is favoured. [145] *Bound* and *free* molecules have identical chemical structures, but different geometries, suggesting that this difference is induced by the

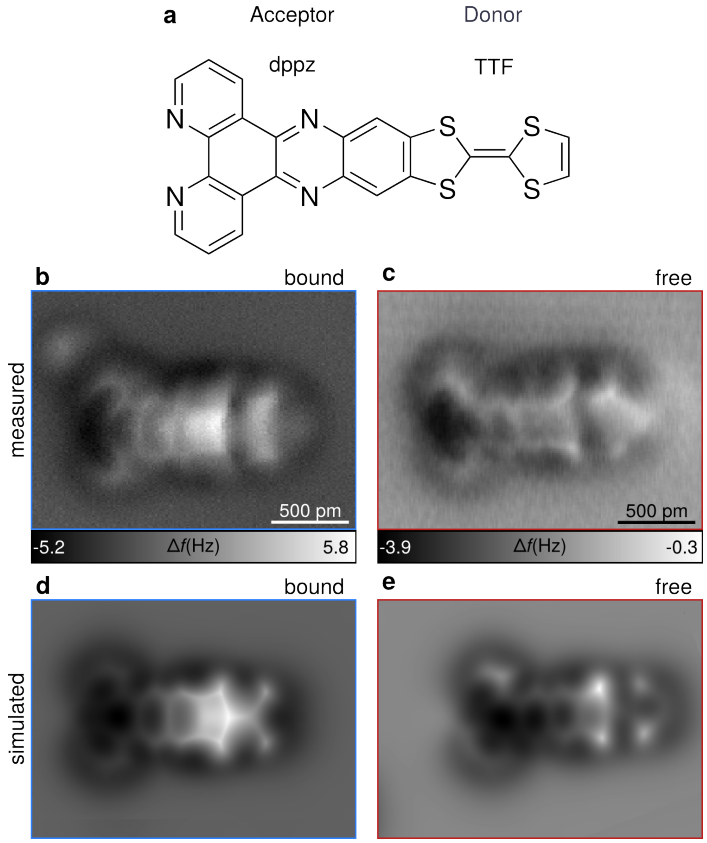

Fig. 5.3: Structure determination of TTF-dppz on NaCl(2 ML)/Cu(111). ***a,*** *The chemical structure can be compared directly to the measured AFM images of the bound (**b**) and free molecule (**c**). At the top left in the AFM image in **b** a CO molecule is adsorbed close to the molecule. **d,e** Corresponding simulated AFM images with the probe-particle model [145, 264].*

adsorption site.

5.1.2 Determination of adsorption sites

The position of the molecules on the NaCl lattice is determined by resolving the underlying NaCl lattice by AFM (Fig. 5.4). After scanning the molecule structures, the tip is approached by approximately 200 pm to image the NaCl film. The CO tip probes the negatively charged Cl ions which appear as bright protrusions in the AFM images. [265] Thus, the Cl sites are identified and used to define the adsorption positions of the molecules. Additionally, based on the experimental data, DFT simulations are performed to obtain optimized molecular structures and adsorption sites (Fig. 5.5). The calculated adsorption sites coincide with the measured adsorption positions.

The *bound* molecules are adsorbed along the apolar axis of NaCl (Fig. 5.5a). The two N atoms of the pyridyl units are located above a Na^+ cation. In the sideview on the molecular structure (Fig. 5.5b), a lifting up of the Na^+ cation as well as a downwards bending of the dppz unit can be observed. This geometry coincides with

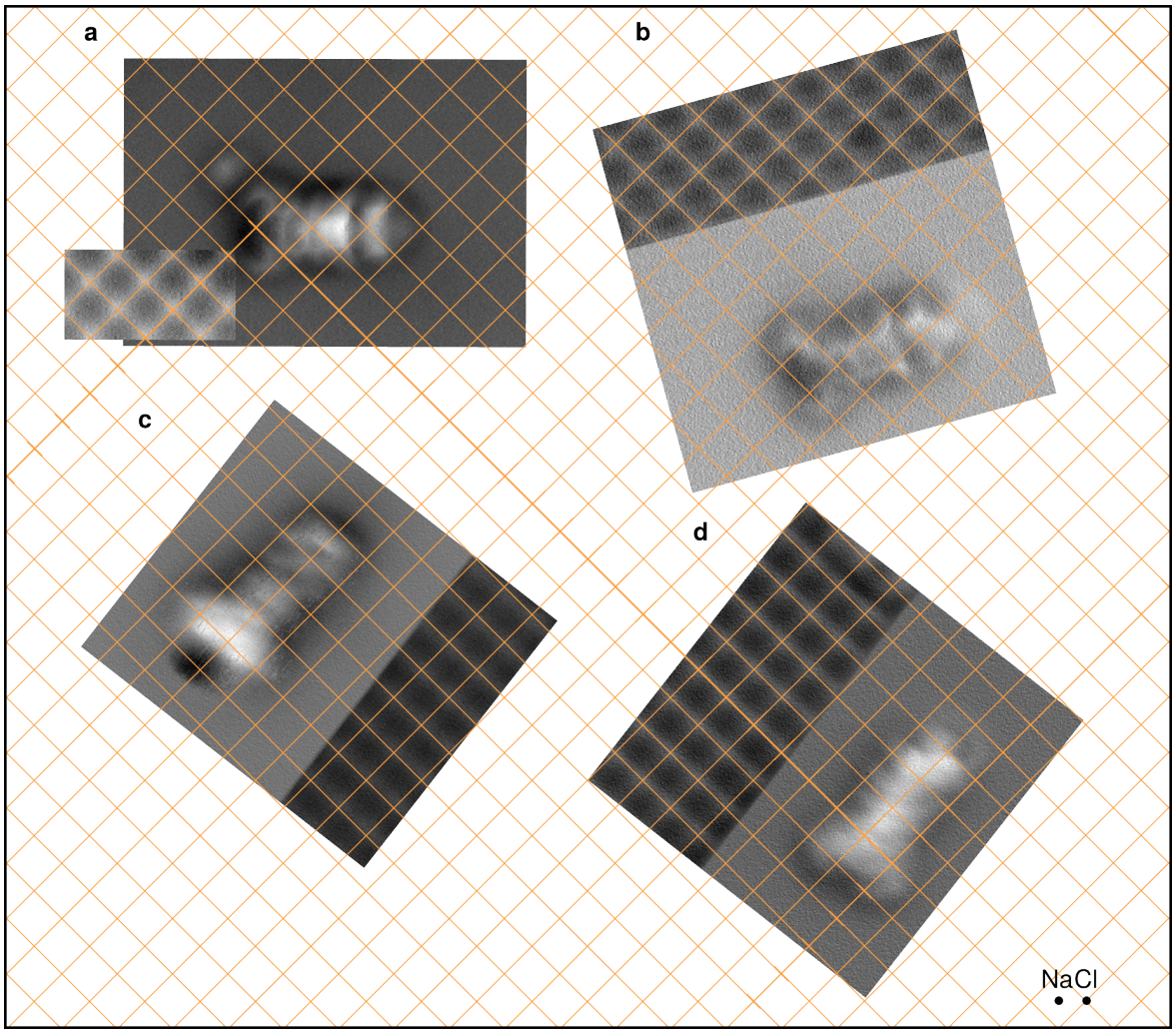

Fig. 5.4: Adsorption sites of TTF-dppz on NaCl(2 ML)/Cu(111) determined by AFM. *AFM images of molecules and the underlying NaCl film showing the adsorption sites for* ***a,*** *bound,* ***b,*** *free1,* ***c,*** *free2 and* ***d,*** *free3 molecule. The protrusions in the AFM images of the NaCl lattice are the Cl ions, so that the crossing points of the grid correspond to their positions. [265] The dark depression in* ***c*** *is assumed to be a Cl vacancy since the position corresponds to a Cl site.*

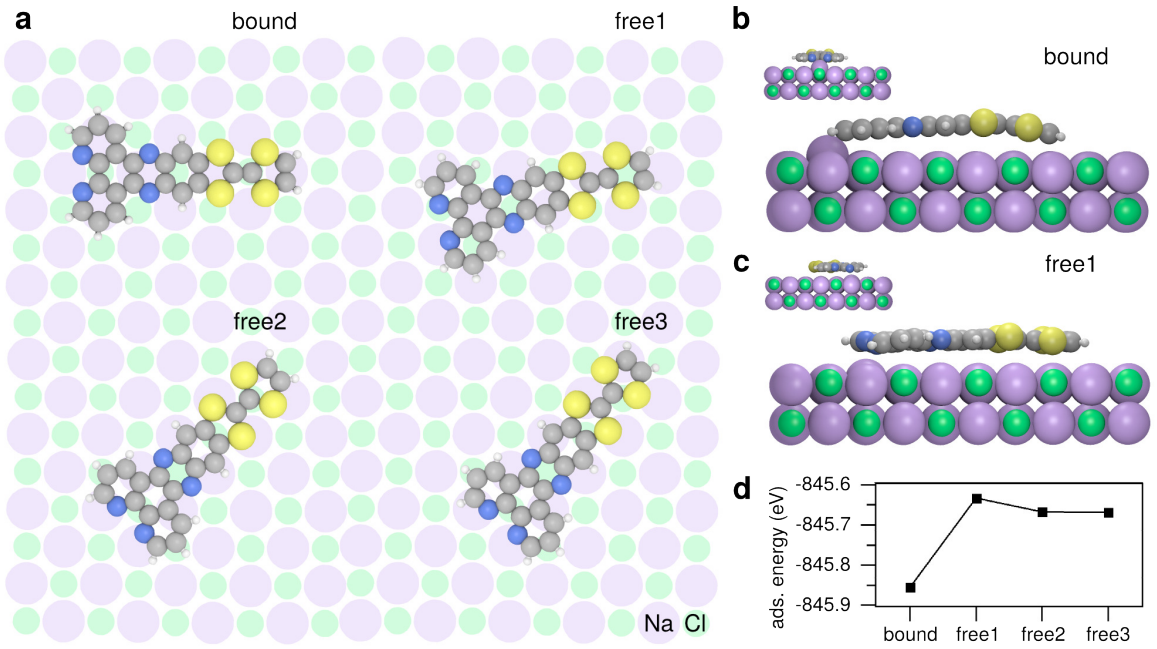

Fig. 5.5: Adsorption sites of TTF-dppz on NaCl(2 ML)/Cu(111). ***a,*** *DFT simulated adsorption sites of the relaxed molecular structures.* ***b,c,*** *Back- and side view on the bound and free molecule, respectively, highlighting the lifting up of the Na^+ cation and bending down of the dppz for the bound molecule.* ***d,*** *Decrease of the adsorption energy for the bound molecule. The DFT simulations are performed by P. Jelinek and P. Hapala [145]. Atomic radii are used for Na and Cl atoms.*

the experimentally revealed bridge-shape of the *bound* molecules in STM and AFM (Figs. 5.2, 5.3). It should be emphasized that the Na^+ cation is still part of the NaCl layer and located relatively far away from the tip during AFM scans. Because of this reason the Na^+ cation cannot be seen in the high-resolution AFM images. Approaching the tip further would lead to uncontrolled manipulation of the molecule or a tip crash.

Several adsorption sites are found for the *free* molecules (*free*1, *free*2, *free*3). They have in common their flat geometries (Fig. 5.5c), orientated in a certain angle with respect to the apolar axis of the *bound* type. Especially, the two N atoms of the pyridyl units are not centered above a Na^+ cation. The missing adsorption pecularity above Na^+ cations leads to an increase of the adsorption energy of $\approx 200\,\mathrm{meV}$ of the *free* molecules compared to the energies of the *bound* ones according to the DFT simulations (Fig. 5.5d). The decrease in energy is in agreement with the experimental observation that most of the molecules ($\approx 70\%$) are in the *bound* state. [145]

*Free*2 and *free*3 molecules are aligned along the polar Cl^- axis which explains the observed angle of 45° between the *bound* and *free* molecule in the STM image in Fig. 5.2a. The S atoms also contribute to the geometrical alignment of the molecules. The lone pairs of the S atoms prefer to be located above a positively charged Na^+ cation. For the *bound* molecule the two middle S atoms are lying above Cl^- anions which repels the S atoms, so that they stick out of the molecular plane. Experimentally this is observed in the bright stripe in the AFM frequency shift image (Fig. 5.3b). For

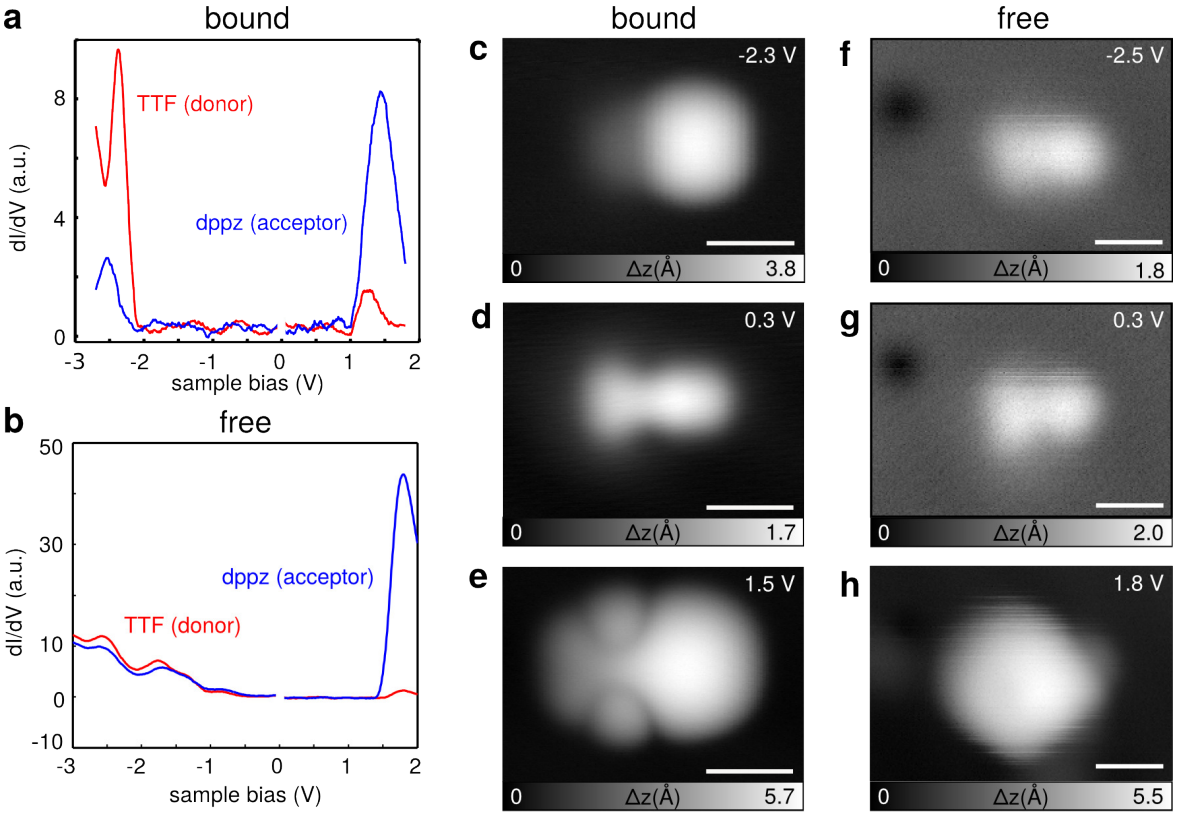

Fig. 5.6: Electronic states of the TTF-dppz molecules. ***a,b,*** *STS spectra of the bound and free molecule, respectively.* ***c-e,*** *Constant current STM images at the resonances of the bound molecule.* ***f-h,*** *Constant current STM images at the resonances of the free molecule. The scale bars are* 1 *nm. [145]*

the adsorption site of the *free*1 molecule corresponding to the AFM image in Fig. 5.3c, one of the two middle S atoms is also positioned above a Cl^- anion. As a consequence the S atom has a higher adsorption height than the other three S atoms.

Different adsorption geometries of TTF-dppz induced by interactions with the ions of the NaCl film are found. In the following, the electronic properties of the *bound* and *free* molecules are analyzed.

5.1.3 Electronic properties

To investigate the electronic properties of the molecules on the different adsorption sites STS spectra are recorded to determine the energetic positions of the molecular orbitals of the DA molecules (Fig. 5.6). [100] Additionally, the spatial distribution of the orbitals is examined by measuring STM images at the resonances in the STS spectra.

The energy of the HOMO for the *bound* molecule is detected at −2.3 V in the STS spectra (Fig. 5.6a). The topography image at this bias voltage reveals that the HOMO is located on the donor side of the molecule, *i.e.* on TTF (Fig. 5.6c). Only a small tail of the HOMO is visible towards the acceptor side. The measured HOMO distribution

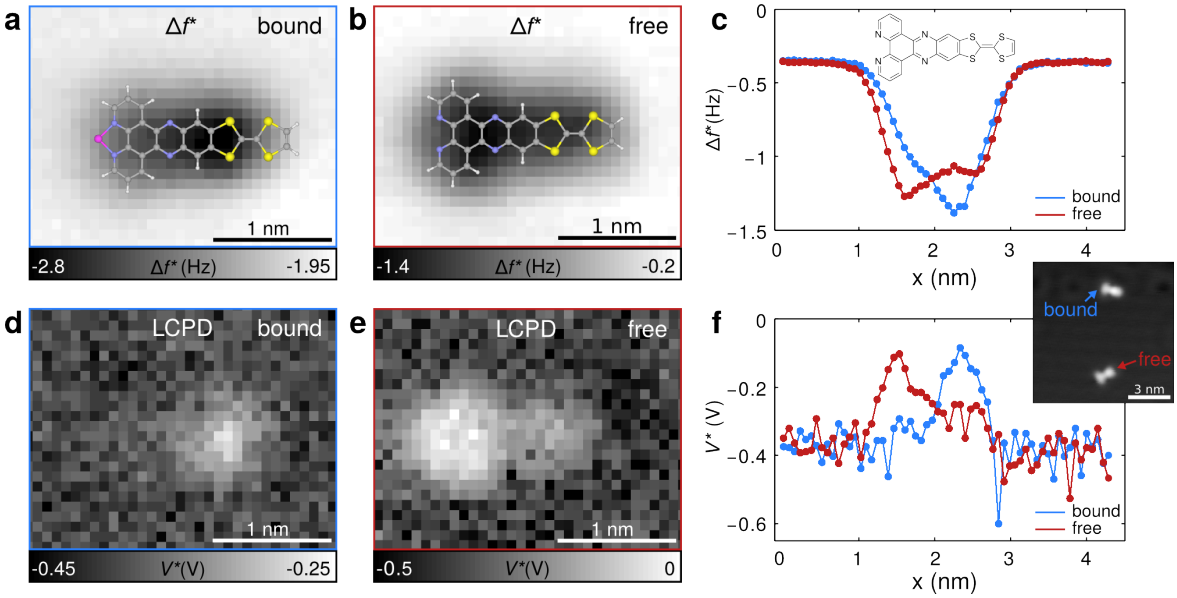

Fig. 5.7: Force spectroscopy mapping and line scans of TTF-dppz molecules on NaCl thin films. ***a,d,*** *Δf^* and corresponding LCPD map of the bound molecule. A Cu tip is used.* ***b,e,*** *Δf^* and corresponding LCPD map of the free molecule showing different charge distributions within the molecules.* ***c,f,*** *Line scans over the longitudinal axes of the two molecules depicted in the inset (and shown in Fig. 5.2a). Exactly the same Cu tip is used for the line scans to exclude tip artefacts. [145]*

is in good agreement with the calculated spatial distribution of the orbital for the molecule in the gas-phase (Sec. 2.4.8).

At 1 V the STS spectra show the onset of a peak, indicating the LUMO. In Fig. 5.6e two new lobes, compared to the image in the gap (Fig. 5.6d), appear on the nitrogen positions of the phenazine subunit which points out that the LUMO is partially positioned on the acceptor. However, a considerable LUMO weight is observed on the TTF donor side which is not expected in theory (Fig. 2.11) since the molecular orbitals are supposed to be spatially separated.

In contrast to the *bound* molecule, the LUMO of the *free* molecule is centered solely on the acceptor as predicted in the gas-phase model for DA molecules (Sec. 2.4.8). The shape of the LUMO of the *free* molecule differs from *bound* one. Moreover, the energetic position of the LUMO onset is at 1.5 V which is 0.5 V higher than for the *bound* molecule. In the negative range of the bias voltage, the HOMO energy of the *free* molecule shifts towards the Fermi energy which further reduces the HOMO-LUMO gap. The different energetic positions of the HOMO and LUMO imply an influence of the adsorption position on the electronic states of the molecules. The alternating charges of the ionic thin film may interact with the charge distribution of the DA molecule.

To study this hypothesis, force spectroscopy is applied to map the LCPD and access the intramolecular charge distributions of the *bound* and *free* molecule as reported for other molecules in literature. [10, 93, 94, 266] Fig. 5.7 shows Δf^* and LCPD maps as

well as line scans on single DA molecules.

The Δf^* map of the *bound* molecule exhibits one region with more negative Δf^* at the position between the phenazine subunit and the edge of TTF whereas above the *free* molecule an elongated decrease of Δf^* can be observed (Fig. 5.7a,b). The most negative Δf^* value is detected on the dppz side for the *free* molecule. The Δf^* map follows the different geometries of the molecules which depend on the adsorption sites. The bridge-shape as well as the flat geometry are reflected by the evolution of Δf^* over the molecule.

Looking at the LCPD maps reveals drastic differences between the *bound* and *free* molecules (Fig. 5.7d,e). *Bound* molecules show a negative charge at the position between the phenazine subunit and the edge of TTF indicated by a more positive LCPD value. It is located at the same position where the topographic maximum is observed in AFM and STM images as well as in the DFT simulations (Figs. 5.2, 5.3).

However, for *free* molecules an even more negative charge is located on the dppz moiety in addition to the negative charge in the center of the molecule. This observation highlights that the acceptor of the *free* molecule is more negatively charged than the surrounding substrate in contrast to the *bound* molecule where the acceptor has the same charge state as the surrounding substrate. Furthermore, the slight decrease of the LCPD at the TTF position for the *free* molecule suggests positive charge on the donor compared to the substrate.

To exclude tip effects, line scans over the two molecules from Fig. 5.2a are scanned with exactly the same Cu tip (Fig. 5.7c,f). The Δf^* curves have the same features as the Δf^* maps. The LCPD lines highlight that the negative charge is laterally shifted within the molecule. Thus, by recording line scans, qualitatively the same Δf^* and LCPD contrast is achieved which excludes tip artefacts in the interpretation of the observed contrast. Note that the LCPD contrast depends on the tip-sample distance especially in the close-distance regime with CO terminated tips where repulsive forces can lead to a complex contrast. [94] In the presented measurements Cu tips are used which prevents approaching to the close-distance regime because of possible uncontrolled molecule manipulations. Consequently, the LCPD measurements are performed at a medium distance range where the contrast in LCPD corresponds to the partial charge distribution of the molecules.

The force spectroscopy measurements in combination with STS and STM demonstrate that the same molecular species adsorbed on different sites on the NaCl lattice have different electronic states and charge distributions. Hence, the origin of these differences has to be searched in the interaction with the underlying NaCl film.

5.1.4 On-surface complex formation of donor-acceptor molecules

The interaction of the TTF-dppz molecules with ions of the NaCl film is explained by the results of the structural and electronic characterization by STM and AFM. The dppz part of the *bound* molecules is located above Na^+ cations which induces the different geometrical alignment and electronic properties. Dppz is a phenantroline based bidentate ligand which is mainly known to couple with transition metal ions, such as Fe(II) or Ru(II) [116,147], or to rare earth metal ions (Sec. 5.2). [267,268] The

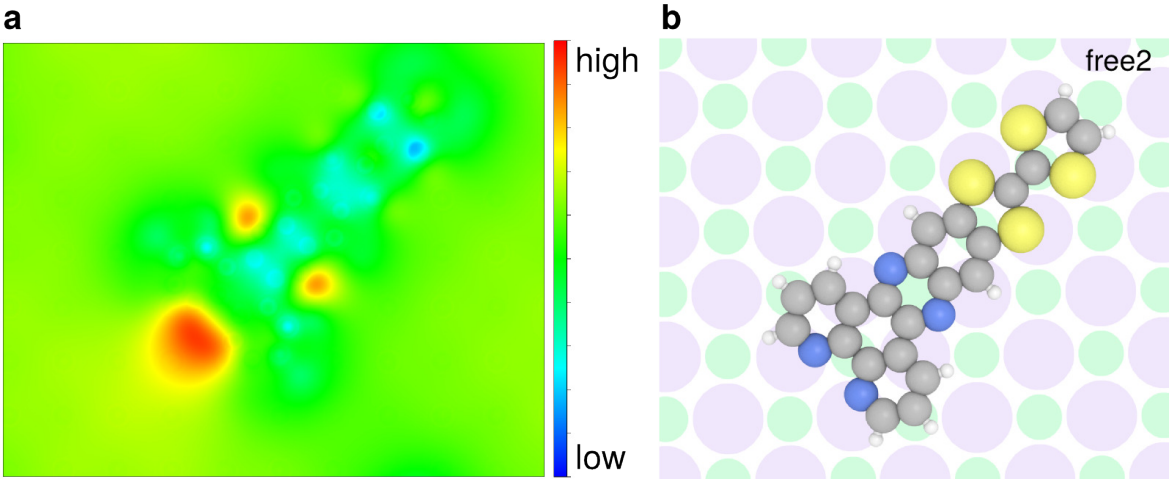

Fig. 5.8: Electrostatic potential of the *free* molecule. ***a,*** *Hartree-Fock potential of the TTF-dppz molecule on the adsorption site indicated in* ***b*** *on 2 ML NaCl on Cu(111). On the pyridyl units, negative charge is accumulated due to the lone pairs of the N atoms. [145]*

interaction with alkali metal ions is chemically less favoured since the alkali metals exhibit weaker complexing abilities. [269] Consequently, bidentate bond formation is usually required for complex formation between ligands and alkali metals.

Following the Hard-Soft-Acid-Base theory oxygen as a hard donor preferentially coordinates with Na^+ which is a hard acid. Although nitrogen is defined as soft donor, chelate complexes between phenantroline based ligands and Na^+ (N-Na-N) are observed in few studies in literature. [270–272] A chelate complex is characterized by multiple coordination bonds between ligands of a molecule to a single metal ion. For a molecule with two ligands, a mono- and bidentate bond formation is possible.

Interestingly, Qian *et al.* found mono- and bidentate complexes, for which they extracted the bond lengths. [272] For the monodentate mode, coordination bonds with a length between 266 to 273 pm are formed. Bidentate linkage for the chelating N^N coordination reduces the bond length to values between 244 to 246 pm. For comparison, the uncoordinated bond length Na...N is larger than 319 pm. As expected, coordination of O^O ligands with Na leads to shorter bonds with a length of 232 pm. [273] From the DFT model of the TTF-dppz molecule on 2 ML of NaCl (Fig. 5.5b) a bond length of 263 pm is extracted which is in the range of the bond length for complex formation. The extracted bond length is slightly less than the length of the monodentate mode and larger than for the chelate complex. The symmetric alignment of the pyridyl units above the Na^+ indicates a bidentate complex formation. The difference of the bond length to the literature values for the bidentate mode is presumably induced by the Na^+ cation which is still part of the NaCl lattice in contrast to a free ion.

The adsorption sites of the *bound* molecules triggers a on-surface chelate complex formation between the pyridyl units in dppz and the alkali metal ion Na^+ of the NaCl film. The dppz part of the molecules bends down because the lone pairs of the N atoms of the pyridyl units are attracted by the positively charged Na^+ cation and

form a chelate complex. Thus, charges in the molecules are redistributed. Especially, the negative charge of the acceptor dppz is transferred towards the Na^+ cation. This reduction of negative charge is observed in the LCPD map and line scan for the *bound* molecule (Fig. 5.7d,f). The different electronic state of the molecule is further confirmed by STS which shows that the LUMO shifts towards the Fermi level (Fig. 5.6a) as typically observed for complex formation. [116] Note that the charge state of the Na^+ cation cannot be measured directly since the tip-sample distance is too high to obtain a contrast in force spectroscopy. Further approaching is excluded due to the vicinity of the molecule.

The adsorption sites of the *free* molecules do not induce a binding with Na^+ cations. As a consequence the charge distribution remains as predicted by theory (Fig. 5.8a). In DFT simulations the TTF-dppz molecule has a partially negative charged acceptor and positively charged donor as also observed in the corresponding LCPD measurements for the *free* molecule (Fig. 5.7e,f). The calculated map of the electrostatic potential for the *bound* molecule forming a chelate complex does not change as significantly as in the experiments.

To further demonstrate the interaction between the adsorption site and the charge state of the TTF-dppz molecules, manipulation experiments to change the adsorption site by using inelastic electron tunneling are performed. [103] By sweeping the bias voltage to a value close to the HOMO or LUMO resonance, vibration modes of the molecules can be inelastically excited which leads to a switch of the adsorption site.

In Fig. 5.9, first, both molecules are in the *bound* state which is deduced by the STM topography. The tip is placed in the middle of the molecule (indicated by a black cross). After a bias sweep to 2.5 V the molecule switches the adsorption site induced by inelastic electron tunneling. It is rotated by approximately 45° and the topographical shape changes. By switching the molecules the presence of defects at the previous adsorption site could be excluded. The AFM image reveals the flat geometry and the tilting of the S axis of the donor as described for the *free* molecules (Sec. 5.1.1). In contrast, the other molecule shows the typical bridge-shape geometry of the *bound* type. Since the adsorption site along the apolar axis is preferred, a small perturbation of the *free* molecule by scanning with the tip or sweeping the bias voltage is sufficient to switch it to the *bound* state. Hence, the switching in the opposite direction, meaning from *free* to *bound*, is also possible. Thus, the chelate complex formation of Na^+-TTF-dppz and, thereby, the charge state of a single DA molecule on the NaCl film can be controllably reversed by changing the adsorption site by tip manipulation.

In the following, tip manipulation is used to controllably attach a single adatom to the DA molecule.

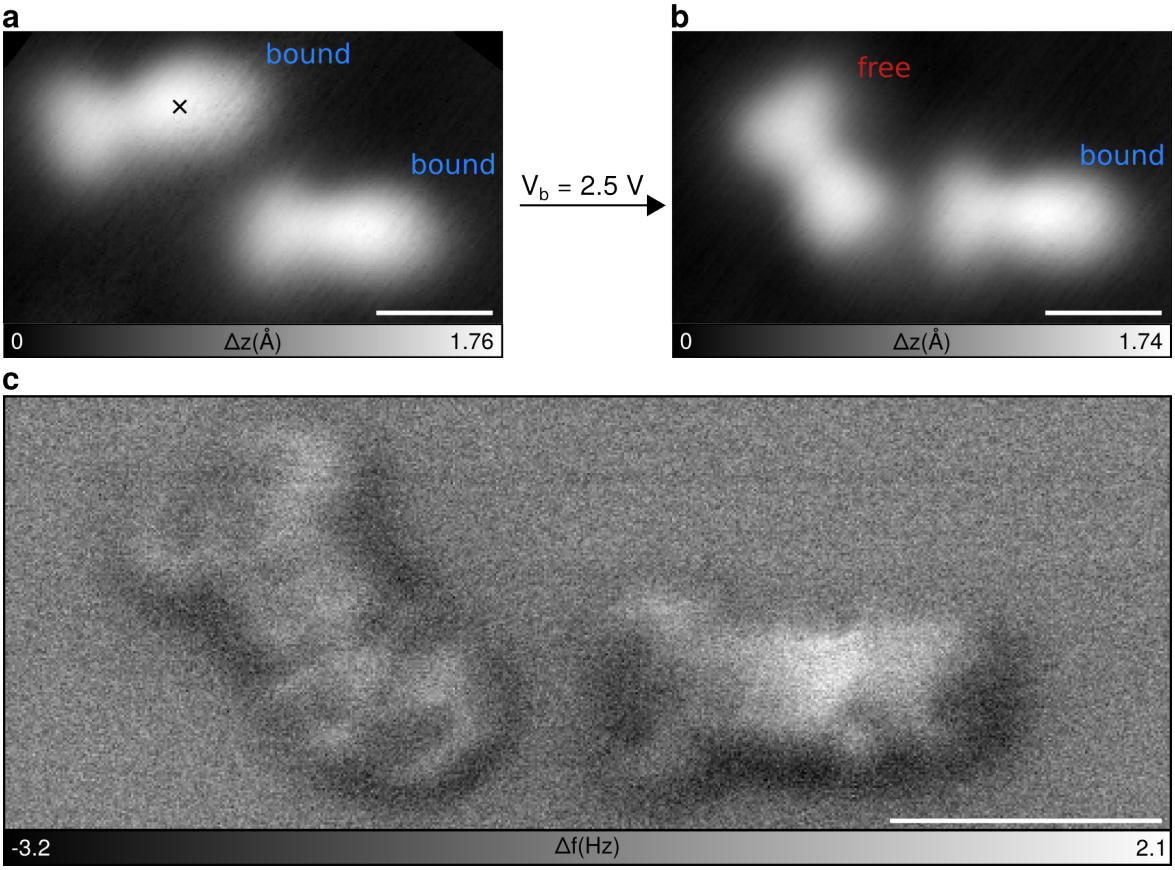

Fig. 5.9: Switching between *bound* and *free* state of the molecule of the TTF-dppz molecule. ***a,*** *STM image of two bound molecules before performing a bias sweep to* 2.5 *V on the position indicated by the black cross.* ***b,*** *STM image after bias sweep. The first molecule is rotated and show the features of a free molecule.* ($V_b = 0.5\ V$, $I_t = 200\,fA$) ***c,*** *AFM image of both molecules shown in* ***b*** *highlighting the flat and the bridge-shape geometry of the free and bound molecules, respectively. All scale bars are* 1 *nm.*

5.2 Manipulated complex formation

The dppz moiety of the fused DA molecule TTF-dppz has a metal-chelating character which leads to on-surface complex formation on NaCl thin films. In general, the coordination to transition metals such as Fe is used to create metal-ligand charge transfer in addition to the intramolecular charge transfer. [116, 147] Thus, new absorption bands are formed which broadens the spectral range of absorbable light. This is beneficial for charge separating systems [147, 274] or photoredox switches [275].

Motivated by the on-surface complex formation of TTF-dppz on NaCl and the observation of spontanously formed SND-Au complexes on Au(111) (Sec. 4.2), experiments are performed to bring a single Fe atom to the metal-chelating dppz site of the DA molecule to form a coordination complex by tip manipulation. Ideally, the coordination complex is decoupled from a metal by a NaCl thin film to study the electronic

properties. However, on NaCl thin films, the manipulated complex formation has to be performed with *free* molecules since they are not bound to Na^+ cations as the *bound* molecules. The *free* molecules easily rotate and change their adsorption site during scans which is explained by the energetically favoured adsorption site of the *bound* types (Sec. 5.1.2). Moreover, tip changes occur frequently on NaCl which complicates the manipulation experiments. Therefore, experiments are first performed on Au(111) to show the feasibility of the manipulated complex formation. Second, complexes are formed on NaCl thin films.

Manipulated complex formation on Au(111) In this study of principle, TTF-dppz molecules are deposited on a clean Au(111) substrate. The molecules align preferentially on the elbow sites of the herringbone reconstruction as also observed for the SND molecules (Sec. 4.2). At higher coverages TTF-dppz molecules are also located in the valleys (Fig. 5.10a).

Fe atoms are deposited by using the mobile Fe evaporator specially designed for the deposition on the cold sample (Sec. 2.3.2) to obtain single adatoms. Fe adatoms can be recognized on the surface as small round shaped protrusions (red arrow in Fig. 5.10a). Since the controlled displacement of the DA molecule is experimentally more complex than the Fe manipulation, Fe atoms are moved towards the dppz site. The tip is placed next to a single Fe atom (red cross in Fig. 5.10c) and the bias voltage is typically swept down to $-2\,\mathrm{V}$ (Fig. 5.10b). At these voltage values an abrupt current jump occurs in the $I_t(V_b)$ curves indicating that the atom is repelled and displaced further away from the tip.

In Fig. 5.10c, all manipulation steps to displace the Fe adatom to the dppz site are shown. Between subsequent images, a bias sweep is applied next to the Fe adatom. After a manipulation step, the Fe atom is placed closer to the molecule, hence it moves away from the tip position which is used to control the direction of its displacement. During some of the STM scans the Fe atom is unstable which suggests that it is not located on its energetically favoured adsorption site. By several bias sweeps the Fe atom is brought into vicinity of the dppz site of the DA molecule. For the final sweep the tip polarity is reversed to attract the atom towards the dppz. After this last bias sweep, the STM signal of the atom and the molecule overlap (Fig. 5.10d) and the molecule is slightly rotated (last image in Fig. 5.10c).

The shape of the TTF-dppz molecule and the Fe atom are seen with sharper contrast by imaging with a CO tip (Fig. 5.10e) suggesting that the Fe atom is attached to the dppz to form a coordination complex. Interestingly, on the TTF side an asymmetric protrusion of the molecule is observed.

By means of constant height AFM the chemical structure of the molecule and the connected Fe atom is revealed (Fig. 5.10f). The observed protrusion in the STM image refers to one of the two inner S atoms of the TTF which is lifted up indicated by a higher frequency shift value compared to the opposite S atom which appears dark. The dppz moiety can be unambiguously identified and the Fe atom is symmetrically located at the position of the N atoms of the pyridyl units indicating the complex formation. The TTF-dppz-Fe complex has a flat geometry in contrast to the TTF-dppz-Na complex

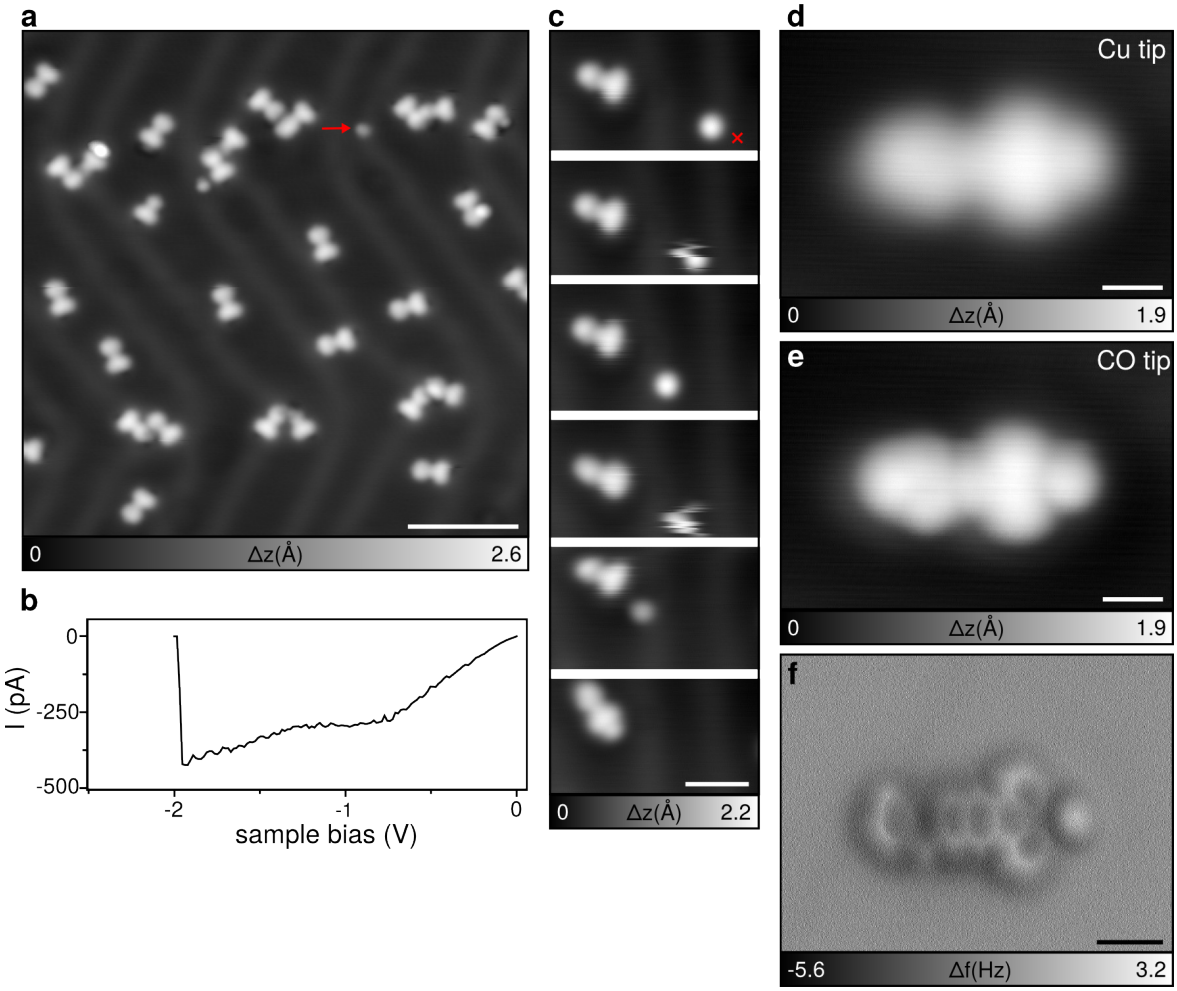

Fig. 5.10: Manipulated complex formation of TTF-dppz-Fe on Au(111) ***a,*** *Overview STM image of TTF-dppz molecules and Fe adatoms (red arrow) on Au(111) ($V_b = -0.3\ V$, $I_t = 1\ pA$). Scale bar is 5 nm.* ***b,*** *Recorded $I_t(V_b)$ curve of a bias sweep to move a Fe adatom. The current jump indicates the displacement of the adatom. The $I_t(V_b)$ curve is stopped after the current jump to avoid further manipulation.* ***c,*** *STM images of sequences of atom manipulations approaching the Fe adatom to the molecule ($V_b = -0.3\ V$, $I_t = 1\ pA$). The red cross in the first image indicates the tip position for manipulation. The scale bar is 2 nm.* ***d,*** *STM image of the TTF-dppz-Fe complex with a Cu tip and a CO tip (**e**) ($V_b = -0.3\ V$, $I_t = 1\ pA$).* ***f,*** *Corresponding AFM image demonstrating the attachment of the Fe atom to the dppz unit. Scale bars in **d-f** are 500 pm.*

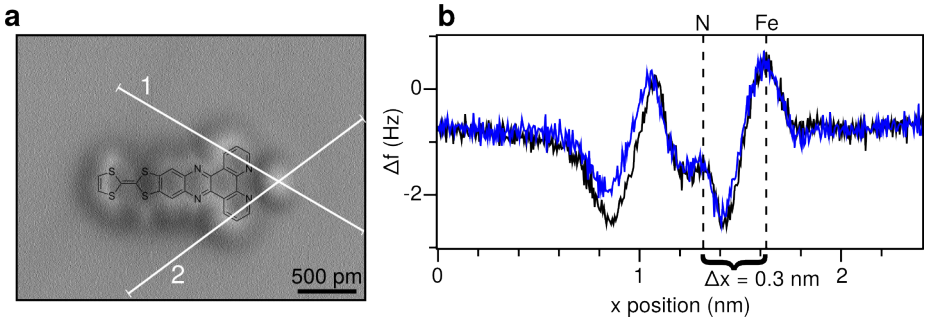

Fig. 5.11: Measured bond length of DA complex with Fe. ***a,*** *Locations of the line profiles taken.* ***b,*** *Profile of line 1 (blue) and line 2 (black) showing the measured bond length of approximately* 0.3 *nm.*

on the NaCl film. This is attributed to the Fe atom which is adsorbed and lying on the surface whereas the Na^+ is part of the NaCl thin film. The bond length between the N atoms and the Fe atom are extracted by line profiles of the AFM image (Fig. 5.11a).

The small peak at a position of 1.35 nm in the profile corresponds to the N atom of the pyridyl unit (Fig. 5.11b). The Fe atom is seen as the peak with the most positive frequency shift at 1.65 nm in the profile. Consequently, the bond length is approximately 0.3 nm which is substantially longer than for the TTF-dppz-Na complex where a length of 0.26 nm is extracted from the DFT model (Sec. 5.1.4). This difference is presumably caused by the two dimensional alignment of the complex with Fe compared to the more three dimensional geometry of the TTF-dppz-Na^+ complex. On a metal substrate such as Au(111) the molecular orbitals are hybridized with the metal electrons which prevents the investigation of the electronic properties of the manipulated TTF-dppz-Fe complex on gold. Especially, the coordinated Fe atom cannot be positively charged (Fe (II)) as observed in coordination complexes in solutions. [116] Decoupling is required which is achieved on NaCl thin films.

Manipulated complex formation on NaCl thin films The manipulation procedure on Au(111) is applied to Fe atoms and molecules adsorbed on NaCl films. Thus, decoupling of the complexes from the metal substrate is obtained. However, new difficulties arise on NaCl since manipulation experiments on NaCl often lead to tip changes or uncontrolled displacements of molecules and ions of the thin film. Furthermore, the decoupled adatoms are more sensitive to high voltages and tend to jump to the tip. Additionally, the TTF-dppz molecules are also attracted by the Na^+ cations which results in on-surface coordination and could potentially prevent the coupling to Fe atoms.

Despite various experimental challenges, TTF-dppz molecules and Fe atoms are deposited on two monolayers of NaCl on Cu(111). Fig. 5.12a shows a STM image of a *bound* and *free* TTF-dppz molecule as well as a single Fe adatom on NaCl.

Since the *bound* molecule already builds a coordination complex to the Na^+ of the NaCl thin film, the Fe adatom is displaced towards the dppz side of the *free* molecule. For the single atom manipulation on NaCl, the sample bias is swept between 0 and 1.6 V

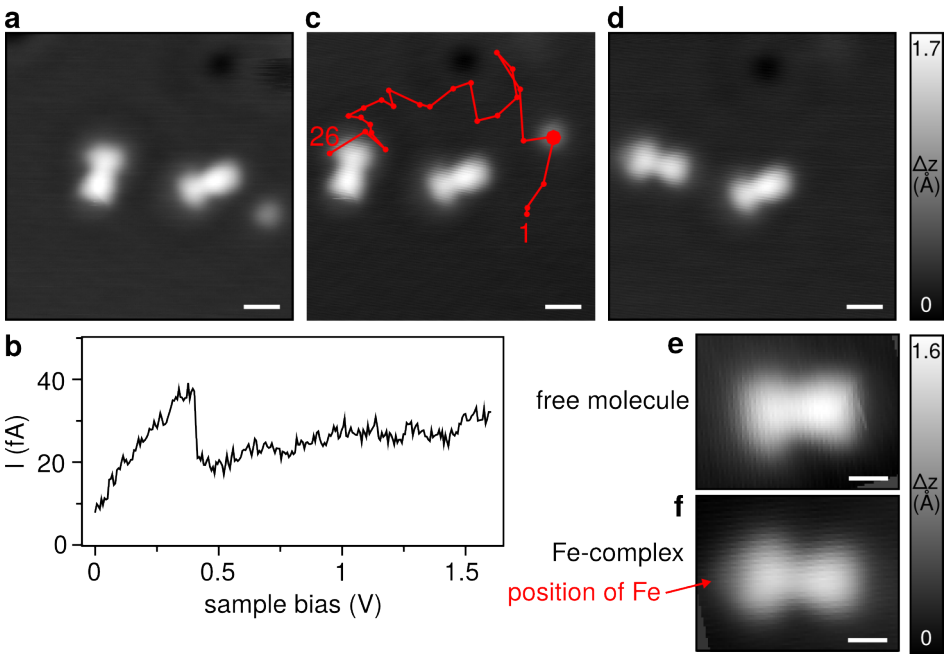

Fig. 5.12: Manipulated complex formation on NaCl thin film. ***a,*** *STM image of free molecule (left), bound molecule (right) and Fe adatom on NaCl thin film (2 ML) on Cu(111)* ***b,*** *Bias sweep to move Fe adatom. The current jump indicates the displacement of the adatom further away from the tip position.* ***c,*** *Manipulation path (red line) and positions (red dots) of the Fe adatom during the 26 manipulation sequences (shown in Fig. 5.13). Between image* ***a*** *and* ***c*** *the adatom is moved from point 3 to 4.* ***d,*** *STM image showing the TTF-dppz-Fe complex and the bound molecule on a NaCl thin film.* ***e,*** *Magnified image of the free molecule before complex formation and* ***f,*** *after complex formation with the manipulated Fe adatom. All images recorded at* $V_b = 0.3\ V$, $I_t = 500\,fA$. *Scale bars in* ***a***, ***c***, ***d*** *are* $1\,nm$, *scale bars in* ***e*** *and* ***f*** *are* $500\,pm$.

which displaces the adatom away from the tip position (Fig. 5.12b). Interestingly, the repulsion of the adatom occurs at opposite polarity in comparison with the Au(111) substrate suggesting a different adatom-surface interaction (Fig. 5.10b). On NaCl, the Fe adatom easily jumps on the tip which interrupts the manipulation experiment. Consequently, the tip is set to a distance that only extremely small current values in the range of few tens of femtoampere are obtained in the bias sweeps to prevent picking up the adatom. In comparison, on Au(111) the tunneling current for manipulation reaches values in a range of a few hundred of picoampere pointing out the stronger coupling to the substrate for Fe adatoms on Au(111) (Fig. 5.10b). In Fig. 5.12b, an abrupt current change from higher to lower values indicates the displacement of the adatom at a voltage of around 0.4 V.

Fig. 5.12c demonstrates the complex displacement path of 26 single atom manipulations to reach the dppz side of the *free* molecule. Each red dot of the connected line corresponds to a position of the Fe adatom after a bias sweep. Repelling the adatom by applying a suitable bias voltage leads to a limited directionality of the displacement.

The adatom moves away from the tip, but the angle is uncontrolled. As a consequence many deviations are necessary to displace the adatom to the molecule resulting in a complex trajectory.

In Fig. 5.13 all sequences of the 26 manipulations are shown. During one of the STM scans after a completed manipulation, the target molecule rotates due to the interaction with the tip and changes its adsorption position (Fig. 5.13r). However, the molecule remains in the *free* state because the angle with respect to the *bound* molecule is not 0° or a multiple of 90° which would be the case for an adsorption along the apolar axis as defined for the *bound* molecule (Fig. 5.5a).

The shape of the dppz moiety appears different which might be induced by the different adsorption site or the interaction with a defect or Na^+ cation of the thin film. Additionally, a dark depression is observed next to the dppz moiety which might indicate the presence of a defect (Fig. 5.13s). Since the single atom manipulation is focused here, the structural and electronic properties of exactly this molecule are not further investigated.

For the final bias sweep which connects the adatom and the dppz moiety, the tip polarity is inverted and a positive voltage is applied to the tip (negative sample bias). Since the molecule is decoupled from the metal, the charge distribution is unaffected on the *free* adsorption site. Hence, a positive tip polarity leads to an attractive force between the negatively charged acceptor and the tip. By positioning the tip between the acceptor dppz and the Fe adatom, both can be attracted and thus, be connected to a TTF-dppz-Fe coordination complex (Fig. 5.12d). The Fe adatom is attached to the dppz moiety indicated by the different shape and size of the dppz moiety of the target molecule (Fig. 5.12e, f). In comparison, the *bound* molecule does not change at all which excludes any tip effect as reason of the different shape of the former *free* molecule.

This experiment highlights that single Fe adatoms can be displaced on a NaCl thin film and can be connected to the dppz moiety of the DA molecule. Such metal-molecule complex formation on NaCl induced by tip manipulation can be used to study chemical and electronic properties of single molecules on surfaces influenced by the coupling of a single atom.

5.3 Optical excitation

The question whether the spatial separation of the molecular orbitals and the intrinsic charge distribution of DA molecules are maintained on a surface is addressed in a previous sections of this chapter (Sec. 5.1). Here, the investigations go beyond the study of ground state properties by performing the challenging experiment to image a single adsorbed molecule and probe its properties under illumination. In solution, TTF-dppz molecules can be optically excited by light of suitable wavelength which leads to an intramolecular charge transfer between the donor and acceptor. [144]

On a surface, the charge transfer property could be studied on a submolecular level by investigating TTF-dppz molecules on NaCl films with current and force spectroscopy under illumination. The results could be compared to the observed electronic

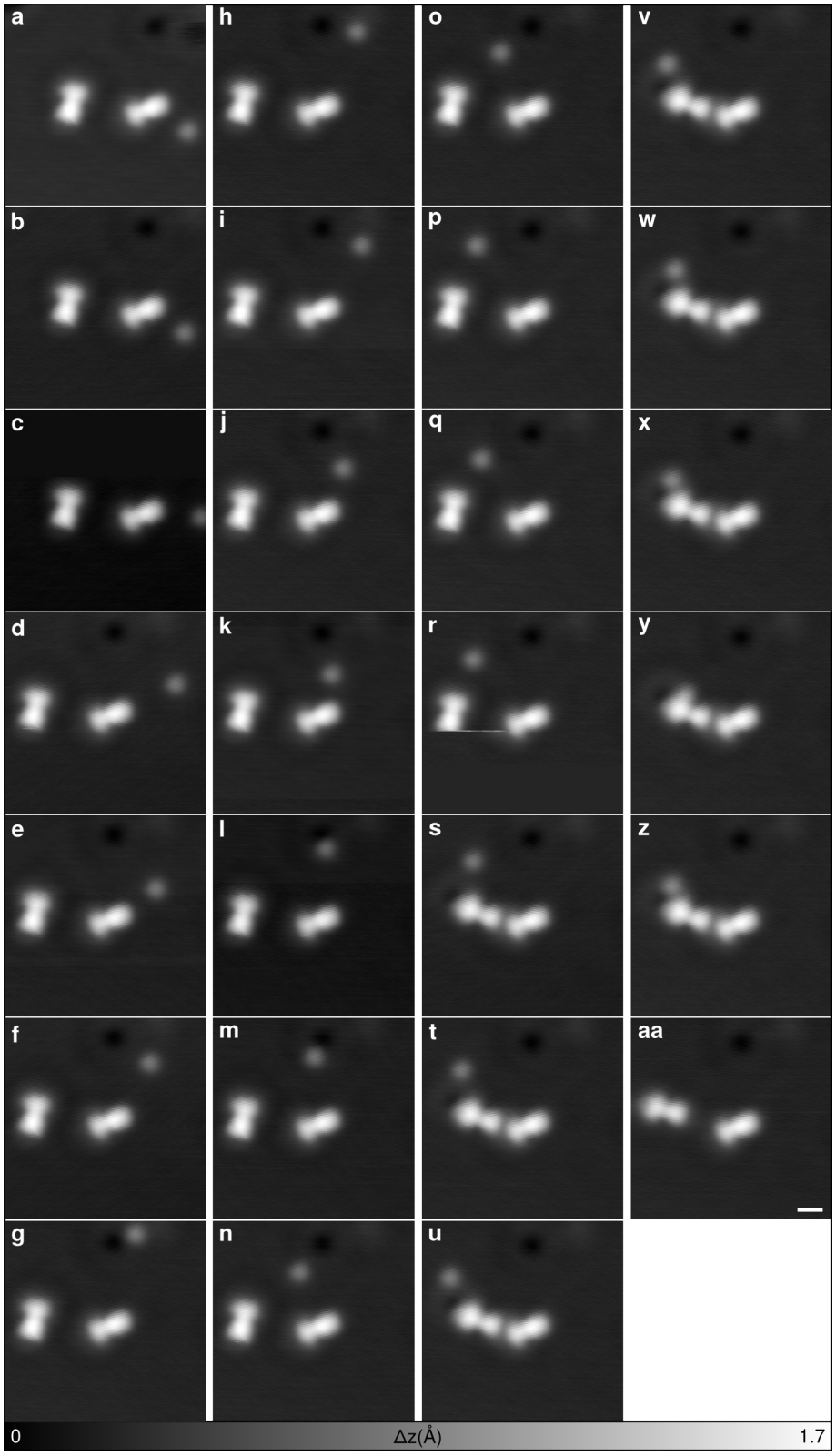

Fig. 5.13: Detailed images of manipulated complex formation on NaCl. *a-aa,* *STM images of all 26 manipulation sequences of the Fe adatom ($V_b = 0.3\,V$, $I_t = 500\,fA$). In image **r** the target molecule is moved during the STM scan. The scale bar is $1\,nm$.*

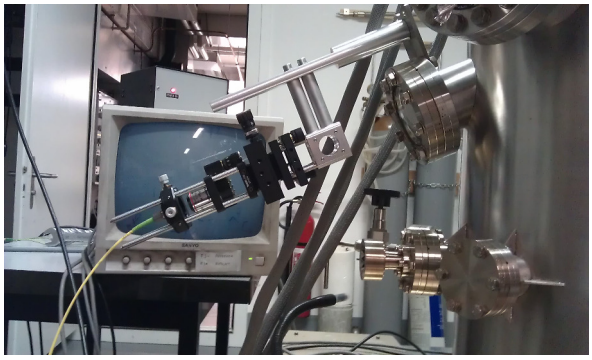

Fig. 5.14: Optical setup for laser illumination. *Mounting stage with connected optical fiber from the laser source and the objective to collimate the light. The window of the UHV chamber enables access to the sample surface.*

properties in the ground state on thin NaCl films. It was demonstrated that single molecules on metals can be investigated by tip-enhanced Raman spectroscopy (TERS) showing typical vibration spectra. [276] Furthermore, electroluminescence of molecules adsorbed on NaCl thin films could be detected by exciting the molecule with the tunneling current. [277, 278] As in the case of TERS, the enhancement of the light intensity in the tip-sample junction could be beneficial for the optical excitation of a single molecule and allow to perform current or force spectroscopy of the excited molecule. Such an experiment is experimentally challenging since it requires stable operation conditions under illumination. In this section, the results of force spectroscopy measurements under illumination on a single DA molecule are shown which highlights the feasibility of combined force spectroscopy and optical excitation.

5.3.1 Optical setup

To illuminate the tip-sample junction, the beam of a NKT superkontinuum EXW-12 laser [i] is transferred by an optical fiber towards an objective mounted in front of a window of the UHV chamber (Fig. 5.14). From this window the sample surface can be accessed directly. The objective (numerical aperture of 0.10, magnification 4×) is used to collimate the light and send it to the tip position by adjusting the screws of the mounting stage.

The center wavelength as well as the bandwidth of the beam of the superkontinuum laser source can be tuned in a range between 400 and 840 nm with variable intensity. Since the optical absorption band of TTF-dppz corresponding to the intramolecular charge transfer between HOMO and LUMO is centered at 540 nm (18500 cm^{-1}) in CH_2Cl_2 solution [144], a center wavelength λ of 540 nm with a bandwidth of ±50 nm is chosen for the laser excitation. Integration of the emission spectrum over this range of wavelengths yields a power of 315 mW for the maximum laser intensity. The used intensity is 15% of the maximum intensity resulting in a power of 47.25 mW. In similar illumination experiments in other UHV systems in the group, a transmission of 10%

[i] www.nktphotonics.com

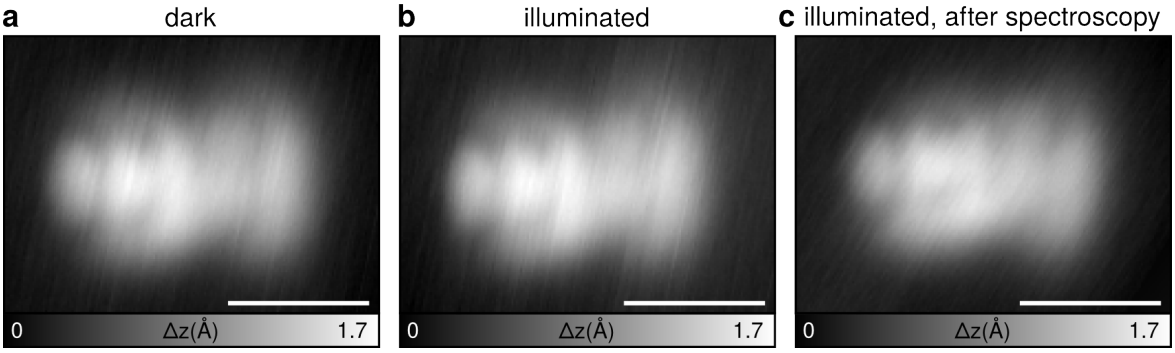

Fig. 5.15: STM images in dark and under illumination. *STM images of the same molecule with the same CO tip on NaCl(2 ML)/Cu(111).* ***a,*** *in dark* ***b,*** *under illumination and* ***c,*** *under illumination after force spectroscopy line scan ($V_b = 0.3$ V, $I_t = 3$ pA). Scale bars are 1 nm.*

through gratings, fibres and lenses is achieved. [279] Considering the same transmission and estimating a spot size of 2 mm^2 on the sample surface, the power density is 118 mW/cm^2.

After switching on the laser with these parameters, the temperature rises by approximately 100 mK and remains on that level afterwards. Due to the temperature increase at the beginning, thermal drift in x-y direction in a range of 2 to 4 nm occurs. Furthermore, the tip retracts by approximately 5 nm to maintain the STM setpoint. The microscope stabilizes after 30 to 60 minutes of illumination which is crucial for scanning single molecules and performing spectroscopy. In Fig. 5.15, STM images of the same *bound* molecule, adsorbed on a NaCl film, with the same CO tip in dark and under illumination are shown. After switching on the illumination and waiting for temperature stabilization, the shape of the molecule does not change compared to the dark (Fig. 5.15a,b) indicating stable scanning conditions of tip and sample at this bias voltage. The illumination could excite HOMO-LUMO transitions which might lead to a different STM image since it probes the LDOS. However, a change of the molecular orbital, respectively of the shape of the molecule in STM, is not observed since the applied voltage of 0.3 V is in the HOMO-LUMO gap of the molecules in dark conditions (Fig. 5.6a). *Free* molecules cannot be investigated since they move to *bound* adsorption sites when the surface is illuminated.

5.3.2 Force spectroscopy under illumination

Upon excitation the dipole moment of the TTF-dppz molecule is expected to change from 0.9 D in the ground state to 5.9 D in the excited state as calculated by time dependent DFT. [144] The change of the dipole moment is caused by internal redistribution of charges due to the intramolecular charge transfer (ICT) which causes electrons to be transferred from the donor to the acceptor (Fig. 2.11 in Sec. 2.4.8). Since the charge distribution of the DA molecule can be accessed by measuring the LCPD with force spectroscopy experiments, as performed in the dark (Fig. 5.7), the charge redistribution under illumination induced by ICT might be measured by force spectroscopy as

well.

The radiative decay time of the excited state is in the range of ns which is much shorter than one oscillation cycle of the tip at a resonance frequency of $f_0 = 25\,\mathrm{kHz}$ ($t_{\mathrm{osc}} = 4 \cdot 10^{-5}\,\mathrm{s}$). [144] Consequently, single excitations of the molecule cannot be observed directly with the used experimental setup. It is assumed that the molecule can be excited many times during the acquisition of the frequency shift leading to a change in the measured signal because it is averaged over many excitations compared to the signal without illumination. Time resolution of the excitation could be achieved using the pump-probe technique as proposed by Schumacher *et al.*. [280, 281]

To increase the sensitivity of the tip to the electrostatic field caused by the charge distribution of the molecule, the tip is terminated with a CO molecule. The charge distribution of the CO causes a repulsive interaction between the CO probe and electrons of the sample due to the lone pairs of the O atom. [264, 282] The metal tip builds a dipole moment because positive charge is located at the tip apex. Therefore, a metal tip terminated with a CO is modelled as a sum of the dipole moment of the metal tip with the charge distribution of the CO molecule. [265] With a CO tip, the tip-sample interaction is dominated by electrostatic forces at large and medium tip-sample distances, comparable to molecular dimensions, whereas at close distances the interaction is governed by Pauli repulsion which leads to tilting of the CO. In conclusion, to probe electrostatic forces, spectroscopy measurements should be performed in the medium distance regime to avoid tilting effects of the CO as observed in AFM topography scans at close distances with repulsive interaction.

First, the LCPD of the molecule with a CO tip is investigated without illumination by recording line profiles over the longitudinal axis varying the tip-sample distance (Figs. 5.16a,b). The tip is approached in steps of 20 pm with respect to the initial height at the STM setpoint ($V_b = 300\,\mathrm{mV}$, $I_t = 3\,\mathrm{pA}$) on the topographic maximum of the molecule. By reducing the distance, the Δf^* values become more negative suggesting that the interaction regime is attractive. Only at a position of $x = 1.5\,\mathrm{nm}$, Δf^* increases by approaching which might be induced by the S atoms at this position. At approximately $x = 1.8\,\mathrm{nm}$ Δf^* reaches its minimum value and the most positive LCPD is measured ($V^*_{\mathrm{max,\,dark}} = -0.23\,\mathrm{V}$). This position is located in the center of the molecule where the topographic maximum is observed for the *bound* type (Fig. 5.5b) as well as the most positive LCPD in the force spectroscopy measurement with a Cu tip (Fig. 5.7d).

On the dppz side, the LCPD decreases slightly to more negative values. The difference of the most positive LCPD to the most negative is around 0.15 V and increasing by approaching the tip. The small LCPD difference as well as the decreasing Δf^* values may indicate that the tip is still relatively far away from the molecule, meaning in a medium distance regime comparable to the molecular dimensions. Similar LCPD differences in LCPD maps with CO tips remaining in the attractive interaction regime (negative Δf^* on the molecule) have been measured by Schuler *et al.*. [94]

The same measurement as in the dark is repeated under illumination ($\lambda = 540\,\mathrm{nm}$ with a bandwidth of $\pm 50\,\mathrm{nm}$) on exactly the same molecule with the same CO tip. The results are shown in Figs. 5.16c,d. The black curve corresponds to the measurement

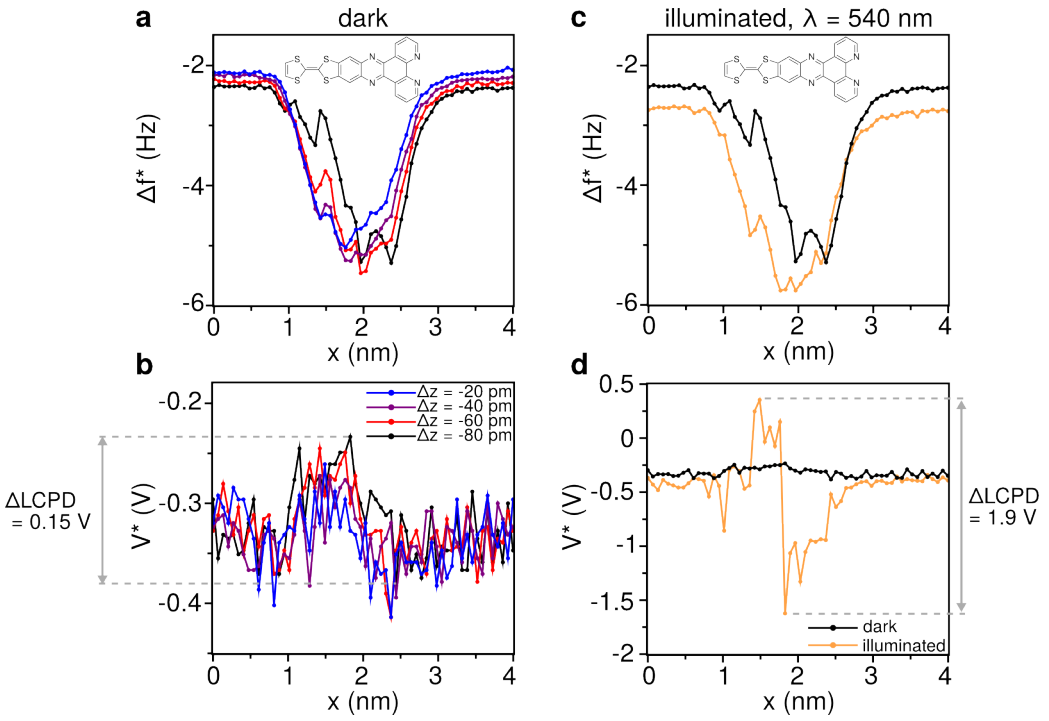

Fig. 5.16: Force spectroscopy under illumination. ***a,*** *Δf^* and* ***b,*** *LCPD line scan along the longitudinal axis of a bound molecule with a CO tip in dark at several tip-sample distances with respect to the STM setpoint at $V_b = 0.3\,V$, $I_t = 3\,pA$.* ***c,d*** *Δf^* and LCPD profile of the same molecule with the same CO tip at a distance of $\Delta z = -80\,pm$ under illumination (yellow curve). For comparison the line scan at the same height in dark from* ***a,b*** *is also plotted (dark curve).*

in the dark at a Δz-offset of $\Delta z = -80\,\text{pm}$. The same Δz-offset is used to record the line scan under illumination at 540 nm (yellow line). The Δf^* curve shows more negative values and a slight lateral shift under illumination. The LCPD values change dramatically under illumination compared to the dark. The most positive LCPD is $V^*_{\text{max, illu}} = 0.3\,\text{V}$ and the most negative is $V^*_{\text{min, illu}} = -1.6\,\text{V}$ resulting in a LCPD difference of $\Delta\text{LCPD}_{\text{illu}} = 1.9\,\text{V}$. Importantly, the direction of the LCPD contrast remains the same. The LCPD of the center of the molecule becomes more positive and of the dppz more negative with a very sharp transition at around $x = 1.8\,\text{nm}$. The observed LCPD difference is extremely high compared to values from literature without illumination which are about 500 mV recorded on DA molecules with CO tips [94] or about 700 mV between a positively charged Cl vacancy and a Cl^- anion of NaCl recorded with a Cu tip [95].

The measured high LCPD difference under illumination is suspicious and the interpretation has to be done with caution. It is not clear if the high LCPD difference is induced by a ICT or artefacts. Nevertheless, the presented force spectroscopy measurement with a CO tip under illumination is a first step towards the investigation of optically induced ICT in single molecules on surfaces. Consequently, the discussion of this challenging experiment in the following helps to clarify the origin of the observed

high LCPD difference under illumination which might be used for further experiments.

Distance dependence The tip-sample distance for the force spectroscopy is determined by the STM setpoint used for atom tracking. After each $\Delta f(V_b)$ curve the topographic maximum of the the molecule is tracked and the height as well as the x-y values are adjusted to compensate for drift. If the conductance or the topography of the molecule at the tracking position changes under illumination, the force spectroscopy curve will be recorded closer or further away from the molecule compared to the dark. This offset of the tip-sample distance may explain that the complete Δf^* curve is shifted towards more negative values. On the NaCl film at positions between $x = 0\,\text{nm}$ to $x = 1.1\,\text{nm}$ and $x = 2.8\,\text{nm}$ to $x = 4\,\text{nm}$ as well as on the molecule ($x = 1.2\,\text{nm}$ to $x = 2.7\,\text{nm}$) the Δf^* values are more negative which indicates that the tip-sample interaction is more attractive in general under illumination. This might be caused by a reduced tip-sample distance.

On the molecule, the huge increase of the LCPD difference under illumination could be induced by such a reduced distance. However, the Δf^* curve remains in the negative range which excludes a close tip-sample interaction regime where complex LCPD contrasts occur due to repulsion (hence positive Δf values) as observed in ref [94]. Additionally, at the position $x = 1.5\,\text{nm}$ where an increase of Δf^* is observed by reducing the tip-sample distance, the Δf^* value under illumination decreases more (from $-3\,\text{Hz}$ to $-4.8\,\text{Hz}$) than the minimum Δf^* value at $x = 2\,\text{nm}$ ($-5.6\,\text{Hz}$ to $-5.8\,\text{Hz}$) and the rest of Δf^* curve under illumination. Hence, at this position the Δf^* curve under illumination resembles more the Δf^* curves in dark at larger tip-sample distances (*e.g.* red curve in Fig. 5.16a). In summary, the Δf^* curve does not show repulsive interaction under illumination and indicates a similar tip-sample distance regime than in the dark at the same $\Delta z = -80\,\text{pm}$.

A further indicator for a distance regime under illumination comparable to the dark is the tunneling current simultaneously recorded in the spectroscopy measurements (Fig. 5.17). The maximum tunneling current during the bias sweeps under illumination does not show any deviations from the values in the dark (Fig. 5.17a). If the tip was closer to the molecule and assuming a constant conductance, the tunneling current would be higher. In contrast, the current remains constant and even decreases for $I_{\text{t,min}}$ (I_t at $V_{\text{b,min}} = -0.5\,\text{V}$) values by keeping the same overall features (Fig. 5.17b). Thus, it can be excluded that single events during the atom tracking, as for example geometric changes of the molecule, lead to a reduced tip-sample distance and consequently to an huge increase of the LCPD. If this was the case, the current would also jump to higher values during the acquisition of the $\Delta f(V_b)$ curves. Furthermore, the STM images recorded under illumination and in dark (Fig. 5.15a,b) show the same contrasts of the molecule recorded with the same STM setpoint which points out that the tracking position is spatially stable.

In Figs. 5.17c-e single $I_t(V_b)$ curves are shown. The curve of the molecule center and of the dppz correspond to the extreme LCPD values at $x = 1.3\,\text{nm}$ and $x = 1.8\,\text{nm}$. The curves look similar to the dark in the positive bias range demonstrating that abrupt current changes do not occur. Interestingly, they differ in the negative range.

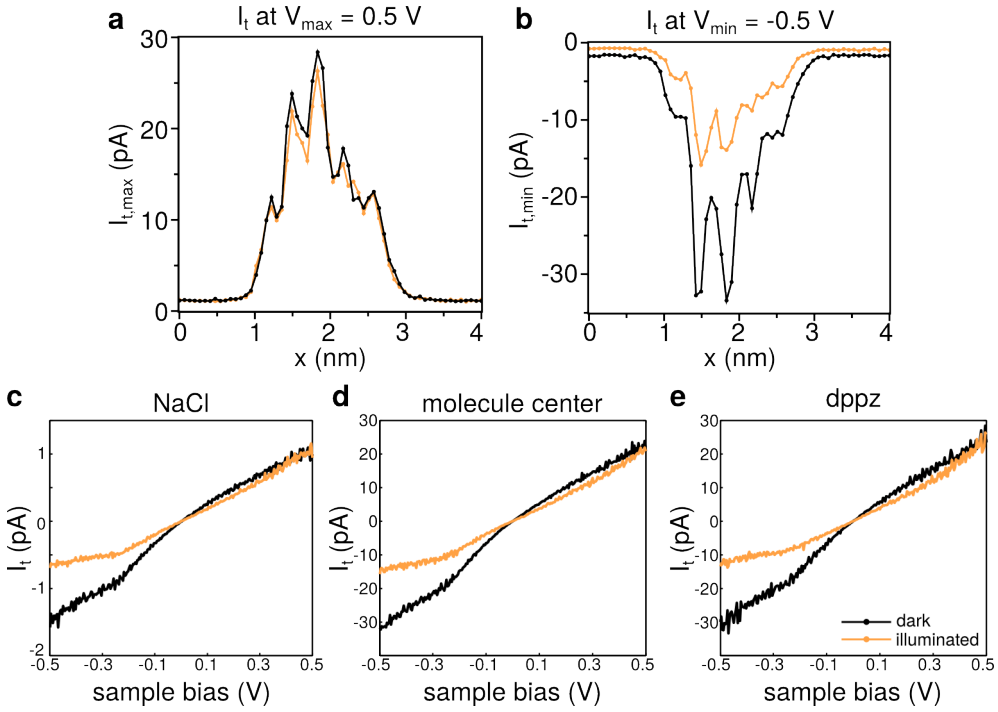

Fig. 5.17: Current *vs.* voltage under illumination. ***a,*** *Maximum current and* ***b****, minimum current during the force spectroscopy line scans shown in 5.16c,d in dark (black) and under illumination (yellow). The current is recorded simultaneously to* Δf*.* ***c,*** *Single* $I_t(V_b)$ *curve on NaCl,* ***d,*** *on the molecule center (most positive* V^**) and* ***e,*** *on dppz (most negative* V^**) in dark (black) and under illumination (yellow).*

The current curve under illumination exhibits less negative values as observed in the plot of $I_{t,\mathrm{min}}$. This deviation is systematic and observed on NaCl as well as on the whole molecule indicating that it is the tunneling junction in total that changes under illumination at negative sample bias without a specific contribution of the molecule. The STM setpoint used for atom tracking is $V_b = 0.3\,\mathrm{V}$, $I_t = 3\,\mathrm{pA}$. Since the tracking is done in the positive bias range, a different conductance at positive sample bias would be compensated by reducing or increasing the tip-sample distance which might lead to the observed evolution of the $I_t(V_b)$ curves differing in the negative range. The difference in the negative bias range points out that either the conductance changes for the positive values leading to a different tip height because of the atom tracking or it changes in the negative range leading to different current values at a comparable distance. Both effects could also occur in parallel.

The investigations of the tunneling current support the assumption of a conductance change under illumination that is observed on the molecule and on NaCl. This effect is not molecule specific. Therefore, the conductance change could also be induced by a tip change. Indeed, the STM contrast of the molecule after the spectroscopy measurements looks slightly different to the previous ones (Fig. 5.15). However, the consequences of a tip change on the tip-sample distance are assumed to be minor since a drastic change of the distance regime to distances where repulsion occurs is excluded

by the negative Δf^* values. Abrupt height changes are also not observed which is highlighted by I_t values during the whole line scan under illumination which are in a similar range as in dark.

In summary, based on the experimental observations a similar distance regime for the force spectroscopy measurement under illumination as in the dark is assumed. To determine the tip-sample distance, $\Delta f(z)$ measurements have to be performed in dark and under illumination. The distance dependence of the LCPD measurements has to be further investigated by acquiring $\Delta f(V_b)$ curves over a distance range of few hundred pm to reveal the evolution of the LCPD values as function of z.

Influence from the CO tip A tip change might cause a different electrostatic interaction between tip and sample. Thus, a further explanation for the observed huge LCPD contrast under illumination may come from an artefact caused by the CO at the tip apex. Comparing the STM image of the same molecule with the same CO tip before (Fig. 5.15b) and after (Fig. 5.15c) recording the force spectroscopy line scans reveals that a slight change occurred during the measurements. The difference of the molecular topography suggests a slight displacement of the CO at the tip apex caused during the line scan *e.g.* when the CO is bend due to repulsive tip-molecule interaction. In AFM scans the CO at the tip enhances the contrast by bending due to repulsion which creates sharp lines above locations of high electron density, especially covalent bonds. [8] The abrupt transition between positive and negative LCPD at $x = 1.8\,\mathrm{nm}$ could be induced by flipping of the CO from one side to the other at the maximum of the molecule. The position at $x = 1.8\,\mathrm{nm}$ corresponds to the maximum where a bright stripe is observed in AFM images (Fig. 5.3b). The orientation of the CO at the tip with respect to the molecule could change by crossing this position which could result in a different electrostatic interaction. Indeed, the bending of the CO compared to a Xe tip can be used to extract the electrostatic force of AFM scans on molecules. [283] However in the case of illumination, it is unclear if the bending of the CO strongly modifies the LCPD contrast or *vice versa* if the electrostatic force from the illuminated molecule interacts with the CO which leads to a different orientation at the tip apex. Again, it has to be emphasized that the observed CO bending in AFM images [8] used to extract electrostatic forces [283] is obtained in the repulsive interaction regime. The measured Δf^* values do not indicate such an interaction in the presented force spectroscopy measurements.

In summary, a change of the orientation or position of the CO on the tip might be responsible for the abrupt LCPD change at $x = 1.8\,\mathrm{nm}$. The influence of the CO tip could be studied by measuring LCPD maps in dark and under illumination to compare the spatial distribution of the LCPD changes and to reveal possible asymmetries coming from CO displacements on the tip.

Charging events outside bias sweep range Another issue that has to be taken into account is the data evaluation outside the bias sweep range. The observed huge LCPD difference of 1.9 V is much higher than the bias sweep range. The most negative LCPD values lie outside the sweep range of -0.5 to $0.5\,\mathrm{V}$, whereas the positive values are

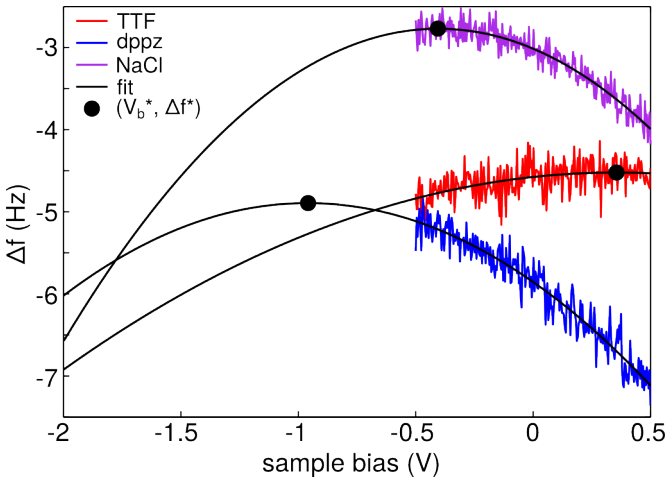

Fig. 5.18: $\Delta f(V_b)$ curves under illumination. *Recorded $\Delta f(V_b)$ curves on different positions on the molecule with corresponding parabolic fit. The black dot indicates the position of the maximum where V^* and Δf^* are extracted. The sweep range is from -0.5 V to 0.5 V. The maxima of the spectra above dppz lie outside the sweep range, so that extrapolation is required to obtain the V^* and Δf^* values.*

inside the sweep range (Fig. 5.18). Parabola maxima at bias voltages lower than -1 V or higher than 1 V are hardly detectable on TTF-dppz on two monolayers of NaCl since the current increases which leads to inelastic excitation and molecular displacements.

The measured $\Delta(V_b)$ curves are fitted with a parabola and the values of the maximum $(V^*, \Delta f^*)$ are extracted. For all curves with a maximum at less than -0.5 V, extrapolation is required to determine the values of the maximum. Thus, the frequency shift is not continuously recorded as a function of the bias voltage until the maximum occurs. A quadratic dependency is assumed for the extrapolation and it cannot be experimentally shown or theoretically stated with certainty that the $\Delta f(V_b)$ curves evolve in that way outside the sweep range. Especially, charging of the molecules leads to dips in the $\Delta f(V_b)$ curves and transitions between different parabolas. [284–288] Similar features might be caused under illumination, since a charge transfer is expected between the molecular moieties due to the short-lived excited state. It cannot be excluded that these features appear at bias voltages less than -0.5 V and such features could alter the values of the parabola maximum. However, for the range between -0.5 to 0.5 V dips or transitions between parabolas are not observed. Consequently, the LCPD values in the center of the molecules rising from $V^*_{\text{max, dark}} = -0.23$ V to $V^*_{\text{max, illu}} = 0.3$ V can be validated which indicates a tremendous change of the LCPD of 0.53 V on the same position of the molecule. For comparison, the *free* molecule shows a difference of 0.5 V between the donor and acceptor which are positively and negatively charged, respectively (Fig. 5.7e).

Charge state of donor and acceptor The observed LCPD difference in the middle of the molecule might be induced by the illumination since it occurs before the abrupt jump at $x = 1.8$ nm and the $\Delta f(V_b)$ curves lie entirely in the bias sweep range. The

LCPD value of $V^*_{\text{max, illu}} = 0.3\,\text{V}$ suggests an increased negative charge at this location (Fig. 5.16d). It is consistent with the measurements with Cu tips and CO tips in the dark where the center is also negative for the *bound* molecule (Figs. 5.7d, 5.16b). On the extremity of TTF, the LCPD under illumination does not show positive charge compared to the substrate which is similarly observed with a Cu tip and a CO tip in the dark. However, on the dppz side, the extrapolated LCPD values decrease down to $-1.6\,\text{V}$ which points out that the acceptor is positively charged. This is different to the observations with a Cu tip where the acceptor of the *bound* molecule is neutral compared to the substrate (Fig. 5.7d). The decreased LCPD under illumination follows the trend in the LCPD curve with a CO tip (Fig. 5.16b) where a slight decrease is seen on the dppz. A more positively charged acceptor is contradictory to the charge transfer process which leads to the accumulation of electrons in the acceptor, hence negative charge. However, Schuler *et al.* also observe decreasing LCPD values on the acceptor of the bipolar TTF-PYZ_2 molecule in dark with a CO tip. [94] This opposing contrast suggesting positive charge on the acceptor is explained by the influence of the complex three-dimensional electron distribution leading to a different LCPD contrast than expected for partial point charges. Furthermore, the *bound* molecule forms a chelate complex with a Na^+ cation which leads to an altered charge distribution as observed in force spectroscopy with Cu tips. This might also contribute to the observed negative LCPD values on the acceptor under illumination. Since the *free* molecules change their adsorption sites and become *bound* molecules, they cannot be investigated in the performed force spectroscopy experiment under illumination.

Conclusion The LCPD difference between the molecular moieties increases dramatically by shining light at a wavelength of the absorption band of the DA molecule. The results suggest a high increase of positive charge on the acceptor site and an increase of negative charge in the center of the molecule. This charge redistribution might be induced by illumination, but it cannot be separated from other influences with the presented experimental data. Various factors which are not related to the intramolecular charge transfer, could contribute to the measured LCPD values such as varying tip-sample distance, CO displacement at the tip, LCPD contrast formation or extrapolation of the data. Based on the presented analysis, a reorientation of the CO tip during the scan might be the major contribution to the high LCPD difference pointed out by the sharp transition of the LCPD value at $x = 1.8\,\text{nm}$ in Fig. 5.16d. The impact of the CO tip and distance dependence on the measured LCPD has to be further investigated in experiments to state the observation of an intramolecular charge transfer in a single molecule upon photo excitation.

Potential improvements of the experiments To improve the informational value of the experiments, the spectroscopy measurements could be repeated with different wavelengths to verify that the LCPD difference is caused by light absorption corresponding to a S_0-S_1 transition as theoretically predicted (Sec. 2.4.8). The mentioned influences on the LCPD measurement might not change by varying the wavelength, but the intramolecular charge transfer should respond. Hence, the measurement could

be used to separate the optical excitation of the molecule from other effects.

The distance dependence of the LCPD could be studied by recording $\Delta f(V_b)$ spectroscopy with variation of z by few hundred of pm on different molecular sites. $\Delta f(z)$ spectroscopy could reveal the tip-sample distance regimes in dark and under illumination. Thus, the distance regimes could be compared and z-offsets due to conductance changes could be compensated by adjusting the tip height accordingly. Furthermore, atom tracking could be done on a elevated or depressed sites on NaCl which are assumed to be unaffected from illumination.

The CO bending at the tip apex could be investigated by recording two-dimensional LCPD maps to elucidate possible tip asymmetries or abrupt contrast changes. Distance dependent measurements with CO tips could reveal an onset of possible bending or reorientation effects. Furthermore, DFT simulations could estimate the influence of the CO orientation or bending on the spectroscopy results.

Technical improvements could be done by developing new measurement techniques combining STM and AFM with optical excitation and detection. Pump-probe experiments where the tip oscillation is coupled to the pulsed excitation of the laser by a lock-in is opening new possibilities for time resolved measurements of excited states. [280, 281] Exciting molecules on surfaces by a shining light on the tip-sample junction comparable to TERS [276, 277] and detecting the emitted light in parallel to frequency shift and current would provide a complete data set to analyse the charge transfer in DA molecules.

5.4 Complex fused donor-acceptor molecules on Au(111)

The results presented in this section have been published in the journal Nanoscale.[b] *[179] Figures are reproduced with permission from the Royal Society of Chemistry.*

Complex fused DA molecules consist of a DA core with peripheral side groups. Side groups can act as anchoring groups to the substrate and are used in solar cell devices to create stable molecule-surface interfaces and enhance the efficiency. [148,152] Furthermore, on surfaces, the molecular assembly formation can be controlled by the interaction between the molecular side groups. By thermal deposition, for example used for the preparation of samples with TTF-dppz molecules, the peripheral side groups of complex fused DA molecules likely break which prevents the study of their chemical structure and alignment on the surface.

The electrospray deposition (ESD) technique is capable of transferring complex molecular structures from solution onto a surface under vacuum conditions as described for the $HBC6C_{12}$ molecules in Sec. 3.2. Thus, ESD opens the way to study complex fused DA molecules by STM and AFM. The TTF-dye molecule (Sec. 2.4.9)

[b] Hinaut, A., Meier, T., Pawlak, R., Freund, S., Jöhr, R., Glatzel, T., Decurtins, S., Müllen, K., Narita, A., Liu, S.-X., Meyer, E. Electrospray Deposition of Structurally Complex Molecules Revealed by Atomic Force Microscopy. *Nanoscale* **10,** 1337 (2018).

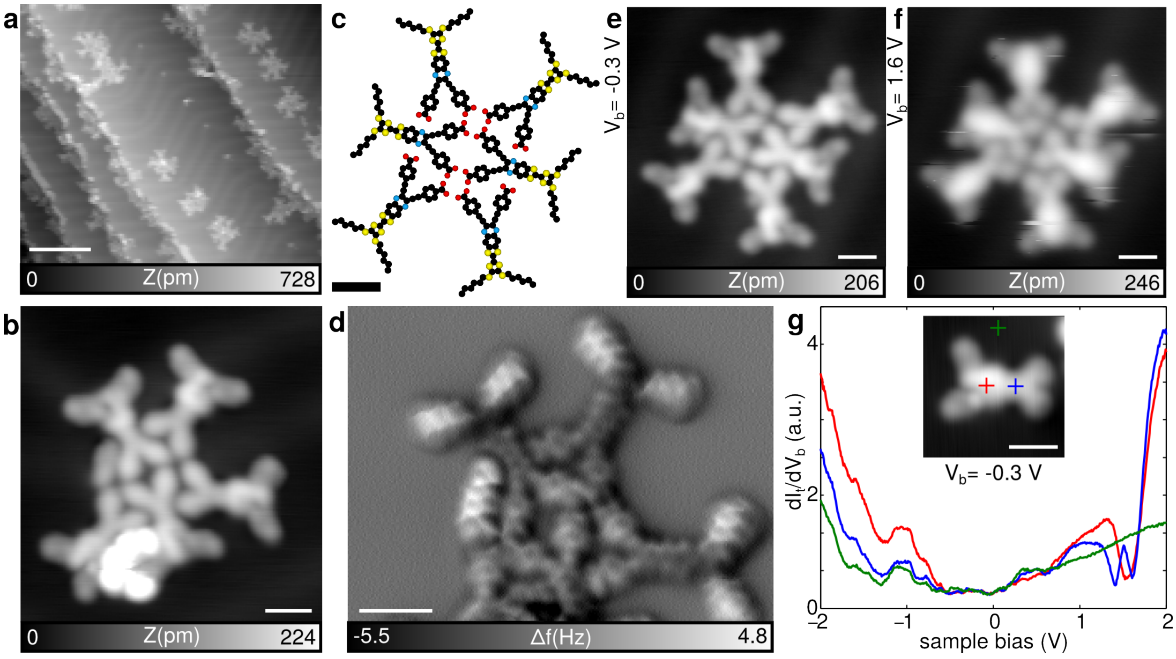

Fig. 5.19: TTF-dye molecules on Au(111) ***a,*** *STM overview image showing the assembling of TTF-dye molecules in small islands ($I_t = 10\,pA$, $V_b = -0.5\,V$, scale bar 10 nm). In some of the islands, fragments are observed after ESD deposition.* ***b, d*** *STM image of such an island ($I_t = 5\,pA$, $V_b = -0.3\,V$) and corresponding constant height AFM image with a CO terminated tip ($V_b = 0\,V$).* ***c,*** *Model of the arrangement of the TTF-dye molecules representing the island in image (**e**) experimentally observed by STM ($I_t = 5\,pA$, $V_b = -0.3\,V$).* ***f,*** *STM image of the same island at $I_t = 1\,pA$, $V_b = 1.6\,V$.* ***g,*** *STS spectra of TTF-dye. The tip position is indicated by the cross in red (TTF moiety), in blue (quinoxaline moiety) and in green (Au(111) substrate) in the inset. (**b-g**) the scale bars are 1 nm. [179]*

has a TTF based electron donor exhibiting two long alkyl chains. The electron acceptor moiety consists of quinoxaline where two benzoic acid end groups are attached, used in applications as anchoring groups. [152] TTF-dye molecules absorb light of a wide spectral range which leads to one of the highest power conversion efficiencies of TTF based dyes used in organic solar cells. [148]

5.4.1 Structure determination by STM and AFM

After ESD of TTF-dye molecules, small molecular islands can be found on the Au(111) surface without annealing of the sample after deposition (Fig. 5.19a). Between the islands the clean Au(111) substrate with the herringbone reconstruction is observed which indicates the low amount of contaminations and solvent molecules on the surface. The islands are formed by three to six molecules which are aligned in a way that always the same molecular unit faces the center of the island resulting in a symmetric shape of the island (Fig. 5.19e). In some assemblies molecular fragments are present leading to the formation of asymmetric islands (Fig. 5.19b). High resolution AFM with CO

terminated tips at constant height reveals the structural alignment of the molecules (Fig. 5.19d). The benzoic acids end groups face each other in the center of the islands whereas the alkyl chains are oriented towards the edges of the islands. The alkyl chains appear as bright zig-zag structures in the AFM image. The more positive frequency shift on the alkyl chains compared to the molecular core suggests a smaller tip-sample distance. Additionally by scanning with the tip, the alkyl chains tend to move which reflects their high mobility on the Au(111) surface (see stripes in Fig. 5.19f). The flat-lying core of the TTF-dye molecules, consisting of the TTF and quinoxaline, is clearly recognized in the AFM image as well as the benzoic acid end groups. The molecules are chemically intact which demonstrates their successful deposition by electrospray.

5.4.2 Electronic properties of TTF-dye molecules

The electronic properties of the TTF-dye molecules are investigated by STS on different positions on the molecule in comparison to the Au(111) substrate (Fig. 5.19g). At negative bias range only peaks which coincide with the Au(111) substrate are observed. Hence, a determination of the occupied states of the molecules is not possible due to the strong contribution of the metal substrate. On the positive bias range, resonances which differ from the Au(111) substrate, are detected at approximately 1 V for quinoxaline and 1.3 V for the TTF moiety. These resonances refer to the LUMO of the molecule. The STM image in Fig. 5.19g at a voltage around the LUMO energy shows that the molecules appear larger at the position of the TTF moiety. This is contrary to DFT calculations of the molecule in the gas phase where the LUMO is found to be centered on the acceptor quinoxaline (Fig. 2.12 in Sec. 2.4.9). [148] Thus, the metallic substrate influences significantly the electronic states of the TTF-dye which explains the observed differences to the simulations.

5.4.3 Hydrogen bonding motive of the molecular islands

Using the observations from the AFM image (Fig. 5.19d), the bonding motive of the molecular islands can be illustrated in a model depicted in Fig. 5.19c. The benzoic acid groups of the two inner molecules face each other. Each of the benzoic acid end groups of the inner molecules meet with two other benzoic acid end groups from two outer molecules. Thus, at two locations in the islands, four benzoic acid end groups are circularly aligned which reveals the interaction by hydrogen bonds between the benzoic acid groups. Hydrogen bonds are also responsible for the alignment of the second benzoic acid groups of the outer molecules towards the N atoms of the pyrazine. Therefore, the bonding motive of the molecular islands is driven by hydrogen bonds. Interdigitation of long alkyl chains as observed for the $HBC6C_{12}$ molecules in Sec. 3.2 does not contribute significantly to the formation of the molecular islands which demonstrates that the hydrogen bonding dominates over the van der Waals bonding for molecules with both, benzoic acid and alkyl end groups. Since the number of available and accessible binding sites for hydrogen bonds is limited in the islands, not more than six molecules participate in the formation of symmetric islands.

5.5 Conclusion

In summary, it was demonstrated that TTF-dppz molecules interact with single Na^+ cations of NaCl thin films forming a chelate complex depending on the adsorption position. Thus, the charge inside the molecule is redistributed which leads to the loss of the intrinsic DA properties. On different adsorption sites, not favouring the bond formation between the molecules and a Na^+ cation, the electronic states and DA charge distribution of the molecules is unaffected. By tip manipulation, the adsorption site of the molecules on the NaCl film can be reversibly changed which induces or prevents the bond formation. Consequently, single TTF-dppz molecules on NaCl thin films can be used as molecular switches where the DA properties can be controllably activated or deactivated.

Furthermore, by displacing single Fe adatoms into the vicinity of the metal chelating binding site of the DA molecules, TTF-dppz-Fe coordination complexes are formed on gold as well as on NaCl thin films. These manipulation experiments open the way to study new optical absorption bands of metal-organic systems and electronic states as observed in solution chemistry on the level of a single molecule on a surface.

The combination of optical excitation with scanning probe techniques, offering various imaging and spectroscopic methods, is promising to study the charge transfer in DA molecules. First results with optical excitation are presented in this chapter which suggest a non-negligible difference of the measured charge distribution of the DA molecules under photon irradiation compared to the measurements in the dark. Further experiments are needed to clarify the origin of the measured charge distribution difference and to investigate the distance dependence under illumination, the effect of the CO at the tip apex and of the underlying substrate.

In organic solar cells applications, anchor groups are added to the molecular core to create stable interfaces and enhance the efficiency. The specially designed DA molecules with anchor groups lead to more complex structures and higher thermal fragility preventing thermal deposition in UHV conditions. By electrospray deposition, it was shown that complex DA molecules with peripheral side groups can be successfully deposited on a surface in vacuum and analyzed by STM and AFM. This broadens the field of explorable molecules used in chemistry or biology. Beyond DA systems, DNA strings, large three-dimensional molecules and new chemical reaction sites on molecular structures might be studied in this way with unravelled lateral resolution.

Electrospray deposition in combination with optical excitation and decoupling from metal substrates, as shown with the model experiments in this chapter, would allow to study a variety of processes from nature, such as light-harvesting complexes for photosynthesis, or from devices, such as synthetically designed dye molecules, on the level of atoms under well defined conditions.

6 Conclusions and Outlook

To reach the prospects of single-molecule electronics and machinery, electronic characteristics and mechanical motion have to be controlled on the level of an individual molecule adsorbed on a surface. In this thesis, single molecules are investigated using STM and AFM which reveals the control of structures, properties and diffusion as well as their interplay with surfaces.

Control of covalent bond formation between and within molecules is achieved using on-surface chemical reactions. Molecular structures are controllably transformed which leads to covalent linking of the molecules or new intramolecular bonds. These experiments point out the possibility to use the interaction with the surface of single molecules as trigger for chemical processes which open new possibilities for synthesis and bottom-up fabrication. [175]

Electronic states caused by topological superconductivity are investigated by STM which can be linked to the structure of atomic wires revealed by AFM. Force spectroscopy allows to quantify the hydrogen bond interaction between a CO tip and hydrogen atoms of molecules on the surface. Interdigitation of long alkyl chains caused by van der Waals interactions is observed by AFM. These findings highlight the capability of STM and AFM to quantify interaction forces and to resolve chemical properties and structures on surfaces with atomic resolution.

Tip manipulation is used to controllably displace molecular vehicles. In the first NanoCar Race a single molecule is propelled and steered over a complex race track of 133 nm. [230] This result demonstrates the high level of repeatability and directional control of the used molecular manipulation mechanism induced by field-assisted vibrational excitation. [224] From a fundamental point of view, these results show the local interaction of surfaces on the molecular diffusion properties. The findings might be used to adapt molecular machines in order to control adhesion and friction on surfaces and to transform electrical power in molecular motion. [15]

The donor-acceptor properties defining the diode-like characteristics of a specifically designed molecule are investigated on thin insulating films. The DA molecules interact with single Na^+ cations of the NaCl thin films forming a chelate complex depending on the adsorption position. Consequently, the negative charge of the acceptor is redistributed which alters the intrinsic DA properties. The DA character of the molecules

is maintained if they are adsorbed on positions that prevent the interaction with single Na^+ cations. By tip manipulation the adsorption sites of the molecules can be reversibly changed which creates a molecular switch since the DA states are turned on and off. These results reveal the impact of the surface on electronic properties which is relevant for potential applications of DA molecules as components of electronic circuits or of organic solar cells.

In organic solar cells applications, side groups are added to the molecular core with DA character to promote efficient charge transfer to the electrode. Thus, the molecules have a more complex structure which prevents thermal deposition in UHV due to possible decomposition. By electrospray deposition, complex DA molecules with peripheral side groups are successfully deposited on a surface in vacuum. The bonding motive of assembly formation triggered by the interaction between the molecular side groups is revealed by STM and AFM with atomic precision. This result shows that more complex molecular structures used in chemistry or biology such as DNA strings or large three-dimensional molecules might be explored with unravelled lateral resolution of STM and AFM.

Single Fe adatoms are displaced and controllably connected to the metal-chelating site of DA molecules which induces the formation of a coordination complex. This manipulation experiment is a prerequisite for tip-induced on-surface reactions leading to new electronic properties. Different adatoms, *e.g.* Ru, could be deposited to study the alignment of electronic states due to complex formation leading to new optical absorption bands as observed in solutions. [147, 289] Test experiments show the non-negligible change of the charge distribution of the DA molecule under illumination with a laser beam. The origin might be an intramolecular charge transfer between donor and acceptor moiety, however contributions from the CO tip, the tip-sample distance and wavelength dependence have to be clarified. These results demonstrate the possibility to connect atoms and molecules on surfaces forming new chemical compounds and observing their optical properties with the lateral resolution of STM and AFM.

The combination of STM/AFM and optics is a promising approach to study absorption and emission properties of single molecules on surfaces as well as internal charge transfer processes with atomic precision and spectral resolution. Recently, several methods have been applied to access vibrational modes [276, 277], electroluminescence [278, 290] or time-resolution of electronic states. [280, 291] Combining these novel techniques with the achieved control of single molecules and atoms by tip manipulation, presented in this thesis, opens up the way to study opto-electronic characteristics of diode-like molecules as a function of their adsorption sites or coupling to atoms.

The theoretically proposed molecular p-n junction composed of donor and acceptor parts from Aviram and Ratner triggered the research on molecular electronics more than 40 years ago. [1] The recent developments in the field of molecular machinery have opened new routes and refounded these concepts of molecular electronics. [292, 293] The fields of molecular electronics and machinery mutually benefit from each other leading to promising new ideas. Electronic components are created by mechanical switches consisting of single molecular machines which is, for example, realised in a prototypical memory chip consisting of rotaxane [294] or catenane molecules [295].

Stoddart, Feringa and Sauvage were awarded with the Nobel Prize in Chemistry in 2016 for such groundbreaking achievements allowing controlled mechanical motions of molecular systems creating molecule based memory chips [294], pumps [296], shuttles [297] or motors [298]. Interestingly, some of those molecular systems are based on the donor-acceptor character of their molecular parts. [297, 299–301] Hence, similar buildings blocks, as proposed by Aviram and Ratner and orignally envisioned as a p-n junction, are used in this context as a "motor" of the nanomachines. This aspect reveals the interconnections of scientific ideas and fields leading to unforeseeable progress! In this line of thoughts, the fundamental knowledge acquired from STM/AFM by allowing to access single molecules on surfaces will continue to contribute to the advent of molecular electronics and machinery.

Bibliography

[1] Aviram, A. & Ratner, M. A. Molecular Rectifiers. *Chem. Phys. Lett.* **29**, 277–283 (1974). URL https://doi.org/10.1016/0009-2614(74)85031-1.

[2] Binnig, G., Rohrer, H., Gerber, C. & Weibel, E. Tunneling through a controllable vacuum gap. *Appl. Phys. Lett.* **40**, 178–179 (1982). URL http://aip.scitation.org/doi/pdf/10.1063/1.92999.

[3] Binnig, G., Rohrer, H., Gerber, C. & Weibel, E. Surface studies by Scanning Tunneling Microscopy. *Phys. Rev. Lett.* **49**, 57–61 (1982). URL https://journals.aps.org/prl/pdf/10.1103/PhysRevLett.49.57.

[4] Binnig, G., Quate, C. F. & Gerber, C. Atomic force microscope. *Phys. Rev. Lett.* **56**, 930–933 (1986). URL https://journals.aps.org/prl/pdf/10.1103/PhysRevLett.56.930.

[5] Crommie, M. F., Lutz, C. P. & Eigler, D. M. Confinement of electrons to quantum corrals on a metal surface. *Science* **262**, 218–220 (1993). URL http://science.sciencemag.org/content/262/5131/218.

[6] Repp, J., Meyer, G., Olsson, F. E. & Persson, M. Controlling the charge state of individual gold adatoms. *Science* **305**, 493–5 (2004). URL http://dx.doi.org/10.1126/science.1099557.

[7] Repp, J., Meyer, G., Stojković, S., Gourdon, A. & Joachim, C. Molecules on Insulating Films: Scanning-Tunneling Microscopy Imaging of Individual Molecular Orbitals. *Phys. Rev. Lett.* **94**, 026803 (2005). URL http://link.aps.org/doi/10.1103/PhysRevLett.94.026803.

[8] Gross, L., Mohn, F., Moll, N., Liljeroth, P. & Meyer, G. The chemical structure of a molecule resolved by atomic force microscopy. *Science* **325**, 1110–4 (2009). URL http://dx.doi.org/10.1126/science.1176210.

[9] Gross, L. *et al.* Measuring the charge state of an adatom with noncontact atomic force microscopy. *Science* **324**, 1428–31 (2009). URL http://dx.doi.org/10.1126/science.1172273.

[10] Mohn, F., Gross, L., Moll, N. & Meyer, G. Imaging the charge distribution within a single molecule. *Nat. Nanotechnol.* **7**, 227–31 (2012). URL http://dx.doi.org/10.1038/nnano.2012.20.

[11] Koumura, N., Zijistra, R. W. J., Van Delden, R. A., Harada, N. & Feringa, B. L. Light-driven monodirectional molecular rotor. *Nature* **401**, 152–155 (1999). URL http://dx.doi.org/10.1038/43646.

[12] Fletcher, S. P., Dumur, F., Pollard, M. M. & Feringa, B. L. A reversible, unidirectional molecular rotary motor driven by chemical energy. *Science* **310**, 80–82 (2005). URL http://science.sciencemag.org/content/310/5745/80.

[13] Liu, Y. *et al.* Linear artificial molecular muscles. *J. Am. Chem. Soc.* **127**, 9745–9759 (2005). URL http://dx.doi.org/10.1021/ja051088p.

[14] Shirai, Y., Osgood, A. J., Zhao, Y., Kelly, K. F. & Tour, J. M. Directional control in thermally driven single-molecule nanocars. *Nano Lett.* **5**, 2330–2334 (2005). URL http://dx.doi.org/10.1021/nl051915k.

[15] Kudernac, T. *et al.* Electrically driven directional motion of a four-wheeled molecule on a metal surface. *Nature* **479**, 208–211 (2011). URL http://dx.doi.org/10.1038/nature10587.

[16] Pavliček, N. *et al.* Atomic Force Microscopy Reveals Bistable Configurations of Dibenzo[a,h]thianthrene and their Interconversion Pathway. *Phys. Rev. Lett.* **108**, 086101 (2012). URL http://link.aps.org/doi/10.1103/PhysRevLett.108.086101.

[17] Planck, M. Ueber das Gesetz der Energieverteilung im Normalspectrum. *Ann. Phys.* **309**, 553–563 (1901). URL http://dx.doi.org/10.1002/andp.19013090310.

[18] Einstein, A. Ueber einen die Erzeugung und Verwandlung des Lichtes betreffenden heuristischen Gesichtspunkt. *Ann. Phys.* **322**, 132–148 (1905). URL http://dx.doi.org/10.1002/andp.19053220607.

[19] Bohr, N. I. On the constitution of atoms and molecules. *Philosophical Magazine* **26**, 1–25 (1913). URL http://dx.doi.org/10.1080/14786441308634955.

[20] Bohr, N. XXXVII. On the constitution of atoms and molecules, Part II. Systems containing only a single nucleus. *Philosophical Magazine* **26**, 476–502 (1913). URL http://dx.doi.org/10.1080/14786441308634993.

[21] De Broglie, L. Recherches sur la théorie des quanta. *Ann. Phys.* **10**, 22–128 (1925). URL https://doi.org/10.1051/anphys/192510030022.

[22] Gerlach, W. & Stern, O. Der experimentelle Nachweis der Richtungsquantelung im Magnetfeld. *Zeitschrift für Physik* **9**, 349–352 (1922). URL https://doi.org/10.1007/BF01326983.

[23] Gerlach, W. & Stern, O. Das magnetische Moment des Silberatoms. *Zeitschrift für Physik* **9**, 353–355 (1922). URL https://doi.org/10.1007/BF01326984.

[24] Gerlach, W. & Stern, O. Der experimentelle Nachweis des magnetischen Moments des Silberatoms. *Zeitschrift für Physik* **8**, 110–111 (1922). URL https://doi.org/10.1007/BF01329580.

[25] Heisenberg, W. Über den anschaulichen Inhalt der quantentheoretischen Kinematik und Mechanik. *Zeitschrift für Physik* **43**, 172–198 (1927). URL https://doi.org/10.1007/BF01397280.

[26] Hund, F. Zur Deutung der Molekelspektren. I. *Zeitschrift für Physik* **40**, 742–764 (1927). URL https://doi.org/10.1007/BF01400234.

[27] Hund, F. Zur Deutung der Molekelspektren. III. *Zeitschrift für Physik* **43**, 805–826 (1927). URL https://doi.org/10.1007/BF01397249.

[28] Gamow, G. Zur Quantentheorie des Atomkernes. *Zeitschrift für Physik* **51**, 204–212 (1928). URL https://doi.org/10.1007/BF01343196.

[29] Giessibl, F. J. Atomic resolution on Si(111)-(7x7) by noncontact atomic force microscopy with a force sensor based on a quartz tuning fork. *Appl. Phys. Lett.* **76**, 1470–1472 (2000). URL http://aip.scitation.org/doi/10.1063/1.126067.

[30] Giessibl, F. J. Advances in atomic force microscopy. *Rev. Mod. Phys.* **75**, 949–983 (2003). URL https://link.aps.org/doi/10.1103/RevModPhys.75.949.

[31] Günther, P., Fischer, U. C. & Dransfeld, K. Scanning near-field acoustic microscopy. *Applied Physics B* **48**, 89–92 (1989). URL https://doi.org/10.1007/BF00694423.

[32] Binnig, G., Rohrer, H., Gerber, C. & Weibel, E. 7x7 Reconstruction on Si(111) Resolved in Real Space. *Phys. Rev. Lett.* **50**, 120–123 (1983). URL https://journals.aps.org/prl/pdf/10.1103/PhysRevLett.50.120.

[33] Feenstra, R. M. & Stroscio, J. A. Tunneling spectroscopy of the gaas(110) surface. *Journal of Vacuum Science & Technology B: Microelectronics Processing and Phenomena* **5**, 923–929 (1987). URL http://avs.scitation.org/doi/abs/10.1116/1.583691.

[34] Becker, R. S., Golovchenko, J. A. & Swartzentruber, B. S. Tunneling images of germanium surface reconstructions and phase boundaries. *Phys. Rev. Lett.* **54**, 2678–2680 (1985). URL https://link.aps.org/doi/10.1103/PhysRevLett.54.2678.

[35] Slough, C. G., McNairy, W. W., Coleman, R. V., Drake, B. & Hansma, P. K. Charge-density waves studied with the use of a scanning tunneling microscope. *Phys. Rev. B* **34**, 994–1005 (1986). URL https://link.aps.org/doi/10.1103/PhysRevB.34.994.

[36] Becker, R. S., Golovchenko, J. A. & Swartzentruber, B. S. Atomic-scale surface modifications using a tunnelling microscope. *Nature* **325**, 419 (1987). URL http://dx.doi.org/10.1038/325419a0http://10.0.4.14/325419a0.

[37] Eigler, D. M. & Schweizer, E. K. Positioning single atoms with a scanning tunnelling microscope. *Nature* **344**, 524–526 (1990). URL http://www.nature.com/doifinder/10.1038/344524a0.

[38] Crommie, M. F., Lutz, C. P. & Eigler, D. M. Imaging standing waves in a two-dimensional electron gas. *Nature* **363**, 524 (1993). URL http://dx.doi.org/10.1038/363524a0.

[39] Bardeen, J. Physical Review Letters. *Phys. Rev. Lett.* **6**, 57–59 (1961). URL https://journals.aps.org/prl/pdf/10.1103/PhysRevLett.6.57.

[40] Tersoff, J. & Hamann, D. R. Theory of the scanning tunneling microscope. *Phys. Rev. B* **31**, 805–813 (1985). URL https://journals.aps.org/prb/pdf/10.1103/PhysRevB.31.805.

[41] Lang, N. 2. Theory of Scanning Tunneling Microscopy . In Wiesendanger, R. & Güntherodt, H.-J. (eds.) *Scanning Tunneling Microscopy III: Theory of STM and Related Scanning Probe Methods*, Surface Sciences, 7 – 21 (Springer, 1996).

[42] Tersoff, J. & Hamann, D. R. Theory and application for the scanning tunneling microscope. *Phys. Rev. Lett.* **50**, 1998 (1983). URL http://journals.aps.org/prl/abstract/10.1103/PhysRevLett.50.1998.

[43] Stoll, E., Baratoff, A., Selloni, A. & Carnevali, P. Current distribution in the scanning vacuum tunnel microscope: a free-electron model. *Journal of Physics C: Solid State Physics* **17**, 3073 (1984). URL http://stacks.iop.org/0022-3719/17/i=17/a=016.

[44] Chen, C. J. Theory of Scanning Tunneling Spectroscopy. *J. Vac. Sci. Technol. a-Vacuum Surfaces Film.* **6**, 319–322 (1988). URL http://avs.scitation.org/doi/pdf/10.1116/1.575444.

[45] Tersoff, J. & Lang, N. 1. Theory of Scanning Tunneling Microscopy. In Stroscio, J. A. & Kaiser, W. J. (eds.) *Scanning Tunneling Microscopy*, vol. 27 of *Methods in Experimental Physics*, 1 – 29 (Academic Press, 1993). URL http://www.sciencedirect.com/science/article/pii/S0076695X0860006X.

[46] Martin, Y., Williams, C. C. & Wickramasinghe, H. K. Atomic force microscope-force mapping and profiling on a sub 100-a scale. *Journal of Applied Physics* **61**, 4723–4729 (1987). URL http://dx.doi.org/10.1063/1.338807.

[47] Albrecht, T. R., Grütter, P., Horne, D. & Rugar, D. Frequency modulation detection using high-q cantilevers for enhanced force microscope sensitivity. *Journal of Applied Physics* **69**, 668–673 (1991). URL http://dx.doi.org/10.1063/1.347347.

[48] García, R. & Pérez, R. Dynamic atomic force microscopy methods. *Surf. Sci. Rep.* **47**, 197–301 (2002). URL http://linkinghub.elsevier.com/retrieve/pii/S0167572902000778.

[49] Ohnesorge, F. & Binnig, G. True atomic resolution by atomic force microscopy through repulsive and attractive forces. *Science* **260**, 1451–1456 (1993). URL http://science.sciencemag.org/content/260/5113/1451.

[50] Giessibl, F. J. Atomic resolution of the silicon (111)-(7x7) surface by atomic force microscopy. *Science* **267**, 68–71 (1995). URL http://science.sciencemag.org/content/267/5194/68.

[51] Ueyama, H., Ohta, M., Sugawara, Y. & Morita, S. Atomically Resolved InP(110) Surface Observed with Noncontact Ultrahigh Vacuum Atomic Force Microscope. *Japanese Journal of Applied Physics* **34**, L1086 (1995). URL http://stacks.iop.org/1347-4065/34/i=8B/a=L1086.

[52] Kitamura, S. & Iwatsuki, M. Observation of silicon surfaces using ultrahigh-vacuum noncontact atomic force microscopy. *Japanese Journal of Applied Physics* **35**, L668 (1996). URL http://stacks.iop.org/1347-4065/35/i=5B/a=L668.

[53] Sugawara, Y. *et al.* True atomic resolution imaging with noncontact atomic force microscopy. *Applied Surface Science* **113-114**, 364 – 370 (1997). URL http://www.sciencedirect.com/science/article/pii/S016943329600877X.

[54] Giessibl, F. J. & Trafas, B. M. Piezoresistive cantilevers utilized for scanning tunneling and scanning force microscope in ultrahigh vacuum. *Review of Scientific Instruments* **65**, 1923–1929 (1994). URL https://doi.org/10.1063/1.1145232.

[55] Bammerlin, M. *et al.* True atomic resolution on the surface of an insulator via ultrahigh vacuum dynamic force microscopy. *Probe Microscopy* **1**, 3 (1997).

[56] Sugawara, Y., Ohta, M., Ueyama, H. & Morita, S. Defect motion on an inp(110) surface observed with noncontact atomic force microscopy. *Science* **270**, 1646–1648 (1995). URL http://science.sciencemag.org/content/270/5242/1646.

[57] Fukui, K.-i., Onishi, H. & Iwasawa, Y. Atom-resolved image of the tio_2(110) surface by noncontact atomic force microscopy. *Phys. Rev. Lett.* **79**, 4202–4205 (1997). URL https://link.aps.org/doi/10.1103/PhysRevLett.79.4202.

[58] Reichling, M. & Barth, C. Scanning force imaging of atomic size defects on the caf_2(111) surface. *Phys. Rev. Lett.* **83**, 768–771 (1999). URL https://link.aps.org/doi/10.1103/PhysRevLett.83.768.

[59] Loppacher, C. *et al.* Phase variation experiments in non-contact dynamic force microscopy using phase locked loop techniques. *Applied Surface Science* **140**, 287 – 292 (1999). URL http://www.sciencedirect.com/science/article/pii/S016943329800542X.

[60] Orisaka, S., Minobe, T., Uchihashi, T., Sugawara, Y. & Morita, S. The atomic resolution imaging of metallic ag(111) surface by noncontact atomic force microscope. *Applied Surface Science* **140**, 243 – 246 (1999). URL http://www.sciencedirect.com/science/article/pii/S0169433298005340.

[61] Loppacher, C. *et al.* Dynamic force microscopy of copper surfaces: Atomic resolution and distance dependence of tip-sample interaction and tunneling current. *Phys. Rev. B* **62**, 16944–16949 (2000). URL https://link.aps.org/doi/10.1103/PhysRevB.62.16944.

[62] Loppacher, C. *et al.* Direct determination of the energy required to operate a single molecule switch. *Phys. Rev. Lett.* **90**, 066107 (2003). URL https://link.aps.org/doi/10.1103/PhysRevLett.90.066107.

[63] Nony, L. *et al.* Cu-tbpp and ptcda molecules on insulating surfaces studied by ultra-high-vacuum non-contact afm. *Nanotechnology* **15**, S91 (2004). URL http://stacks.iop.org/0957-4484/15/i=2/a=019.

[64] Marti, O., Drake, B. & Hansma, P. K. Atomic force microscopy of liquid-covered surfaces: Atomic resolution images. *Applied Physics Letters* **51**, 484–486 (1987). URL https://doi.org/10.1063/1.98374.

[65] Rugar, D. & Hansma, P. Atomic Force Microscopy. *Phys. Today* **43**, 23–30 (1990). URL http://physicstoday.scitation.org/doi/10.1063/1.881238.

[66] Anselmetti, D. *et al.* Attractive-mode imaging of biological materials with dynamic force microscopy. *Nanotechnology* **5**, 87–94 (1994). URL http://dx.doi.org/10.1088/0957-4484/5/2/004.

[67] Möller, C., Allen, M., Elings, V., Engel, A. & Müller, D. J. Tapping-mode atomic force microscopy produces faithful high-resolution images of protein surfaces. *Biophys. J.* **77**, 1150–1158 (1999). URL http://dx.doi.org/10.1016/S0006-3495(99)76966-3.

[68] San Paulo, A. & García, R. High-resolution imaging of antibodies by tapping-mode atomic force microscopy: attractive and repulsive tip-sample interaction regimes. *Biophys. J.* **78**, 1599–1605 (2000). URL http://dx.doi.org/10.1016/S0006-3495(00)76712-9.

[69] Reiter, G. *et al.* Morphologies of diblock copolymer thin films before and after crystallization. *Eur. Phys. J. E* **2**, 319 (2000). URL http://link.springer.com/10.1007/s101890050014.

[70] Gross, L. *et al.* Bond-order discrimination by atomic force microscopy. *Science* **337**, 1326–9 (2012). URL http://dx.doi.org/10.1126/science.1225621.

[71] Hamaker, H. The london—van der waals attraction between spherical particles. *Physica* **4**, 1058 – 1072 (1937). URL http://www.sciencedirect.com/science/article/pii/S0031891437802037.

[72] Israelachvili, J. N. 6 - Van der Waals Forces . In Israelachvili, J. N. (ed.) *Intermolecular and Surface Forces*, 107 – 132 (Academic Press, San Diego, 2011), third edition edn. URL https://www.sciencedirect.com/science/article/pii/B9780123751829100065.

[73] Guggisberg, M. *et al.* Separation of interactions by noncontact force microscopy. *Phys. Rev. B* **61**, 11151–11155 (2000). URL https://link.aps.org/doi/10.1103/PhysRevB.61.11151.

[74] Israelachvili, J. N. 7 - Repulsive Steric Forces, Total Intermolecular Pair Potentials, and Liquid Structure. In Israelachvili, J. N. (ed.) *Intermolecular and Surface Forces*, 133 – 149 (Academic Press, San Diego, 2011), third edition edn. URL https://www.sciencedirect.com/science/article/pii/B9780123751829100077.

[75] Lantz, M. A. *et al.* Quantitative measurement of short-range chemical bonding forces. *Science* **291**, 2580–2583 (2001). URL http://science.sciencemag.org/content/291/5513/2580.

[76] Hudlet, S., Saint Jean, M., Guthmann, C. & Berger, J. Evaluation of the capacitive force between an atomic force microscopy tip and a metallic surface. *The European Physical Journal B - Condensed Matter and Complex Systems* **2**, 5–10 (1998). URL `https://doi.org/10.1007/s100510050219`.

[77] Giessibl, F. J. Forces and frequency shifts in atomic-resolution dynamic-force microscopy. *Phys. Rev. B* **56**, 16010–16015 (1997). URL `https://link.aps.org/doi/10.1103/PhysRevB.56.16010`.

[78] Dürig, U. Relations between interaction force and frequency shift in large-amplitude dynamic force microscopy. *Applied Physics Letters* **75**, 433–435 (1999). URL `https://doi.org/10.1063/1.124399`.

[79] Dürig, U. Extracting interaction forces and complementary observables in dynamic probe microscopy. *Applied Physics Letters* **76**, 1203–1205 (2000). URL `https://doi.org/10.1063/1.125983`.

[80] Hölscher, H. *et al.* Measurement of conservative and dissipative tip-sample interaction forces with a dynamic force microscope using the frequency modulation technique. *Phys. Rev. B* **64**, 075402 (2001). URL `https://link.aps.org/doi/10.1103/PhysRevB.64.075402`.

[81] Custance, O., Oyabu, N. & Sugimoto, Y. *Force Spectroscopy on Semiconductor Surfaces. In: Morita S., Giessibl F., Wiesendanger R. (eds) Noncontact Atomic Force Microscopy*, vol. 2, 31–68 (Springer, Berlin, Heidelberg, 2009). URL `https://link.springer.com/chapter/10.1007/978-3-642-01495-6_3`.

[82] Gotsmann, B., Anczykowski, B., Seidel, C. & Fuchs, H. Determination of tip–sample interaction forces from measured dynamic force spectroscopy curves. *Applied Surface Science* **140**, 314 – 319 (1999). URL `http://www.sciencedirect.com/science/article/pii/S0169433298005479`.

[83] Giessibl, F. J. A direct method to calculate tip-sample forces from frequency shifts in frequency-modulation atomic force microscopy. *Applied Physics Letters* **78**, 123–125 (2001). URL `https://doi.org/10.1063/1.1335546`.

[84] Sader, J. E. & Jarvis, S. P. Accurate formulas for interaction force and energy in frequency modulation force spectroscopy. *Applied Physics Letters* **84**, 1801–1803 (2004). URL `https://doi.org/10.1063/1.1667267`.

[85] Pawlak, R., Kawai, S., Glatzel, T. & Meyer, E. *Single Molecule Force Spectroscopy. In: Morita S., Giessibl F., Meyer E., Wiesendanger R. (eds) Noncontact Atomic Force Microscopy*, vol. 3, 195–222 (Springer, Cham, 2015). URL `https://doi.org/10.1007/978-3-319-15588-3_11`.

[86] Pawlak, R. *et al.* Single-molecule manipulation experiments to explore friction and adhesion. *J. Phys. D. Appl. Phys.* **50**, 113003 (2017). URL `http://stacks.iop.org/0022-3727/50/i=11/a=113003`.

[87] Pawlak, R., Kawai, S., Fremy, S., Glatzel, T. & Meyer, E. Atomic-Scale Mechanical Properties of Orientated C_{60} Molecules Revealed by Noncontact Atomic Force

Microscopy. *ACS Nano* **5**, 6349–6354 (2011). URL http://dx.doi.org/10.1021/nn201462g.

[88] Pawlak, R. *et al.* Directed Rotations of Single Porphyrin Molecules Controlled by Localized Force Spectroscopy. *ACS Nano* **6**, 6318–6324 (2012). URL http://dx.doi.org/10.1021/nn301774d.

[89] Schuler, B. *et al.* Adsorption geometry determination of single molecules by atomic force microscopy. *Phys. Rev. Lett.* **111**, 106103 (2013). URL https://link.aps.org/doi/10.1103/PhysRevLett.111.106103.

[90] Sugimoto, Y. *et al.* Chemical identification of individual surface atoms by atomic force microscopy. *Nature* **446**, 64–67 (2007). URL http://dx.doi.org/10.1038/nature05530.

[91] Kelvin, L. V. contact electricity of metals. *The London, Edinburgh, and Dublin Philosophical Magazine and Journal of Science* **46**, 82–120 (1898). URL https://doi.org/10.1080/14786449808621172.

[92] Sadewasser, S. & Glatzel, T. *Kelvin Probe Force Microscopy* (Springer, 2012). URL http://onlinelibrary.wiley.com/doi/10.1002/cbdv.200490137/abstract.

[93] Kawai, S. *et al.* Obtaining Detailed Structural Information about Supramolecular Systems on Surfaces by Combining High-Resolution Force Microscopy with ab Initio Calculations. *ACS Nano* **7**, 9098–9105 (2013). URL http://dx.doi.org/10.1021/nn403672m.

[94] Schuler, B. *et al.* Contrast formation in kelvin probe force microscopy of single π-conjugated molecules. *Nano Letters* **14**, 3342–3346 (2014). URL http://dx.doi.org/10.1021/nl500805x.

[95] Gross, L. *et al.* Investigating atomic contrast in atomic force microscopy and Kelvin probe force microscopy on ionic systems using functionalized tips. *Phys. Rev. B* **90**, 155455 (2014). URL http://link.aps.org/doi/10.1103/PhysRevB.90.155455.

[96] Bettac, A. *et al.* Qplus: atomic force microscopy on single-crystal insulators with small oscillation amplitudes at 5 k. *Nanotechnology* **20**, 264009 (2009). URL http://stacks.iop.org/0957-4484/20/i=26/a=264009.

[97] Lobo-Checa, J. *et al.* Band formation from coupled quantum dots formed by a nanoporous network on a copper surface. *Science* **325**, 300–3 (2009). URL http://dx.doi.org/10.1126/science.1175141.

[98] Riss, A. *et al.* Imaging and tuning molecular levels at the surface of a gated graphene device. *ACS Nano* **8**, 5395–401 (2014). URL http://dx.doi.org/10.1021/nn501459v.

[99] Bathon, T., Sessi, P., Kokh, K. A., Tereshchenko, O. E. & Bode, M. Systematics of molecular self-assembled networks at topological insulators surfaces. *Nano Letters* **15**, 2442–2447 (2015). URL http://dx.doi.org/10.1021/nl5048434.

[100] Tao, C. *et al.* Spatial resolution of a type II heterojunction in a single bipolar molecule. *Nano Lett.* **9**, 3963–7 (2009). URL http://dx.doi.org/10.1021/nl901860n.

[101] Olsson, F. E., Paavilainen, S., Persson, M., Repp, J. & Meyer, G. Multiple Charge States of Ag Atoms on Ultrathin NaCl Films. *Phys. Rev. Lett.* **98**, 176803 (2007). URL http://link.aps.org/doi/10.1103/PhysRevLett.98.176803.

[102] Pascual, J. I., Lorente, N., Song, Z., Conrad, H. & Rust, H.-P. Selectivity in vibrationally mediated single-molecule chemistry. *Nature* **423**, 525–528 (2003). URL http://www.nature.com/doifinder/10.1038/nature01649.

[103] Swart, I., Sonnleitner, T., Niedenführ, J. & Repp, J. Controlled lateral manipulation of molecules on insulating films by STM. *Nano Lett.* **12**, 1070–1074 (2012). URL http://dx.doi.org/10.1021/nl204322r.

[104] Sonnleitner, T., Swart, I., Pavliček, N., Pöllmann, A. & Repp, J. Molecular symmetry governs surface diffusion. *Phys. Rev. Lett.* **107**, 186103 (2011). URL https://link.aps.org/doi/10.1103/PhysRevLett.107.186103.

[105] Chiang, C.-l., Xu, C., Han, Z. & Ho, W. Real-space imaging of molecular structure and chemical bonding by single-molecule inelastic tunneling probe. *Science* **344**, 885–8 (2014). URL http://dx.doi.org/10.1126/science.1253405.

[106] Vitali, L. *et al.* Portrait of the potential barrier at metal–organic nanocontacts. *Nat. Mater.* **9**, 320 (2010). URL http://dx.doi.org/10.1038/nmat2625http://10.0.4.14/nmat2625.

[107] Heyde, M., Sterrer, M., Rust, H.-P. & Freund, H.-J. Atomic resolution on mgo(001) by atomic force microscopy using a double quartz tuning fork sensor at low-temperature and ultrahigh vacuum. *Applied Physics Letters* **87**, 083104 (2005). URL https://doi.org/10.1063/1.2012523.

[108] Majzik, Z. *et al.* Simultaneous current, force and dissipation measurements on the Si(111) 7×7 surface with an optimized qPlus AFM/STM technique. *Beilstein Journal of Nanotechnology* **3**, 249–259 (2012). URL https://doi.org/10.3762/bjnano.3.28.

[109] Bartels, L., Meyer, G. & Rieder, K.-H. Controlled vertical manipulation of single co molecules with the scanning tunneling microscope: A route to chemical contrast. *Applied Physics Letters* **71**, 213–215 (1997). URL https://doi.org/10.1063/1.119503.

[110] Bartels, L. *et al.* Dynamics of electron-induced manipulation of individual co molecules on cu(111). *Phys. Rev. Lett.* **80**, 2004–2007 (1998). URL https://link.aps.org/doi/10.1103/PhysRevLett.80.2004.

[111] Lee, H. J. & Ho, W. Single-bond formation and characterization with a scanning tunneling microscope. *Science* **286**, 1719–1722 (1999). URL http://science.sciencemag.org/content/286/5445/1719.

[112] Hinaut, A., Pawlak, R., Meyer, E. & Glatzel, T. Electrospray deposition of organic molecules on bulk insulator surfaces. *Beilstein J. Nanotechnol.* **6**, 1927–1934 (2015). URL https://doi.org/10.3762/bjnano.6.195.

[113] Fenn, J., Mann, M., Meng, C., Wong, S. & Whitehouse, C. Electrospray ionization for mass spectrometry of large biomolecules. *Science* **246**, 64–71 (1989). URL http://science.sciencemag.org/content/246/4926/64.

[114] Fenn, J. B. Ion formation from charged droplets: roles of geometry, energy, and time. *Journal of the American Society for Mass Spectrometry* **4**, 524 – 535 (1993). URL http://www.sciencedirect.com/science/article/pii/1044030593850140.

[115] Bergkamp, J. J., Decurtins, S. & Liu, S.-X. Current advances in fused tetrathiafulvalene donor-acceptor systems. *Chem. Soc. Rev.* **44**, 863–74 (2015). URL https://doi.org/10.1039/c4cs00255e.

[116] Dupont, N. *et al.* A donor-acceptor tetrathiafulvalene ligand complexed to iron(II): synthesis, electrochemistry, and spectroscopy of [Fe(phen)2(TTF-dppz)](PF6)2. *Inorg. Chem.* **52**, 306–12 (2013). URL http://dx.doi.org/10.1021/ic3019277.

[117] Grill, L. *et al.* Nano-architectures by covalent assembly of molecular building blocks. *Nat. Nanotechnol.* **2**, 687–91 (2007). URL http://www.ncbi.nlm.nih.gov/pubmed/18654406.

[118] Okamoto, T. *et al.* V-shaped organic semiconductors with solution processability, high mobility, and high thermal durability. *Adv. Mater.* **25**, 6392–6397 (2013). URL http://dx.doi.org/10.1002/adma.201302086.

[119] Ullmann, F. & Bielecki, J. Ueber synthesen in der biphenylreihe. *Berichte der deutschen chemischen Gesellschaft* **34**, 2174–2185 (1901). URL http://dx.doi.org/10.1002/cber.190103402141.

[120] Hla, S.-W., Bartels, L., Meyer, G. & Rieder, K.-H. Inducing All Steps of a Chemical Reaction with the Scanning Tunneling Microscope Tip: Towards Single Molecule Engineering. *Phys. Rev. Lett.* **85**, 2777–2780 (2000). URL http://dx.doi.org/10.1103/PhysRevLett.85.2777.

[121] McCarty, G. S. & Weiss, P. S. Formation and manipulation of protopolymer chains. *J. Am. Chem. Soc.* **126**, 16772–16776 (2004). URL http://dx.doi.org/10.1021/ja038930g.

[122] Lipton-Duffin, J. A., Ivasenko, O., Perepichka, D. F. & Rosei, F. Synthesis of polyphenylene molecular wires by surface-confined polymerization. *Small* **5**, 592–597 (2009). URL http://dx.doi.org/10.1002/smll.200801943.

[123] Eichhorn, J. *et al.* On-surface ullmann coupling: The influence of kinetic reaction parameters on the morphology and quality of covalent networks. *ACS Nano* **8**, 7880–7889 (2014). URL http://dx.doi.org/10.1021/nn501567p.

[124] Gutzler, R. *et al.* Ullmann-type coupling of brominated tetrathienoanthracene on copper and silver. *Nanoscale* **6**, 2660–2668 (2014). URL http://dx.doi.org/10.1039/C3NR05710K.

[125] Chen, M. *et al.* Combined photoemission and scanning tunneling microscopy study of the surface-assisted ullmann coupling reaction. *The Journal of Physical Chemistry C* **118**, 6820–6830 (2014). URL http://dx.doi.org/10.1021/jp4121468.

[126] Koch, M., Gille, M., Viertel, A., Hecht, S. & Grill, L. Substrate-controlled linking of molecular building blocks: Au(111) vs. cu(111). *Surface Science* **627**, 70 – 74 (2014). URL http://www.sciencedirect.com/science/article/pii/S0039602814001113.

[127] Tahara, K. *et al.* Control and induction of surface-confined homochiral porous molecular networks. *Nat. Chem.* **3**, 714–719 (2011). URL http://www.nature.com/doifinder/10.1038/nchem.1111.

[128] Bradshaw, J. D., Solooki, D., Tessier, C. A. & Youngs, W. J. Lithium-Induced Cyclization of Tetrabenzocyclyne. A Novel Zipper Reaction of Cyclic o-Ethynylbenzenes. *Journal of the American Chemical Society* **116**, 3177–3179 (1994). URL http://dx.doi.org/10.1021/ja00087a001.

[129] Kawai, S. *et al.* Competing Annulene and Radialene Structures in a Single Anti-Aromatic Molecule Studied by High-Resolution Atomic Force Microscopy. *ACS Nano* **11**, 8122–8130 (2017). URL http://pubs.acs.org/doi/pdf/10.1021/acsnano.7b02973.

[130] Kubo, T. *et al.* A facile synthesis of trinaphtho[3.3.3]propellane and its [small pi]-extension and the formation of a two-dimensional honeycomb molecular assembly. *Chem. Commun.* **51**, 3801–3803 (2015). URL http://dx.doi.org/10.1039/C4CC09883H.

[131] Samorí, P., Simpson, C. D., Müllen, K. & Rabe, J. P. Ordered monolayers of nanographitic sheets processed from solutions via oxidative cyclodehydrogenation. *Langmuir* **18**, 4183–4185 (2002). URL http://dx.doi.org/10.1021/la015760h.

[132] Tahara, K. *et al.* Two-dimensional porous molecular networks of dehydrobenzo[12]annulene derivatives via alkyl chain interdigitation. *Journal of the American Chemical Society* **128**, 16613–16625 (2006). URL http://dx.doi.org/10.1021/ja0655441.

[133] De Feyter, S. & De Schryver, F. C. Two-dimensional supramolecular self-assembly probed by scanning tunneling microscopy. *Chem. Soc. Rev.* **32**, 139–150 (2003). URL http://xlink.rsc.org/?DOI=b206566p.

[134] Marie, C., Silly, F., Tortech, L., Müllen, K. & Fichou, D. Tuning the packing density of 2d supramolecular self-assemblies at the solid-liquid interface using variable temperature. *ACS Nano* **4**, 1288–1292 (2010). URL http://dx.doi.org/10.1021/nn901717k.

[135] Constable, E. C., Housecroft, C. E., Price, J. R. & Zampese, J. A. When five are six: the myth of five-coordinate copper(II) in supramolecular chemistry. *CrystEngComm* **12**, 3163–3171 (2010). URL http://dx.doi.org/10.1039/C0CE00019A.

[136] Bozic-Weber, B., Constable, E. C. & Housecroft, C. E. Light harvesting with earth abundant d-block metals: Development of sensitizers in dye-sensitized solar cells (dscs). *Coordination Chemistry Reviews* **257**, 3089 – 3106 (2013). URL http://www.sciencedirect.com/science/article/pii/S0010854513001331.

[137] Kawai, S. *et al.* Quantifying the atomic-level mechanics of single long physisorbed molecular chains. *Proc. Natl. Acad. Sci.* **111**, 3968–3972 (2014). URL http://www.pnas.org/cgi/doi/10.1073/pnas.1319938111.

[138] Morteani, A. C., Friend, R. H. & Silva, C. Exciton trapping at heterojunctions in polymer blends. *The Journal of Chemical Physics* **122**, 244906 (2005). URL https://doi.org/10.1063/1.1924504.

[139] Deibel, C., Strobel, T. & Dyakonov, V. Role of the charge transfer state in organic donor–acceptor solar cells. *Advanced Materials* **22**, 4097–4111 (2010). URL http://dx.doi.org/10.1002/adma.201000376.

[140] Hoppe, H. & Sariciftci, N. S. Organic solar cells: An overview. *Journal of Materials Research* **19**, 1924–1945 (2011). URL http://www.journals.cambridge.org/abstract{_}S0884291400094498.

[141] Faist, M. a. *et al.* Competition between the charge transfer state and the singlet states of donor or acceptor limiting the efficiency in polymer:fullerene solar cells. *Journal of the American Chemical Society* **134**, 685–92 (2012). URL http://dx.doi.org/10.1021/ja210029w.

[142] Clarke, T. M. & Durrant, J. R. Charge photogeneration in organic solar cells. *Chemical Reviews* **110**, 6736–6767 (2010). URL http://dx.doi.org/10.1021/cr900271s.

[143] Bernardo, B. *et al.* Delocalization and dielectric screening of charge transfer states in organic photovoltaic cells. *Nature communications* **5**, 3245 (2014). URL http://dx.doi.org/10.1038/ncomms4245.

[144] Jia, C. *et al.* An experimental and computational study on intramolecular charge transfer: a tetrathiafulvalene-fused dipyridophenazine molecule. *Chem. Eur. J.* **13**, 3804–12 (2007). URL http://dx.doi.org/10.1002/chem.200601561.

[145] Meier, T. *et al.* Donor-acceptor properties of a single-molecule altered by on-surface complex formation. *ACS Nano* **11**, 8413–8420 (2017). URL http://dx.doi.org/10.1021/acsnano.7b03954.

[146] Brunetti, F. G., López, J. L., Atienza, C. & Martín, N. π-Extended TTF: a versatile molecule for organic electronics. *Journal of Materials Chemistry* **22**, 4188 (2012). URL http://xlink.rsc.org/?DOI=c2jm15710a.

[147] Goze, C. *et al.* Fused Donor–Acceptor Ligands in RuII Chemistry: Synthesis, Electrochemistry and Spectroscopy of [Ru(bpy)3-n(TTF-dppz)n](PF6)2. *ChemPhysChem* **8**, 1504–1512 (2007). URL http://doi.wiley.com/10.1002/cphc.200700066.

[148] Amacher, A. *et al.* A quinoxaline-fused tetrathiafulvalene-based sensitizer for efficient dye-sensitized solar cells. *Chem. Commun. (Camb).* **50**, 6540–2 (2014). URL http://dx.doi.org/10.1039/c4cc02696a.

[149] Metzger, R. M. Unimolecular electrical rectifiers. *Chem. Rev.* **103**, 3803–34 (2003). URL http://dx.doi.org/10.1021/cr020413d.

[150] Lörtscher, E. *et al.* Transport properties of a single-molecule diode. *ACS Nano* **6**, 4931–4939 (2012). URL http://dx.doi.org/10.1021/nn300438h.

[151] Yella, A. *et al.* Porphyrin-sensitized solar cells with cobalt (ii/iii)–based redox electrolyte exceed 12 percent efficiency. *Science* **334**, 629–634 (2011). URL http://science.sciencemag.org/content/334/6056/629.

[152] Jöhr, R. *et al.* Thermally induced anchoring of a zinc-carboxyphenylporphyrin on rutile tio2 (110). *The Journal of Chemical Physics* **146**, 184704 (2017). URL https://doi.org/10.1063/1.4982936.

[153] Yokoyama, T., Yokoyama, S., Kamikado, T., Okuno, Y. & Mashiko, S. Selective assembly on a surface of supramolecular aggregates with controlled size and shape. *Nature* **413**, 619–621 (2001). URL http://dx.doi.org/10.1038/35098059.

[154] Theobald, J. A., Oxtoby, N. S., Phillips, M. A., Champness, N. R. & Beton, P. H. Controlling molecular deposition and layer structure with supramolecular surface assemblies. *Nature* **424**, 1029–1031 (2003). URL http://dx.doi.org/10.1038/nature01915.

[155] Yokoyama, T., Kamikado, T., Yokoyama, S. & Mashiko, S. Conformation selective assembly of carboxyphenyl substituted porphyrins on Au (111). *J. Chem. Phys.* **121**, 11993–11997 (2004). URL http://dx.doi.org/10.1063/1.1819877.

[156] Jung, T. A., Schlittler, R. R. & Gimzewski, J. K. Conformational identification of individual adsorbed molecules with the STM. *Nature* **386**, 696–698 (1997). URL http://dx.doi.org/10.1038/386696a0.

[157] Stöhr, M. *et al.* Controlling molecular assembly in two dimensions: The concentration dependence of thermally induced 2D aggregation of molecules on a metal surface. *Angew. Chemie - Int. Ed.* **44**, 7394–7398 (2005). URL http://dx.doi.org/10.1002/anie.200502316.

[158] Lin, N., Dmitriev, A., Weckesser, J., Barth, J. V. & Kern, K. Real-time single-molecule imaging of the formation and dynamics of coordination compounds. *Angew. Chemie - Int. Ed.* **41**, 4779–4783 (2002). URL http://dx.doi.org/10.1002/anie.200290046.

[159] Dmitriev, A., Spillmann, H., Lin, N., Barth, J. V. & Kern, K. Modular assembly of two-dimensional metal-organic coordination networks at a metal surface. *Angew. Chemie - Int. Ed.* **42**, 2670–2673 (2003). URL http://dx.doi.org/10.1002/anie.200250610.

[160] Stepanow, S. *et al.* Steering molecular organization and host-guest interactions using two-dimensional nanoporous coordination systems. *Nat. Mater.* **3**, 229–233 (2004). URL http://www.nature.com/doifinder/10.1038/nmat1088.

[161] Pawin, G., Wong, K. L., Kwon, K.-Y. & Bartels, L. A homomolecular porous network at a cu(111) surface. *Science* **313**, 961–962 (2006). URL http://science.sciencemag.org/content/313/5789/961.

[162] Spillmann, H. *et al.* A two-dimensional porphyrin-based porous network featuring communicating cavities for the templated complexation of fullerenes. *Adv. Mater.* **18**, 275–279 (2006). URL http://dx.doi.org/10.1002/adma.200501734.

[163] Stöhr, M., Wahl, M., Spillmann, H., Gade, L. H. & Jung, T. A. Lateral manipulation for the positioning of molecular guests within the confinements of a highly stable self-assembled organic surface network. *Small* **3**, 1336–1340 (2007). URL http://dx.doi.org/10.1002/smll.200700099.

[164] Zwaneveld, N. A. *et al.* Organized formation of 2D extended covalent organic frameworks at surfaces. *J. Am. Chem. Soc.* **130**, 6678–6679 (2008). URL http://dx.doi.org/10.1021/ja800906f.

[165] Hoffmann, R., Kantorovich, L. N., Baratoff, A., Hug, H. J. & Güntherodt, H. J. Sublattice identification in scanning force microscopy on alkali halide surfaces. *Phys. Rev. Lett.* **92** (2004). URL http://dx.doi.org/10.1103/PhysRevLett.92.146103.

[166] Pohl, D. W. & Möller, R. "Tracking" tunneling microscopy. *Review of Scientific Instruments* **59**, 840–842 (1988). URL https://doi.org/10.1063/1.1139790.

[167] Abe, M., Sugimoto, Y., Custance, O. & Morita, S. Room-temperature reproducible spatial force spectroscopy using atom-tracking technique. *Applied Physics Letters* **87**, 173503 (2005). URL https://doi.org/10.1063/1.2108112.

[168] Setvín, M. *et al.* Chemical identification of single atoms in heterogeneous III-IV chains on Si(100) surface by means of nc-AFM and DFT calculations. *ACS Nano* **6**, 6969–6976 (2012). URL http://dx.doi.org/10.1021/nn301996k.

[169] Ashino, M., Schwarz, A., Behnke, T. & Wiesendanger, R. Atomic-Resolution Dynamic Force Microscopy and Spectroscopy of a Single-Walled Carbon Nanotube: Characterization of Interatomic van der Waals Forces. *Phys. Rev. Lett.* **93**, 136101 (2004). URL https://link.aps.org/doi/10.1103/PhysRevLett.93.136101.

[170] Ternes, M. *et al.* Interplay of conductance, force, and structural change in metallic point contacts. *Phys. Rev. Lett.* **106**, 016802 (2011). URL https://link.aps.org/doi/10.1103/PhysRevLett.106.016802.

[171] Albers, B. J. *et al.* Three-dimensional imaging of short-range chemical forces with picometre resolution. *Nat. Nanotechnol.* **4**, 307 (2009). URL http://dx.doi.org/10.1038/nnano.2009.57.

[172] Kawai, S. *et al.* Van der Waals interactions and the limits of isolated atom models at interfaces. *Nat. Commun.* **7**, 11559 (2016). URL https://www.nature.com/articles/ncomms11559.pdf.

[173] Kawai, S. *et al.* Organometallic Bonding in an Ullmann-Type On-Surface Chemical Reaction Studied by High-Resolution Atomic Force Microscopy. *Small* **12**, 5303–5311 (2016). URL http://onlinelibrary.wiley.com/doi/10.1002/smll.201601216/pdf.

[174] Lafferentz, L. *et al.* Conductance of a single conjugated polymer as a continuous function of its length. *Science* **323**, 1193–1197 (2009). URL http://science.sciencemag.org/content/323/5918/1193.

[175] Cai, J. *et al.* Atomically precise bottom-up fabrication of graphene nanoribbons. *Nature* **466**, 470–473 (2010). URL http://www.nature.com/doifinder/10.1038/nature09211.

[176] Hämäläinen, S. K. *et al.* Intermolecular contrast in atomic force microscopy images without intermolecular bonds. *Phys. Rev. Lett.* **113**, 186102 (2014). URL https://link.aps.org/doi/10.1103/PhysRevLett.113.186102.

[177] Eichhorn, J. *et al.* On-surface ullmann polymerization via intermediate organometallic networks on ag(111). *Chem. Commun.* **50**, 7680–7682 (2014). URL http://dx.doi.org/10.1039/C4CC02757D.

[178] Boneschanscher, M. P., Hämäläinen, S. K., Liljeroth, P. & Swart, I. Sample corrugation affects the apparent bond lengths in atomic force microscopy. *ACS Nano* **8**, 3006–3014 (2014). URL http://dx.doi.org/10.1021/nn500317r.

[179] Hinaut, A. *et al.* Electrospray deposition of structurally complex molecules revealed by atomic force microscopy. *Nanoscale* **10**, 1337–1344 (2018). URL http://dx.doi.org/10.1039/C7NR06261C.

[180] Hauptmann, N. *et al.* Surface control of alkyl chain conformations and 2D chiral amplification. *J. Am. Chem. Soc.* **135**, 8814–8817 (2013). URL http://dx.doi.org/10.1021/ja4036187.

[181] Mali, K. S., Adisoejoso, J., Ghijsens, E., De Cat, I. & De Feyter, S. Exploring the complexity of supramolecular interactions for patterning at the liquid-solid interface. *Acc. Chem. Res.* **45**, 1309–1320 (2012). URL http://dx.doi.org/10.1021/ar200342u.

[182] Shi, D. *et al.* Role of lateral alkyl chains in modulation of molecular structures on metal surfaces. *Phys. Rev. Lett.* **96**, 226101 (2006). URL http://dx.doi.org/10.1103/Physrevlett.96.226101.

[183] Schuler, B. *et al.* Characterizing aliphatic moieties in hydrocarbons with atomic force microscopy. *Chem. Sci.* **8**, 2315–2320 (2017). URL http://xlink.rsc.org/?DOI=C6SC04698C.

[184] Tahara, K., Lei, S., Adisoejoso, J., De Feyter, S. & Tobe, Y. Supramolecular surface-confined architectures created by self-assembly of triangular phenylene-ethynylene macrocycles via van der Waals interaction. *Chem. Commun.* **46**, 8507 (2010). URL http://xlink.rsc.org/?DOI=c0cc02780d.

[185] Swarbrick, J. C., Taylor, J. B. & O'Shea, J. N. Electrospray deposition in vacuum. *Appl. Surf. Sci.* **252**, 5622–5626 (2006). URL http://dx.doi.org/10.1016/j.apsusc.2005.12.025.

[186] Molecularspray Ltd. Molecularspray. http://www.molecularspray.co.uk/ (2017-07-10).

[187] Satterley, C. J. *et al.* Electrospray deposition of fullerenes in ultra-high vacuum: in situ scanning tunneling microscopy and photoemission spectroscopy. *Nanotechnology* **18**, 455304 (2007). URL http://dx.doi.org/10.1088/0957-4484/18/45/455304.

[188] Saywell, A. *et al.* Electrospray deposition of C60 on a hydrogen-bonded supramolecular network. *J. Phys. Chem. C* **112**, 7706–7709 (2008). URL http://dx.doi.org/10.1021/jp7119944.

[189] Erler, P. *et al.* Highly Ordered Surface Self-Assembly of Fe4 Single Molecule Magnets. *Nano Lett.* **15**, 4546–4552 (2015). URL http://dx.doi.org/10.1021/acs.nanolett.5b01120.

[190] Bodin, A. *et al.* An energy-filtering device coupled to a quadrupole mass spectrometer for soft-landing molecular ions on surfaces with controlled energy. *Review of Scientific Instruments* **84**, 095104 (2013). URL https://doi.org/10.1063/1.4818961.

[191] Rauschenbach, S. *et al.* Two-Dimensional Folding of Polypeptides into Molecular Nanostructures at Surfaces. *ACS Nano* **11**, 2420–2427 (2017). URL http://dx.doi.org/10.1021/acsnano.6b06145.

[192] Hamann, C. *et al.* Ultrahigh vacuum deposition of organic molecules by electrospray ionization. *Rev. Sci. Instrum.* **82**, 033903 (2011). URL http://aip.scitation.org/doi/10.1063/1.3553010.

[193] Glowatzki, H. *et al.* Hexa-pm-hexabenzocoronene on Ag(111): Monolayer/multilayer transition of molecular orientation and electronic structure. *J. Phys. Chem. C* **112**, 1570–1574 (2008). URL http://dx.doi.org/10.1021/jp0774894.

[194] Weigelt, S. *et al.* Chiral switching by spontaneous conformational change in adsorbed organic molecules. *Nat. Mater.* **5**, 112–117 (2006). URL http://www.nature.com/doifinder/10.1038/nmat1558.

[195] Kawai, S. *et al.* Direct quantitative measurement of the C=O...H–C bond by atomic force microscopy. *Science Advances* **3** (2017). URL http://advances.sciencemag.org/content/3/5/e1603258.

[196] Moll, N., Gross, L., Mohn, F., Curioni, A. & Meyer, G. The mechanisms underlying the enhanced resolution of atomic force microscopy with functionalized tips. *New Journal of Physics* **12**, 125020 (2010). URL http://stacks.iop.org/1367-2630/12/i=12/a=125020.

[197] Kollman, P. A. & Allen, L. C. The theory of the Hydrogen Bond. *Chemical Reviews* **72**, 283–303 (1972). URL http://pubs.acs.org/doi/pdf/10.1021/cr60277a004.

[198] Veljković, D. v., Janjić, G. V. & Zarić, S. D. Are C–H...O interactions linear? The case of aromatic CH donors. *CrystEngComm* **13**, 5005–5010 (2011). URL http://pubs.rsc.org/en/content/articlepdf/2011/CE/C1CE05065F.

[199] Hartman, A. & Hirshfeld, F. L. Structure of cis -1 2,3-tricyanocyclopropane. *Acta Crystallogr.* **20**, 80–82 (1966). URL http://scripts.iucr.org/cgi-bin/paper?S0365110X66000148.

[200] Lothrop, W. C. Biphenylene. *J. Am. Chem. Soc.* **63**, 1187–1191 (1941). URL http://pubs.acs.org/doi/pdf/10.1021/ja01850a007.

[201] Hine, J., Ahn, K., Gallucci, J. C. & Linden, S. M. Structures of double-hydrogen-bonded adducts of 1,8-biphenylenediol and related compounds. *Acta Crystallogr. Sect. C Cryst. Struct. Commun.* **46**, 2136–2146 (1990). URL http://scripts.iucr.org/cgi-bin/paper?S0108270190000890.

[202] Ferrara, J. D., Solooki, D., Tessier-Youngs, C. & Youngs, W. J. Structure of benzo[b]biphenylene. *Acta Crystallogr. Sect. C Cryst. Struct. Commun.* **45**, 57–60 (1989). URL http://scripts.iucr.org/cgi-bin/paper?S0108270188008765.

[203] Bowen Jones, J., Brown, D. S., Hales, K. A. & Massey, A. G. Structure of octamethylbiphenylene. *Acta Crystallogr. Sect. C Cryst. Struct. Commun.* **44**, 1757–1759 (1988). URL http://scripts.iucr.org/cgi-bin/paper?S0108270188006328.

[204] Weymouth, A. J., Hofmann, T. & Giessibl, F. J. Quantifying molecular stiffness and interaction with lateral force microscopy. *Science* **343**, 1120–1122 (2014). URL http://science.sciencemag.org/content/343/6175/1120.

[205] Kawai, S. *et al.* Thermal control of sequential on-surface transformation of a hydrocarbon molecule on a copper surface. *Nat. Commun.* **7**, 12711 (2016). URL http://dx.doi.org/10.1038/ncomms12711.

[206] Bieri, M. *et al.* Two-dimensional polymer formation on surfaces: Insight into the roles of precursor mobility and reactivity. *J. Am. Chem. Soc.* **132**, 16669–16676 (2010). URL http://dx.doi.org/10.1021/ja107947z.

[207] Fix, A. G., Chase, D. T. & Haley, M. M. Indenofluorenes and derivatives: Syntheses and emerging materials applications. *Top. Curr. Chem.* **349**, 159–196 (2014). URL http://dx.doi.org/10.1007/128_2012_376.

[208] Pawlak, R. *et al.* Probing atomic structure and Majorana wavefunctions in mono-atomic Fe chains on superconducting Pb surface. *npj Quantum Inf.* **2**, 16035 (2016). URL http://www.nature.com/articles/npjqi201635.

[209] Emmrich, M. *et al.* Subatomic resolution force microscopy reveals internal structure and adsorption sites of small iron clusters. *Science* (2015). URL http://science.sciencemag.org/content/early/2015/03/18/science.aaa5329.

[210] Nadj-Perge, S. *et al.* Observation of majorana fermions in ferromagnetic atomic chains on a superconductor. *Science* **346**, 602–607 (2014). URL http://science.sciencemag.org/content/346/6209/602.

[211] Majorana, E. Teoria simmetrica dell'elettrone e del positrone. *Il Nuovo Cimento (1924-1942)* **14**, 171 (2008). URL https://doi.org/10.1007/BF02961314.

[212] Kitaev, A. Unpaired Majorana fermions in quantum wires. *Phys.-Usp* **44**, 131 (2001). URL http://dx.doi.org/10.1070/1063-7869/44/10S/S29.

[213] Alicea, J. New directions in the pursuit of Majorana fermions in solid state systems. *Rep. Prog. Phys.* **75**, 076501 (2012). URL http://dx.doi.org/10.1088/0034-4885/75/7/076501.

[214] Sato, M., Takahashi, Y. & Fujimoto, S. Non-abelian topological orders and majorana fermions in spin-singlet superconductors. *Phys. Rev. B* **82**, 134521 (2010). URL https://link.aps.org/doi/10.1103/PhysRevB.82.134521.

[215] Oreg, Y., Refael, G. & von Oppen, F. Helical liquids and majorana bound states in quantum wires. *Phys. Rev. Lett.* **105**, 177002 (2010). URL https://link.aps.org/doi/10.1103/PhysRevLett.105.177002.

[216] Lutchyn, R. M., Sau, J. D. & Das Sarma, S. Majorana fermions and a topological phase transition in semiconductor-superconductor heterostructures. *Phys. Rev. Lett.* **105**, 077001 (2010). URL https://link.aps.org/doi/10.1103/PhysRevLett.105.077001.

[217] Nadj-Perge, S., Drozdov, I. K., Bernevig, B. A. & Yazdani, A. Proposal for realizing majorana fermions in chains of magnetic atoms on a superconductor. *Phys. Rev. B* **88**, 020407 (2013). URL https://link.aps.org/doi/10.1103/PhysRevB.88.020407.

[218] Pientka, F., Glazman, L. I. & von Oppen, F. Topological superconducting phase in helical shiba chains. *Phys. Rev. B* **88**, 155420 (2013). URL https://link.aps.org/doi/10.1103/PhysRevB.88.155420.

[219] Mourik, V. *et al.* Signatures of majorana fermions in hybrid superconductor-semiconductor nanowire devices. *Science* **336**, 1003–1007 (2012). URL http://science.sciencemag.org/content/336/6084/1003.

[220] Deng, M. T. *et al.* Anomalous zero-bias conductance peak in a nb–insb nanowire–nb hybrid device. *Nano Letters* **12**, 6414–6419 (2012). URL http://dx.doi.org/10.1021/nl303758w.

[221] Das, A. *et al.* Zero-bias peaks and splitting in an Al–InAs nanowire topological superconductor as a signature of Majorana fermions. *Nat. Phys.* **8**, 887–895 (2012). URL http://www.nature.com/doifinder/10.1038/nphys2479.

[222] Churchill, H. O. H. *et al.* Superconductor-nanowire devices from tunneling to the multichannel regime: Zero-bias oscillations and magnetoconductance crossover. *Phys. Rev. B* **87**, 241401 (2013). URL https://link.aps.org/doi/10.1103/PhysRevB.87.241401.

[223] Ruby, M. *et al.* End states and subgap structure in proximity-coupled chains of magnetic adatoms. *Phys. Rev. Lett.* **115**, 197204 (2015). URL https://link.aps.org/doi/10.1103/PhysRevLett.115.197204.

[224] Pawlak, R. *et al.* Design and Characterization of an Electrically Powered Single Molecule on Gold. *ACS Nano* **11**, 9930–9940 (2017). URL http://dx.doi.org/10.1021/acsnano.7b03955.

[225] Eigler, D. M. & Schweizer, E. K. Positioning single atoms with a scanning tunnelling microscope. *Nature* **344**, 524–526 (1990). URL http://www.nature.com/doifinder/10.1038/344524a0.

[226] Hla, S.-W., Braun, K.-F. & Rieder, K.-H. Single-atom manipulation mechanisms during a quantum corral construction. *Phys. Rev. B* **67**, 201402 (2003). URL https://link.aps.org/doi/10.1103/PhysRevB.67.201402.

[227] Jung, T. A., Schlittler, R. R., Gimzewski, J. K., Tang, H. & Joachim, C. Controlled Room-Temperature Positioning of Individual Molecules: Molecular Flexure and Motion. *Science (80-.).* **271**, 181–184 (1996). URL http://www.sciencemag.org/cgi/doi/10.1126/science.271.5246.181.

[228] Moresco, F. *et al.* Recording intramolecular mechanics during the manipulation of a large molecule. *Phys. Rev. Lett.* **87**, 883021–883024 (2001). URL http://dx.doi.org/10.1103/PhysRevLett.87.088302.

[229] Castelvecchi, D. Drivers gear up for world's first nanocar race. *Nature* **544**, 278–279 (2017). URL http://dx.doi.org/10.1038/544278a.

[230] Rapenne, G. & Joachim, C. The first nanocar race. *Nat. Rev. Mater.* **2**, 17040 (2017). URL http://dx.doi.org/10.1038/natrevmats.2017.40.

[231] Stipe, B. C., Rezaei, M. a. & Ho, W. Coupling of Vibrational Excitation to the Rotational Motion of a Single Adsorbed Molecule. *Phys. Rev. Lett.* **81**, 1263–1266 (1998). URL http://dx.doi.org/10.1103/PhysRevLett.81.1263.

[232] Stipe, B. C., Rezaei, M. A. & Ho, W. Inducing and Viewing the Rotational Motion of a Single Molecule. *Science (80-.).* **279**, 1907–1909 (1998). URL http://dx.doi.org/10.1126/science.279.5358.1907.

[233] Hla, S.-W., Bartels, L., Meyer, G. & Rieder, K.-H. Inducing All Steps of a Chemical Reaction with the Scanning Tunneling Microscope Tip: Towards Single Molecule Engineering. *Phys. Rev. Lett.* **85**, 2777–2780 (2000). URL http://dx.doi.org/10.1103/PhysRevLett.85.2777.

[234] Harikumar, K. R. *et al.* Directed long-range molecular migration energized by surface reaction. *Nat. Chem.* **3**, 400–408 (2011). URL http://dx.doi.org/10.1038/nchem.1029.

[235] Pavliček, N. *et al.* On-surface generation and imaging of arynes by atomic force microscopy. *Nat. Chem.* **7**, 623–8 (2015). URL http://dx.doi.org/10.1038/nchem.2300.

[236] Schuler, B. *et al.* Reversible Bergman cyclization by atomic manipulation. *Nat. Chem.* **8**, 220–4 (2016). URL http://dx.doi.org/10.1038/nchem.2438.

[237] Ohara, M., Kim, Y. & Kawai, M. Electric field response of a vibrationally excited molecule in an STM junction. *Phys. Rev. B - Condens. Matter Mater. Phys.* **78** (2008). URL http://dx.doi.org/10.1103/PhysRevB.78.201405.

[238] Repp, J. *et al.* Charge-State-Dependent Diffusion of Individual Gold Adatoms on Ionic Thin NaCl Films. *Phys. Rev. Lett.* **117**, 146102 (2016). URL https://link.aps.org/doi/10.1103/PhysRevLett.117.146102.

[239] Echeverria, J., Monturet, S. & Joachim, C. One-way rotation of a molecule-rotor driven by a shot noise. *Nanoscale* **6**, 2793–9 (2014). URL http://dx.doi.org/10.1039/c3nr05814j.

[240] Nickel, A. *et al.* Moving nanostructures: Pulse-induced positioning of supramolecular assemblies. *ACS Nano* **7**, 191–197 (2013). URL http://dx.doi.org/10.1021/nn303708h.

[241] Ohmann, R. *et al.* Supramolecular Rotor and Translator at Work: On-Surface Movement of Single Atoms. *ACS Nano* **9**, 8394–8400 (2015). URL http://dx.doi.org/10.1021/acsnano.5b03131.

[242] Eisenhut, Frank, Durand, Corentin, Moresco, Francesca, Launay, Jean-Pierre & Joachim, Christian. Training for the 1st international nano-car race: the dresden molecule-vehicle. *Eur. Phys. J. Appl. Phys.* **76**, 10001 (2016). URL https://doi.org/10.1051/epjap/2016160259.

[243] Shirai, Y. *et al.* Surface-rolling molecules. *Journal of the American Chemical Society* **128**, 4854–4864 (2006). URL http://dx.doi.org/10.1021/ja058514r.

[244] Grill, L. *et al.* Rolling a single molecular wheel at the atomic scale. *Nature Nanotechnology* **2**, 95 (2007). URL http://dx.doi.org/10.1038/nnano.2006.210http://10.0.4.14/nnano.2006.210.

[245] Grillo, F., Früchtl, H., Francis, S. M. & Richardson, N. V. Site selectivity in the growth of copper islands on au (111). *New Journal of Physics* **13**, 013044 (2011). URL http://stacks.iop.org/1367-2630/13/i=1/a=013044.

[246] Cheng, Z. H. *et al.* Adsorption behavior of iron phthalocyanine on Au(111) surface at submonolayer coverage. *J. Phys. Chem. C* **111**, 9240–9244 (2007). URL http://dx.doi.org/10.1021/jp070388l.

[247] Kocić, N. *et al.* Control of reactivity and regioselectivity for on-surface dehydrogenative aryl-aryl bond formation. *J. Am. Chem. Soc.* **138**, 5585–5593 (2016). URL http://dx.doi.org/10.1021/jacs.5b13461.

[248] Zint, S. *et al.* Imaging Successive Intermediate States of the On-Surface Ullmann Reaction on Cu(111): Role of the Metal Coordination. *ACS Nano* **11**, 4183–4190 (2017). URL http://dx.doi.org/10.1021/acsnano.7b01109.

[249] Hapala, P. *et al.* Mechanism of high-resolution STM/AFM imaging with functionalized tips. *Phys. Rev. B - Condens. Matter Mater. Phys.* **90** (2014). URL http://dx.doi.org/10.1103/PhysRevB.90.085421.

[250] Komeda, T., Kim, Y. & Kawai, M. Lateral motion of adsorbate induced by vibrational mode excitation with inelastic tunneling electron. In *Surf. Sci.*, vol. 502-503, 12–17 (2002). URL http://dx.doi.org/10.1016/S0039-6028(01)01892-1.

[251] Ternes, M., Lutz, C. P., Hirjibehedin, C. F., Giessibl, F. J. & Heinrich, A. J. The Force Needed to Move an Atom on a Surface. *Science (80-.).* **319**, 1066–1069 (2008). URL http://www.sciencemag.org/cgi/doi/10.1126/science.1150288.

[252] Langewisch, G., Falter, J., Fuchs, H. & Schirmeisen, A. Forces during the controlled displacement of organic molecules. *Phys. Rev. Lett.* **110** (2013). URL http://dx.doi.org/10.1103/PhysRevLett.110.036101.

[253] Jarvis, S. P. *et al.* Measuring the mechanical properties of molecular conformers. *Nat. Commun.* **6**, 8338 (2015). URL http://dx.doi.org/10.1038/ncomms9338{%}5Cn.

[254] Kawai, S. *et al.* Superlubricity of graphene nanoribbons on gold surfaces. *Science (80-.).* **351**, 957–961 (2016). URL http://www.sciencemag.org/cgi/doi/10.1126/science.aad3569.

[255] Pawlak, R. *et al.* Single-molecule tribology: Force microscopy manipulation of a porphyrin derivative on a copper surface. *ACS Nano* **10**, 713–722 (2016). URL http://dx.doi.org/10.1021/acsnano.5b05761.

[256] Pawlak, R. *et al.* Single-molecule manipulation experiments to explore friction and adhesion. *Journal of Physics D: Applied Physics* **50**, 113003 (2017). URL http://stacks.iop.org/0022-3727/50/i=11/a=113003.

[257] Meyer, J. *et al.* Tuning the formation of discrete coordination nanostructures. *Chem. Commun.* **51**, 12621–12624 (2015). URL http://xlink.rsc.org/?DOI=C5CC02723C.

[258] Joachim, C. & Rapenne, G. Molecule concept nanocars: Chassis, wheels, and motors? *ACS Nano* **7**, 11–14 (2013). URL http://dx.doi.org/10.1021/nn3058246.

[259] Pawlak, R. & Meier, T. Fast and curious. *Nature Nanotechnology* **12**, 712–712 (2017). URL http://www.nature.com/doifinder/10.1038/nnano.2017.141.

[260] CNRS. Official website of the NanoCar Race. http://nanocar-race.cnrs.fr/indexEnglish.php (2018-04-25).

[261] Simpson, G. J., García-López, V., Petermeier, P., Grill, L. & Tour, J. M. How to build and race a fast nanocar. *Nature Nanotechnology* **12**, 604 (2017). URL http://dx.doi.org/10.1038/nnano.2017.137.

[262] Díez-Pérez, I. *et al.* Rectification and stability of a single molecular diode with controlled orientation. *Nature Chemistry* **1**, 635 (2009). URL http://dx.doi.org/10.1038/nchem.392.

[263] Leoni, T. *et al.* Controlling the Charge State of a Single Redox Molecular Switch. *Phys. Rev. Lett.* **106**, 216103 (2011). URL http://link.aps.org/doi/10.1103/PhysRevLett.106.216103.

[264] Hapala, P., Temirov, R., Tautz, F. S. & Jelínek, P. Origin of High-Resolution IETS-STM Images of Organic Molecules with Functionalized Tips. *Phys. Rev. Lett.* **113**, 226101 (2014). URL http://link.aps.org/doi/10.1103/PhysRevLett.113.226101.

[265] Ellner, M. *et al.* The Electric Field of CO Tips and Its Relevance for Atomic Force Microscopy. *Nano Lett.* **16**, 1974–80 (2016). URL http://dx.doi.org/10.1021/acs.nanolett.5b05251.

[266] Moll, N. *et al.* Image distortions of a partially fluorinated hydrocarbon molecule in atomic force microscopy with carbon monoxide terminated tips. *Nano Lett.* **14**, 6127–31 (2014). URL https://doi.org/10.1021/nl502113z.

[267] Lapadula, G. *et al.* One-photon near-infrared sensitization of well-defined Yb(III) surface complexes for NIR-to-NIR single nanoparticle imaging. *Chem. Mater.* **27**, 2033–2039 (2015). URL http://dx.doi.org/10.1021/acs.chemmater.5b00306.

[268] Pointillart, F. *et al.* Luminescence and single-molecule magnet behavior in lanthanide complexes involving a tetrathiafulvalene-fused dipyridophenazine ligand. *Inorg. Chem.* **54**, 5384–5397 (2015). URL http://dx.doi.org/10.1021/acs.inorgchem.5b00441.

[269] Poonia, N. S. & Bajaj, A. V. Coordination chemistry of alkali and alkaline earth cations. *Chemical Reviews* **79**, 389–445 (1979). URL http://dx.doi.org/10.1021/cr60321a002.

[270] Schmidt, E., Hourdakis, A. & Popov, A. I. Multinuclear nmr study of 2,2'-bipyridine complexes with alkali cations in nonaqueous solvents. *Inorganica Chimica Acta* **52**, 91 – 95 (1981). URL http://www.sciencedirect.com/science/article/pii/S0020169300885795.

[271] Hughes, D. L. Alkali-metal complexes. Part VII. Crystal and molecular structures of the o-nitrophenolatobis(1,10-phenanthroline) complexes of sodium and rubidium. *J. Chem. Soc., Dalton Trans.* 2347–2354 (1973). URL http://dx.doi.org/10.1039/DT9730002347.

[272] Qian, H. F. *et al.* Four sodium tetrafluoroborate directed supramolecular networks having 3- and 3,8-disubstituted 1,10-phenanthroline ligands. *Inorganica Chim. Acta* **405**, 1–8 (2013). URL http://dx.doi.org/10.1016/j.ica.2013.04.050.

[273] Decurtins, S. *et al.* A Concept for the Synthesis of 3-Dimensional Homo- and Bimetallic Oxalate-Bridged Networks [M2(ox)3]n. Structural, Moessbauer, and Magnetic Studies in the Field of Molecular-Based Magnets. *J. Am. Chem. Soc.* **116**, 9521–9528 (1994). URL http://pubs.acs.org/doi/abs/10.1021/ja00100a016.

[274] Wu, H. *et al.* Intramolecular electron transfer within the substituted tetrathiafulvalene-quinone dyads: Facilitated by metal ion and photomodulation in the presence of spiropyran. *J. Am. Chem. Soc.* **129**, 6839–6846 (2007). URL http://dx.doi.org/10.1021/ja0702824.

[275] Fang, C.-J., Zhu, Z., Sun, W., Xu, C.-H. & Yan, C.-H. New ttf derivatives: several molecular logic gates based on their switchable fluorescent emissions. *New J. Chem.* **31**, 580–586 (2007). URL http://dx.doi.org/10.1039/B618397B.

[276] Zhang, R. *et al.* Chemical mapping of a single molecule by plasmon-enhanced Raman scattering. *Nature* **498**, 82–86 (2013). URL http://dx.doi.org/10.1038/nature12151.

[277] Zhang, Y. *et al.* Visualizing coherent intermolecular dipole-dipole coupling in real space. *Nature* **531**, 623–627 (2016). URL http://dx.doi.org/10.1038/nature17428.

[278] Doppagne, B. *et al.* Vibronic spectroscopy with submolecular resolution from stm-induced electroluminescence. *Phys. Rev. Lett.* **118**, 127401 (2017). URL https://link.aps.org/doi/10.1103/PhysRevLett.118.127401.

[279] Gysin, U. *et al.* Large area scanning probe microscope in ultra-high vacuum demonstrated for electrostatic force measurements on high-voltage devices. *Beilstein Journal of Nanotechnology* **6**, 2485–2497 (2015). URL http://dx.doi.org/10.3762/bjnano.6.258.

[280] Schumacher, Z., Miyahara, Y., Spielhofer, A. & Grutter, P. Measurement of surface photovoltage by atomic force microscopy under pulsed illumination. *Phys. Rev. Applied* **5**, 044018 (2016). URL https://link.aps.org/doi/10.1103/PhysRevApplied.5.044018.

[281] Schumacher, Z., Spielhofer, A., Miyahara, Y. & Grutter, P. The limit of time resolution in frequency modulation atomic force microscopy by a pump-probe approach. *Applied Physics Letters* **110**, 053111 (2017). URL https://doi.org/10.1063/1.4975629.

[282] Schneiderbauer, M., Emmrich, M., Weymouth, A. J. & Giessibl, F. J. Co tip functionalization inverts atomic force microscopy contrast via short-range electrostatic forces. *Phys. Rev. Lett.* **112**, 1–5 (2014). URL http://dx.doi.org/10.1103/PhysRevLett.112.166102.

[283] Hapala, P. *et al.* Mapping the electrostatic force field of single molecules from high-resolution scanning probe images. *Nat. Commun.* **7**, 11560 (2016). URL `http://dx.doi.org/10.1038/ncomms11560`.

[284] Steurer, W. *et al.* Manipulation of the Charge State of Single Au Atoms on Insulating Multilayer Films. *Phys. Rev. Lett.* **114**, 036801 (2015). URL `http://link.aps.org/doi/10.1103/PhysRevLett.114.036801`.

[285] Kocić, N. *et al.* Periodic Charging of Individual Molecules Coupled to the Motion of an Atomic Force Microscopy Tip. *Nano Lett.* **15**, 4406–11 (2015). URL `http://dx.doi.org/10.1021/acs.nanolett.5b00711`.

[286] Bocquet, F., Nony, L. & Loppacher, C. Polarization effects in noncontact atomic force microscopy: A key to model the tip-sample interaction above charged adatoms. *Phys. Rev. B - Condens. Matter Mater. Phys.* **83**, 1–13 (2011).

[287] Miyahara, Y., Roy-Gobeil, A. & Grutter, P. Quantum state readout of individual quantum dots by electrostatic force detection. *Nanotechnology* **28**, 064001 (2017). URL `http://stacks.iop.org/0957-4484/28/i=6/a=064001`.

[288] Stomp, R. *et al.* Detection of single-electron charging in an individual inas quantum dot by noncontact atomic-force microscopy. *Phys. Rev. Lett.* **94**, 056802 (2005). URL `https://link.aps.org/doi/10.1103/PhysRevLett.94.056802`.

[289] Balzani, V. & Juris, A. Photochemistry and photophysics of ru(ii)-polypyridine complexes in the bologna group. from early studies to recent developments. *Coordination Chemistry Reviews* **211**, 97 – 115 (2001). URL `http://www.sciencedirect.com/science/article/pii/S0010854500002745`.

[290] Chong, M. C. *et al.* Narrow-Line Single-Molecule Transducer between Electronic Circuits and Surface Plasmons. *Phys. Rev. Lett.* **116**, 036802 (2016). URL `http://dx.doi.org/10.1103/PhysRevLett.116.036802`.

[291] Cocker, T. L., Peller, D., Yu, P., Repp, J. & Huber, R. Tracking the ultrafast motion of a single molecule by femtosecond orbital imaging. *Nature* **539**, 263 (2016). URL `http://dx.doi.org/10.1038/nature19816`.

[292] Heath, J. R. Molecular electronics. *Annual Review of Materials Research* **39**, 1–23 (2009). URL `https://doi.org/10.1146/annurev-matsci-082908-145401`.

[293] Coskun, A. *et al.* High hopes: can molecular electronics realise its potential? *Chem. Soc. Rev.* **41**, 4827–4859 (2012). URL `http://dx.doi.org/10.1039/C2CS35053J`.

[294] Green, J. E. *et al.* A 160-kilobit molecular electronic memory patterned at 10^{11} bits per square centimetre. *Nature* **445**, 414 (2007). URL `http://dx.doi.org/10.1038/nature05462`.

[295] Collier, C. P. *et al.* A [2]catenane-based solid state electronically reconfigurable switch. *Science* **289**, 1172–1175 (2000). URL `http://science.sciencemag.org/content/289/5482/1172`.

[296] Cheng, C. *et al.* An artificial molecular pump. *Nat. Nanotechnol.* **10**, 547 (2015). URL `http://dx.doi.org/10.1038/nnano.2015.96`.

[297] Bissell, R. A., Córdova, E., Kaifer, A. E. & Stoddart, J. F. A chemically and electrochemically switchable molecular shuttle. *Nature* **369**, 133 (1994). URL http://dx.doi.org/10.1038/369133a0http://10.0.4.14/369133a0.

[298] Kassem, S. *et al.* Artificial molecular motors. *Chem. Soc. Rev.* **46**, 2592–2621 (2017). URL http://dx.doi.org/10.1039/C7CS00245A.

[299] Ashton, P. R. *et al.* A [2] catenane made to order. *Angewandte Chemie International Edition in English* **28**, 1396–1399 (1989). URL http://dx.doi.org/10.1002/anie.198913961.

[300] Anelli, P. L., Spencer, N. & Stoddart, J. F. A molecular shuttle. *Journal of the American Chemical Society* **113**, 5131–5133 (1991). URL http://dx.doi.org/10.1021/ja00013a096.

[301] Asakawa, M. *et al.* A chemically and electrochemically switchable [2]catenane incorporating a tetrathiafulvalene unit. *Angewandte Chemie International Edition* **37**, 333–337 (1998). URL http://dx.doi.org/10.1002/(SICI)1521-3773(19980216)37:3<333::AID-ANIE333>3.0.CO;2-P.

List of Figures

Nomenclature

Symbols

Latin letters

A	Amplitude
A_{H}	Hamaker constant
b	bond length
$C(z)$	Capacitance of plate capacitor
d	closest tip-sample distance
$d\boldsymbol{S}$	Surface element of integral
dI_t/dV_b	Differential conductance
E	Energy
E_{abs}	Energy of optical absorption at S_0-S_1 transition
E_{bond}	Bonding energy
E_{CT}	Energy of the charge transfer state
E_F	Fermi energy
$E_{\mathrm{F,tip}}$	Fermi energy of the tip
$E_{\mathrm{F,s}}$	Fermi energy of the sample
E_{vac}	Vacuum level
E_μ	Energy of the state Ψ_μ of the tip
E_ν	Energy of the state Ψ_ν of the sample
e	Elementary charge
F	Force
F_{chem}	Chemical force between tip and sample
F_{elec}	Electrostatic force
$F_{\mathrm{elec,lr}}$	Long-range electrostatic force between tip and sample
$F_{\mathrm{elec,sr}}$	Short-range electrostatic force between tip and sample
F_{L}	Lateral force

F_{LJ}	Force of Lennard-Jones potential
F_{ts}	Total tip-sample force
F_{vdW}	Van der Waals force between tip and sample
f	Frequency
$f(E)$	Fermi function
f_0	Eigenfrequency
h	Planck constant
$\hbar$	Reduced Planck constant
I_{Si}	Current to heat Si plate of the mobile evaporator
I_t	Tunneling current
k_c	Stiffness of the tuning fork/cantilever
k_{ts}	Tip-sample stiffness
k^*	Effective spring constant
$M_{\mu\nu}$	Tunneling matrix element between the states Ψ_μ and Ψ_ν
m	Electron mass
m^*	Effective mass
n	Positive integer
P_{elec}	Electrical power
p_A	Pressure in the analysis chamber
$\boldsymbol{p}_{\mathrm{ind}}$	Induced dipole moment
Q	Quality factor
R	Radius of curvature of the tip
$\boldsymbol{r}_{\mathrm{tip}}$	Position of the tip
S_0	Singlet ground state
S_1	Singlet excited state
$s(t)$	Vertical motion of the oscillation of the tuning fork
T	Temperature
T_c	Critical temperature for superconductivity
T_{evap}	Evaporation temperature of molecules
$T_{\mathrm{B,He}}$	Boiling temperature of helium
$T_{\mathrm{B,N2}}$	Boiling temperature of nitrogen
t	Time
t_{osc}	Period of an oscillation cycle of the tuning fork
U	Potential
$U_{\mathrm{attr}}(z)$	Attractive interaction potential between two dipoles
U_{el}	Electrostatic potential
$U_{\mathrm{dip}}(z)$	Potential energy of a dipole
U_{LJ}	Lennard-Jones potential
U_{Morse}	Morse potential
U_{ts}	Tip-sample potential
U_{vdW}	Van der Waals potential
u	Substitute of $\cos(2\pi f_0 t)$

V_b	Sample bias voltage
V_{CPD}	Voltage compensating the contact potential difference
V_{ESD}	Applied voltage between capillary and entrance to the chamber for ESD
V_{Si}	Voltage to heat Si plate of the mobile evaporator
V^*	Bias voltage where the electrostatic force is compensated (voltage at maximum of $\Delta f(V_b)$ parabola)
w	Energy of electron or hole to excite phonons
x	Coordinate of one horizontal axis in the sample surface plane
y	Coordinate of one horizontal axis in the sample surface plane
z	Coordinate of the vertical axis between tip and sample

Greek letters

α_{A}	polarizability of atom A
α_{B}	polarizability of atom B
ΔA	Amplitude change
Δf	Frequency shift
Δf^*	Frequency shift at the maximum of a $\Delta f(V_b)$ parabola (frequency shift at voltage V^*
$\mathcal{E}$	Electric field
ϵ	Absorptivity
ϵ_0	Vacuum permittivity
ε	Emissivity of a surface
κ	Minimum inverse decay length for tunneling electrons
λ	Wavelength
ν	Frequency of photons
ξ	Decay length of Morse potential
$\rho(\boldsymbol{r}_{\mathrm{tip}}, E_F)$	Local density of states at the Fermi energy at the tip position
$\rho_{\mathrm{tip}(E_F)}$	Density of states per unit volume
σ	Equilibrium distance
Φ	Work function
Φ_{tip}	Work function of the tip
Φ_{s}	Work function of the sample
Ψ_μ	State of tip
Ψ_ν	State of sample

Abbreviations

A chamber	Analysis chamber
AFM	Atomic force microscopy or atomic force microscope
AM	Amplitude-modulation
BCS	Bardeen-Cooper-Schrieffer
Ch.	Chapter
CT	Charge transfer
CTC	Charge transfer complex
CPD	Contact potential difference
DA	Donor-acceptor
DBBN	3,3'-dibromo-2,2'-binaphthalene
DSSC	dye sensitized solar cell
ESD	Electrospray deposition
Eq.	Equation
FIB	Focused ion beam
Fig.	Figure
FM	Frequency-modulation
fcc	Face-centered-cubic
$HBC6C_{12}$	Hexadodecyl-hexa-perihexabenzocoronene
hcp	Hexagonal-close-packed
HOMO	Highest occupied molecular orbital
ICT	Intramolecular charge transfer
I-DNT-VW	V-shaped dinaphthothiophene core with two iodine atoms attached
KPFM	Kelvin Probe Force Microscopy
LCPD	Local contact potential difference
LDOS	Local density of states
LUMO	Highest unoccupied molecular orbital
LT	Low temperature
MBS	Majorana bound state
ML	Monolayer
P chamber	Preparation chamber
PDOS	Projected density of stats
RT	Room temperature
Sec.	Section
SND	Swiss Nano Dragster (4'-(4-methylphenyl)-2,2':6',2"-terpyridine)
STM	Scanning tunneling microscopy or scanning tunneling microscope
STS	Scanning tunneling spectroscopy

Tab.	Table
TERS	Tip-enhanced Raman spectroscopy
TFAP	Trifluorantheno[3.3.3]propellane
TNP	Trinaphtho[3.3.3]propellane
TTF-dye	Tetrathiafulvalene-quinoxaline
TTF-dppz	Tetrathiafulvalene-fused dipyridophenazine
tDBA	Triangular dehydrobenzo[12]annulene
UHV	Ultra-high vacuum
vdW	Van der Waals
ZBP	Zero bias peak
3D	Three-dimensional

Acknowledgements

The results presented in this thesis have been achieved due to the work and contributions of many people.

- Prof. Ernst Meyer created a research group with excellent knowledge and long-term experience in the field of scanning probe techniques. I thank him for giving me the opportunity to work in his group, for his advices and especially for the open-minded environment where scientific ideas can grow.

- I thank Dr. Thilo Glatzel for his great support, his enthusiasm about research and many ideas I have got from him. It was always possible to discuss with him and find new perspectives for a given scientific problem. I am also grateful for proofreading the manuscript of my thesis and for his help during the whole time as a PhD student.

- Dr. Rémy Pawlak spent a lot of time with me in the lab where he taught me how to use the „LT“and how to conduct experiments on the level of single atoms and molecules. He was never tired to answer my questions or show me something in the lab. The knowledge he shared with me allowed me to realize my research for this thesis. He proofread my manuscript and drafts for publications. I could assist at the experiments he performed about the Majorana fermion (sec. 3.4). Additionally, our team work lead to our great success at the NanoCar Race and some victories on the football field. Merci pour tout!

- I thank Dr. Shigeki Kawai for his support with the experiments, especially the spectroscopy measurements where I could benefit from his broad experience. I would also like to acknowledge his introduction to the measurement system and the experiments he performed about on-surface chemical reactions and bond analysis (secs. 3.2, 3.3) where I could learn a lot about chemistry, publishing and efficient experimental procedures.

- Dr. Antoine Hinaut prepared the samples by the electrospray deposition technique which I analyzed by STM and AFM. I thank him for this work and for

helping me with scientific and technical problems. Furthermore, he is also an excellent office neighbour and host for BBQs. I am grateful for the time we spent together at work and in free time.

- I thank Prof. Alexis Baratoff for sharing his tremendous knowledge in extensive discussions about the donor-acceptor molecule which showed me the theoretical background of my experimental work.

- I thank Prof. Silvio Decurtins and Dr. Shi-Xia Liu for the excellent collaboration, the synthesis of the donor-acceptor molecules and many discussions about molecular properties.

- I would like to thank Dr. Delphine Sordes, Dr. Corentin Durand, Dr. We-Hyo Soe and Dr. Christian Joachim for their help, the organization and preparation of the NanoCar Race at the CEMES in Toulouse.

- I thank Dr. Pavel Jelínek and Dr. Prokop Hapala for the DFT calculations of the TTF-dppz molecule and the possibility to get an introduction to DFT at the Academy of Sciences in Prague. I also thank Dr. Nicolas Renaud for the simulations he performed about the Swiss Nano Dragster on Au(111).

- I thank the whole technical staff for supporting me in maintaining, repairing or constructing equipment for the measurements, especially Yves Pellmont with whom I built the mobile evaporators.

- I thank Sara Freund, my PhD mate who started at the same time in the group, for the everyday chats and deep discussions in the office, the jokes and stories we told each other, for her help and for many activities she organized.

- Dr. Lucas Moser, Dr. Marcin Kisiel, Olha Popova, Dr. Res Jöhr, Dilek Yildiz and all other group members made my time as a PhD student with all its ups and downs to a great time of pleasure and personal development! I thank you all for the many times you made me laugh and the moments we shared at work, at conferences, during breaks and beyond.

- I thank my parents, Wolfgang and Rosmarie, my aunt Verena, brother Hannes and sister Lea and my whole family for being there for me at any moment and for all the energy and love I have got from them. I am grateful for the support of my friends who are willing to listen to my stories if it is about physics or not.

List of publications & communications

Peer-reviewed journal publications

I authored 12 publications in peer-reviewed journals: ACS Nano (3), Nature Communications (2), Nature Nanotechnology (1), Nanoscale (1), npj Quantum Information (1), Small (1), Science Advances (1), J. Phys. Chem. C (1), J. Phys. D: Appl. Phys. (1).
The publication list can be found online: Orcid ID 0000-0003-0606-5131

1. **Meier, T.**; Pawlak, R.; Kawai, S.; Geng, Y.; Liu, X.; Decurtins, S.; Hapala, P.; Baratoff, A.; Liu, S.-X.; Jelínek, P.; Meyer, E.; Glatzel, T. Donor-Acceptor Properties of a Single-Molecule Altered by On-Surface Complex Formation. *ACS Nano* **11,** 8413 (2017). DOI: 10.1021/acsnano.7b03954

2. Pawlak, R.; **Meier, T.**; Renaud, N.; Kisiel, M.; Hinaut, A.; Glatzel, T.; Sordes, D.; Durand, C.; Soe, W-H.; Baratoff, A.; Joachim, C.; Housecroft, C. E.; Constable, E. C.; Meyer, E. Design and Characterization of an Electrically Powered Single Molecule on Gold. *ACS Nano* **11,** 9930 (2017). DOI: 10.1021/acsnano.7b03955

3. Hinaut, A.; **Meier, T.**; Pawlak, R.; Freund, S.; Jöhr, R.; Glatzel, T.; Decurtins, S.; Müllen, K.; Narita, A.; Liu, S.-X.; Meyer, E. Electrospray Deposition of Structurally Complex Molecules Revealed by Atomic Force Microscopy. *Nanoscale* **10,** 1337 (2018). DOI: 10.1039/C7NR06261C

4. Pawlak, R. & **Meier, T.** Fast and Curious. *Nat. Nano,* **12,** 712 (2017). DOI: 10.1038/nnano.2017.141

5. Kawai, S.; Sadeghi, A.; Okamoto, T.; Mitsui, C.; Pawlak, R.; **Meier, T.**; Takeya, J.; Goedecker, S.; Meyer, E. Organometallic Bonding in an Ullmann-Type On-Surface Chemical Reaction Studied by High-Resolution Atomic Force Microscopy *Small* **12,** 5303 (2016). DOI: 10.1002/smll.201601216

6. Kawai, S.; Nishiuchi, T.; Kodama, T.; Spijker, P.; Pawlak, R.; **Meier, T.**; Tracey, J.; Kubo, T.; Meyer, E.; Foster, A. S. Direct quantitative measurement of the C=O...H-C bond by atomic force microscopy. *Sci. Adv.* **3,** 1603258 (2017). DOI: 10.1126/sciadv.1603258

7. Kawai, S.; Haapasilta, V.; Lindner, B. D.; Tahara, K.; Spijker, P.; Buitendijk, J. A.; Pawlak, R.; **Meier, T.**; Tobe, Y.; Foster, A. S.; Meyer, E. Thermal Control of Sequential On-Surface Transformation of a Hydrocarbon Molecule on a Copper Surface. *Nat. Commun.* **7,** 12711 (2016). DOI: 10.1038/ncomms12711

8. Kawai, S.; Takahashi, K.; Ito, S.; Pawlak, R.; **Meier, T.**; Spijker, P.; Canova, F. F.; Tracey, J.; Nozaki, K.; Foster, A. S.; Meyer, E. Competing Annulene and Radialene Structures in a Single Anti-Aromatic Molecule Studied by High-Resolution Atomic Force Microscopy *ACS Nano* **11,** 8122 (2017). DOI: 10.1021/acsnano.7b02973

9. Pawlak, R.; Kisiel, M.; Klinovaja, J.; **Meier, T.**; Kawai, S.; Glatzel, T.; Loss, D.; Meyer, E. Probing Atomic Structure and Majorana Wavefunctions in Mono-Atomic Fe Chains on Superconducting Pb Surface. *npj Quantum Information* **2,** 16035 (2016). DOI: 10.1038/npjqi.2016.35

10. Pawlak, R.; Kawai, S.; **Meier, T.**; Glatzel, T.; Baratoff, A.; Meyer, E. Single–Molecule Manipulation Experiments to Explore Friction And Adhesion. *J. Phys. D: Appl. Phys.* **50,** 113003 (2017). DOI: 10.1088/1361-6463/aa599d

11. Pawlak, R.; Sadeghi, A.; Jöhr, R.; Hinaut, A.; **Meier, T.**; Kawai, S.; Zajac, L.; Olszowski, P.; Godlewski, S.; Such, B.; Glatzel, T. Goedecker, S.; Szymónski, M.; Meyer, E. Hydroxyl-Induced Partial Charge States of Single Porphyrins on Titania Rutile. *J. Phys. Chem. C,* **121,** 3607 (2017). DOI: 10.1021/acs.jpcc.6b11873

12. Piquero-Zulaica, I.; Lobo-Checa, J.; Sadeghi, A.; Abd El-Fattah, Z.; Mitsui, C.; Okamoto, T.; Pawlak, R.; **Meier, T.**; Arnau, A.; Ortega, J. E.; Takeya, J.; Goedecker, S.; Meyer, E.; Kawai, S. Precise Engineering of Quantum Dot Array Coupling Through Their Barrier Widths *Nat. Commun.* **8,** 787 (2017). DOI: 10.1038/s41467-017-00872-2

Presentations

1. **Meier, T.**; Pawlak, R.; Kawai, S.; Liu, S.-X.; Decurtins, S.; Glatzel, T.; Meyer, E. Probing Single Donor-Acceptor Molecules on Thin Insulating Films. International Workshop: High-Resolution AFM/STM Imaging, Prague, Czech Republique (23/02/2015).

2. **Meier, T.**; Pawlak, R.; Kawai, S.; Liu, S.-X.; Decurtins, S.; Meyer, E.; Glatzel, T. Probing Single Donor-Acceptor Molecules on Thin Insulating Films. DPG-Frühjahrstagung, Berlin, Germany (18/03/2015).

3. **Meier, T.**; Pawlak, R.; Kawai, S.; Geng, Y.; Liu, S.-X.; Hapala, P.; Baratoff, A.; Decurtins, S.; Jelínek, P.; Meyer, E; Glatzel, T. Charge distribution of adsorbed single molecules: the effect of the underlying surface. Seminar at Czech Academy of Science, Prague, Czech Republic (11/02/2016)

4. **Meier, T.**; Pawlak, R.; Kawai, S.; Liu, S.-X.; Geng, Y.; Hapala, P.; Jelínek, P.; Baratoff, A.; Decurtins, S.; Meyer, E; Glatzel, T. Interdependence of Adsorption site and Charge Distribution in a Single Donor-Acceptor Molecule Adsorbed on an Ionic Crystal. DPG-Frühjahrstagung, Regensburg, Germany (07/03/2016).

5. **Meier, T.**; Pawlak, R.; Kawai, S.; Geng, Y.; Liu, S.-X.; Hapala, P.; Baratoff, A.; Decurtins, S.; Jelínek, P.; Meyer, E; Glatzel, T. The Charge Distribution of a Donor-Acceptor Molecule Altered by an Ionic Thin Film. 19th International Conference on NC-AFM, Nottingham, United Kingdom (27/07/2016).

6. **Meier, T.**; Pawlak, R.; Kawai, S.; Geng, Y.; Liu, S.-X.; Hapala, P.; Baratoff, A.; Decurtins, S.; Jelínek, P.; Meyer, E; Glatzel, T. The Charge Distribution of a Donor-Acceptor Molecule Altered by an Ionic Thin Film. The 26th Conference of the Condensed Matter Division of the EPS, Groningen, Netherlands (05/09/2016).

7. **Meier, T.**; Pawlak, R.; Kawai, S.; Geng, Y.; Liu, X.; Decurtins, S.; Hapala, P.; Baratoff, A.; Liu, S.-X.; Jelínek, P.; Meyer, E; Glatzel, T. Modification des Propriétés Electroniques d'une Molécule Donneuse-Acceptrice Unique par Interaction avec un Cation de Sodium, Forum Des Microscopies A Sonde Locale. Vichy Spa de Juvignac, France (22/03/2017)

8. **Meier, T.**; Pawlak, R.; Kawai, S.; Geng, Y.; Liu, X.; Decurtins, S.; Hapala, P.; Baratoff, A.; Liu, S.-X.; Jelínek, P.; Meyer, E; Glatzel, T. The Donor-Acceptor Properties of a Single Molecule Altered by On-Surface Complex Formation. Workshop on SPM & On-Surface Chemistry, Prague, Czech Republic (23/05/2017)

9. **Meier, T.**; Pawlak, R.; Kawai, S.; Geng, Y.; Liu, X.; Decurtins, S.; Hapala, P.; Baratoff, A.; Liu, S.-X.; Jelínek, P.; Meyer, E; Glatzel, T. The Donor-Acceptor Properties of a Single Molecule Altered by On-Surface Complex Formation & the Swiss Team at the NanoCar Race in Toulouse. molCHsurf Meeting, Bern, Switzerland (16/06/2017)

10. **Meier, T.**; Pawlak, R.; Kawai, S.; Hinaut, A.; Glatzel, T.; Meyer, E. On-Surface Chemical Reactions, Single Molecule Manipulations and Donor-Acceptor Properties Studied by STM and AFM. Seminar at nanoGUNE, San Sebastian, Spain (23/10/2017)

Posters

1. **Meier, T.**; Pawlak, R.; Kawai, S.; Liu, S.-X.; Decurtins, S.; Meyer, E.; Glatzel, T. Probing Single Donor-Acceptor Molecules on Thin Insulating Films. 18th International Conference on NC-AFM, Cassis, France (08/09/2015).

2. **Meier, T.**; Pawlak, R.; Kawai, S.; Geng, Y.; Liu, S.-X.; Hapala, P.; Baratoff, A.; Decurtins, S.; Jelínek, P.; Meyer, E; Glatzel, T. Interdependence of Adsorption Site and Charge Distribution in a Single Donor-Acceptor Molecule Adsorbed on an Ionic Crystal. Forum Des Microscopies A Sonde Locale, Sochaux, France (21/03/2016).

3. **Meier, T.**; Pawlak, R.; Kawai, S.; Geng, Y.; Liu, X.; Decurtins, S.; Hapala, P.; Baratoff, A.; Liu, S.-X.; Jelínek, P.; Meyer, E; Glatzel, T. Donor-Acceptor Properties of Prototypical and "Real" Dyes Investigated by AFM. 20th International Conference on NC-AFM, Suzhou, China (26/09/2017).